Formulation of a Dynamic Material Point Method and Applications to Soil–Water–Geotextile Systems

Von der Fakultät für Bau– und Umweltingenieurwissenschaften
der Universität Stuttgart
zur Erlangung der Würde eines Doktors der Ingenieurwissenschaften (Dr.-Ing.)
genehmigte Abhandlung,

vorgelegt von

FURSAN M. HAMAD

aus Bagdad, Irak

Hauptberichter:	Prof. Dr.-Ing. Pieter A. Vermeer
Mitberichter:	Prof. Dr.-Ing. habil. Zdzisław Więckowski
Mitberichter:	Prof. Dr.-Ing. habil. Christian Moormann
Mitberichter:	Prof. Dr.-Ing. habil. Bernhard Westrich

Tag der mündlichen Prüfung: 28. Mai 2014

Institut für Geotechnik der Universität Stuttgart

2014

Mitteilung 70
des Instituts für Geotechnik
Universität Stuttgart, Germany, 2014

Editor:
Prof. Dr.-Ing. habil. Christian Moormann

Institut für Geotechnik
Universität Stuttgart
Pfaffenwaldring 35
70569 Stuttgart

Keywords: Material point method, membrane modelling, soil–water–geotextile systems

Printed by e.kurz + co, druck und medientechnik GmbH, Stuttgart, Germany, 2014

ISBN 978-3-921837-70-2
(D93 - Dissertation, Universität Stuttgart)

Preface of the editor

The Institute of Geotechnical Engineering at the University of Stuttgart (IGS) publishes with issue no. 70 of its proceedings the dissertation of Dr.-Ing. Fursan M. Hamad titled 'Formulation of a Dynamic Material Point Method and Applications to Soil–Water–Geotextile Systems'. The thesis presents a new and unique approach to simulate the installation process and the behaviour of geosynthetics systems for geomechanical applications.

In recent decades geosynthetic materials have been increasingly used in geotechnical and water engineering applications comprising reinforcement, protection, filtration and screening. Especially in coastal and scour protection new geosynthetic concepts combining geotextiles with available or dredged materials such as sand or slurry mixture have proven as an efficient technical and economical alternative to conventional construction materials like rock or concrete amour units. Such geosynthetic–soil systems, like geotextile bags, tubes or containers, have to be designed and manufactured in a way to survive the installation process considering large displacements and withstand the often forbidding working conditions.

The numerical simulation of such systems, i.e. modelling of a thin membrane in interaction with soil of complex constitutive behaviour under large deformation, is a challenging task especially when additionally the fluid–structure interaction should also be simulated. On modelling these problems with a Lagrangian finite element method, the mesh can become too distorted and remeshing is essential. In the past decades, considerable efforts have been made to adopt what is called meshfree methods to mitigate the problems related to mesh distortion. One of these methods is the Material Point Method (MPM) that represents the continuum field as Lagrangian material points (particles), which can move through the fixed background computational mesh. Within the MPM framework Dr. Hamad elaborated a new membrane development which models a tensile membrane using two–dimensional tri–angular elements. This membrane mesh is free to move through a three–dimensional mesh of non–structured tetrahedral elements. Coupling the finite element membrane with the MPM soil has more accurate and less stress oscillation than the classical MPM membrane.

Dr. Hamad shows the great potential of the MPM method with the coupled formulation of membrane by modelling different geotechnical applications of geosynthetics. A challenging and very impressive application is to model the releasing of a geocontainer from a split barge considering the interaction between the filled geotextile and the barge as well as the fluid–geocontainer interaction during container sinking. The effect of geocontainers' interaction has been investigated by dropping a second geocontainer. Another application which demonstrates the potential of the new approach for many onshore geosynthetic systems is the investigation of the stability of a reinforced embankment by simulating its failure mechanism. The effect of the embedded geotex-

tile is clearly illustrated on the displacement field which is referred to a non–reinforced embankment.

The thesis of Dr. Hamad demonstrates that the simulation model he developed is a powerful and versatile tool for a better understanding of the complex soil–water–geotextile interaction as well as for the technical and economical optimisation of innovative geosynthetic systems.

Christian Moormann
Stuttgart, July 2014

Preface of the supervisor

In recent years coupled Eulerian–Lagrangian Finite Element Methods have been applied successfully for solving large–deformation problems, e.g. for simulating pile driving, but it is difficult to extend this approach straightforwardly to soil–fluid interaction problems as typical in branches of geotechnical engineering. For this reason, I have introduced the so–called Material Point Method (MPM) at the Institute for Geotechnical Engineering of Stuttgart University in 2005. Professor Zdzisław Więckowski, the second supervisor of this thesis by Fursan M. Hamad, largely inspired me to do so.

This thesis by Fursan M. Hamad is the third one in row on MPM that I supervised at Stuttgart University. The first one by Lars Beuth (2012) is on quasi–static problems and single–phase material behaviour. The second one by Issam Al–Kafaji (2013) includes dynamical problems and two–phase material behaviour, i.e. the generation and dissipation of excess pore–pressures in water–saturated soil. In the present thesis on MPM by Fursan Hamad extension is made to free water, i.e. the field of Computational Fluid Dynamics (CFD). Moreover a novel elegant way of modelling geomembranes is introduced and shown to be by far superior to an existing approach. Finally numerical procedures are applied to simulate the dropping of so–called geocontainers in water.

On considering both free water and groundwater, numerical solutions of boundary–value problems tend to suffer from spurious pressure oscillations, at least on using MPM. I am extremely happy that Fursan found a remedy by introducing an averaged (nodal) water pressure.

Before coming to Stuttgart Fursan Hamad as well as his colleague Issam Al–Kafaji were employed at the University of Baghdad, but because of the political situation it was hardly possible to maintain contact to this university. No doubt, the fracturing of Iraq has significantly damaged this previously strong university. However, I am happy to observe that alumni, like Fursan Hamad, are doing so well.

After his first year as a PhD student at the University of Stuttgart Fursan continued his work for nearly two years at the consulting and research establishment 'Deltares' in Delft, The Netherlands. This stay at Deltares was possible with financial support from the European Commission, being embedded in the so–called 'Geo–Install' project; an IAPP project within the framework of the European Marie Curie FP7 research funding programme. It provided Fursan the opportunity of working also in an industry environment and obviously in another European country. No doubt, Fursan had to adjust himself to different ways of working and together with his family he had to get used to different places of living. However, despite such disruptions Fursan maintained full focus on his work and contributed significantly to further developments of MPM.

Pieter A. Vermeer
Nederhorst den Berg, Netherlands, July 2014

Acknowledgments

First and foremost, I would like to express my sincere appreciation to my thesis supervisor Professor Pieter Vermeer for his guidance, inspiration and patience throughout my PhD study. His advices on research as well as professional practice have been priceless without it, I would never walk so far on the academic road. My gratitude extends to Professor Zdzisław Więckowski for the precious contribution with the precision of a mechanical engineer. I want also to thank Professor Christian Moormann for the significant support to get my thesis done. Last but not least, I warmly thank Professor Bernhard Westrich for the invaluable daily discussions.

Here, I would like to especially thank Professor Dieter Stolle for sharing ideas and the friendly encouragements, you have been a tremendous mentor for me. Likewise, I express my appreciation to Dr. Issam Al–Kafaji and Dr. Corné Coetzee for introducing me to the MPM world. Special thanks to the European project (Geo–Install) represented by its coordinator Professor Minna Karstunen and the people involved in this project: Professor Adam Bezuijen, Dr. Alexander Rohe, Shuhong Tan, Phuong Nguyen, Wiep Hellinga and others. Furthermore, I feel glad to Dr. Martino Leoni as well as Dr. David Mašín for their help.

In Stuttgart, I have shared nice memories with great support. Particularly, from the IGS people: Bernd Zweschper, Dr. Maximilian Huber, Dr. Annette Lächler, Dr. Axel Möllmann, Ruth Rose, Nadja Springer, Sylvia Eckard, Dr. Syawal Satibi, Dr. Marcus Schneider, Reinhold Mößner, Stephan Ries, Johannes Aschrafi, Seyedfarzad Fatemizadeh, Linus Klein, Julia Knopp, Patrik Buhmann and Dominik Günther. From the University of Baghdad, I acknowledge the support of Oday Abdullah, Dr. Asmaa Rashid, and Yihya Hamad.

Finally, I am deeply indebted to my parents, brothers and sisters. A special appreciation to my wife and my little daughter for their endless love, support and understanding.

Fursan Hamad
Stuttgart, July 2014

Contents

Abstract

Geosynthetic materials have a growing use in geomechanical applications as a construction material employed largely for reinforcement, protection and screening. In coastal and hydraulic engineering, the innovative use of thin geosynthetics combined with dredged materials provides efficient alternative for conventional materials. Major concern of manufacturers and engineers is to built soil–geosynthetic units able to survive the installation process and withstand the working conditions. Loading condition might not only be time dependent, though it is commonly associated with large material movement and deformation.

Numerical modelling of thin–structures joined with history–dependent materials under large deformation is challenging topic for the traditional methods. Additional difficulty is expected if water or liquid behaviour material is involved such that treatment of the fluid–structure interaction formulation is necessary. Several modern methods, employing the concepts of particles in meshless or mesh–based scheme, offer the ability to handle multiphysics problem in one computational framework. The material point method (MPM) is an arbitrary Lagrangian–Eulerian description suited for granular material and geomechanical simulations. Although MPM represents the continuum by material points, solution is performed on the computational mesh. Thus, imposing boundary conditions in MPM is not aligned with the material representation. In this thesis, two sets of material points are introduced. The first is obtained by tracking the surface orientation and hence traction boundary condition is applied accurately. On the other hand, the prescribed boundary particles set is designed for tracking the non–zero kinematic boundary condition.

Coupled FE–MP method is a novel scheme introduced in this research to incorporate the thin membrane using finite element formulation in the MPM frame allowing large movement of the thin structure. The FE membrane and other MPM substances contribute to the same computational mesh where the equations of motion are solved. The proposed approach has shown less mesh sensitivity and smoother stress distribution as compared to an existing MPM membrane formulation. Furthermore, it has been found that the suggested methodology predicts lateral deformation much accurately than the other. Giving the explicit nature of the current MPM algorithm obliges assigning sensible mass to all materials, which causes numerical difficulties when geotextile material has extremely small mass as compared to soil. Even though, the coupled approach was able to estimate the correct solution for negligible amount of membrane mass.

Similar to other Lagrangian particle methods, MPM accommodates material convection by the natural movement of the material points. Therefore, fluid is integrated in MPM in a similar fashion to the solid materials considering the difference in the material evolution. However, the high bulk modulus of liquids causes numerical instability, which requires applying a stabilisation technique. Therefore, a combination of nodal

mixed discretisation and average nodal pressure approaches is found to be essential to achieve fairly smooth pressure distribution. The capacity of the algorithm to capture the real time dynamic behaviour and the steady–state solution has been examined for two validation cases. On top of that, an algorithm based on the continuous density field is suggested in order to detect the free surface condition in the flowing fluid.

Geocontainers are large geotextile containers filled with sandy materials and dropped in place using a split barge. Special attention has been paid to simulate this problem in MPM. The container releasing stage from the barge is carried out where the effect of the frictional contact between the barge and geotextile material is investigated. After seating the container on a subsoil layer, a second container is released where interaction between the two containers is taking place. Proceeding with the stage of dropping geocontainers into water, the results of two experiments have been reproduced: lab scale test and full–model test. While validating the fluid model with the controlled lab test is the aim of the first test, more focus has been addressed to the geotextile forces as compared to the field measurements in the second simulation.

Zusammenfassung

In den vergangenen Jahrzehnten wurden immer häufiger Geotextilien in der Baupraxis eingesetzt mit dem Ziel der Bewehrung, Filtration, Schutz und Trennung von Bodenmaterialien. Vor allem in der marinen Geotechnik und im Wasserbau werden Geotextilien für innovative Lösungen eingesetzt: Hier werden Geocontainer bei der Herstellung von z. B. Dämmen, Deichen oder Wellenbrechern eingesetzt, welche von einem Schiff direkt ins Wasser abgelassen werden. Bei der Bemessung dieser Geocontainer, einer Verbundkonstruktion aus Geotextil und Boden, sind der Phasen des Herstellungsprozesses und der Verwendung z. B. als Damm maßgebend. Die Bemessung muss die dynamischen Belastungen berücksichtigen, welche aus der Herstellung und der Belastung z. B. aus Wellen resultiert. Praktische Anwendungen und Laborversuche zeigen, dass hierbei große Verformungen der Verbundkonstruktion auftreten.

Diese Dissertation ist thematisch in die folgenden Teile unterteilt:

Kapitel 2: In diesem Kapitel werden die kontinuumsmechanischen Grundlagen zusammengestellt, welche für die Simulation von großen Verformungen mittels numerischer Methoden erforderlich sind. Es werden die Euler'schen und Lagrange'schen Methode erläutert und miteinander verglichen. In diesem Zusammenhang werden netzfreie Methoden und die netzabhängige Material Point Methode (MPM) erklärt. Beide numerische Methoden werden bei der Simulation einer inkompressiblen Flüssigkeit und von dünnwandigen Strukturen beispielhaft angewendet.

In **Kapitel 3** wird eine detaillierte kontinuumsmechanische Herleitung der dynamischen Material Point Methode (MPM) vorgestellt. Die Weiterentwicklung und Verbesserung dieser numerischen Simulationsmethode ermöglicht die realitätsnahe Abbildung von vorgeschriebenen kinematischen Bedingungen und Oberflächen, welche exemplarisch in einer Parameterstudie angewendet werden. Die Ergebnisse der Simulation des Kollapses eines granularen Materials mit MPM werden mit experimentellen Messwerten verglichen.

Kapitel 4: Aufbauend auf diesen Erkenntnissen, werden zwei Formulierungen zur Abbildung einer Membran hergeleitet: Die erste Herangehensweise verwendet eine MPM Formulierung in Kombination mit der klassischen Membrantheorie [191]. Die zweite, alternative neue Herangehensweise simuliert die Membrane als Lagrange'sches Kontinuum, welche sich durch das MPM Netz bewegt. Beide Methoden werden hergeleitet und miteinander verglichen. An Hand eines Feder–Masse Systems werden die Netzsensitivität und die Prognose von Spannungen und Verformungen untersucht. Die neue Methode zeigt in allen untersuchten Fällen Vorteile gegenüber der klassischen MPM Theorie

in Kombination mit der klassischen Membrantheorie [191]. Dieser Ansatz wird für die Simulation einer dreidimensionalen Fragestellung erweitert, wodurch die Interaktion von Boden und Geotextil unter Berücksichtigung von großen Verformungen möglich ist. Dies wird in einem Validierungsbeispiel aufgezeigt.

In **Kapitel 5** wird die MPM Modellierung von inkompressiblen Flüssigkeiten dargestellt. Um die explizite Zeitintegration einer inkompressiblen Flüssigkeit durchführen zu können, wird dem Fluid eine geringfügige Kompressibilität zugewiesen. Stabilisierung dieser numerische Methodik, werden Algorithmen aufgezeigt, mit deren Hilfe realistisches von Druck– und Geschwindigkeitsfeldern berechnet werden können. Darüber hinaus wird ein Algorithmus zur Bestimmung der Wasseroberfläche abgeleitet. Diese Modellierungsansätze werden an einem theoretischen Fallbeispiel angewendet, das den Kollaps einer Wassersäule simuliert. In einer weiteren Parameterstudie zur Interaktion zwischen Fluid und Struktur wird die Effizienz der verwendeten Algorithmen beispielhaft dargestellt.

Kapitel 6 beinhaltet eine umfassende Fallstudie zur Simulation von Geocontainern. Ein Geocontainer ist ein mit Sand gefülltes Geotextil, welches von einem Schiff ins Wasser ablassen wird und vor allem im Küstenschutz eingesetzt wird. Zur untersuchung des Komplexen Herstellungsvorgangs wurden verschiedene experimentelle Untersuchungen durchgeführt, welche Grundlage für analytische Näherungslösungen in der Bemessung waren und in dieser Fallstudie zum Vergleich mit den MPM Simulationsergebnissen dienen. Die dynamische Material Point Methode wurde zum Abbilden dieses Prozesses verwendet, um die komplexe Interaktion zwischen Boden, Fluid und Geotextil abzubilden. Dieser Vorgang wird zweistufig simuliert, um die Effektivität der entwickelten Algorithmen darzustellen: In einem erste schnitt wird das Wasser vernachlässigt, um die Zugkräfte im Geotextil als auch die Interaktion zwischen dem Geotextil und dem Schiff zu untersuchen. In weiterführenden Untersuchungen wird auch das Wasser berücksichtigt, um den Vergleich mit Labor– und Feldmessungen durchführen zu können. In diesem Kontext wurden die beobachteten Geschwindigkeitsfelder miteinander verglichen. Neben diesen Untersuchungen wurde auch der Herstellungsvorgang von mehreren Geocontainern untersucht, wobei besonderes Augenmerk auf die Interaktion gelegt wurde.

Im abschließenden **Kapitel 7** werden die Themen dieser Dissertation zusammengefasst und Empfehlungen für zukünftige Forschung gegeben.

Chapter 1

Introduction

In recent decades, geosynthetic materials are becoming more popular as a construction material in civil engineering. The growing applications of these materials are mainly tailored in reinforcement, filtration, protection and separation. For at least one of such functions, different products are available like geotextiles, geomembranes, geogrids, and other geocomposites [144].

In coastal and hydraulic engineering, conventional construction materials like rock or concrete armour units might be expensive or not accessible. Therefore, geotextile systems are acknowledged as an efficient economical alternative built on site by combining geotextile with available materials such as sand or slurry mixture. The geotextile systems or *geosystems* can take different shapes according to the purpose of the design. Examples of famous geosystems used for bank construction and protection structures are illustrated in Figure 1.1. Furthermore, geosystems are widely applied for land reclamation and temporary structures.

The *geocontainer* is a large sand or dredged material unit capsulated inside a prefabricated geotextile and placed in the desired position using a split barge. Single container can be employed to isolate contaminated materials, or structure of many containers is commonly used for constructing breakwaters and dams, or to build artificial reefs. For dam construction, the core or the deep layer is built of geocontainers whereas *geotubes* are applied for the upper layers. The geotube is made of highly resistant permeable geotextile forming long tube, which is then filled with soil and water mixture. Beside dikes construction, geotubes are frequently adopted for erosion and shoreline protection. For river bank stabilisation or slope protection, contained soil in geotextile fabric can be applied as well as *geocurtain* in which the permeable geotextile is holding the solid materials while water flows through, see Figure 1.1. More geotechnical applications using geosynthetic materials are highlighted in numerous references; e.g. [92, 101, 144].

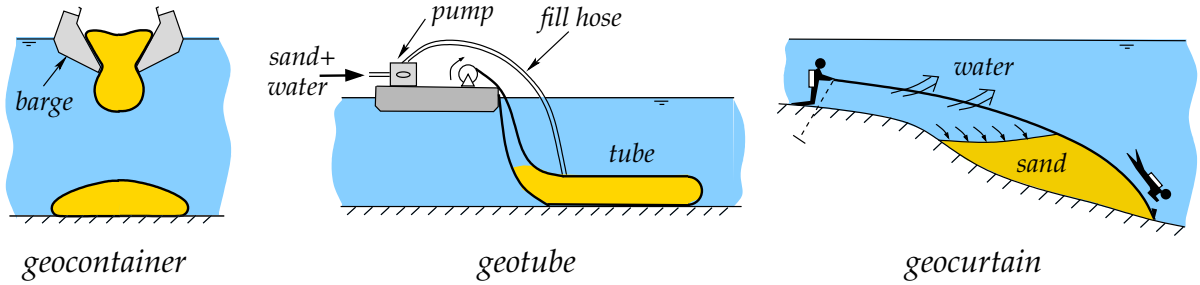

Figure 1.1: Applications of getextile systems [144]

1.1 Motivation

Owing to the variation in application type, different geosynthetic materials are produced [64, 173]. One of the key issues for the manufacturer is to deliver products able to sustain various working conditions where the geosystem might be subjected to heavily dynamic loads like geotubes under a wave attack, or the stability of a containers structure due to possible failure mechanisms. In some applications, the construction procedure has more significance than the running condition itself, which might not vary so much. For such cases, studying the installation effects on the geosystem unit becomes an obligation. Beside concerns of the geosynthetic manufacturer to deliver products able to survive the severe conditions, contractors and engineers are interested in the feasibility of implementing such a relatively new construction methods. For example, safe dumping of a geocontainer on the sea bed without rupture is excellent job, however, it is economically questionable if it is drifted far away from the tolerable zone. Therefore, studying installation and working conditions of geosystems should be covered where soil, water and geotextile are involved.

Theoretical models based on equilibrium analysis provide the basic understanding to the physics of soil–water–geotextile systems. However, field measurements offer more reliable formulas though reproducing tests with similar conditions is not possible. Beside high expenses and technical difficulties, the large–scale measurements require control of many parameters depending on the objective of the test. In addition to the field tests, scaled lab tests are also popular in this area where the focus is oriented toward specific phenomena as scaling the entire model properly is difficult. Figure 1.2 shows different physical modelling of dropping sand filled container in water where the dropping velocity and stability of structure of containers are well predicted.

In general, numerical modelling provides a flexible tool to analyse the physical field in full scale and to investigate the effects of controlling parameters. Accordingly, the experiments can be steered in more economic direction. In spite of the enormous expand in numerical techniques, there is a lack of developing a unified scheme able to simulate applications of geosystems in which granular material and thin structures might experience large movement and deformation in the presence of water.

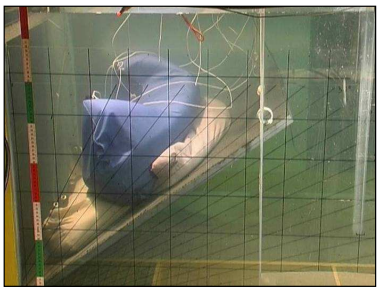

tank model test [23, 25]

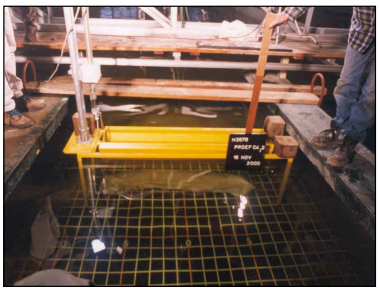

open channel test [32, 49]

field measurements [26, 152]

Figure 1.2: Various physical test of dumping geocontainer in water

1.2 Research aims

The research aims of the present work are to develop a numerical framework capable of modelling the dynamics of granular materials under large deformation combined with the thin–walled structure. More focus is attributed to geosystem applications during installation stage. Since most of these geotextile–soil systems are designed for coastal engineering and shoreline protection, water effects should be included. Acknowledging the efforts being dedicated by scientists for decades to develop numerical methods for soil, water and geotextile or coupling two of them, the sought numerical scheme must exploit this experience. In other words, the development direction should be guided more in coupling schemes and algorithms to be suitable for the intended applications.

To this end, the material point method (MPM) is an attractive numerical scheme to tackle the problem of large deformation in granular materials. The MPM algorithm including membrane formulation is implemented in a unified framework. Performing basic tests for the existing membrane algorithm [191] prove that it suffers from spurious stress distribution as well as underprediction of lateral deformation. As a result, the method requires very fine discretisation to improve. Moreover, the explicit nature of the adopted MPM version obliges assigning sensible mass to the geotextile, which has practically negligible mass as compared to soil. Thus, a novel treatment for the membrane is introduced here, which is shown to be free of the previously mentioned drawbacks associated with the existing algorithm.

Aiming for the simulation of geocontainers release, the split barge should be modelled as a prescribed velocity condition. For this purpose, material points with prescribed velocity are incorporated in MPM. Furthermore, the concepts of surface discretisation has proven to be efficient to track the interface surface between the barge and the geocontainer. As next, the releasing process of a granular material inside geotextile material is simulated in MPM where some control parameters are discussed.

To accomplish the previously mentioned goals, water is integrated in the computational scheme. Implementing high bulk modulus fluid in explicit scheme requires some stabilisation techniques. Two enhancement methods found in finite element literature are applied and validated. Although there is no intention to build sophisticated fluid dynamics model in this thesis, however, the free surface formulation was necessary to introduce in some validation cases.

1.3 Thesis layout

The thesis is divided into seven chapters. The present chapter, **Chapter 1**, provides an introduction to the geomechanical applications involving soil, water and geosynthetic textile in which the objective of the research is outlined. **Chapter 2** reviews continuum–based numerical methods being developed for large deformation problems. A brief overview about Eulerian and Lagrangian methods is given. Furthermore, the concepts of the meshless methods are highlighted briefly, whereas more elaboration has been given to the material point method (MPM) as one of the mesh–based methods. In spite of the

different motive for developing MPM and meshless methods, both are applied to model compressible fluid and thin–walled structures as demonstrated in this chapter as well.

Chapter 3 details the MPM formulations for a continuum solid material. Two types of material points are added: boundary particles obtained from the surface discretisation and particles with prescribed velocities where the non–zero kinematic conditions are applied. Some development and enhancement methods are also included in this chapter due to their necessity for later cases. In order to prove the validity of the current MPM implementation for modelling the dynamics of granular material, collapse of granular column is compared with experimental measurements.

Chapter 4 describes two membrane formulations. The first follows the standard MPM considering the membrane theories [191], while the second given the name *coupled FE–MP method* is more novel formulation treating the membrane as a Lagrangian continuum moving through the computational mesh. Mathematical background of both methods is given along with simple test of spring–mass system. In all tests of mesh sensitivity, stress prediction and lateral deformation, the coupled FE–MP approach shows advantages over the other method. For the rest of the chapter, a procedure of suppressing compression stresses in the membrane to resemble geotextile materials as well as required modification to accommodate for large deformations are presented. Validation example about soil–geotextile interaction is given by the end of this chapter.

As water is being involved for most geosystem applications, **Chapter 5** underlines the modelling of fully incompressible fluid using fractional step method. Little compressibility has been assigned to the water so that the explicit integration scheme is applicable. In order to stabilise the numerical scheme, two enhancement schemes are shown to be essential in order to get acceptable pressure and velocity fields. Moreover, an algorithm based on a continuous density field is developed so that the free surface can be detected. The free surface algorithm as well as the smoothening schemes are examined for the simulation of water column collapse. The efficiency of the fluid model to converge toward the steady–state solution with enhancement is tested for the problem of geotube.

More focus has been given to the application of dropping geocontainer in **Chapter 6**, which is quite challenging application to simulate. Similar to the tradition in conducting experimental tests, the MPM container is assumed to be released from the split barge in dry condition without water. The experience of adding some folds in the geotextile along the barge has shown its effectiveness in the numerical model. The effect of geotextile–barge friction coefficient on the geotextile tensile forces has been investigated for different values. Furthermore, interaction of multigeocontainers has been studied by simulating the installation process of two containers. Evaluating the terminal velocity of dropping container in water is important to identify the most critical condition of stress peak when the container hits the ground. Therefore, the MPM fluid model is evaluated first with a lab controlled test. As next, the numerical model is extended to compare with field measurements. In spite of the two–dimensional assumption in the numerical model, some figures and numbers of the real three–dimensional model are captured.

As a final summary and conclusion, **Chapter 7** presents the key issues and findings in this research with some recommendations for further research in this area.

Chapter 2

Computational methods for large deformation analysis

Numerical simulations are an indispensable active field of the modern engineering and science development. Considerable effort has been devoted by researchers to develop numerical methods that are able to simulate practical applications. These are more challenging when large deformation is involved.

Literally, granular materials can be simulated either using a continuum–based representation or particle–based. In spite of the capability of the latter family, such as the *discrete element method* (DEM), to model the interaction of grains, it is limited to small scale problems. Setting parameters for DEM model is difficult to achieve in a reliable way. Therefore, continuum models such as the *finite element method* (FEM) are usually prefered over discrete representations. Methods like MPM or SPH are classified by most researchers as a combination of the two schemes that is typically used to solve continuum problems.

In continuum–based models, the traditional description of kinematics is either based on Lagrangian or Eulerian approach where each has its pros and cons. Coupling the two descriptions in one approach by exploiting the best features of each is desirable. An overview of the basic two descriptions, as well as concepts of combined schemes, is provided in Section 2.1. Lagrangian, Eulerian, and coupled methods all indirectly solve the partial differential equations using a grid with fixed topology. The idea of replacing the fixed connectivity mesh with points that are free to build neighbour list is introduced by the meshless methods in Section 2.2.

The inspiration of replacing the continuum with material points able to follow the movement in a natural manner has the beauty of linearising the convection–diffusion equation. However, it is not necessary to perform the solution of the equation of motion on the material points like in meshless methods [116, 128]. Instead it can be accomplished on a fixed background computational mesh [73]. The evolved version of the last method is called the *material point method* (MPM) [167, 169], which is presented in Section 2.3. The section includes development and enhancement of the basic algorithm as well as various engineering applications.

In geosynthetics applications, thin–walled structures or more specifically membrane elements are usually employed. Thin elements often experience large displacement, which might be combined with moderate deformation. Section 2.4 is dedicated to give an overview of large deformation in thin structural elements, whereas Section 2.5 and 2.6 provide brief reviews for incompressible fluid modelling and the treatment of fluid interface, respectively. Some concluding remarks are drawn in Section 2.7.

2.1 Lagrangian, Eulerian and coupled methods

In order to develop solutions for problems described in terms of differential equations, several numerical approaches are available. These approaches tend to follow either *Lagrangian* or *Eulerian* descriptions. The bookkeeping strategy is the essential difference between the two. In the Lagrangian approach, the motion of each material point is tracked in time as it moves through space. On the contrary, the Eulerian frame assumes that the spatial domain is fixed and the material is studied as it passes through this domain.

In both, the Lagrangian and Eulerian formulations, the governing equations are approximated throughout the computational domain using for example finite element (FE) or finite difference (FD) procedures. It is more common to use FD discretisation when the mesh is fixed such as with the Eulerian methods. On the other hand, the FE approximation is frequently adopted when the mesh is attached to the material. Owing to this attachment, numerical difficulties are expected when the material is heavily distorted unless the discretisation is updated. Albeit tying the mesh to the material in the Lagrangian description limits the deformation, it has an advantage to track the moving material easily where the history can be remembered at the grid nodes. Furthermore, the boundary tracking is trivial, whereas this is not the case with the Eulerian description. For the same reason, the treatment of the material interfaces is resolved naturally and the application of the constitutive equations are straight forward. Important to mentioned here is that by adopting Lagrangian description the nonlinear convective term in the governing equations is omitted. Finally, following the material deformation does not restrict the analysis to a predefined spatial domain, however, discretisation in Eulerian methods should cover the whole region where material is expected to move. More details about the comparison can be found, for example, in [19].

According to the aforementioned, adopting purely Lagrangian or Eulerian description for the material kinematics has advantages and drawbacks. Indeed, combining the positive features of both gives a better approach that is logically more computationally demanding. *Arbitrary Lagrangian–Eulerian* (ALE) is a numerical scheme that makes use of the classical kinematic descriptions in one computational framework [123]. In ALE, the relevant governing equations are decoupled into Lagrangian and Eulerian counterparts by splitting the differential operator. Therefore, the solution algorithm consists of three steps. The first, which is similar to the updated Lagrangian algorithm, followed next by the meshing step where the finite element discretisation is updated while the topology is preserved. Owing to updating the mesh, a third step is essential to map the state variables that is equivalent to the convection equation. A lot of effort have been devoted to the last two steps and consequently many versions of ALE are available [18, 19, 54]. As a conclusion, the difference between the three schemes Lagrangian, Eulerian and ALE is attributed to the location of the reference configuration, from where the physical motion of the body is described. The three approaches are depicted in Figure 2.1. In this figure, the freedom with moving the computational nodes within the ALE description allows arbitrarily large deformation and avoid mesh entanglement.

Although ALE methods allows moving the mesh nodes in a predefined manner, the discretisation and the mesh topology are maintained. Therefore, for modelling fluid

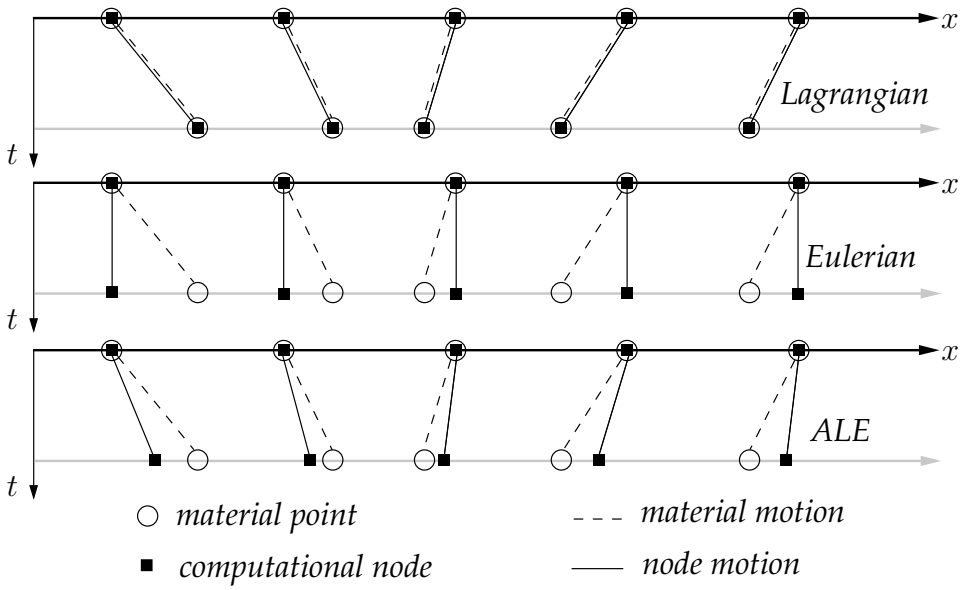

Figure 2.1: One–dimensional illustration of Lagrangian, Eulerian and ALE motions [54]

that undergoes extreme deformation, this approach has limitations. Another form of exploiting the two classical configurations is observed in problems dealing with fluid–solid interfaces. For such problems, two discretisations are employed instead of a single mesh. The *coupled Eulerian–Lagrangian* (CEL) methods are based on coupling between Lagrangian body, which is most commonly solid material, and Eulerian for the fluid behaviour material. For such an analysis strategy, explicit coupling is obtained by applying pressure boundary condition on the Lagrangian body, whereas velocity boundary condition prescribed on the Eulerian discretisation for the fluid as demonstrated in Figure 2.2 [19, 138]. More about other coupling methods are provided by Brown et al. [34]. The method has shown its applicability for geomechanical applications of a Lagrangian object being pushed into an Eulerian soil [131, 145].

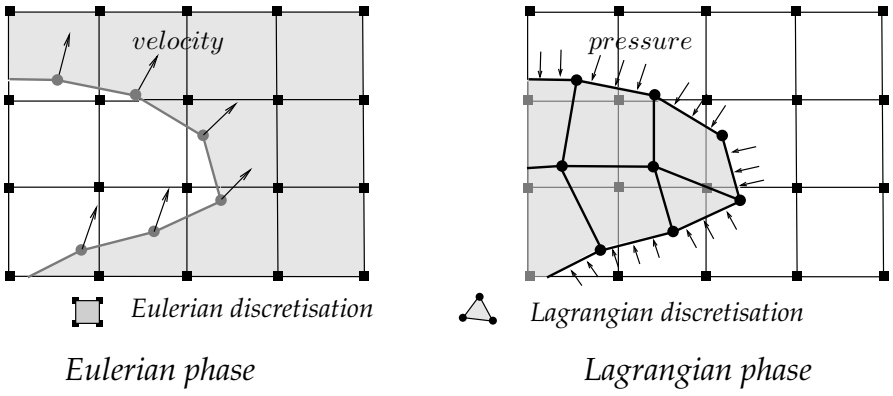

Figure 2.2: Explicit coupling solutions of CEL methods

2.2 Meshless methods

In all previously mentioned methods, the discretised continuum is divided into computational cells connected together via a topological connectivity or mesh, thus, they can be classified as *grid–based methods* [112]. In the Lagrangian FE formulation for instance, the variables are approximated inside each element by employing interpolation functions. Since building interpolation functions is linked to the mesh and its fixed topology, it is difficult to accommodate large material distortion. As a solution to this problem, the *meshless* or *meshfree methods* replace the mesh interpolation functions with functions based on interpolation points able to follow the material movement. The connectivity between these points is variable and updated within the solution procedure, which gives these methods an adaptive nature capable of modelling excessive deformation. Li and Liu [105] provide an elaborated overview about these methods and their history.

Numerous names are given to methods that appear under the meshless umbrella. Belytschko et al. [17] summarise these methods as: *smoothed particle hydrodynamics* (SPH), *moving least square* (MLS) and *partition of unity method*. Without going into details of the last two, the SPH is considered as one of the most attractive and efficient computational technique to solve solid and fluid mechanics problems [116, 128]. The history of the method goes back to the seventies when it was firstly applied to analyse astrophysical and cosmological phenomenon. The SPH formulation makes use of the basic integration concept of a continuous function $f(\boldsymbol{x})$, with $\boldsymbol{x}$ being the position vector that is defined

$$f(\boldsymbol{x}_i) = \int_{-\infty}^{\infty} \delta(\boldsymbol{x} - \boldsymbol{x}_i)\ f(\boldsymbol{x})\ d\boldsymbol{x}, \tag{2.1}$$

where $\delta(\boldsymbol{x} - \boldsymbol{x}_i)$ is the Dirac delta function, which is infinity at $\boldsymbol{x} = \boldsymbol{x}_i$ and zero elsewhere. Now, if the Dirac function is replaced with a smoothing function W, the integration reads

$$f(\boldsymbol{x}_i) = \int_{-\infty}^{\infty} W(\boldsymbol{x} - \boldsymbol{x}_i, h)\ f(\boldsymbol{x})\ d\boldsymbol{x}, \tag{2.2}$$

with h being a measure of the smoothing length, which can take circular or rectangular shape. The smoothing function must satisfy some conditions [17] and can be constructed as exponential or spline functions. According to this definition, the integration point is always *smoothened* with a non–zero spatial space that only becomes *exact* with the Dirac delta function. Following this theory, the continuum is represented by a cloud of particles where Equation 2.2 is numerically integrated over these material points, which carry material information in Lagrangian manner. The particles interact with each other through the conservation laws where the influence of the individual particle is controlled by the smoothing length, which in turn affect the solution quality [112].

Unlike other meshfree methods where the points are used only as interpolation points, the combination of the Lagrangian formulation and particle approximation in SPH gives the method the power in simulating a wide range of multiphysics applications [4, 105, 106]. For example, Anghileri et al. [4] investigate the impact of a tank filled with water on rigid ground. In their simulations, four particular fluid models were tested: Lagrangian

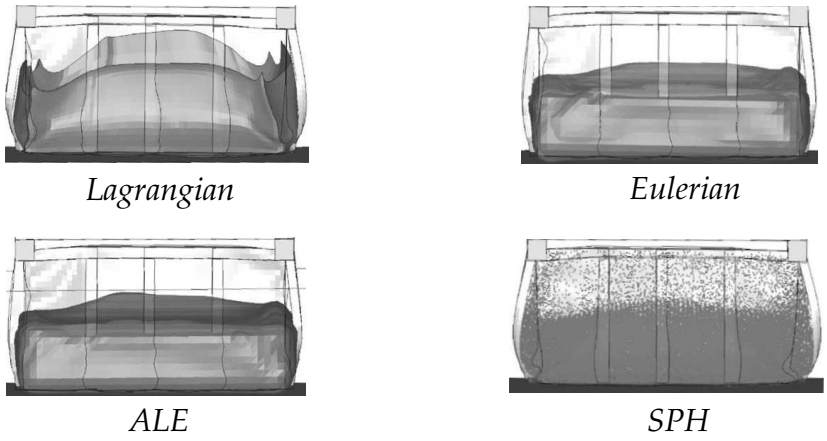

Figure 2.3: Water sloshing with different models inside tank modelled with FEM [4]

FE, Eulerian FE, ALE, and SPH methods. Apart from the coupling methodology between the tank and fluid, the SPH model shows better reproduction for water sloshing inside the tank as pictured in Figure 2.3.

Like other numerical schemes, SPH also has drawbacks or research points to be explored, such as the stability of the method under tension [171]. Imposing kinematic boundary conditions are not defined precisely and requires special treatment. Furthermore, the particles are highly disordered when they undergo large deformations and impulsive loadings that make the results not always reliable [112].

2.3 Material point method (MPM)

The *material point method* (MPM) is a numerical method that is developed to treat large deformation problem of the history–dependent materials. The method is based on the combination of Lagrangian and Eulerian material descriptions. With regard to the Lagrangian description, a body is represented by collection of material points, which carry permanent information. The description keeps track of the movement and deformation of material domain. Interaction of material points is however described by solving the governing equations on a computational mesh that corresponds to the Eulerian description of motion. Therefore, the method can be considered as a finite element method formulated in an arbitrary Lagrangian–Eulerian frame of motion.

The Lagrangian material points carry all material properties as well as external loads, whereas no permanent information are stored on the computational mesh. During one computational step, the information that is required to solve the equation of motion is transferred from the material points to the grid nodes. After determining the primary variables at nodes, as well as strains and stresses at material points, the material points are convected following the deformed mesh. It is essential to emphasise here that all materials points belong to different bodies are updated with the same velocity field that is determined via the computational mesh. While the locations of the material points

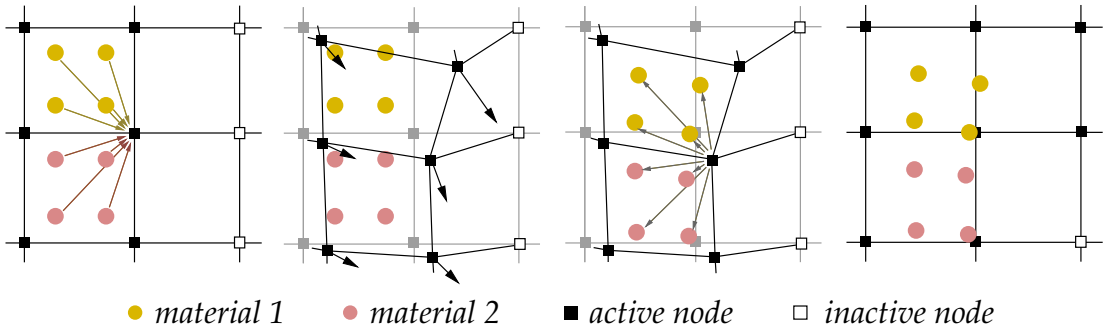

Figure 2.4: Solution procedure of an MPM computational step

are kept, mesh is reset back to its initial configuration. A schematic representation of one computational step in MPM is illustrated in Figure 2.4. Frequently, this procedure is regarded in three phases: initialisation, Lagrangian and convection phase [169, 189].

2.3.1 Historical background

The *particle–in–cell* (PIC) method introduced by Harlow [73] for fluid mechanics is regarded as the origin of MPM. PIC evolved later to the *fluid implicit particle* (FLIP) by Brackbill and Ruppel [30] as the PIC suffered excessive energy dissipation. The idea of PIC or FLIP is to solve the equations of motion on a computational grid where the spatial derivatives can be constructed. Material points are convected naturally by transferring information from nodes to the Lagrangian points. The essential difference between the two comes from the procedure of sweeping information between the two discretisations.

Sulsky and Schreyer [166] and their co–workers at New Mexico extend the method for solid mechanics applications, which was afterward given the name Material Point Method (MPM) [167]. The weak formulation of the MPM is provided in terms of finite elements formulation [168, 169]. In the MPM version, the field variables are evaluated at the material points, which carry the state variables and material parameters. No permanent information is stored on the computational grid that serves as a spatial domain for solving the equations of motion. MPM, as a particle–based Lagrangian method, has the advantage of conserving the mass inherently.

Within the MPM procedure, the mapping of information takes place between the mass points and the grid nodes. Burgess et al. [36] prove that mapping of data between material points and the computational nodes implies that the kinetic energy and momentum are conserved. Owing to the dynamic algorithm used with the MPM, explicit integration scheme is frequently used [165, 167, 189]. Lumping the mass matrix is computationally efficient as the inversion of the diagonal matrix is trivial. However, this lumping comes with the price of dissipating kinetic energy that is evaluated for history dependent and independent materials in [30, 31, 168].

2.3.2 Development and enhancement

Over the past two decades, MPM has became increasingly attractive for solving large deformation problems. References [168, 169] have largely contributed to outline the basis of the method. Consequently, several developments to enhance or improve the mathematical principles of MPM as well as applying the method in various engineering disciplines grew in parallel. Tracking all these developments or enhancements in one section of a thesis is not practical. Nevertheless, some of the milestones relevant to this thesis are highlighted in the following paragraphs.

2.3.2.1 Contact interaction treatment

Owing to the single value velocity field integrated in MPM for updating the locations of the material points, the no–slip condition between different bodies is applied automatically with no change to the standard MPM algorithm. The interaction of two materials in the MPM context is shown in Figure 2.4, which shows in the third step (from left to right) both material points types being updated with a common velocity field obtained at the grid nodes, whereas the contact surface is detected implicitly. For two bodies in contact, there should be a limit when the contact relation is broken. The inherent no–slip condition assumes the two always in contact that causes non–physical extra resistance with no guarantee of solving the problem with the mesh refinement [169].

An algorithm to detect approaching or separation of different bodies that improves the energy conservation of the colliding bodies is introduced by York et al. [192]. The algorithm is based on detecting a variation between the individual body velocity field of when it combines with others. With similar concepts, Bardenhagen et al. [14] extend the method to include sliding and rolling with the Coulomb friction criterion using a non–iterative algorithm able to detect the interface explicitly. Bardenhagen et al. [15] replace the velocity field criterion with the normal traction criterion that requires the normal traction at the surface to be in compression. By comparing the two, the latter gives more reasonable results for a granular material under shear deformation [13]. Nairn [130] prove that both Bardenhagen's methods either detect contact too soon or unreliably in the case of an internal crack, therefore, the velocity criterion algorithm was modified involving the corresponding nodal volume for this purpose. The different velocity fields around the crack tip provided an efficient algorithm capable of detecting a discontinuity within the continuum model applied for two and three–dimensional problems [69, 70].

By the same token, Hu and Chen [81] propose using momentum as a criterion for the contact detection implemented in a multi–mesh environment to avoid the unphysical behaviour that might be associated with the velocity field algorithm [14]. Owing to the treatment of tangential velocities of bodies in different discretisations, the method was unable to simulate friction contact. The multi–mesh approach was improved by combining the velocity criterion algorithm for the tangential component [190] showing its applicability for different applications [121, 190]. Moreover, the method has been extended to model the drag interaction of multi–phase material [122, 195].

In the previously mentioned contact methods, the MPM algorithm follows the original

MPM formulation of collocating the mass of the material point at one point [167, 169]. However, as it will be shown in the context of this chapter, there are some material point methods that assume a spatial domain in which the mass is distributed [12, 151]. Defining a space for the material points allowed Zheng et al. [198] to improve the accuracy of the detecting the contact surface. The overlap of the material points spaces is used as a criterion to apply contact instead of the nodal velocity fields.

2.3.2.2 Energy conservation and integration scheme

According to the original MPM [169], the stresses are obtained at the end of a computational cycle known as *update stress last* (USL). This procedure, as well as the *update stress first* USF where the stresses are updated according to the updated velocity field are examined by Bardenhagen [11] in terms of energy conservation in the material point method. According to this investigation, the USL dissipates more energy when compared to USF. In the work of [182], where both schemes are tested as well as central difference, it is shown that the central difference method and USL is considerably better than USF regarding stability problem and spatial convergence. Furthermore, Wallstedt and Guilkey [181] explore that the accuracy of the MPM solution heavily depends on the material point density and location. Hence, they enhanced the linear projection of the velocity field by making use of the velocity gradient information.

Explicit time integration scheme has been implemented in many MPM applications [39, 169, 189]. In order to utilise the benefit of the explicit procedure being computationally inexpensive within a time step, the mass matrix must be diagonalised or lumped. Lumping the mass matrix has the consequence of some numerical dissipation in the kinetic energy [36]. In MPM, this matrix is assembled from the discrete distribution of the mass density concentrated at the material points locations. Więckowski [186] replaces the concentrated mass by a continuous density function, which was shown to exhibit less oscillation and better energy conservation for the one–dimensional wave propagation problem. In other words, the collocated mass is smeared over the element span.

To improve the solution quality or to increase the small time step size with the explicit scheme, implicit integration has been introduced to the MPM. Some of these schemes either based on Newmark integration method [67, 110] where the stiffness matrix is built, or by implementing a matrix–free iterative procedure [164]. For the applications where the inertia effect is not of interest, a quasi–static solution is obtained in a fashion similar to the FE procedure by constructing a global stiffness matrix [22]. However, the expense of building this matrix can be avoided when dynamic relaxation procedure is employed [162, 187], where an artificial or viscous damping is introduced helping the energy to dissipate and the solution converges eventually to the static solution.

2.3.2.3 Grid–crossing error

Low–order elements are often used in most of the MPM codes [39, 169, 189]. By implementing linear interpolation functions for mapping information between the computa-

tional grid nodes and the material points, a change in the derivative sign causes artificial oscillation in the internal force commonly referred to as a *grid crossing error* [12, 68]. As a proposed remedy for the crossing error, use of higher–order functions that has continuous derivatives at the element boundary has been proposed. By implementing quadratic functions, lumping the mass matrix is not possible anymore as it might ends up with negative components due to the nature of the quadratic functions. Beside the expenses of solving a consistent mass matrix, it might be singular and therefore the approach falls apart [57]. As an alternative, Steffen et al. [161] propose B–spline functions to mitigate the numerical noise corresponding to the crossing error, which shows significant improvement against the piecewise functions.

In the work of Bardenhagen and Kober [12], the *generalised interpolation material point method* (GIMP) introduced a spatial domain for the material point where the characteristic functions are distributed instead of concentrating them at one point. The method was able to reduce the crossing error, however, it did not eliminate it completely. In recent years, similar concepts which will be described later in this chapter, have been employed [151, 198]. Since the material points are distributed over space in all these methods, two points interact with each other as soon as parts of their domains contribute to the same computational node. Therefore, one would expect less material separation occurs under tensile load as compared to the traditional MPM. It should be realised that tracking the evolution of the material points costs extra computation to the MPM that is computationally expensive by itself. For example, GIMP is slower than the traditional MPM with a factor of 2.7 in the case of analysing a simple tension bar [57].

Zhang et al. [194] eliminate the discontinuity in the gradients of the linear functions by introducing a *dual domain material point* (DDMP). In contrast to GIMP where the shape functions are modified, their gradients only are modified in DDMP. In this way, the influence domain of the material points is enlarged for stresses and consequently the internal forces provide smoother crossing. All other quantities are computed similarly to the original MPM where the influence of a material point is bounded by its element. The method has shown its effectiveness to alleviate the crossing problem for Cartesian coordinates and has more recently been extended to cylindrical coordinates [110, 120].

2.3.2.4 Volumetric locking

In addition to the crossing error linked to employing low–order elements, a non–physical increase in the resistance against volume change is taking place, which is commonly known as *volumetric locking* [18]. Although the locking problem is not related to MPM itself, spurious variation in the stress field is detected when the material is becoming nearly incompressible. In the finite element framework, Zienkiewicz and Taylor [202] supply several methods either based on introducing multi–field variable or by splitting the governing equation into deviatoric and isochoric parts.

Stolle et al. [162] accommodate incompressibility with enhancement procedure using an explicit scheme and compared it to an implicit model based on operator splitting within an MPM framework. As a conclusion of their work, the explicit solution con-

verged faster to the quasi–static solution when *nodal mixed discretisation* (NMD) is used. NMD is a strain enhancement technique derived from involving an assemble of elements to satisfy the volumetric strain constraint while the deviatoric components are kept without changes [53]. The NMD has proven to be noticeably efficient in the case of large–deformation single phase granular material [22, 89], or the case of multi–phase material with small deformation [90].

In the concepts of splitting up the multi–field, Shin [155] applies the enhancement scheme to model the simulation of landslide and debris flows. Mast et al. [127] show that applying the smoothening approach on deviatoric and volumetric components, shear and volumetric locking were healed. In this work, a smoothening procedure is proposed on two levels: inside the computational cell, and on the supported zone of the grid node. However, the combination of both the levels gives smoother pressure distribution for the break of a water dam problem [126].

2.3.2.5 Material points with spatial domain

In order to mitigate the numerical instability caused by a sudden jump in the gradient of the shape functions as a material point move between elements, Bardenhagen and Kober [12] propose the generalised interpolation material point method (GIMP). In this method, the concentrated mass of a subdomain at one point is replaced by defining a finite spatial domain. In other words, the Dirac delta function employed in MPM is *smoothened* by a characteristic function χ. The general definition for the modified weighting function is established with [12]

$$\bar{N}_{ip} = \frac{1}{V_p} \int_{\Omega_p} \chi_p \left(\boldsymbol{x} - \boldsymbol{x}_p \right) \, N_i \, d\Omega_p, \tag{2.3}$$

where $\bar{N}_{ip}$ is a modified function of N_{ip}, which is the shape function of node i evaluated at the material point p, with V_p and Ω_p being the volume and the support domain of p, respectively. Replacing the characteristic function in Equation 2.3 by the delta function yields the original MPM in which $\bar{N}_{ip} = N_{ip}$. Alternatively, imposing a unit value instead of χ limits a weighting function with support in adjacent cells and in the nearest neighbour cells. When Equation 2.3 is compared to the SPH formulation, Equations 2.1 and 2.2, it is seen that GIMP use the smoothing characteristics of the meshless methods.

Material points in GIMP are commonly initialised with rectangular shape, which is unchanged during computation. Thus, the method suffers from extension instability when the space between the material points is bigger than the support domain of these points. To overcome this problem, Sadeghirad et al. [151] suggest to update the material point shapes with a parallelogram domain that is consistently updated using the deformation gradient. As the proposed method convects the initially rectangular domains into parallelograms, it is called *convected particle domain interpolation* (CPDI) method. The CPDI demonstrates its effectiveness for excessive tensile deformation problems [151] or dynamic impact on fully saturated media [198].

For the case of large deformation, the shape of a material point domain should be up-

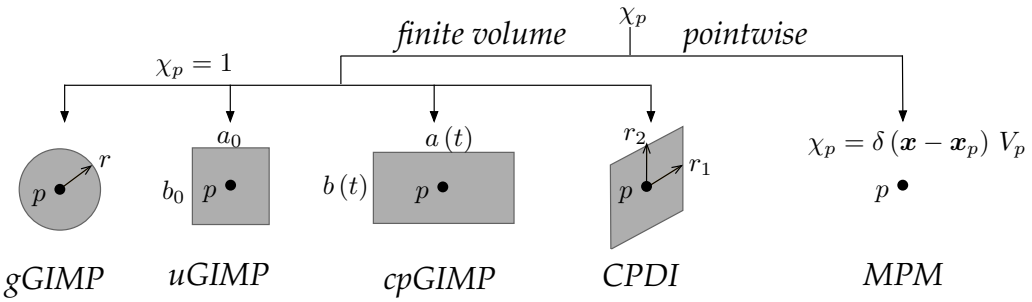

Figure 2.5: Material point with spatial domain and characteristic function [126]

dated. The GIMP version of updating the material point shape in orthogonal directions is referred to cpGIMP, and uGIMP when the shape is kept fixed [151]. As the initial shape of the domain is not necessarily rectangular, Mast [126] adds a circular shape and denoted it as gGIMP. Although cpGIMP behaves better than uGIMP in terms of material points separation, but it is unable to predict the distortion by shear. Graphical illustration of the original MPM with other methods with support spatial domain is shown in Figure 2.5.

Spreading material points to a spatial domain mitigates the instability crossing problem. On the other hand, one should realise the complexity and computational effort to track material points shape in the three–dimensional case. Furthermore, imposing compatibility between material points borders in a Lagrangian fashion within CPDI raises the issue of mesh distortion associated with Lagrangian methods.

2.3.2.6 Discretisations

Regular mesh with bi–linear interpolation functions was adopted by early MPM version [167, 169], whereas Więckowski et al. [189] implement irregular triangular discretisation to model the silo discharge problem. Low–order triangular discretisation is extended in the case of three–dimensional problem to four–noded tetrahedral elements that have been applied to many geotechnical problems with large–deformation [2, 21, 22, 89].

In spite of the convenience of implementing fixed mesh discretisation, refining the mesh at a region of high deformation gradient is necessary. Andersen [3] suggests the concepts of local mesh refinement for a regular triangular grid at the region where the material points gradient tensor exceeds a tolerance level. The refinement at the material points through a splitting up procedure is consistent with the fine mesh zone. In a related work by Tan and Nairn [172], a hierarchical refinement of bi–linear rectangular mesh is applied for the problem of tracking a crack tip. Using this procedure, the computational mesh is divided into multiple nested levels of refinement where each level has a different element size. The adaptation technique by partitioning material points is also applied to the shaped charges modelling where the jet formed exhibits massive straining [150].

2.3.2.7 Coupling of numerical methods

While different numerical methods are applied in different engineering areas, selection of the most suitable method depends on the type of application. Coupling numerical methods in one computational tool utilising the best features of each gives more flexible scheme to model multiphysics problems. Often FEM is used to model solid materials, which can be joined with discrete models to simulate structural–granular material interaction; e.g., [175].

In the work by Zhang et al. [196], for instance, an explicit coupling between FEM and MPM is introduced in a uniform formulation and applied to a hyper–velocity impact simulations in which the projectile is discretised as a Lagrangian FE object while a regular background grid is provided for the MPM target, which is the potential large deformation zone. Once the Lagrangian body moves into the predefined computational grid, nodes are converted into material points whose momentum equations are solved on the predefined grid. The FEM–MPM explicit coupling in this procedure is carried out by adopting one method through two predefined regions. In the large deformation zone, however, both projectile and target are treated similar to the pure MPM. Lian et al. [108] propose a different type of FEM–MPM coupling for modelling reinforced concrete subjected to impact loading. The reinforced bar is discretised using one–dimensional line element. While the steel bar forces are evaluated on the FE grid and then transferred to the background mesh, the concrete is modelled in a traditional MPM procedure. More about coupling MPM with the hybrid immersed boundary method to model the fluid–structure interaction problems can be found in Gilmanov and Acharya [66].

2.3.3 Applications

The material point method has been applied to a wide range of engineering problems. Considering that MPM is well suited for modelling solids with history–dependent state variables, the pioneering works were devoted to model impact problems [165, 165, 167, 169] and impact–penetration [166]. Bardenhagen et al. [13, 14] apply MPM to model granular materials exploiting the advantage of the frictional contact algorithm.

Some applications related to mechanical and industrial engineering include: modelling extrusion and cutting processes [185], simulating an upsetting compression model [164], surrogate shaped charge [150], explosion and fragmentation phenomena [10], as well as gears conjugation action [81]. Furthermore, MPM has been used to model the impact of Taylor bar [120, 167]. Propagation of internal crack has also been carried out in MPM with the aid of the frictional contact algorithm [130, 172]. Different contact algorithms have been tested for the impact–penetration problem [83, 190]. It is common for such applications to have relatively small deformation in the projectile, while the target suffers from large deformation or is even fragmented. A coupling procedure of FEM Lagrangian model with MPM provides a convenient framework to model reinforced concrete subjected to impact load [107–109, 196].

As a powerful tool for large deformation in history–dependent materials, MPM has been applied to geotechnical applications extensively. Więckowski [185] models the fail-

ure of a retaining wall, whereas different related slope stability problems are treated in [3, 162, 187]. The flow pattern of a granular material due to filling or discharging process in silo has been widely investigated with MPM [39, 184, 189], as well as flowing of granular materials during the collapse of a sand column [3, 158]. The inherent feature of detecting the structure–soil interface in MPM encourages using the method to simulate the anchor pull–out problem [39, 40], or hammering pile into soil [2, 110]. Another type of applications about debris flow in a channel with structures interaction can be found in [126, 155]. Structural elements have also been implemented in MPM to model a landfills reinforced by a geomembrane [199].

The dynamics of soil–water interaction is brought to MPM by implementing the water as well as soil material points. For example, the impact problem of saturated porous media is investigated in [195, 198]. On the same topic with different implementation, the dissipation of excess pore water pressure for a dike under wave attack has been studied by Jassim et al. [90]. Providing that the root of MPM development was dedicated for fluid modelling [73], the modern MPM is able to model the compressible [193] or incompressible fluid encapsulated in membrane [63]. Fluid flow problems also have been employed in MPM like the collapse of water column [127, 155].

Within the previously mentioned applications, there are validations for MPM via comparisons with experimental results; e.g., [10, 39] or with other numerical schemes like SPH for the hypervelocity impact problem by Ma et al. [119].

2.4 Thin–walled structures modelling

Numerical modelling of thin–walled structures is well defined and formulated in the FEM literature; e.g., [18, 93, 157]. For geomechanical applications presented in Chapter 1, thin structures and soil material often develop large displacements that might be combined with large deformation as well.

Meshfree methods have been used to model thin–walled structures. Early contribution in this regard is attributed to Krysl and Belytschko [94] who applied the thin shell theory using the *Element–Free Galerkin* (EFG) method where essential boundary conditions were imposed using Lagrange multipliers. The three–dimensional modelling of thin shell structures were formulated for large deformation problems using meshfree methods [106]. In this work, essential boundary conditions were implemented by modifying the shape functions of points near the boundary. Numerical stability problems due to shear and volumetric locking associated with Lagrangian methods are eliminated when higher order interpolation is implemented. Liu [111] provides an extensive survey about applying meshless methods for thin–walled structures.

In MPM, Banerjee [9] adopts plate formulation for curved shell together with explicit time stepping. He concluded that the stiff nature of the rotational inertia may require implicit time stepping scheme for shell materials. Ionescu et al. [87] study the failure of anisotripic soft tissue subjected to finite deformation using MPM. The prominent feature of the spatially thin structures is the mechanics coupling effect of the curved surface modelling and the in–plane membrane deformation [204]. For geomechanical applica-

tions involving thin geosynthetics materials, the membrane effects dominate so that the flexural rigidity is often neglected. York et al. [192] introduce a membrane element to the MPM formulation for two–dimensional problems. The MPM algorithm was modified by considering the in–plane membrane effect of a single layer of material points. This development was applied for the fluid–structure interaction where the inherent MPM feature of no–slip condition is useful [193]. Gan et al. [63] extend the membrane formulation to three–dimensional problem where the effect of in–plane shear stresses was included. The injection process of a sperm is modelled in MPM as a spherical membrane filled with incompressible fluid [62]. Zhou et al. [199] include geomembranes in a landfill under quasi–static conditions. Frictional contact algorithm with the Coulomb criterion was imposed at the soil–membrane interface to relieve the no–slip condition in MPM.

In membrane applications, it is important to have an accurate computation for a local orientation. York [191] examines several algorithms such as distributing a constant function along the membrane and then obtaining the spatial gradient. Among all methods, tracking the material point connectivity is considered the best [191]. Thus, Gan [62] applies the connectivity approach for three–dimensional membrane by connecting the material points with triangular discretisation. An alternative approach is applied by Zheng et al. [198] to detect normal–tangential system based on finding the volume gradient at the grid nodes, which is then interpolated at the material points. Care must be taken that all previously mentioned algorithms are developed and tested for a regular mesh discretisation with no guarantee to work for an irregular mesh.

2.5 Incompressible fluid modelling

In *computational fluid dynamics* (CFD) methods, Eulerian description for the fluid motion is often used. For this purpose, different discretisation methods can be applied such as: finite element, finite difference or finite volume method; see e.g., [58, 203]. In spite of avoiding mesh distortion in Eulerian formulation, it is difficult to update the movement of fluid–structure interface. On the other hand, tracking the movement of the fluid in Lagrangian manner using material points provides a convenient description for the natural convection of the material as well as easy tracking for the interface surface.

Lucy [116] introduces SPH as a powerful tool to model the dynamics of astrophysical problems and galaxy collisions. As a meshless Lagrangian method, SPH can handle extreme fluid deformation including breaking, merging and splashing [128]. The kernel approximation implemented in SPH, Equation 2.2, smoothly interpolates the unknowns of number of surrounding points. Thus, incompressible fluid can be treated without numerical difficulties. The same reason of interpolating variables over spatial domain makes the method challenging in terms of numerical computation [105, 112].

Earlier in this chapter, it has been shown that the use of low–order elements in mesh–based methods is associated with numerical stability problems. Nevertheless, this type of element is becoming more popular for modelling incompressible fluid as it eliminates the non–physical deformation modes that is associated with high–order elements [203]. To mitigate locking and spurious pressure variations, numerical schemes based on split-

ting the differential operator are popular. The velocity correction method or *fractional step method* (FSM) is widely used to obtain the steady–state solution for incompressible fluid problem [134, 205]. An extensive study about these methods is provided in [202, 203] and the references therein.

As an efficient stabilisation technique for FEM discretisation, the FSM is implemented in the *Particle Finite Element Method* (PFEM). In this method, the mesh topology between Lagrangian points is rebuild each time increment where the differential governing equations are integrated. While nodes of the mesh move according to the equation of motion, all physical quantities are stored on the grid nodes before destroying the mesh. Using geometrical algorithms, the connection between particles is established again to advance the solution for the next time step, with the boundary conditions and interface conditions being considered for the new mesh. Oñate et al. [139] and the group in CIMNE (Barcelona) show different applications involving fluid–structure interaction [85, 86, 100]. More recently, Zhang et al. [197] apply the method to model granular material such as collapse of a column or silo discharge problem.

The early development of particle–in–cell method [73] and the later version of fluid implicit particle method [30] were dedicated for fluid modelling. The material point method in its formulation [167, 169] has been utilised to model fluid for various applications such as: compressible [191] and incompressible fluids [62, 63] inside thin membrane, multi–phase debris flow [155], or water flow due to dam breaking [127]. Numerical instability associated with explicit modelling of *near* incompressible fluid has been improved by introducing some enhancement techniques. As the spherical component of the stress is blamed for numerical difficulties, different techniques based on mixed formulation are utilised to circumvent the volumetric locking problem when low–order elements are used. Zienkiewicz and Taylor [202, 203] summarise these methods with the corresponding mathematical background. Detournay and Dzik [53] discuss some methods valid for history–dependent materials. This approach was then examined and adopted for MPM by Stolle et al. [162]. Extending this work to a two–phase material under small deformation analysis is implemented, where the enhancement approach is applied for soil and water separately [90]. For large deformation problem, however, the work of Shin [155] and more recently by Mast et al. [127] an algorithm based on averaging spherical component inside the cell as well as around the computational grid is introduced to mitigate the locking problem.

2.6 Free surface and fluid–structure interaction

According to Ferziger and Perić [58], numerical methods capable of modelling free surface flow are classified as *interface tracking* or *interface capturing*. One of the interface tracking methods is the particle finite element method (PFEM), which tracks the interface surface explicitly by following the movement of the material points placed on the nodes of a Lagrangian mesh [85, 86, 139]. In Eulerian formulations, the *volume–of–fluid* (VoF) method approximated the interface via capturing the discontinuous volume change across the surface [20, 91].

With regard to the free–surface formulations, two methodologies are common in modelling fluid–structure interaction (FSI). The *partition* and the *monolithic* strategies are frequently implemented in numerical methods [52, 79]. While the partitioning scheme is an iterative approach, treating the fluid and the solid in two separate computational domains, the monolithic approach adopts single mesh to handle the interface [91, 179].

Motivations for developing meshless or grid–based methods is the free surface flow problem and the moving fluid–structure interface problem, which arise in many engineering areas with numerous practical aspects. Unlike traditional methods where the determination of the moving free surface is difficult, the Lagrangian particle–based methods can simulate this topic in a relatively easy way. Among several meshless methods, SPH has proven its ability to simulate wide rage of complex engineering problems involving free surface [17, 112, 128]. In MPM, as a grid–based method, both fluid and solid are treated the same inside the mesh except that each of them follows its characteristic constitutive model. In fact, the fluid–structure interface problem has been inherently treated by the no–slip condition in MPM as being applied for different applications [63, 127, 193]. However, the free surface formulation where the fluid material might separate or reattach is not yet well established.

2.7 Concluding remarks

As reviewed in this chapter, various procedures can be used to model large deformation within a continuum mechanics approach. Among all these, there is no best method for all applications. For example, SPH is a powerful method for modelling fluids [112, 116, 128] and thin–walled structures [106, 111] as well as granular material [35]. Owing to its Lagrangian adaptive nature, SPH can handle complex large deformation problems involving free surface. In spite of SPH advantages, one should consider the special treatment of the essential boundary conditions. Furthermore, there is a big computational demand in SPH as it reconstructs the particle neighbour list within the computation, which requires a variable bookkeeping procedure. Finally, the initial spacing setup of the particles needs some experience to obtain good solution, otherwise, poor solution quality might be achieved. The reader is referred to references for more details [106, 112].

Algorithms developed for FE are applicable to the mesh–based methods such as PFEM and MPM. Although the obtained solution in both methods is in Lagrangian manner, the interpretation of material points is different as well as the way of evaluating the constitutive variables. Therefore, most of PFEM applications is related to history–independent materials where the evolution of the field variables are evaluated at the grid nodes [86, 139] with some recent applications to granular material [197]. On the other hand, MPM has been applied to granular material in the presence of plasticity [168]. Więckowski [188] implements different constitutive models for the silo discharge problem. In addition to MPM being well suited for granular material modelling, this thesis is a continuation work of the MPM development for geomechanical applications [2, 21] with more focus on the geotextile and water modelling.

Chapter 3

Dynamic MPM formulation for single–phase solid mechanics problems

To describe a particular phenomenon numerically, the underlying governing equations should be approximated in a proper computational framework. The mathematical description with some continuum mechanics basics are given in Section 3.1. Since large deformations may develop for some problems, simulating these can be challenging for schemes based on Lagrangian or Eulerian descriptions as summarised in Chapter 2. The material point method (MPM) is one of the numerical methods capable of treating these problems without the shortcoming of the traditional methods. As the concepts of MPM are similar to the finite element method (FEM), Section 3.2 is dedicated for the FEM discretisations of a continuum solid body. Two discretisations are adopted in MPM: one to represent the continuum with Lagrangian material points as well as a background computational mesh, which is used to perform the solution for the discretised governing equations. Section 3.3 provides the solution procedure for each time increment to advance the solution and the required manipulation of the boundary conditions. Within the description of the method, two types of particles are introduced in this thesis. The *boundary particles*, which are obtained from the surface discretisation and used to track the orientation of the boundary accordingly. The other type of material points is the *prescribed particles* for defining the non–zero kinematic boundary condition.

Owing to employing low–order element in the current MPM formulation, a non–physical resistance against volume change is expected. Hence, an enhancement procedure is adopted here to relax the behaviour of the numerical model, which has shown its applicability in many geomechanical applications [89, 90, 162]. Furthermore, the frictional contact algorithm [14] is presented and combined with the prescribed velocity boundary particles. These issues and artificial damping necessary for getting gravitational stresses are combined together in Section 3.4. An overview about the numerical implementation sequence of the MPM algorithm is offered in Section 3.5.

Giving that one of the objectives of this research is to provide a numerical scheme capable of handling the dynamics of solid materials under large deformations, the collapse of granular column is considered as a validation for the numerical implementation. The collapse of a sand column is simulated in MPM and compared with experimental results as well as with another numerical method as demonstrated in Section 3.6. By the end of this chapter, we have at hand a powerful numerical tool suitable for geotechnical applications where large deformations are expected to take place. Important to remember here that the pore pressure in granular materials is not considered.

3.1 Basic concepts of continuum mechanics

This section introduces a brief overview about the required basic concepts for the subsequent development. Within the principle of continuum mechanics, it is more convenient to define physical quantities in terms of macroscopic scale without focusing on the microstructure interaction. Hence, the distribution of these quantities is approximated with smooth and continuous variables by ignoring all nonuniformity of the matter.

In order to understand a natural phenomenon via continuum mechanics, three basic ingredients are required: kinematics, balance laws, and material law [123]. Providing that kinematics describes the motion of a continuum body and its related deformation without considering the cause of this motion, the balance laws state how external effects influence this motion. As the last two set of equations are valid for any type of material, the material law provides the mathematical description for the physical characteristics of a particular material. Variational principles provide a more suitable form for the numerical approximation, which will be elaborated in this section, than the balance laws expressed in differential form.

3.1.1 Notation and variables

We define an initial reference configuration of a continuous body Ω_0 enclosed with a boundary Γ_0 at time t_0 in a *reference configuration*, which is subjected to a motion. As a result, the body deforms to the *current configuration* Ω with the boundary Γ corresponding to time t. The position of a certain point belonging to the reference configuration is defined by $\boldsymbol{X}$, whereas the lowercase symbol $\boldsymbol{x}$ denotes its current position. Due to the motion, the *displacement* of a field can be traced giving the two deformation configurations as demonstrated in Figure 3.1.

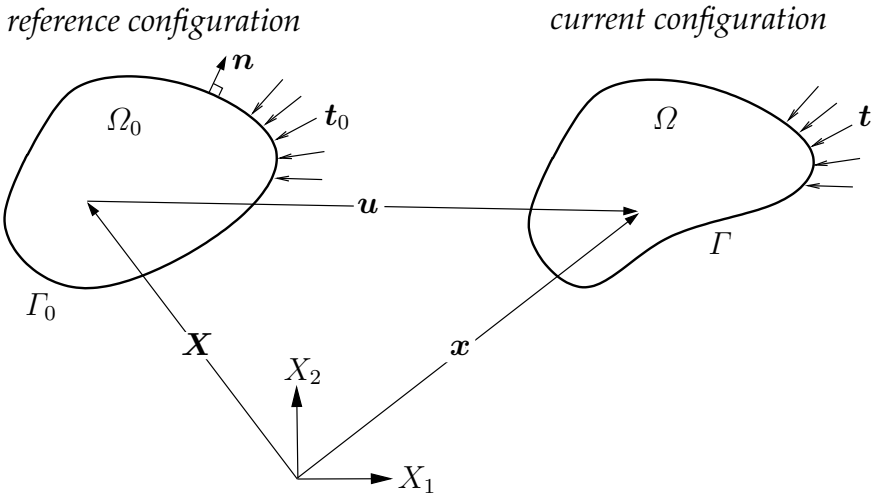

Figure 3.1: Configurations of a continuum body under deformation

Motion The relative motion between the reference and the deformed configurations is introduced as the displacement of a material point, which yields

$$\boldsymbol{u}\left(\boldsymbol{X},t\right)=\boldsymbol{x}\left(\boldsymbol{X},t\right)-\boldsymbol{X}, \tag{3.1}$$

where the displacement $\boldsymbol{u}$ is a vector, which can be written in index notation as u_i with $i\in(1,2,3)$. The time $t\in[t_0,t_f]$, with t_0 and t_f being the initial and final time, respectively. An alternative definition for the displacement can be applied if the deformed configuration $\boldsymbol{x}$ is the independent variable instead of the reference configuration $\boldsymbol{X}$. By definition, the *velocity* $\boldsymbol{v}$ is the rate of change of the position vector for a material point, whereas the *acceleration* $\boldsymbol{a}$ is the second derivative of this vector. Applying these definition in Equation 3.1 and using the chain rule for differentiation, the acceleration reads

$$\frac{dv_i\left(x_i,t\right)}{dt}=\frac{\partial v_i}{\partial t}+v_j\frac{\partial x_i}{\partial x_j}. \tag{3.2}$$

in which, d implies the *substantial derivative*, which is composed of the local and the convective term. The last term is neglected in the case of updated Lagrangian formulation when the material deformation is tracked [123]. Therefore, there will be no discrimination between the derivatives with respect to $\boldsymbol{X}$ or the lowercase.

Strain The *strain* ε_{ij}, defined as the normalised deformation with respect to a reference length, is a second order tensor. More often we write the strain tensor in vector representation such that

$$\boldsymbol{\varepsilon}=\begin{bmatrix}\varepsilon_{11} & \varepsilon_{22} & \varepsilon_{33} & 2\varepsilon_{12} & 2\varepsilon_{23} & 2\varepsilon_{13}\end{bmatrix}^T, \tag{3.3}$$

where the strain vector in Equation 3.3 contains the total strain components. For the sake of material modelling, however, a rate form of strain $\dot{\boldsymbol{\varepsilon}}$ is considered that is given as the symmetric part of the velocity gradient

$$\dot{\varepsilon}_{ij}=\frac{1}{2}\left(\frac{\partial v_i}{\partial x_j}+\frac{\partial v_j}{\partial x_i}\right). \tag{3.4}$$

The strain can be recognised as *Lagrangian* or *Eulerian* if it is based on the reference or the current configuration, respectively [123]. For any measurement reference, strain must disappear for rigid body motion, otherwise, *stress* is developed.

Stress Stress develops through a continuum as a result of deformation. Stress applied on the current configuration is characterised by *Cauchy stress* tensor, which can be written in similar fashion to Equation 3.3 as

$$\boldsymbol{\sigma}\left(\boldsymbol{x},t\right)=\begin{bmatrix}\sigma_{11} & \sigma_{22} & \sigma_{33} & \sigma_{12} & \sigma_{23} & \sigma_{13}\end{bmatrix}^T. \tag{3.5}$$

The Cauchy stress $\boldsymbol{\sigma}$ may be regarded as the *true stress* as it refers to the deformed configuration.

3.1.2 Constitutive equation

The *constitutive equation* is the description of the material characteristics based on its internal constitution. In other words, it describes mathematically the relationships between strains and stresses to permit the formulation of well–posed problems of continuum mechanics. The constitutive equation idealises material response that serves as a model of the behaviour of real materials. Materials often behave differently for different loading conditions. Therefore, the constitutive equation would describe certain particular behaviour of a material instead of describing the material itself.

The principle of *material objectivity* or *material frame indifference* states that the material response is independent of the observer. Strictly speaking the constitutive model should be written taking into account an objective frame of reference [123]. As the time evolves for a body under deformation, difference between the reference and deformed configuration might take place, which can be neglected if small deformation is concerned. In case of finite deformation, however, the non–linear problem can be linearised over small incremental deformation. A general elastic constitutive equation can be constructed in the form

$$\overset{\circ}{\boldsymbol{\sigma}} = f\left(\dot{\boldsymbol{\varepsilon}}\right), \tag{3.6}$$

where $\overset{\circ}{\boldsymbol{\sigma}}$ is an objective stress rate tensor, and f is the constitutive equation. The Cauchy stress $\boldsymbol{\sigma}$ is symmetric and objective, however, its material time derivative can be proven to be not objective. Different forms of objective stress rate can be found in continuum mechanics [18, 47, 123]. For instance, the *Jaumann co–rotational stress rate* can be correlated to the Cauchy stress rate via

$$\overset{\circ}{\sigma}_{ij} = \dot{\sigma}_{ij} - \omega_{ik}\,\sigma_{kj} + \sigma_{ik}\,\omega_{kj} \tag{3.7}$$

with ω_{ij} being the *spin tensor* defined as

$$\omega_{ij} = \frac{1}{2}\left(\frac{\partial v_i}{\partial x_j} - \frac{\partial v_j}{\partial x_i}\right). \tag{3.8}$$

Hill [76] advances Equation 3.7 by introducing the volume change effect. The *Hill rate*, which is also called the *co–rotational rate of Kirchhoff* stress tensor $\overset{\triangledown}{\sigma}_{ij}$, can be written in the form

$$\overset{\triangledown}{\sigma}_{ij} = \dot{\sigma}_{ij} - \omega_{ik}\,\sigma_{kj} + \sigma_{ik}\,\omega_{kj} + \dot{\varepsilon}_{kk}\,\sigma_{ij}, \tag{3.9}$$

where $\dot{\varepsilon}_{kk}$ is the spherical part of the strain rate tensor. The objective stress rate definition, Equation 3.7 or 3.9, is applicable now for the constitutive equation; i.e.,

$$\overset{\triangledown}{\sigma}_{ij} = D_{ijkl}\,\dot{\varepsilon}_{kl}, \tag{3.10}$$

in which D_{ijkl} is the constitutive tensor.

3.1.3 Conservation equations

Conservation equations are based on balance principles that govern material behaviour and independent of material properties. An overview of mass conservations, momentum balance principles, and the balance of energy and entropy are presented here.

Conservation of mass Consider the case of closed system where no mass enters or leaves the boundary Γ of the body Ω. The mass balance reads

$$\int_{\Omega} \left(\frac{d\varrho}{dt} + \varrho \frac{\partial v_i}{\partial x_i} \right) d\Omega = 0, \tag{3.11}$$

where ϱ denotes the material mass density. Since the integral of Equation 3.11 vanishes for arbitrary choice of Ω, it follows that the integrand mush vanish at each point of a region in which no mass is created or destroyed [123].

Conservation of momentum The law of conserving linear momentum states that the rate of change of linear momentum of a continuum body equals the *external forces* applied to it. External forces compose of body forces and surface forces. The body forces act throughout the body and are formulated in terms of unit weight; e.g. gravity force, whereas the surface forces act on the boundary and are presented in terms of unit area; e.g. traction forces. By adopting these forces, the momentum equation is given by

$$\frac{d}{dt} \int_{\Omega} \varrho \, v_i \, d\Omega = \int_{\Omega} \varrho \, g_i \, d\Omega + \int_{\Gamma_t} t_i \, d\Gamma, \tag{3.12}$$

with g_i being the gravitational force vector per unit mass and t_i refereeing to the traction vector exerted on the boundary Γ_t ($\Gamma_t \subset \Gamma$). The material time derivative of the left hand side of Equation 3.12 can be performed on the integrand with the aid of Equation 3.11. *Cauchy's formula* is adopted to establish a relationship between the traction vector and the Cauchy stress tensor in the form

$$\sigma_{ij} \, n_j = t_i, \tag{3.13}$$

in which n_j is the outward unit normal vector. Implementing the definition in Equation 3.13 and the divergence theorem to the last term of Equation 3.12 with rearrangement, finally it reads

$$\varrho \frac{dv_i}{dt} = \frac{\partial \sigma_{ij}}{\partial x_j} + \varrho \, g_i. \tag{3.14}$$

Other considerations Likewise the linear momentum, angular momentum should be conserved. Angular momentum conservation requires that the rate of change of angular momentum of a body equals the sum of the moments applied by the external forces and the distributed body couples. In the absence of distributed body couple, the conservation of angular momentum entail that the stress tensor σ_{ij} is symmetric.

First thermodynamics law, or conservation of energy, must be satisfied as well. Energy balance states that the rate of change of kinetic and internal energy of a body equals

to the rate at which external mechanical work done by external forces plus the rate at which thermal energy is added by heat flux and heat sources. In the class of problems addresses in this thesis, the heat transfer problem is omitted.

Defining a constitutive law in Equation 3.9 for a specific material should satisfy the *entropy inequality*. The entropy inequality, or the second law of thermodynamics, states that the internal entropy production is always greater than or equal to zero, which can mathematically expressed by the *Clausius–Duhem* inequality [123].

3.1.4 Boundary conditions

In order to have a well–posed problem, appropriate boundary conditions are required. Two types of boundary conditions are typically applied. Prescribed displacement on Γ_u and prescribed traction on Γ_t, with $\Gamma = \Gamma_u \cup \Gamma_t$. For the displacement boundary condition, or so–called the *essential boundary condition*, we write

$$\boldsymbol{u}\left(\boldsymbol{x}, t\right) = \bar{\boldsymbol{u}}\left(t\right) \qquad \text{on} \qquad \Gamma_u\left(t\right), \tag{3.15}$$

in which, $\bar{u}_i$ is a definitive value. The traction condition or the *natural condition* is given as

$$\boldsymbol{\sigma}\left(\boldsymbol{x}, t\right) \cdot \boldsymbol{n} = \bar{\boldsymbol{t}}\left(t\right) \qquad \text{on} \qquad \Gamma_t\left(t\right), \tag{3.16}$$

where $\bar{\boldsymbol{t}}$ is the prescribed traction along the boundary Γ_t. Equation 3.16 can also be written in the vector form instead of the tensor form as [204]

$$\boldsymbol{G}^T \boldsymbol{\sigma} = \bar{\boldsymbol{t}}, \tag{3.17}$$

with

$$\boldsymbol{G}^T = \begin{bmatrix} n_1 & 0 & 0 & n_2 & 0 & n_3 \\ 0 & n_2 & 0 & n_1 & n_3 & 0 \\ 0 & 0 & n_3 & 0 & n_2 & n_1 \end{bmatrix} \tag{3.18}$$

in which $\boldsymbol{n} = \begin{bmatrix} n_1 & n_2 & n_3 \end{bmatrix}^T$ are the direction cosines of the normal to the boundary Γ.

3.1.5 Principle of virtual work

Owing to difficulties in solving the differential equations, an integral form is more suitable to reduce the order of the equations. This implies that the underlying equations of the problem are satisfied in an average sense. In order to derive the weak form equations, the principle of virtual displacements is adopted. An example of obtaining the weak form of the momentum equation is obtained by multiplying Equation 3.14 by a *test function* and integrate over the spatial domain. As the test function is chosen arbitrarily, it can be virtual displacement $\delta\boldsymbol{u}$, which yields the *principle of virtual work*. On the other hand, selecting virtual velocity $\delta\boldsymbol{v}$ follows the *principle of virtual power* [18]. Choosing the type of virtual work depends ultimately on the primary field variable being discretised.

This variation is understood to be an arbitrary, infinitesimally small virtual increment, which is imposed upon the system at a fixed time and in a fixed position.

Although the virtual function is selected to be random, however, the solution function $\boldsymbol{u}$ and the test function $\delta\boldsymbol{u}$ should be in the same space [202]. In other words, the test function should satisfy the homogeneous boundary condition; i.e., the essential boundary conditions represented by Equation 3.15. Whereas it need not conform the natural boundary where traction is prescribed. Moreover, the function $\delta\boldsymbol{u}$ should be sufficiently regular, which implies that the divergence theorem is applicable.

Remembering that the *divergence theorem* states that the outward flux of a vector field through a closed boundary equals to the integral of the divergence over the region enclosed by that boundary, which mathematically reads

$$\int_{\Omega} \frac{\partial \sigma_{ij}}{\partial x_j}\, d\Omega = \int_{\Gamma} \sigma_{ij}\, n_j\, d\Gamma, \tag{3.19}$$

with Γ is the boundary of the domain Ω. Applying the principle of virtual work to Equation 3.14 and integrating the high–order derivatives by parts, with the aid of Equations 3.19 and 3.13, yields

$$\int_{\Omega} \delta u_i\, \varrho \frac{dv_i}{dt}\, d\Omega = \int_{\Omega} \delta u_i\, \varrho\, g_i\, d\Omega - \int_{\Omega} \frac{\partial\,(\delta u_i)}{\partial x_j} \sigma_{ij}\, d\Omega + \int_{\Gamma_t} \delta u_i\, t_i\, d\Gamma, \tag{3.20}$$

where the last term is a boundary term appears as a result of integration by part. The weak form in the last equation is equivalent to the strong form in Equation 3.14. However, moving the differentiation from the primary variable to a virtual variable allows us to define stresses on boundary, which is quite useful in the finite element formulation.

3.2 FEM discretisations

A brief overview for the discretisation of the weak form equation into algebraic form using the finite element procedure is presented in this section. Before this, we rewrite Equation 3.14 for a three–dimensional spatial coordinate system x_1, x_2, x_3 in a compact matrix format such that

$$\varrho\, \boldsymbol{a} = \boldsymbol{L}^T\, \boldsymbol{\sigma} + \varrho\, \boldsymbol{g}, \tag{3.21}$$

where $\boldsymbol{a}\,(\boldsymbol{x}, t)$ is the acceleration, and the linear differential operator $\boldsymbol{L}$ is

$$\boldsymbol{L}^T = \begin{bmatrix} \dfrac{\partial}{\partial x_1} & 0 & 0 & \dfrac{\partial}{\partial x_2} & 0 & \dfrac{\partial}{\partial x_3} \\ 0 & \dfrac{\partial}{\partial x_2} & 0 & \dfrac{\partial}{\partial x_1} & \dfrac{\partial}{\partial x_3} & 0 \\ 0 & 0 & \dfrac{\partial}{\partial x_3} & 0 & \dfrac{\partial}{\partial x_2} & \dfrac{\partial}{\partial x_1} \end{bmatrix}, \tag{3.22}$$

which is also used in the kinematics equation as

$$\dot{\boldsymbol{\varepsilon}}\left(\boldsymbol{x},t\right)=\boldsymbol{L}\left(\boldsymbol{x}\right)\,\boldsymbol{v}\left(t\right). \tag{3.23}$$

Similarly, the weak form in Equation 3.20 can be written in the matrix form

$$\int_{\Omega}\varrho\,\delta\boldsymbol{v}^{T}\,\boldsymbol{a}\,d\Omega=\int_{\Omega}\varrho\,\delta\boldsymbol{v}^{T}\,\boldsymbol{g}\,d\Omega-\int_{\Omega}\left(\boldsymbol{L}\,\delta\boldsymbol{v}\right)^{T}\,\boldsymbol{\sigma}\,d\Omega+\int_{\Gamma_{t}}\delta\boldsymbol{v}^{T}\,\boldsymbol{t}\,d\Gamma. \tag{3.24}$$

3.2.1 Spatial discretisation

The aim of the finite element method is to solve a system of differential equations over a spatial domain. Therefore, the continuum domain is approximated into subdomains, or *finite elements*, where the continuous equation is approximated for discrete values. The approximated function is then interpolated via *shape functions* inside all elements, which are linked together via the grid nodes. The mathematical representation of such discretisation is represented by

$$\Omega=\bigcup_{i=1}^{nel}\Omega_{i}\qquad\forall\quad\Omega_{i}\cap\Omega_{j}=0:i\neq j, \tag{3.25}$$

where Ω is the spatial domain being discretised into nel elements, and Ω_i is the domain of element i. The location of any point inside an element is interpolated with the aid of the shape functions as

$$\boldsymbol{x}=\boldsymbol{N}\,\tilde{\boldsymbol{x}}, \tag{3.26}$$

with $\boldsymbol{x}$ being the interpolated position inside the element, $\tilde{\boldsymbol{x}}$ is the location of the element nodes, and $\boldsymbol{N}$ is the shape function matrix given for four–noded tetrahedral elements by

$$\boldsymbol{N}\left(\boldsymbol{x}\right)=\begin{bmatrix}\boldsymbol{N}_{1}\left(\boldsymbol{x}\right) & \boldsymbol{N}_{2}\left(\boldsymbol{x}\right) & \boldsymbol{N}_{3}\left(\boldsymbol{x}\right) & \boldsymbol{N}_{4}\left(\boldsymbol{x}\right)\end{bmatrix}, \tag{3.27}$$

where $\boldsymbol{N}_i$ is a linear interpolation function in the case of the adopted element type as given in Appendix A. Usually, the interpolation functions are polynomials expressed in terms of the *parent coordinates* ξ_1, ξ_2, ξ_3. The role for the parent coordinates will be demonstrated in the course of this section.

Similar to the position vector, the deformation can be interpolated across the element span using an interpolation function. This type of interpolating deformation is called *isoparametric interpolation* when the same functions are used for deformation as for location, which means

$$\boldsymbol{u}\left(\boldsymbol{x},t\right)\approx\boldsymbol{N}\left(\boldsymbol{x}\right)\,\tilde{\boldsymbol{u}}\left(t\right), \tag{3.28}$$

with $\tilde{\boldsymbol{u}}$ being the nodal approximation of the displacement. Impeding the approximated velocity definition in the kinematic equation 3.23 gives

$$\dot{\boldsymbol{\varepsilon}}\left(\boldsymbol{x},t\right)\approx\boldsymbol{B}\left(\boldsymbol{x}\right)\,\tilde{\boldsymbol{v}}\left(\boldsymbol{x},t\right), \tag{3.29}$$

where $\boldsymbol{B} = \boldsymbol{L}\,\boldsymbol{N}$ is the *strain–displacement matrix* . The dimensions of the $\boldsymbol{B}$ matrix are defined by the number of constitutive variables in rows and the number of degrees of freedom per element in column, which then becomes (6×12) in the case of the four–noded tetrahedral element, which is used in this thesis. As the interpolation is linear when using low–order element, the spatial gradients across the element are constant. Therefore, all components of the $\boldsymbol{B}$ matrix are constant, which implies that strain–rate prediction, and accordingly the stress–rate, is constant.

Next step in the finite element procedure is to sum the virtual power of all finite elements by recalling Equations 3.24 and 3.29, which yields

$$\delta\tilde{\boldsymbol{v}}^T \sum_{e=1}^{nel} \left(\int_\Omega \boldsymbol{N}^T \varrho\, \boldsymbol{N}\, \tilde{\boldsymbol{a}}\, d\Omega = \int_\Omega \varrho\, \boldsymbol{N}^T\, \boldsymbol{g}\, d\Omega - \int_\Omega \boldsymbol{B}^T\, \boldsymbol{\sigma}\, d\Omega + \int_\Gamma \boldsymbol{N}^T\, \boldsymbol{t}\, d\Gamma \right), \tag{3.30}$$

in which $\tilde{\boldsymbol{a}}$ is the approximated nodal acceleration vector and $\delta\tilde{\boldsymbol{v}}^T$ is the nodal discretisation of the virtual velocity, which is not function of the spatial coordinates and can therefore be brought outside the integral. One has to recognise we are making use of the thermodynamic property that the mass matrix of the system is the assembly of all elements, as well as the displacement and velocity at the elements boundary both are being continuous. Therefore, we construct the equations here for one element and the extension for the global system must include the aforementioned note. As Equation 3.30 holds for arbitrary virtual velocity, therefore, it arrives at the traditional form of the finite element system of equations

$$\boldsymbol{M}^c\, \tilde{\boldsymbol{a}} = \boldsymbol{F}^{\text{ext}} - \boldsymbol{F}^{\text{int}}, \tag{3.31}$$

with

$$\boldsymbol{M}^c = \int_\Omega \boldsymbol{N}^T\, \varrho\, \boldsymbol{N}\, d\Omega,$$

$$\boldsymbol{F}^{\text{ext}} = \int_\Omega \varrho\, \boldsymbol{N}^T\, \boldsymbol{g}\, d\Omega + \int_\Gamma \boldsymbol{N}^T\, \boldsymbol{t}\, d\Gamma,$$

$$\boldsymbol{F}^{\text{int}} = \int_\Omega \boldsymbol{B}^T\, \boldsymbol{\sigma}\, d\Omega,$$

where $\boldsymbol{M}^c$ is the consistent mass matrix, and the unknown vector $\tilde{\boldsymbol{a}}$ contains the unknown variable of the entire discretised domain, with $\boldsymbol{F}^{\text{ext}}$ and $\boldsymbol{F}^{\text{int}}$ being the external and internal force vectors, respectively. In Equation 3.31, the external forces are composed of body force and the traction force. Although the latter is an assemblage of all boundary elements, only exterior boundaries are considered.

Performing the integration of Equation 3.31 along global coordinate system is quite challenging even though numerical integration is applied. Therefore, it is more common in finite element to transfer the geometry of the element from x_1, x_2, x_3 coordinate system into parent element system ξ_1, ξ_2, ξ_3. As the selection of the parent coordinate is arbitrary, a unit linear tetrahedron is usually chosen to be the reference element. Functions and their derivatives that appear in Equation 3.31 are mapped from global to parent

coordinate system using the *Jacobian matrix*. More details about the mapping procedure can be found in Appendix A. Hence, all matrices in Equation 3.31 can be expressed in parent coordinate system; e.g., the internal force vector becomes

$$\boldsymbol{F}^{\text{int}} = \sum_{e=1}^{nel} \int_{\xi_1=0}^{1} \int_{\xi_2=0}^{1} \int_{\xi_3=0}^{1} |\boldsymbol{J}|\, \boldsymbol{B}^T\, \boldsymbol{\sigma}\, d\xi_1 d\xi_2 d\xi_3, \tag{3.32}$$

where $|\boldsymbol{J}|$ is the determinant of the Jacobian matrix defined in Appendix A. Numerical integration can now be applied in Equation 3.32 easily in the form

$$\boldsymbol{F}^{\text{int}} = \sum_{e=1}^{nel} \sum_{i=1}^{nit} |\boldsymbol{J}_i|\, \boldsymbol{B}_i^T\, \boldsymbol{\sigma}_i\, w_i, \tag{3.33}$$

with w_i denoting the integration weight factor of the integration point i where all variables of the integrand are evaluated, and nit is the total number of integration points inside the element. To ensure highest accuracy and efficiency for the integration, more often such integration point is located at the Gaussian quadrature point.

3.2.2 Time discretisation

The system of algebraic equations given in Equation 3.31 is called the *semi–discretised equation* as yet not discretised in time. For this purpose, *explicit* or *implicit* time integration schemes can be adopted. In the explicit scheme, the sought solution obtained at the end of the computational time step is completely based on known information at the beginning of this step. Explicit integration is computationally cheap as the system matrices are known initially without need for inversion. As a consequence of formulating the differential equation in terms of information of the old time step, no solution can be obtained when the limit of the time step size approaches infinity. Hence, the explicit integration is *conditionally stable* meaning that the time step size is restricted to ensure stability. On the other hand, the updated solution with the implicit scheme couples some or all quantities evaluated at the end of the computational step and therefore no stability restriction of the time step size is needed, which is known as *unconditionally stable*. Adopting this method, the solution is advanced by inverting matrices or an iteration process, for relatively large time steps.

Decision of using implicit or explicit integration scheme depends mainly on the type of problem aimed to solve and the degree of accuracy. Care should be taken when explicit scheme is adopted that the accumulation of the rounding error might drift the numerical solution away from the correct one. Applying implicit approximation reduces this error, which then should be valuable as compared to the computational demands. For a non–linear static problem, the iteration through a sequence of computational steps helps to converge toward the final state solution. For such a type of applications, the implicit scheme is quite attractive to obtain the finial solution with smaller number of steps than if explicit dynamic is used. An extensive talk on explicit and implicit time integration schemes can be found in; e.g., [84, 202].

In this work, only explicit time integration is considered. Owing to the advantage of using explicit scheme is being computationally efficient, the mass matrix must be diagonalised, or *lumped*. Lumping the consistent mass matrix will remove the coupling between the algebraic equations, which makes the solution of the momentum equation easy. Numerous techniques of lumping can be found in literature; see for example [18, 84]. The essential requirement in all these methods can mathematically expressed by

$$\sum_i M_{ii} = \int_\Omega \varrho \, d\Omega, \tag{3.34}$$

where M_{ii} is the diagonal for a component of the lumped mass matrix $\boldsymbol{M}$. The lumping procedure for linear interpolation elements is straight forward, however, the accuracy with higher order elements is questionable. In this regards, Hinton et al. [77] proved the accuracy of obtaining lumped mass matrix by scaling the diagonal terms of the consistent one with the satisfactory of Equation 3.34. By the same token of preserving accuracy of lumping high–order elements, Fried and Malkus [61] used the sampling points at nodes instead of the Gauss quadrature, which allows the off–diagonal terms in the mass matrix to vanish. Such integration by locating the sampling points at the nodes is applicable in the case of structural elements like beams and plates where the Newton–Cotes integration rule might be used. Loosing accuracy is possible not only with the high–order elements where the lumping is not unique, however, low–order element also loss some accuracy, which is not comparable to the advantage of using it [201]. For the four–noded tetrahedral element being adopted in this research, however, using any of the lumping procedure gives the following

$$\boldsymbol{M} = \sum_{e=1}^{nel} \sum_{i=1}^{nit} |\boldsymbol{J}_i| \, \varrho_i \, \boldsymbol{N}\left(\boldsymbol{x}_i\right) \, w_i, \tag{3.35}$$

where $\boldsymbol{M}$ is a vector written in matrix form denotes the lumped mass. It can proven that the components of $\boldsymbol{M}$ in Equation 3.35 is the same as the summation of the corresponding rows of the consistent mass matrix. The inverse of the lumped mass matrix can be obtained directly and therefore Equation 3.31 can be rewritten in the form

$$\tilde{\boldsymbol{a}}^n = \left[\boldsymbol{M}^n\right]^{-1} \left(\boldsymbol{F}^{\text{ext}} - \boldsymbol{F}^{\text{int}}\right)^n, \tag{3.36}$$

with the superscript n being a time step counter. Getting the nodal acceleration from Equation 3.36, the grid velocity is obtained explicitly as

$$\tilde{\boldsymbol{v}}^{n+1} = \tilde{\boldsymbol{v}}^n + \Delta t \, \tilde{\boldsymbol{a}}^n, \tag{3.37}$$

where Δt denotes the time increment, $\tilde{\boldsymbol{v}}^n$ and $\tilde{\boldsymbol{v}}^{n+1}$ are the nodal velocity vectors at the beginning and the end of the time step, respectively. Finally, the increment of nodal displacement is used to update the grid implicitly via

$$\tilde{\boldsymbol{u}}^{n+1} = \tilde{\boldsymbol{u}}^n + \Delta t \, \tilde{\boldsymbol{v}}^{n+1}, \tag{3.38}$$

in which $\tilde{\boldsymbol{u}}$ is the nodal displacement vector.

Since the material might be history dependent, the internal variables must be updated

as well as kinematics quantities; i.e.,

$$\boldsymbol{\sigma}^{n+1} = \boldsymbol{\sigma}^{n} + \int_{t}^{t+\Delta t} \dot{\sigma}\left(\boldsymbol{\sigma}, \boldsymbol{\varepsilon}, \dot{\boldsymbol{\varepsilon}}, \cdots\right)\, dt, \tag{3.39}$$

where the last term is obtained by integrating the constitutive equation, Equation 3.10. The incremental strain tensor $\Delta\boldsymbol{\varepsilon}_i$ for an integration point i is obtained from

$$\Delta\boldsymbol{\varepsilon}_i^{n+1} = \Delta t\, \boldsymbol{B}_i^{n+1}\, \tilde{\boldsymbol{v}}_e^{n+1}, \tag{3.40}$$

where the subscript e indicates the element where the integration point i is located. As the mass of the material point is kept constant during the calculation, the density of the material is implicitly updated since the volume of the integration point is updated through

$$w_i^{n+1} = w_i^{n}\left(1 + \Delta\varepsilon_{v,i}\right), \tag{3.41}$$

in which, $\Delta\varepsilon_{v,i}$ is the volumetric strain increment of the integration point i. This linearisation is reasonable given the small time steps that are taken when using an explicit time marching scheme.

As mentioned earlier, the explicit integration has limited time step size. Therefore, in order to get stable solution, the maximum time step size of the explicit finite difference scheme is bounded with [16, 18]

$$\Delta t_{\mathrm{crt}} = \frac{2}{\omega_{\max}}, \tag{3.42}$$

where Δt_{crt} is the critical time step, and $\omega_{\max}$ is the maximum frequency of the system. For the purpose of getting maximum frequency, an eigenvalue analysis should be carried by solving

$$\|\boldsymbol{K} - \omega_{\max}^2 \boldsymbol{M}\| = 0, \tag{3.43}$$

in which $\boldsymbol{K}$ is the stiffness matrix of the system. Since the stiffness matrix is not constructed during the explicit procedure, Equation 3.43 is applied on element level rather than on the entire system. The *Courant–Friedrichs–Lewy* (CFL) stability condition [41] is often considered, which has been detailed in finite element books [16, 84]. This condition replaces Equation 3.43 by the form

$$\Delta t_{\mathrm{crt}} = \frac{l_c}{c_p}, \tag{3.44}$$

with l_c being the characteristics length of the element, and c_p is the compression wave speed computed from

$$c_p = \sqrt{\frac{E_c}{\varrho}}, \tag{3.45}$$

where E_c is the constraint elastic modulus and ϱ is the material mass density. The characteristic length l_c conducted in this study as the minimum height of the tetrahedral

element [2]. However, there are some ways of defining l_c for the tetrahedral element; e.g., as triple the tetrahedral element divided by the maximum triangular area [136].

The minimum time step presented in Equation 3.44 is in fact to ensure stability of the explicit scheme only. To achieve accuracy in the time integration of the system in Equation 3.31 and the constitutive law, Equation 3.39, smaller time should be considered. Therefore, Equation 3.44 is multiplied with α, $0 < \alpha < 1$, which is a factor introduced to improve stability and accuracy of the explicit algorithm. The reader is referred to more specific references where the constitutive equation development is the focus of interest, see for example [163, 183, 200].

3.3 Dynamic MPM representation

The material point method (MPM) is a numerical technique for solving continuum problems in fluid and solid mechanics. MPM has its origin from the particle in cell (PIC) for fluid mechanics in the fifties, thereafter, it became more applicable in dynamics of history dependent materials in the nineties, as reviewed in Chapter 2. The concepts of the method is based on combining the advantages of Eulerian and Lagrangian methods to deal with the problems of large displacements and deformations.

In MPM, the computational domain is discretised using two type of discretisations. First, the Lagrangian discretisation where the continuum body is represented by *material points*, or particles, which are tracked during the computation. To solve the momentum equation, the *computational mesh* is introduced as a second discretisation that provides a convenient means of calculating discrete derivatives and carrying out integration. Whereas for FEM, the material points are tied tightly to the elements, for MPM the material points are allowed to move from one element to another in Eulerian fashion

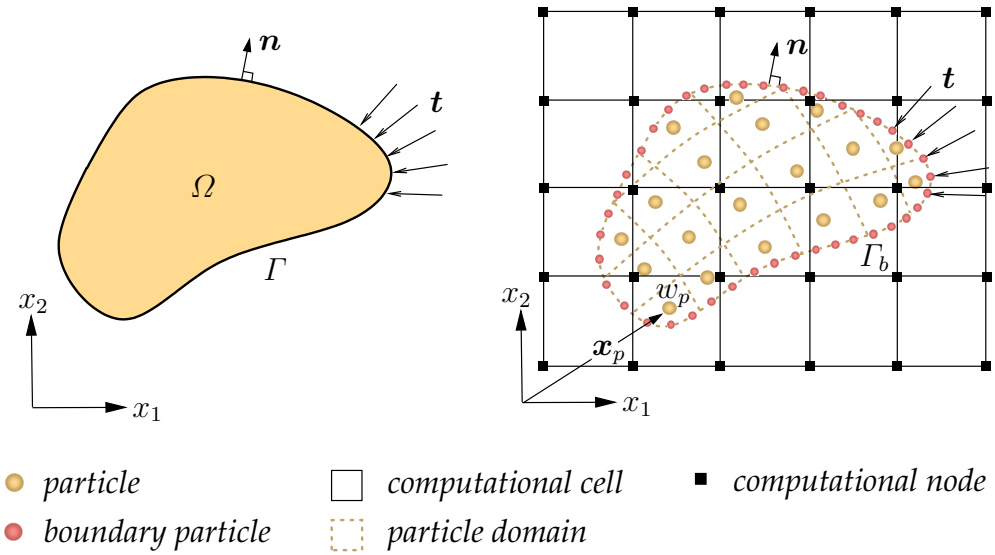

Figure 3.2: Continuum body (left) discretised with MPM (right)

such that the state properties remain with the material points. Care should be taken here to make a clear distinction between pure Eulerian process, where the total derivative of local and convective components is applied, while the latter does not exist within the MPM framework. Giving that the movement of the Lagrangian material points through the computational cell is traced, the convection of the material is resembled naturally. Illustration of MPM discretisations for a continuum body is shown in Figure 3.2.

In this thesis we follow the original MPM formulation [166, 169], in which a body is defined in terms of material points. In other words, the properties and state variables such as stress and momentum are collocated at the material points. Other description for the descretisation; e.g. GIMP and CPDI where the material points domains are spatially extended, which is not considered in this research. Chapter 2 of this thesis provides the concepts of these methods, while more details can be found in [12, 151, 198] and the references mentioned therein.

3.3.1 MPM discretisation

Following the original MPM description, the continuum body Ω shown in Figure 3.2 is discretised into subdomains, where the mass of the subdomain w is concentrated at the location $\boldsymbol{x}_p$ of the material point p such that

$$\varrho\left(\boldsymbol{x}\right) = \sum_{p=1}^{n_p} m_p \, \delta\left(\boldsymbol{x} - \boldsymbol{x}_p\right), \tag{3.46}$$

in which m_p is the mass of the material point p, n_p is the number of material points, and the Dirac delta function δ is defined by

$$\delta\left(\boldsymbol{x} - \boldsymbol{x}_p\right) = \begin{cases} 0, & \boldsymbol{x} \neq \boldsymbol{x}_p \\ +\infty, & \boldsymbol{x} = \boldsymbol{x}_p \end{cases} \qquad \text{with} \quad \int_{-\infty}^{+\infty} \delta\left(\boldsymbol{x} - \boldsymbol{x}_p\right) \, d\boldsymbol{x} = 1, \tag{3.47}$$

where Equation 3.46 is not applicable to the boundary particles, see Figure 3.2, as these particles represent the boundary Γ. The concept of performing integration at material concentration point in MPM is similar to FEM, except that the material points are able to move within the computation and therefore not to be surely at the Gaussian point. The discretised system, Equation 3.31, can be written in terms of material points as

$$\boldsymbol{M}\,\tilde{\boldsymbol{a}} = \boldsymbol{F}^{\mathrm{ext}} - \boldsymbol{F}^{\mathrm{int}}, \tag{3.48}$$

in which, the associated changes to the FE description are considered next.

3.3.1.1 Mass matrix

Within the MPM procedure, mapping of information is taking place between the two discretisation configurations presented earlier. Burgess et al. [36] had shown that mapping of data between particles and the nodes implies that the kinetic energy and momentum

are conserved. Furthermore, diagonalising the mass matrix by lumping causes a dissipation in the kinetic energy with the order of magnitude $(\Delta t)^2$ [169], which compensate the cost of inverting this matrix in explicit procedure. The kinetic energy amount being dissipated is evaluated for history dependent and independent materials [30, 31, 168].

Considering that the MPM particles might change elements during the computation, the mass matrix changes accordingly. Each diagonal entry of the lumped mass matrix is obtained from the corresponding row sum of the consistent one. Alternatively, the mass (m_i) associated to node i referring to the element level can be expressed as

$$m_i = \sum_{p=1}^{n_p} m_p \, N_i \left(\boldsymbol{x}_p \right), \tag{3.49}$$

where n_p is the number of material points and m_p is the mass of material point p. The variable $\boldsymbol{x}_p$ indicates the location where the shape function N_i is evaluated. The shape function acts as a weighting function to correctly distribute the mass among the nodes.

3.3.1.2 External forces

The external forces contain traction applied at the exterior boundary of the region and body forces. The body forces in this research contains the gravitational force only. Both forces, traction and gravitational, are defined so far in terms of fixed number of grid vertices in the FE framework. In MPM, however, the size of the equations of motion is varying during the computation as the particles change elements. Hence, the external forces should be represented on the particles, which represents the Lagrangian body.

Body force The body force, which is represented as a unit force per unit volume or mass, is assigned to the material points. After initialising the mass of the material points from Equation 3.46, the gravitational force is initialised at the material points via

$$\boldsymbol{f}_p^{\mathrm{grv}} = m_p \, \boldsymbol{g}, \tag{3.50}$$

with $\boldsymbol{f}_p^{\mathrm{grv}}$ being the gravitational force vector carried by the particle p. As the discretised form of the governing equations given in Equation 3.48 is performed in terms of the computational mesh, the gravitational force in Equation 3.50 should be transferred from the material points to the grid nodes at the beginning of each time step. The transferring of this force is weighted by the interpolation function as

$$\boldsymbol{F}^{\mathrm{grv}} = \sum_{p=1}^{n_p} \boldsymbol{N}^T \left(\boldsymbol{\xi}_p \right) \, \boldsymbol{f}_p^{\mathrm{grv}}, \tag{3.51}$$

where $\boldsymbol{F}^{\mathrm{grv}}$ is the gravitational nodal force defined for the entire mesh.

Traction force In MPM with small deformations, the load can be applied directly at the boundary grid nodes with no distinction from FE, whereas this treatment for the

traction boundary is not applicable if large deformations exist. Therefore, it is more convenient to follow the motion of the deformed body in a Lagrangian manner by applying the traction force on the material points.

At the beginning of the computation, the external load can be directly assigned to the material points, or alternatively, mapped from the computational grid nodes. Actual boundary should be tracked each time step by mapping information back and forth between the particles and the mesh [2, 198]. This procedure has been extended in the present thesis by introducing surface discretisation wrapping the Lagrangian body, see Appendix B. As the coarseness of this surface is not related to the MPM discretisation, it can be selected reasonably fine to improve the traction mapping instead of the first row of particles [2]. In this way, the surface orientation can be tracked easily, which becomes important in the case of large surface deformation. Furthermore on the purpose of defining this surface that the local normal vector can be detected easily by tracking this surface during the calculation as will be demonstrated later.

Let us assume an irregular mesh discretisation, as described in Appendix B, and the traction load is properly integrated and discretised at the preprocessing stage on the boundary nodes. Therefore, we start by giving the surface traction as nodal force $\tilde{\boldsymbol{t}}$, which then is mapped to the boundary points as illustrated in Figure 3.3 and given by

$$\boldsymbol{f}_b^{\mathrm{trc}} = \sum_{i=1}^{n_t} N_i\left(\boldsymbol{\xi}_b\right)\, \tilde{\boldsymbol{t}}\left(x_i, t\right)\, \frac{\Gamma_b}{\Gamma_i}, \tag{3.52}$$

where $\boldsymbol{f}_b^{\mathrm{trc}}$ is the surface traction force associated to the boundary particle b, N_i is the interpolation function of node i on the triangular face, with n_t being the number of nodes per face, which is reduced to 3 in the case of the 4–noded tetrahedral element. Equation 3.52 clearly indicates that the surface traction force is weighted by the corresponding surface area of the boundary particle Γ_b and the area being represented at node Γ_i. As the particle b is overlain on the surface, the interpolation function $\boldsymbol{N}$ of the tetrahedral el-

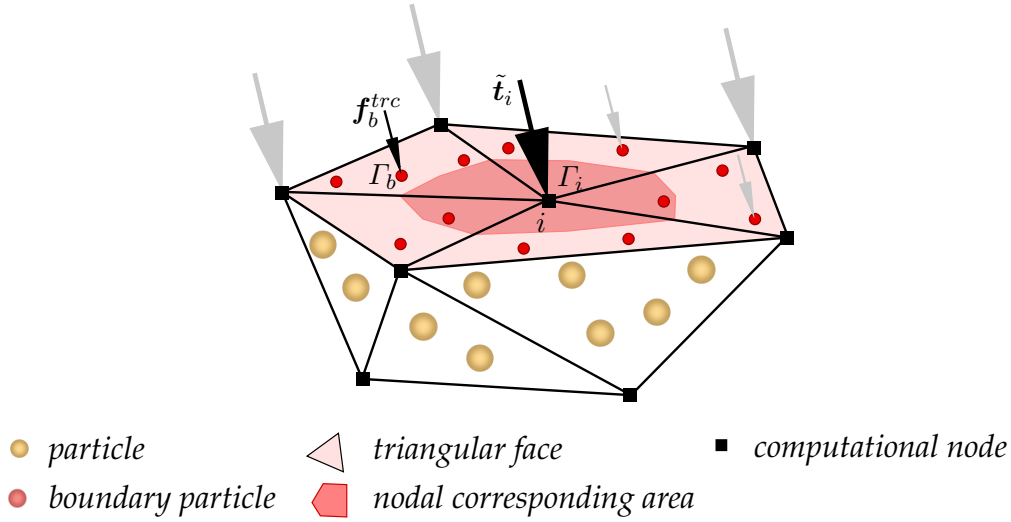

Figure 3.3: Mapping surface load from nodes to the boundary particles

ement is reduced to the surface triangular interpolation function. Taking the advantage of introducing the boundary particles to present an alternative to Equation 3.52, where the surface traction force can be obtained directly on the material points without the aid of the computational mesh as

$$\boldsymbol{f}_b^{\mathrm{trc}} = \boldsymbol{t}\left(\boldsymbol{\xi}_b, t\right)\ \Gamma_b, \tag{3.53}$$

in which, the continuous traction $\boldsymbol{t}$ is approximated in a stepwise manner over the particle domain for a fairly fine surface discretisation. Similar to Equation 3.51, the traction force can be mapped to the computational discretisation using the shape function evaluated at the boundary material point, in the form

$$\boldsymbol{F}^{\mathrm{trc}} = \sum_{b=1}^{n_b} \boldsymbol{N}^T\left(\boldsymbol{\xi}_b\right)\ \boldsymbol{f}_b^{\mathrm{trc}}, \tag{3.54}$$

where $\boldsymbol{F}^{\mathrm{trc}}$ denotes the traction nodal force vector, and n_b is the number of boundary particles where the traction is applied.

3.3.2 MPM solution process

The MPM calculation cycle goes through three phases: initialisation where information is transferred from the material points to the computational grid nodes; Lagrangian phase that parallels a finite element calculation; and a convection phase where the location of particles is updated [40, 169, 189].

3.3.2.1 Initialisation phase

In spite of defining two discretisations in the framework of MPM solution procedure, however, the solution of the momentum equation is performed in a Lagrangian manner. Therefore, Equation 3.48 is expressed in terms of the computational nodes by transforming information from the material points to the nodes. For this purpose, Equation 3.35 is recalled to get the lumped mass matrix, whereas the internal force is obtained from Equation 3.33. We keep in mind that the external force is the combination of the gravity force and the traction force formulated in Equations 3.51 and 3.54, respectively. Within the initialisation phase of the MPM solution cycle, the initial velocity of the grid nodes at the beginning of the time step is obtained by solving the following equation system

$$\boldsymbol{M}^n\,\boldsymbol{v}^n = \sum_{p=1}^{n_p} m_p\,\boldsymbol{N}^T\left(\boldsymbol{\xi}_p^n\right)\ \boldsymbol{v}_p^n, \tag{3.55}$$

where $\boldsymbol{v}$ and $\boldsymbol{v}_p$ are the velocity evaluated at the grid nodes and the material points, respectively, with n being a time step counter. Equation 3.55 follows from the least square method in which the masses of material points play a role of weights [169].

3.3.2.2 Lagrangian phase

After initialising data at nodes, the solution of the discrete momentum equation becomes

$$\boldsymbol{a}^n = (\boldsymbol{M}^n)^{-1} \left(\boldsymbol{F}^{\text{ext}} - \boldsymbol{F}^{\text{int}}\right)^n, \tag{3.56}$$

where $\boldsymbol{a}^n$ denotes the acceleration vector at the beginning of the time step, which then is exploited to update the velocity of the material points as

$$\boldsymbol{v}_p^{n+1} = \boldsymbol{v}_p^n + \Delta t \sum_{i=1}^{n_n} N_i(\boldsymbol{\xi}_p^n)\, \boldsymbol{a}_i^n, \tag{3.57}$$

where n_n is the total number of nodes. In a similar fashion to Equation 3.55, the velocity field across the mesh is obtained via mapping the particles momentum to the nodes as

$$\boldsymbol{M}^n\, \boldsymbol{v}^{n+1} = \sum_{p=1}^{n_p} m_p\, \boldsymbol{N}^T \left(\boldsymbol{\xi}_p^n\right)\, \boldsymbol{v}_p^{n+1}. \tag{3.58}$$

Giving the nodal velocity at the end of the time step in Equation 3.58, the incremental nodal displacement $\Delta \boldsymbol{u}^{n+1}$ is achieved as described in the Lagrangian FEM formulation in Section 3.2 implicitly using

$$\Delta \boldsymbol{u}^{n+1} = \Delta t\, \boldsymbol{v}^{n+1}, \tag{3.59}$$

where Δt denotes the time step size. Equation 3.59 is then employed to get the strain increment and the material evolution through the constitutive equation and finally contribute to the calculation of internal force in the next time step. Simultaneously, the material points are advanced for new positions as a last step in the Lagrangian phase,

$$\boldsymbol{x}_p^{n+1} = \boldsymbol{x}_p^n + \Delta t \sum_{i=1}^{n_n} N_i(\boldsymbol{\xi}_p^n)\, \boldsymbol{v}_i^{n+1}, \tag{3.60}$$

where $\boldsymbol{x}_p^n$ and $\boldsymbol{x}_p^{n+1}$ are the position of the material point p at the beginning and the end of the time step, respectively. It can be clearly noticed that the present MPM procedure is slightly different from the Lagrangian procedure mentioned in Section 3.2 by using the momentum instead of the velocity when information is mapped from the material points to the computational mesh [164]. The advantage of adopting the momentum formulation scheme can be recognised when a material point crosses the element boundary to an empty element. Therefore, the interpolation function to the other side of the empty element being evaluated at the material point location will have very small value, and eventually very small mass, which leads to unphysical large acceleration at the outer element edge. In the case of momentum formulation, however, the division by nodal mass is avoided and therefore the small mass problem is eliminated. In other words, the mass matrix lumping in this procedure improves the robustness of the MPM by smoothening the acceleration to update the nodal velocity [169].

3.3.2.3 Convection phase

Up to now, the position of material points is advanced in time and the internal variables are updated. Within the convective phase, the material points are kept fixed [164] and new mesh discretisation can be introduced [31, 168], or to use the same existing mesh by resetting it back to the undeformed configuration. Although using one mesh discretisation is more convenient, adaptive mesh can be introduced to solve the sharp deformation gradient in the evolving solution and the interface [40]. For example, particles can split into smaller particles when the determinant of the deformation tensor exceed certain tolerance [150]. While increasing the number of material points for the same discretisation improves the instability of the grid crossing problem, refining the grid is essential to improve the accuracy of the gradient evaluation. Therefore, Tan and Nairn [172] introduced a hierarchical elements that automatically refine into smaller elements and more material points in regions of high gradients.

3.3.3 Initial and boundary conditions in MPM

As the solution of the discretised momentum equation in MPM is performed for the computational mesh, the boundary conditions should be enforced at the mesh nodes, which might be varying during the computation. The weak formulation is built in a way that the virtual velocity is kinematically admissible. In other words, it satisfies the essential boundary condition where the velocity is prescribed. In contrast to the essential boundary conditions, the natural boundary condition should be carried by particles. Assigning surface traction to the boundary particles leads to spreading these forces across one element thickness that can be improved by refining the mesh, or moving the boundary surface where the traction is applied [21].

In the following, the treatment of the initial and boundary conditions is explained in the context of MPM. More elaboration has been given to the prescribed velocity condition, which is implemented in the problem of dropping geocontainer in Chapter 6. Furthermore, frictional contact boundary condition can be resembled by a traction boundary condition. Finally, the silent boundary boundary is reviewed in the framework of MPM when the infinite domain is truncated at the computational domain boundary, therefore, the effect of the reflected waves off the rigid boundary are eliminated or reduced.

3.3.3.1 Initial condition

For the initial boundary value problem, initial condition need to be defined for the entire domain. In Lagrangian FEM, initial kinematic and stress fields are prescribed at the grid nodes and the integration points, respectively. Moreover for constitutive equations initialisation with initial values of the internal variables in terms of which they evolve in time must be given. Similar treatment can be adopted in MPM at the beginning of the computation when the material points are initialised inside the mesh, except that the nodal velocity is obtained from Equation 3.55. In addition to initialising velocity and

stresses, external forces should be assigned at the material points as well.

For some cases where the quasi–static solution is sought using the dynamic formulation, local damping is introduced to facilitate dissipating the kinetic energy. Different damping factor can be given for different materials, or for the same material with different loading condition. In contrast to the material damping, which is initialised with the material parameters, the local damping is artificial and should be updated at the beginning of each load step.

3.3.3.2 Prescribed kinematic condition

The prescribed displacement, or *prescribed velocity* in the dynamic analysis, is to define the kinematic constraint for part of the boundary as given in Equation 3.15. Constraining the movement of the node can be alternated by applying a reaction force and momentum in the direction of the constraint with respect to a local coordinate system.

In MPM, the easier case would be if the node is constraint with zero value or free to move, which then no specific treatment for the boundary is needed comparing to FEM. In the case of non–zero prescribed value, however, the active boundary nodes should be tracked. Tracking the active boundary is not trivial especially for more than one–dimensional problems, where the concept of moving mesh has limitation [2, 21].

In this thesis, the non–zero kinematic condition is developed as shown in Figure 3.4 where additional set of particles is introduced. The task of these particle is to resemble the moving boundary by carrying the time–dependent boundary evolution. At the beginning of the time step, the velocity $\bar{v}_p\left(\boldsymbol{x}_p, t\right)$ of the *prescribed particle* p is assigned. Next, the prescribed velocity should be mapped from the prescribed particles to the computational nodes, where the discrete equations are solved. Nodes belonging to the elements where the prescribed particles are located are then tagged to be *boundary nodes*. Indeed, the thickness of the boundary now becomes of one computational element, which we will try to improve when the prescribed velocity is transferred to the boundary nodes. The prescribed values can be assigned directly at the boundary nodes. As an alternative, a weighted mapping procedure can be used, which is more consistent with the princi-

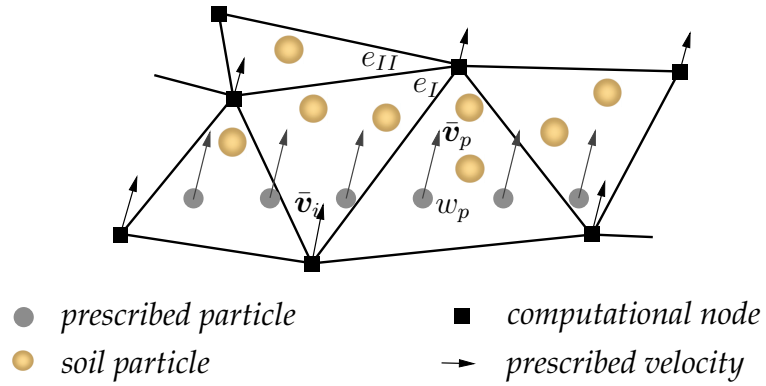

Figure 3.4: Prescribed velocity in MPM with the prescribed particles

ples of MPM. In which, the velocity of the boundary nodes is obtained from

$$\bar{\boldsymbol{v}}_i = \frac{\sum\limits_p N_i\left(\boldsymbol{\xi}_p\right)\ w_p\,\bar{\boldsymbol{v}}_p}{\sum\limits_p N_i\left(\boldsymbol{\xi}_p\right)\ w_p}, \tag{3.61}$$

where $\bar{\boldsymbol{v}}_i$ is the prescribed velocity of node i, $N_i\left(\boldsymbol{x}_p\right)$ is the shape function of node i being evaluated at the location of the material point p, w_p is a mass or volume dependent property of the prescribed particle p, whereas the summations in this equation run over the number of prescribed particles. According to the location of the boundary particles, the number of the boundary nodes is updated consequently as well as their values from Equation 3.61. Knowing these information at hand allow us to apply Equation 3.55 easily after considering the prescribed velocity condition.

Following the present formulation of defining the prescribed velocity in MPM, one should expect that the accuracy of defining the boundary is within the order of one element thickness. For example, the triangular element e_I in Figure 3.4 has all its nodes recognised as boundary nodes having different values depending on the location of the prescribed particles inside. Therefore, the deformation of this element might not be properly reproduced and consequently some stress oscillation might be detected along this layer. On the other hand, the next element e_{II} should produce more physical deformation. This fact is demonstrated better in the geocontainer releasing problem in Chapter 6 where an oscillation of stresses next to the prescribed rigid barge has been shown. Of course, refining the mesh reduces the thickness of this layer.

3.3.3.3 Traction condition

As mentioned earlier, surface discretisation is proposed in this research as boundary particles to refine the description of the solid boundary particle [2, 37]. The concept of moving the mesh for time–independent problem [21] is extended for dynamic problems [2], in which part of the computational mesh follows the velocity of the body, while the rest of the mesh either is being compressed or stretched. Therefore, a precise description for the surface traction always exists. However, aligning the discretisation of a body for certain velocity is valid for hardly deformable body only when it is moving in one–direction. Even though giving different velocities for different parts of the deformable body is plausible, whereas it is not efficient and practical for some applications.

3.3.3.4 Frictional boundary

In the kinematic constraint condition, the body is assumed to follow the boundary surface without possibility of relative tangential movement. If relative movement is allowed, frictional forces will be developed, which can be evaluated for example with Coulomb friction law as demonstrated in Figure 3.5. The interpretation of this figure that the bodies in contact are sticking to each other and the tangential forces are directly

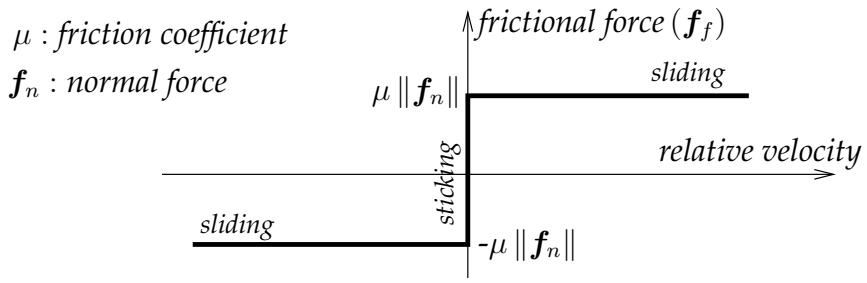

Figure 3.5: Coulomb frictional force of a dry friction

proportional to the normal force. The *friction coefficient* (μ) is the constant of proportionality, which depends on the surface type. More common is to define this coefficient in terms of the *friction angle* (ϕ) is such that $\mu = \tan\phi$. Up to a limit condition, the sticking or also called *static contact* is valid. While exceeding this condition is not allowed, sliding between the surfaces will take place. Empirically, the frictional coefficient got higher values during sticking than those in slipping, or the *dynamic contact*. Due to the relative movement of the body along boundary, part of the kinetic energy will be dissipated as thermal energy. The non–linearity of the frictional boundary condition can be linearised in a step–wise manner during the explicit numerical scheme. For this purpose, the MPM contact algorithm introduced by Bardenhagen et al. [14] is employed in this thesis and will be reviewed shortly in later section.

3.3.3.5 Silent boundary

When semi–infinite problem is modelled in finite domain analysis, the boundary conditions should be able to absorb the outgoing wave, which resembles the real case. The principle of infinite element [201] and the viscous boundary [117], which have long tradition in finite element literature can be applied. The latter introduces dashpots in the vertical and horizontal directions of the rigid boundary to reduce the effect of primary and secondary waves, respectively. This element is introduced to MPM in the case of fluid model, where the primary wave is dominant [62] or even for the solid materials where shear wave must be suppressed as well [2]. The stresses obtained using viscous boundary are treated as discrete traction applied at the boundary particles similarly to the traction condition, for example the normal component of the surface traction related to the normal dashpot is given as

$$t_p^{vb} = -f^{vb}\,\varrho\,v_p\sqrt{\frac{E\,(1-\nu)}{\varrho\,(1+\nu)\,(1-2\nu)}}, \tag{3.62}$$

where t_p^{vb} is the normal traction assigned to particle p in the normal direction to the boundary, f^{vb} is a unitless parameter, v_p is the velocity of p, with ϱ, E, and ν being the mass density, elastic modulus, and Poisson's ratio of the considered material, respectively.

3.4 Enhancement and extension of the MPM

MPM is becoming more and more attractive for different engineering applications where large deformations exist. Hence, enclosing the improvement and development of the method in one section is not practical. Thus, the objective of this section is to illustrate the mathematical background of some algorithms being adopted in this research upon the need. For instance, a dynamic relaxation procedure by adding artificial damping is essential to obtain gravity stresses. There might be more one procedure available in literature as given next or in Chapter 2 of this thesis, however, the focus here will be on using one method.

3.4.1 Mitigation of the volumetric locking

When linear shape functions are integrated in displacement finite elements formulation, a *volumetric locking* is expected to appear due to the insufficient representation of an isochoric displacement field [18]. Therefore, the material tends to show non–physical stiffness against deformation when it has high bulk modulus. Numerous methods were presented in the FE framework either based on introducing the volumetric strain as an independent field variable beside displacement [202, 203] or splitting the differential equation into deviatoric and isochoric parts and solve two equations separately [134, 205].

Due to its applicability in MPM [89, 90, 162], the *nodal mixed discretisation* (NMD) is adopted in this research. The mixed discretisation in this method between deviatoric and volumetric strain components is achieved via involving an assembly of elements to satisfy the volumetric strain constraint while keeping the deviatoric components on the element level intact. As a result, the smoothen volumetric part of the strain tensor alleviates the locking problem. To begin with the mixed formulation involving the velocity $\boldsymbol{v}$ and volumetric strain ε_v as independent field variables, the weak form in Equation 3.20 can be rewritten in the form

$$\int_{\Omega} \varrho\, \delta\boldsymbol{v} \cdot \frac{d\boldsymbol{v}}{dt}\, d\Omega = \int_{\Gamma_t} \delta\boldsymbol{v} \cdot \boldsymbol{t}\, d\Gamma + \int_{\Omega} \varrho\, \delta\boldsymbol{v} \cdot \boldsymbol{g}\, d\Omega - \int_{\Omega} \delta\dot{\boldsymbol{\varepsilon}} :\, (\boldsymbol{\tau} + \boldsymbol{\delta}\, \sigma_m)\, d\Omega, \tag{3.63}$$

where the stress tensor $\boldsymbol{\sigma}$ is decomposed into the deviatoric stress tensor $\boldsymbol{\tau}$ and mean stress σ_m with $\boldsymbol{\delta}$ being the Kronecker delta. For an elastic material, it is assumed that the mean stress rate $\dot{\sigma}_m$ can be correlated to the volumetric strain rate $\dot{\varepsilon}_v$. Then, a weak form of such a relationship reads

$$\int_{\Omega} \delta\dot{\varepsilon}_v\, (\dot{\sigma}_m - K_s\, \dot{\varepsilon}_v)\, d\Omega = 0, \tag{3.64}$$

where $\delta\dot{\varepsilon}_v$ is the virtual volumetric strain rate, and K_s the bulk modulus of solid material. However, the mean stress rate in Equation 3.64 can be obtained from the interpolation of the nodal values, such that

$$\int_{\Omega} \delta\dot{\varepsilon}_v\, (\dot{\epsilon}_v + \dot{\varepsilon}_v)\, d\Omega = 0, \tag{3.65}$$

in which $\dot{\epsilon}_v$ is interpolated using the nodal discretisation of the volumetric strain rate $\dot{\boldsymbol{\epsilon}}_v$ and the interpolation function $\boldsymbol{N}$; i.e. $\dot{\epsilon}_v \simeq \boldsymbol{N}\,\dot{\boldsymbol{\epsilon}}_v$. It is important to mention that the strain rate $\dot{\varepsilon}_v$ in Equation 3.65 is computed using nodal velocities in a traditional procedure. For an arbitrary $\delta\dot{\varepsilon}_v$, Equation 3.65 reduces to

$$\int_{\Omega} \boldsymbol{N}^T \left(\boldsymbol{N}\,\dot{\boldsymbol{\epsilon}}_v + \dot{\varepsilon}_v\right)\, d\Omega = 0. \tag{3.66}$$

Equation 3.66 provides a least squares fit for nodal volumetric strain rate. Therefore, the smoothening in this approach is considered as an explicit version of the mixed discretisation where the strains are defined as degrees of freedom beside velocities. Following up on this idea, the strain rate tensor is modified in the following form

$$\bar{\dot{\boldsymbol{\varepsilon}}} = \dot{\boldsymbol{\varepsilon}} - \frac{1}{3}\,\dot{\varepsilon}_v\boldsymbol{\delta} + \frac{1}{3}\,\bar{\dot{\varepsilon}}_v\boldsymbol{\delta}, \tag{3.67}$$

where $\bar{\dot{\varepsilon}}_v$ is obtained for an element with n_{en} nodes as

$$\bar{\dot{\varepsilon}}_v = \frac{1}{n_{en}} \sum_{i=1}^{n_{en}} \bar{\dot{\varepsilon}}_{v,i} \qquad \text{with} \qquad \bar{\dot{\varepsilon}}_{v,i} = \frac{\sum\limits_e \dot{\varepsilon}_{v,e}\,\Omega_e}{\sum\limits_e \Omega_e}, \tag{3.68}$$

where $\bar{\dot{\varepsilon}}_{v,i}$ is the volumetric strain rate evaluated at the node i with e being an element attached to this node. The NMD approach has been applied to strip footing problem using MPM where the analytical solution is available [2]. The bearing capacity of the soil showed an improvement after using the volumetric strain enhancement. Furthermore, the approach has been extended for two phase flow analysis successfully where a sea dike under wave attack was analysed [90].

3.4.2 Artificial damping for quasi–static solution

When talking about dynamic oscillation, damping can be introduced to Equation 3.48 as the force that tends to reduce the amplitude of the oscillation by acting in opposite direction to the motion; i.e.,

$$\boldsymbol{M}\,\tilde{\boldsymbol{a}} = \boldsymbol{F}^{\text{ext}} - \boldsymbol{F}^{\text{int}} + \boldsymbol{F}^{\text{dmp}}, \tag{3.69}$$

with $\boldsymbol{F}^{\text{dmp}}$ being the damping force. In order to obtain the quasi–static solution, *dynamic relaxation* process is adopted. Various types of problems in nonlinear structural analysis have been reviewed by Underwood [176]. As one option, introducing viscous damping based on the mass would be the best. However, solving the eigenvalue problem using modal analysis non–linear problems to find the natural frequencies is demanding task makes this option not practical. In the dynamic relaxation, an artificial damping is introduced to converge the solution to the equilibrium state where the objective is to dissipate energy without focusing on the dynamic response.

Using distinct element codes for geomechanical applications, two approaches are applied to get the static analyses [51]. The *adaptive global damping* is the first, in which the

viscous damping forces are adjusted in such a way that the absorbed power is a constant proportion of the rate of change of kinetic energy [43]. On the contrary, the *local non–viscous* method [44], assumes that the damping force magnitude is not proportional to the velocity but to the unbalanced force, while its direction is still taken contrary to the velocity vector. Although both methods have shown the convergence to the same quasi–static solution [44], experience has shown that the last damping scheme performs very well in non–linear continuum and discrete softwares [51].

In the following MPM implementation, the local non–viscous damping has been applied such that the damping force in Equation 3.70 reads [88]

$$F_i^{\mathrm{dmp}} = -\alpha \left| F_i^{\mathrm{ext}} - F_i^{\mathrm{int}} \right| \mathrm{sign}\left(\mathrm{v_i}\right), \tag{3.70}$$

where α is the damping coefficient and $\mathrm{sign}\left(\mathrm{v_i}\right)$ is the sign of the velocity at node i defined as $v_i/|v_i|$.

By setting up an artificial damping scheme, the solution eventually approach static equilibrium state. The static equilibrium state might be a quasi–static case in the solid problems or steady–state flow in the fluid dynamic. In both cases, a stopping criterion is required to avoid the unnecessary computation. For this purpose, two criteria has been considered in which the first is based on the velocity and the second on the unbalance force; see for example [202]. Therefore, the velocity criterion checks that the velocity field approaches zero in global sense, whereas the force criterion estimates how close the solution is to the quasi–static one. To normalise both criteria, the velocity is replaced with the kinetic energy, which is normalised with respect to the external work as [2]

$$\mathcal{E}_v \geq \frac{KE}{W^{\mathrm{ext}}}, \tag{3.71}$$

with

$$KE = \frac{1}{2} \sum_{i=1}^{n_n} m_i \, \boldsymbol{v}_i^T \boldsymbol{v}_i$$
$$W^{\mathrm{ext}} = W_0^{\mathrm{ext}} + \Delta \boldsymbol{u}^T \boldsymbol{F}^{\mathrm{ext}},$$

where $\mathcal{E}_v$ is the tolerance based on kinetic energy. On the other hand, the force criterion is built such that [33]

$$\mathcal{E}_f \geq \frac{\left\| \boldsymbol{F}^{\mathrm{ext}} - \boldsymbol{F}^{\mathrm{int}} \right\|}{\left\| \boldsymbol{F}^{\mathrm{ext}} \right\|}, \tag{3.72}$$

in which, $\mathcal{E}_f$ is the tolerance based on forces. Although it has be experienced that the kinetic energy criterion is satisfied faster than the force one, a value of 0.01 for both criteria is assumed for all cases along this thesis where the quasi–static solution is obtained.

3.4.3 Frictional contact algorithm

In MPM formulation, the material points are relocated using the nodal information and the interpolation functions for the computational domain, which are continuous be-

tween elements. Therefore, a non–slip condition between particles/objects is enforced with prevention of interpenetration. The existence of such a condition adds extra resistance when a body is penetrating an object, for example. Furthermore, the no–slip condition in MPM glues bodies in contact even though the are moving away from one another. This fact is experienced in the early version of MPM with the underestimation of the penetration depth of an elastic steel ball being thrown into aluminium target [169]. Although the non–physical glue between the two objects exists when they share one computational node, however, no evidence that refining the mesh will solve the problem or at least smoothen it. Thus, developing a contact algorithm consistent with the MPM theory is essential.

As a first improvement in the basic MPM algorithm in modelling two colliding bodies, York et al. [192] introduced a criterion to check whether the bodies are approaching or moving apart. Accordingly, the MPM algorithm applied only when they approach one another, otherwise, separation is taking place and each one should consider its own velocity field without sharing at the common nodes. In other words, the MPM procedure is applied only when the following inequality is satisfied for both bodies, I and II, in contact

$$\left(\tilde{\boldsymbol{v}}_i^{n+1,(I)} - \tilde{\boldsymbol{v}}_i^{n+1,(I+II)}\right) \cdot \boldsymbol{n}_i^{n,(I)} > 0, \tag{3.73}$$

where $\boldsymbol{n}_i^{n,(I)}$ is the outward unit normal of body I at node i at the beginning of the time step, with $\tilde{\boldsymbol{v}}_i^{(I)}$ and $\tilde{\boldsymbol{v}}_i^{(I+II)}$ being the velocity vector of body I alone and the combination of both, respectively. The visual illustration of this formula is shown in Figure 3.6.

As an advancement of the simple approaching/separation algorithm, Bardenhagen et al. [14] proposed an MPM algorithm, which allows sliding and rolling with friction. The traction due to contact is incorporated into the discretised momentum equation as

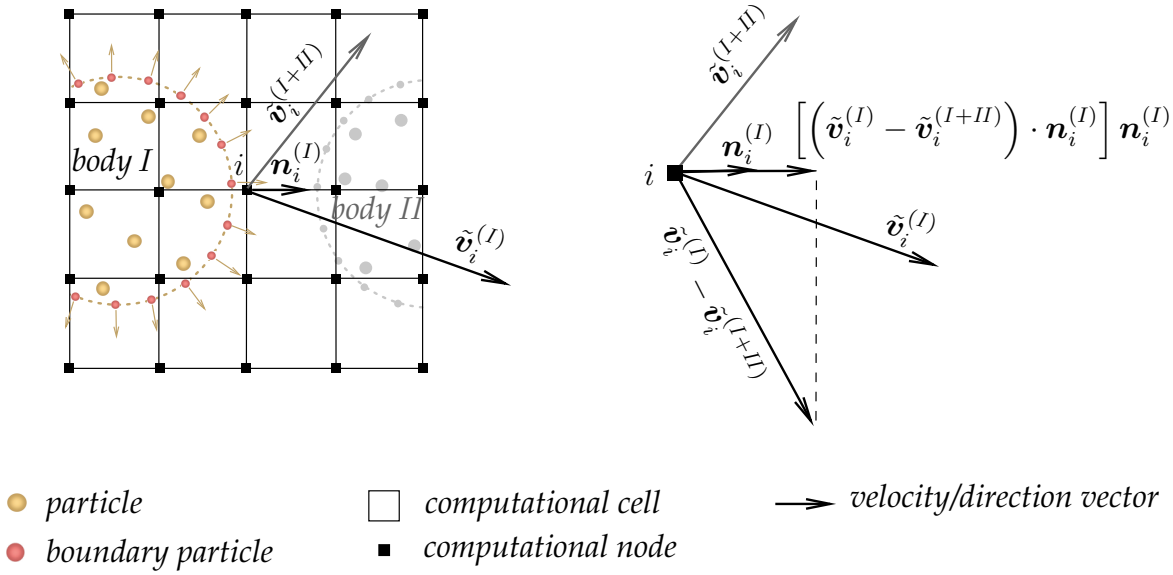

Figure 3.6: Correction procedure in the MPM contact algorithm [14]

an external force, Equation 3.48, where the solution of this equation is performed separately for each body in contact. An extra solution for the combination of all bodies, referred here as the *system*, is needed. Thus, one should expect to solve the equation of motion as many times as the number of bodies in contact plus one. Solving this number of equation actually does not add a cumbersome computation as the solutions of these equations are trivial. Getting the acceleration of the individual solution and consequently the corresponding velocity fields at hand, the non–iterative algorithm detects the contact points by comparing the nodal velocity of each body with the one of the entire system. If a difference is detected, Equation 3.73 is applied to check whether the bodies are approaching or separating from each other. Individual velocity fields are used if separation is taking place with no change, otherwise, the interpenetration of objects is precluded using the following correction

$$\tilde{\tilde{\boldsymbol{v}}}_i^{n+1,(I)} \cdot \boldsymbol{n}_i^{n,(I)} = \tilde{\boldsymbol{v}}_i^{n+1,(I+II)} \cdot \boldsymbol{n}_i^{n,(I)}, \tag{3.74}$$

with $\tilde{\tilde{\boldsymbol{v}}}_i^{n+1,(I)}$ being the modified velocity of body I that is adjusted according to the normal component of the system solution. Equation 3.74 can be rewritten, involving Equation 3.73, in the form

$$\tilde{\tilde{\boldsymbol{v}}}_i^{n+1,(I)} = \tilde{\boldsymbol{v}}_i^{n+1,(I)} - \left[\left(\tilde{\boldsymbol{v}}_i^{n+1,(I)} - \tilde{\boldsymbol{v}}_i^{n+1,(I+II)}\right) \cdot \boldsymbol{n}_i^{n,(I)}\right] \boldsymbol{n}_i^{n,(I)}, \tag{3.75}$$

where the correction term can be interpreted as an external force applied at the interface node such that

$$\boldsymbol{f}_{i,norm}^{n+1,(I)} = -\frac{m_i^{n,(I)}}{\Delta t}\left[\left(\tilde{\boldsymbol{v}}_i^{n+1,(I)} - \tilde{\boldsymbol{v}}_i^{n+1,(I+II)}\right) \cdot \boldsymbol{n}_i^{n,(I)}\right] \boldsymbol{n}_i^{n,(I)}, \tag{3.76}$$

in which $\boldsymbol{f}_{i,norm}^{(I)}$ is the force applied at body I in the normal direction to node i, and $m_i^{(I)}$ is the corresponding mass of node i obtained for body I. While the interpenetration of objects is prevented at this stage, the frictional traction needs to be applied next. Assuming that the two bodies are sticking to each other, the required force keeping them together is obtained from the tangential component of the relative velocity that is illustrated as dashed line in Figure 3.6, which reads

$$\boldsymbol{f}_{i,stick}^{n+1,(I)} = -\frac{m_i^{n,(I)}}{\Delta t}\, \boldsymbol{n}_i^{n,(I)} \times \left[\left(\tilde{\boldsymbol{v}}_i^{n+1,(I)} - \tilde{\boldsymbol{v}}_i^{n+1,(I+II)}\right) \times \boldsymbol{n}_i^{n,(I)}\right], \tag{3.77}$$

with $\boldsymbol{f}_{i,stick}^{(I)}$ is the tangential force required to hold the two bodies glued together. In order to model frictional sliding properly, there should be a limit for the tangential forces; e.g., by the Coulomb friction law as shown in Figure 3.5. Hence, the tangential forces is bounded with Coulomb criterion as

$$\boldsymbol{f}_{i,tang}^{(I)} = \frac{\boldsymbol{f}_{i,stick}^{(I)}}{\|\boldsymbol{f}_{i,stick}^{(I)}\|} \min\left(\mu \|\boldsymbol{f}_{i,norm}^{(I)}\|, \|\boldsymbol{f}_{i,stick}^{(I)}\|\right), \tag{3.78}$$

where $\boldsymbol{f}_{i,tang}^{(I)}$ is the tangential component of the frictional contact force, and μ is the friction coefficient. It is considered that all the forces in Equation 3.78 are obtained at the

end of the time step.

The separation criterion formulated in Equation 3.73 assumes free separation of the two bodies with no influence on each other, whereas it is more logic to have a gradual separation. Therefore, Bardenhagen et al. [15] improved this algorithm by replacing the velocity criterion with the normal traction criterion, which says that separation should take place only if the normal traction is becoming tension. The modified algorithm is found to be dissipating slightly more energy than the original one [13].

Another attempt to model the contact problem in the MPM framework was suggested by Hu and Chen [81]. In their approach, the concept of velocity field is replaced with the momentum by introducing multi–mesh environment, which is more harmonised with the MPM basics and supposed to avoid the unphysical phenomena with Bardenhagen's algorithm. The method was able to simulate contact, sliding and separation of the gear contact process where the normal component is computed in the common background mesh while the tangentials are obtained on the corresponding individual mesh. Because the tangential velocities of different bodies are assumed independent, the method was unable to simulate friction. An improved multi–mesh contact algorithm for three–dimensional problem is proposed by employing the Bardenhagen's velocity criteria to detect the contacting nodes of different bodies whereas the normal and tangential velocities are obtained from the multi–mesh algorithm [190]. Considering this technique of combing the two contact approaches, the collision of plastic spheres and the impact of a Taylor bar are modelled [121, 190]. Similar concepts is also applied to model the drag interaction between multi–phases material [122, 195].

In order to ensure the impenetrability condition between bodies, Huang et al. [83] implemented the Lagrange multiplier form. Furthermore, they compared the impact and penetration simulation with the velocity based algorithm, which shows more stable solution than the first. It is clear from what aforementioned that the velocity contact algorithm [14, 15] is robust and widely used in MPM community. One of the big shortcoming of this algorithm that the bodies in contact feel each other when they share one computational node, or about two elements thickness. In the context of defining particle domain [12, 151] instead of collocated mass at one point in which the contact is detected when the this spatial domain intersect another element [198].

In the present work, as we have followed the original MPM implementation where the density is represented via Equation 3.46, the improvement proposed by Zheng et al. [198] is not applicable. However, the original contact algorithm [14] has shown its efficiency in many geomechanical applications [40, 72, 89]. The improvement we introduced here is about obtaining the normal vector at the material points using the connectivity approach, instead of using other approaches [102, 191] which are not yet appropriate in the case of irregular mesh the discretisation being adopted in this research. In the connectivity approach [62, 191], the normal vector along the boundary particles, Figure 3.6, is tracked during the computation. So that the deformed surface is followed and then mapped to the computational grid node through the following procedure

$$\boldsymbol{n}_i = \frac{\sum \boldsymbol{n}_p}{\| \sum \boldsymbol{n}_p \|}, \tag{3.79}$$

where $\boldsymbol{n}_i$ is the outward unit vector for node i, and the summations runs over the number of boundary particles located inside elements attached to node i.

In the case of prescribing boundary velocity with frictional contact, prescribed particles introduced in Section 3.3 of the present chapter is adopted. For this purpose, the nodal velocity solution should satisfy the prescribed boundary condition. In other words, the nodal prescribed velocity obtained by Equation 3.61 should replace the system velocity $\tilde{\boldsymbol{v}}_i^{n+1,(I+II)}$ at the places where boundary nodes are detected. The rest of the contact algorithm, from Equation 3.74 to Equation 3.78 stays the same with no changes. In order to validate this approach, a square of $1\,\mathrm{m}$ side and unit weight of $10\,\mathrm{kN/m^3}$ supported by prescribed particles with zero velocity being discretised irregularly as depicted in Figure 3.7 is considered. After calculating of the initial stress field caused by the gravity, the layer of prescribed particles underneath is moved suddenly with a horizontal velocity of $2\,\mathrm{m/s}$. As shown in Figure 3.7, the body is travelling together with the bottom if standard MPM is applied. In the other case, where rough contact is introduced, the glue condition is broken if the bottom is fast enough. Finally, the absence of the frictional resistance in the smooth contact case leads to the early separation of the two bodies.

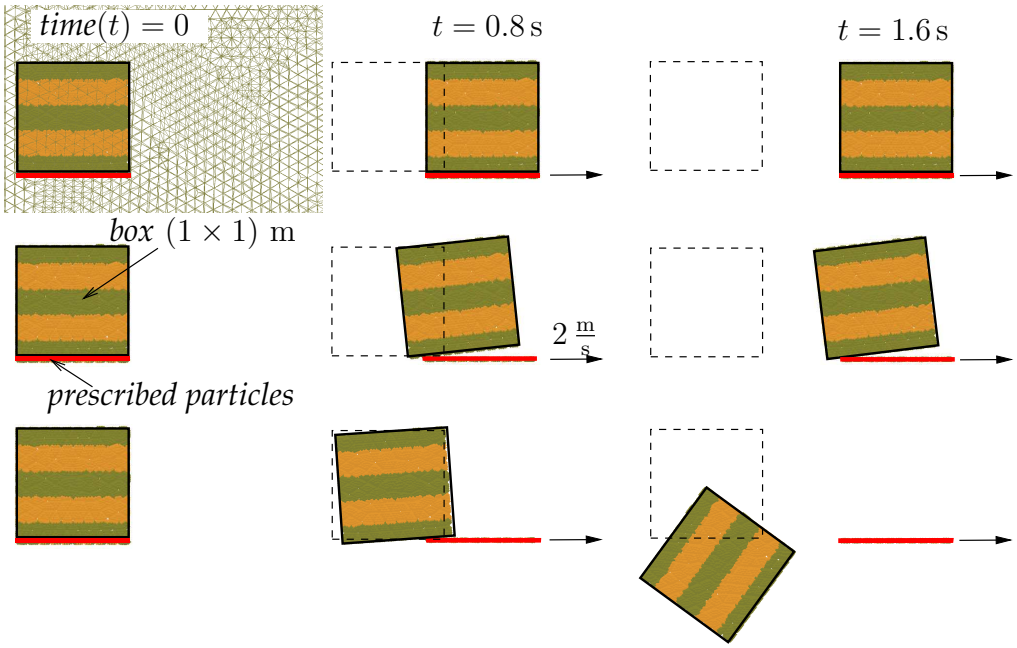

Figure 3.7: Prescribed velocity boundary with contact: (top) standard MPM, (middle) rough contact, and (bottom) smooth contact

3.5 Numerical algorithm

In this section, the initialisation of the MPM model with the solution procedure is presented in steps. The preprocessor being adopted in this thesis is based on irregular tetrahedral mesh discretisation. Initially, the MPM model is created in a similar way to the Lagrangian FE model. As described in Appendix B, particles are initialised in local coordinates. Empty elements are provided in the potential zone of the particles movement. Within the preprocessor phase, surface traction is applied and represented on the computational mesh. Direct constraints are applied at nodes for zero kinematic boundary condition, whereas prescribed boundary particles should be created for the prescribed velocity boundary. After initialising the MPM model, initial conditions and state variables are applied at the material points. As next, the computation MPM cycle is repeated till the end of the calculation. The cycle can be summarised with the following steps:

Step one Update the number of active nodes that belong to elements where particles are located. Excluding empty elements improves the computational efficiency of the computation cycle where loops are taking place only over active nodes. Next, calculate the minimum time step throughout the entire mesh. As irregular mesh is adopted, update the time step according to Equation 3.44 only for active elements is more efficient.

Step two Establish the lumped mass matrices of each body in contact as well as the system matrix using Equation 3.35. Furthermore, internal, gravitational and traction forces are obtained via Equations 3.33, 3.51 and 3.54, respectively. Local damping is constructed if it is applicable. Important to emphasise here that the traction load is transferred from the nodes to the boundary particles at preprocessing stage and stays there during the computation.

Step three Map the particle momentum to the active nodes using Equation 3.55 to obtain the nodal velocity field at the beginning of the current time step.

Step four Considering contact algorithm, the discretised momentum equations are solved for each individual object and one more solution for the entire system.

Step five Update the velocity of all material points by integrating explicitly the discrete nodal values of the acceleration field using values of shape functions at the material points as in Equation 3.57. Consequently, the corresponding nodal velocity distributions, from Equation 3.58, are obtained.

Step six Compare the velocity fields of the corresponding objects with the system velocity and update the individual object velocity accordingly using Equation 3.75. Moreover, the tangential component of the contact force should be bounded by Coulomb friction in Equation 3.78.

Step seven Evaluate the velocity field at the computational grid by evaluating the mo-

mentum at the material points. In other words, repeat *step three* above.

Step eight Obtain the incremental displacement at the computational grid nodes using Equation 3.59 and then evaluate the deformation rate tensor $\dot{\varepsilon}_{ij}$ followed by the constitutive equation 3.10. The particle volume is updated here using Equation 3.41.

Step nine Update the locations of the particles via Equation 3.60. During this stage, the book–keeping that describes the connectivity of particles–mesh and vice versa should be updated as well. The searching algorithm for relocating particles in element for the non–structured mesh is given in Appendix C.

Step ten Track the boundary particles for updating normals. For quasi–static case, the kinetic energy and external forces criteria are obtained through Equations 3.71 and 3.72 to check whether they satisfied the tolerance criteria.

3.6 Experimental validation: collapse of granular column

As the aim of this chapter is to introduce a numerical method able to handle large deformations of granular materials, a validation for the numerical implementation of the method becomes essential. For this purpose, the collapse of granular column is selected. The problem of granular column collapse plays important role in many engineering applications dealing with granular or powder materials. Beside industry, collapse of granular material has numerous applications in geophysics; e.g., landslides, avalanches, debris flows, etc. Due to the limitation of the large–scaled models, experiments consist of sudden releasing an initially confined granular column in response to gravity have been performed. Swinging gate or lifting up container quickly are commonly used [8, 115] to release cylindrical [98, 113] or two–dimensional [8, 55, 114] column. Furthermore, related theoretical studies of the problem are offered by other references [159, 160].

The main outcome of the experimental studies is to correlate the run–out distance to the initial geometry of the column. A power–law relationship between the run–out distance and the normalised initial height, which varies for the axisymmetric and two–dimensional columns [98, 115]. In these laboratory investigations, an initial acceleration stage is detected followed by constant velocity for the high *aspect ratio* column. Aspect ratio is defined as the ratio between the height of the column to its width. Friction becomes important factor only at the last stage of deceleration and final stopping [114].

Numerical simulations of the granular flow have been performed with discrete elements [97, 159] and continuum models [3, 126]. Mangeney et al. [124] have proven that the continuum model overestimates the driving forces involved during the collapse as compared with granular based models and therefore expects higher run–out for aspect ratio greater than 0.7. Similar conclusion has been obtained with an MPM model by Kumar et al. [95], who expected higher run–out distance as compared with the discrete element method (DEM) for aspect ratio greater than 2. The energy evolution for continuum based models is well predicted when the frictional behaviour is predomi-

nant, whereas the lack of collisional energy dissipation mechanism is overpredicting the run–out distance [95]. Therefore, an artificial damping should be added for the granular columns with higher aspect ratio [158]. However, it is not so clear how much damping is required as compared to the physical damping. More details about the mechanism controlling the spreading of the column and the sideways ejection of the mass is examined by Staron and Hinch [159], who propose a proportional approximation for the spreading energy to the initial potential energy [160].

3.6.1 Problem description and reference solutions

The objective of the current MPM analysis is not to reproduce experiments with high accuracy rather than validating our MPM version. For this purpose, the experiment conducted by Lube et al. [115] is selected as a reference in this research. The experiment is performed inside a rectangular channel and initiated by uplifting the supporting wall where the flow remains fairly two–dimensional. Different dimensions for the granular column are tested whereas the one selected has a height of $63.35\,\mathrm{cm}$ and $9.05\,\mathrm{cm}$ width constructed on a $20\,\mathrm{cm}$ deep channel. Rough ground is provided by placing a layer of sandpaper that has a similar roughness order as the internal friction angle of the flowing material. Large range of granular materials has been tested; e.g., sand, rice, and sugar. In all materials, the cohesion effects is negligible. For the quartz sand, the following properties are recorded [114]: solid density $2.6\,\mathrm{g/cm^3}$, and angle of repose 31°. The frontal gate is removed quickly in the upward direction. During collapse, the free surface is captured through a transparent side wall.

The sand column collapse is modelled numerically using the generalised interpolation material point method (GIMP) [158]. Brief description about GIMP is provided in Chapter 2. Two–dimensional bilinear regular elements with the dimension $5\,\mathrm{mm}$ are adopted in that model. Nine particles initially are placed inside each element. The sand is modelled with Mohr–Coulomb failure criteria and given a modulus of elasticity $840\,\mathrm{kPa}$ with Poisson's ratio equals to 0.3. While the angle of repose is used as the friction angle, very small dilatancy angle of 1° is assumed. Following the suggestion in Lube et al. [114], non–slip contact is considered between the sand material and the ground. Using the GIMP analysis, the numerical model expects higher run–out as compared with the experiment, which matches other continuum models conclusion [95, 124]. Therefore, Sołowski and Sloan [158] suggest adding some artificial damping to replace the energy dissipation due to particles rotation. Since this procedure is not fully described, it will be excluded from the current MPM analysis.

3.6.2 MPM modelling

As stated earlier, the aim of this analysis is to validate the current MPM implementation and to prove that the method is able to capture dynamics associated with granular material flow. Therefore, the numerical values suggested by Sołowski and Sloan [158]

will be used in the current MPM model without spending more effort to improve it. The sand column in modelled using 4–noded tetrahedral elements with ten particles initially placed inside each element. Regular mesh discretisation is adopted with $5\,\mathrm{mm}$ grid apart. Strain smoothening technique introduced in Section 3.4 is considered, whereas the Mohr–Coulomb failure criteria is employed. Owing to symmetry, only one half of the domain is modelled and a frictionless side wall is imposed as depicted in Figure 3.8.

Initially, roller support is assumed on both sides of the column to get gravitational initial stresses. The process of removing the side boundary is omitted from the MPM analysis, therefore, the roller boundary to the right are removed instantaneously. The corresponding time for removing the supporting gate is estimated by $0.0417\,\mathrm{s}$, which is subtracted from the experiment time [158]. Gravitational acceleration is assumed in the vertical direction taking the value $10\,\mathrm{m/s^2}$.

The experimental and GIMP results are traced and plotted in combination with MPM in Figure 3.9. As shown in this figure, due to the high aspect ratio about 3.5, bulk mass of the collapsed column is moving downward with little lateral displacement at time $0.17\,\mathrm{s}$. During this time, the MPM results is very close to experiment. As the sand particles start flowing laterally, the difference increases due to the lack of the dissipating energy corresponding to the grains rolling at time $0.33\,\mathrm{s}$. The two flow regimes explained in [114] can be distinguished when looking at the upper right part moving, whereas the no–flow triangular area in the lower left corner almost does not move. Soon after this stage, the column decelerates and comes into rest.

The flowing material passes through two characteristic phases [115]: the *spreading phase*, in which the flowing layer moves as a largely deforming and deep bulk flow. The particles at the free surface layer stay there or are incorporated into a thin layer when the flow overrun the flow front. During this phase, the interface between moving and static particles is continuously propagating upward reducing the volume of the flowing layer. Next flowing phase is the *final avalanching phase*, which consists of the particles flowing

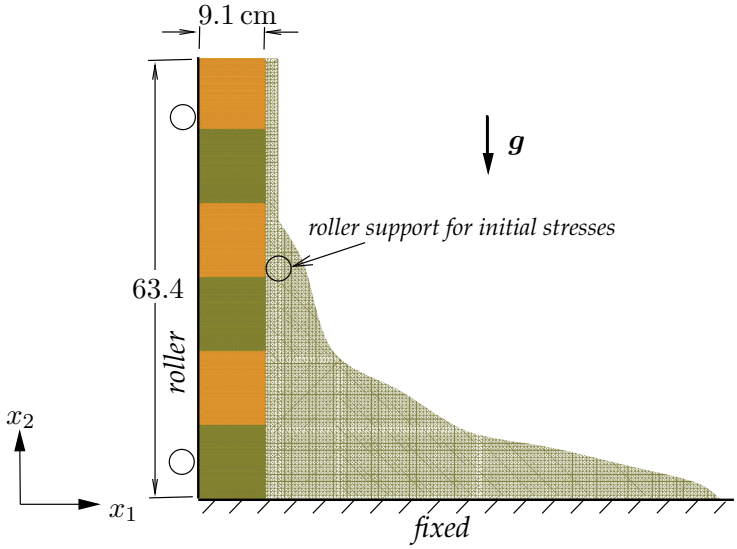

Figure 3.8: MPM model for the granular column described in [115]

along the free surface thin moving layer and the deposit central part. The slow particles take the form of thin avalanches and modify the free surface further till it stopped.

In this analysis, it has been proven that the simple constitutive model is able to reproduce quite complicated dynamic process of granular material. No doubt, more complex constitutive model can improve the quality of the results. For example, considering the pressure dependency in the Drucker–Prager or Matsuoka–Nakai yield criteria does not make a change for the residual height or the run–out only, but rather changes the final shape of the collapsed column [126]. Furthermore in this analysis, it has been shown that the standard MPM is able to reproduce comparative results to GIMP. Although the last introduces spatial domain for the particles, which means that two material points interact with each other even though the gap between them is greater than one computational node, it has been found that some particles at the tip of the collapsing column has lost connection with the neighbours. Similar separation of particles is also detected with MPM, however, it is rather small and limited.

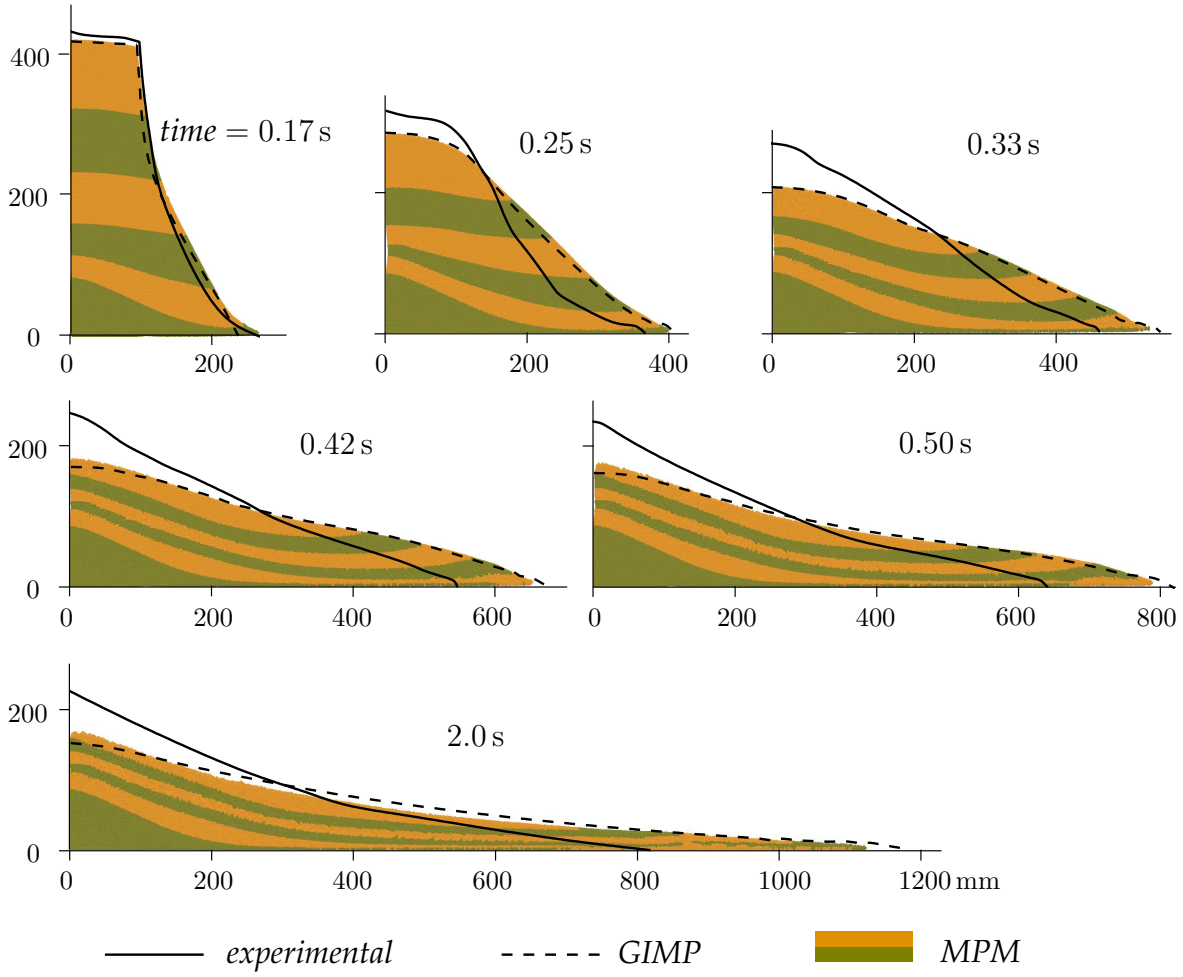

Figure 3.9: Evolution of the granular column collapse obtained by MPM compared with GIMP [158] and experimental results [115]

Chapter 4

Modelling of membranes in MPM

Considering MPM advantages mentioned in Chapter 3, the method can be applied to model structural elements in combination with solid elements. Of course, the theory of these elements should be considered in the basic MPM algorithm. One of the most important structural elements in engineering applications is the *thin–walled structure*. An introduction to the thin–walled structures followed by the mathematical formulation is presented in Section 4.1 with more attention attributed to the membrane element.

Two membrane formulations are presented, the first follows the membrane procedure of York [191]. This MPM formulation is described in Section 4.2, supported by a simple one–dimensional spring–mass system example. A proposed MPM representation for the membrane, called *coupled FEM–MPM membrane* is detailed in Section 4.3, along with the single degree of freedom spring–mass system example.

Both numerical approaches are tested for two other problems with available analytical solutions in Section 4.4. Mesh sensitivity, stress prediction, and minimum required mass to get each of the two approaches working have been tested for uniaxial mass oscillating. Moreover, the transverse motion of laterally oscillated mass is compared with the closed–form solution. Up to this point, these examples are restricted for small deformation theory and tension–compression membrane. Section 4.5 introduces the required modifications to account for large deformations with an example, in which a prestressed membrane is stretched laterally with $80\,\%$ extension relative to its original length. As with other textile materials, the geosynthetic has the property of tensile stiffness only. Therefore, part of Section 4.5 is dedicated to discus what is so–called the *compression cut–off* criterion. Definition of this criterion is accompanied by a validation example of a hemispherical dome subjected to self weight. Section 4.6 presents an application in which the failure of an embankment is studied with and without a reinforcement by geotextile. The analyses of failure mechanism and the embankment stability using undrained conditions were investigated to determine the embankment height and the corresponding geotextile strain.

4.1 Thin–walled structures

This section gives an introduction to the numerical modelling and kinematic descriptions of the thin–walled structures. Furthermore, it shows the required changes in the constitutive equation to accommodate for the structural behaviour of these elements.

4.1.1 Introduction

In modern technology, thin membranes are often used as a structural element. Membrane elements are the structural elements that are capable of transmitting forces tangential to the surface only. Paying special attention to geomechanical applications, this structural element is very useful for the analysis of soil–structure interaction where the membrane has stiffness in tension but not in compression.

The finite element method (FEM) has been widely used to model membranes; see, e.g., [93, 157]. This can be accomplished with plate or shell elements by neglecting the flexural components. In case of large deformations, however, traditional FEM membrane modelling often encounters mesh distortion and element entanglement, which causes numerical difficulties unless continuous remeshing is adopted. As an alternative, the Lagrangian particle method has the potential to model extreme large deformation without the difficulties just mentioned. The material point method (MPM) is a method in which the material is represented by set of particles that are free to move through a computational mesh in the background. York [191] developed MPM for the modelling of thin membranes, in which a two–dimensional membrane is discretised by a collection of material points to define a surface. Similar to other membrane algorithms, the MPM requires an accurate procedure to update the local orientation relative to the global frame of reference. Different algorithms have been investigated to conclude that the most accurate one is accomplished by keep tracking of the membrane particles connectivity [192]. This approach is extended later for three–dimensional membrane by tracing the normal on triangles used to connect the particles. The three–dimensional membrane is combined with a liquid to model sperm injection [62].

In spite of the fact that MPM can handle large deformation successfully, but for small deformation it gives lower accuracy than FEM. Hence, a coupling procedure between FEM and MPM for problems with different deformations scheme produces better results than pure MPM. Zhang et al. [196] developed an *explicit material point finite element* method to study hyper velocity impact. In this method the material domain is discretised by a mesh of finite element, and a regular background grid is defined in the potential large deformation zone. Once moving into the predefined computational grid, nodes are converted into particles whose momentum equations are solved on the predefined grid. The FEM–MPM coupling in this procedure is carried out by adopting one method through the predefined regions. For this reason the coupling procedure might be good for small deformation but not when a membrane experiences relatively large deformation combined with displacement; e.g., the problem of dropping geocontainers.

Lian et al. [108] proposed a *hybrid finite element–material point* (FEMP) method for modelling reinforced concrete subjected to impact loading. The essence of this method is to introduce a hybrid bar element into MPM, where the nodal variables are updated from background grid and the stresses are updated on the element. By this hybrid bar element, the reinforced bar in concrete can be easily discretised.

The hybrid FE–MP approach is extended in this thesis to include membrane elements. Within the context of the analysis, the membrane element has three degrees of freedom per node, although the element is two–dimensional plane element. A membrane material point is placed at each vertex node and the connectivity is preserved throughout the

computations. The integration of membrane stresses is done using the two–dimensional triangular mesh. The computed internal membrane forces are then mapped to the tetrahedral grid, where the momentum equation is solved for the whole system. In the present research, the proposed approach does not only has better stress prediction, but it is also less sensitive to the membrane discretisation than York's membrane approach.

4.1.2 Kinematics of thin–walled structures

The mathematical theory of the thin–walled structures can be established by defining a set of points $\mathfrak{S}$ in the three–dimensional space $\mathbb{R}^3$ as part of a body. The boundary of the body is denoted as Γ. The placement of the surface $\mathfrak{S}$ in $\mathbb{R}^3$ is called *configuration*. Each point $\mathfrak{M}_\mathfrak{i} \in \mathfrak{S}$ has a unique position vector $\boldsymbol{X} \subset \mathbb{R}^3$ defining its location at time $t \in [t_0, \infty]$. The configuration at $t = t_0$ is called *reference configuration*, and it is usually understood to correspond the undeformed state of the structure.

Following the convention of continuum mechanics [18], we mark quantities referring to the reference configuration with uppercase letter, such that, for instance $\boldsymbol{X}$ denotes the position vector of a point at time $t = t_0$. As this coordinate refers to the points of the body, it is called *material coordinates* and its base vectors $\boldsymbol{e}$ are given as [18]

$$\boldsymbol{e}\left(\boldsymbol{X}, t\right) = \begin{bmatrix} e_1 & e_2 & e_3 \end{bmatrix}^T, \tag{4.1}$$

with the superscript T implying transportation. The current or *deformed configuration* of the body at a given time $t > t_0$ can be formulated as a map from the reference configuration to the deformed configuration in $\mathbb{R}^3$. Quantities referring to the deformed configuration are written as lowercase letters. For a material point $\mathfrak{M}_\mathfrak{i}$ identified by its position vector $\boldsymbol{x}$ we therefore write

$$\boldsymbol{x} = \boldsymbol{x}\left(\boldsymbol{X}, t\right). \tag{4.2}$$

The position vector of a given point with respect to the local coordinates on the mid-surface in three–dimensional space $\mathbb{R}^3$ is denoted by $\boldsymbol{X}_c(\hat{X}_1, \hat{X}_2)$ [28], where the coordinates $(\hat{X}_1, \hat{X}_2, \hat{X}_3)$ ought to identify a specific location on the surface as shown in Figure 4.1. Here the thickness coordinate $(\hat{X}_3)$ lies along the unit normal $\boldsymbol{N}$ at an arbitrary point. At this point, the position vector in the undeformed domain is defined such that

$$\boldsymbol{X} = \boldsymbol{X}_c + \boldsymbol{N}\hat{X}_3, \tag{4.3}$$

in which, $\hat{X}_3$ varies in the limits

$$\hat{X}_3 \in \left[-\frac{h\left(\hat{X}_1, \hat{X}_2\right)}{2}, \frac{h\left(\hat{X}_1, \hat{X}_2\right)}{2} \right],$$

where h is the wall thickness and the subscript c indicates quantities defined at the mid-surface as illustrated in Figure 4.1. The displacements $\boldsymbol{u}$ are defined as the difference

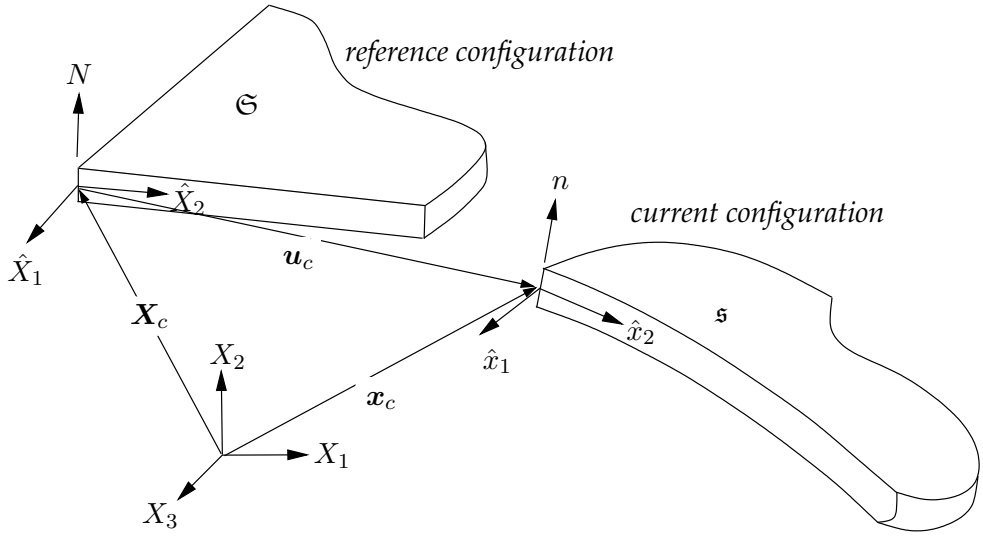

Figure 4.1: Kinematic scheme of thin–walled structure for large deformation

between position vectors in the current and the reference configuration

$$\boldsymbol{u}\left(\boldsymbol{X},t\right)=\boldsymbol{x}\left(\boldsymbol{X},t\right)-\boldsymbol{X}. \tag{4.4}$$

Deformation uniquely maps surface $\mathfrak{S}$ to deformed surface $\mathfrak{s}$, which owing to the convenience of local coordinates are still defined by $\hat{\boldsymbol{X}}$. Originally, the material fibers are straight and normal to $\mathfrak{S}$ and assumed to be kept straight and normal to $\mathfrak{s}$ after stretching. Hence, the position vector is written as

$$\boldsymbol{x}=\boldsymbol{x}_c+\boldsymbol{n}\,\hat{x}_3, \tag{4.5}$$

where $\boldsymbol{n}$ is the outward unit normal to $\mathfrak{s}$. The velocity $\boldsymbol{v}$ and the acceleration $\boldsymbol{a}$ are the first and the second time derivative of displacement respectively, which yields

$$\boldsymbol{v}\left(\boldsymbol{X},t\right)=\frac{d}{dt}\boldsymbol{u}\left(\boldsymbol{X},t\right);\quad \boldsymbol{a}\left(\boldsymbol{X},t\right)=\frac{d}{dt}\boldsymbol{v}\left(\boldsymbol{X},t\right) \tag{4.6}$$

and the strain rate tensor is given by

$$\dot{\varepsilon}_{ij}=\frac{1}{2}\left(\frac{\partial v_i}{\partial x_j}+\frac{\partial v_j}{\partial x_i}\right). \tag{4.7}$$

At this stage, it is important to define a natural approach to allow material rotation with the coordinate system. Defining the *corotational coordinate* makes it easier to deal with structural elements. In the corotational approach, a coordinate system is constructed for each point in the body with base vectors $\hat{\boldsymbol{e}}$, which are defined in a way similar to Equation 4.1 such that

$$T_{ij}=\hat{e}_i\cdot e_j, \tag{4.8}$$

where T_{ij} is the rotation tensor defined in Appendix D. As the rotation tensor is orthogonal, which means that its inverse is given by its transpose, any tensor can be transformed

between the two coordinates systems using the orthogonality condition. In other words, the strain rate tensor defined in Equation 4.7 can be obtained along the corotational coordinated using the following transformation [132]

$$\dot{\hat{\varepsilon}}_{ij} = T_{ik}\,\dot{\varepsilon}_{kl}\,T_{jl}, \tag{4.9}$$

where, the corotational strain rate tensor $\dot{\hat{\varepsilon}}_{ij}$ is defined by

$$\dot{\hat{\varepsilon}}_{ij} = \frac{1}{2}\left(\frac{\partial v_i}{\partial \hat{x}_j} + \frac{\partial v_j}{\partial \hat{x}_i}\right). \tag{4.10}$$

4.1.3 Membrane theory and the constitutive equation

The general structural behaviour of thin–walled structures is characterised by two principally different states of deformation, namely, *membrane* and *bending* action. In contrast to pure bending action where the midsurface fibers preserve length, the membrane dominated deformations have strains in the midsurface. In the present study, the membrane is assumed to have membrane action only. As the typical membrane model assumes all strain and stress components to be constant with respect to the thickness coordinate, the structural behaviour is defined exclusively via in–plane strains of the midsurface. Conceptually, the simplest approach is to consider the actual body being infinitely thin, thus

$$\boldsymbol{X} = \boldsymbol{X}_c, \quad \boldsymbol{x} = \boldsymbol{x}_c, \quad \boldsymbol{x} = \boldsymbol{X} + \boldsymbol{u} \tag{4.11}$$

where, in this sense, thin membrane elements can be considered as curved plane–stress elements. After defining the strain rate of the membrane model a relationship is established between the stresses and strains by the *constitutive equation*. The constitutive equation has to follow the continuum material law and impose the membrane plane–stress theory point wise.

To account for the rotation of the material, the constitutive equation has to be *frame–invariant rate*. Put it differently, the stress rate tensor has to be objective with respect to material rotation. Hence, either objective stress rate has to be considered or the constitutive equation must be applied on the corotated coordinates, which yields [18]

$$\dot{\hat{\sigma}}_{ij} = \hat{D}_{ijkl}\dot{\hat{\varepsilon}}_{kl}, \tag{4.12}$$

where $\hat{D}_{ijkl}$ is the membrane tangent stiffness tensor defined in Appendix D, and $\dot{\hat{\sigma}}_{ij}$ is the corotational Cauchy stress rate tensor where the plane–stress theory is applied, in which

$$\hat{\sigma}_{ij} = \begin{bmatrix} \hat{\sigma}_{11} & \hat{\sigma}_{12} & 0 \\ \hat{\sigma}_{21} & \hat{\sigma}_{22} & 0 \\ 0 & 0 & 0 \end{bmatrix}. \tag{4.13}$$

The Cauchy stress tensor $\boldsymbol{\sigma}$ defined in global coordinate system can be obtained by utilising the rotation tensor $\boldsymbol{T}$ in the inversed direction to Equation 4.9.

4.2 MPM membrane modelling after York

This section, presents the MPM membrane formulation as given by York [191]. The same standard MPM procedure is employed here except that the stresses of the membrane material points are computed with respect to local, rotated coordinate system $\hat{\boldsymbol{x}}$ where a plane–stress condition is satisfied rather than computing them with regard to the global framework. A technique is proposed to initialise the mass of particles for irregular discretisation. A similar technique is used later to tackle the problem of large deformation by updating the membrane surface. In other words, the integration weight of the particles is updated according to the deformed configuration. Solving a single degree of freedom spring–mass system using York's scheme shows good agreement with the analytical solution, whereas care should be taken regarding mesh sensitivity and stress prediction when more complex problem is treated as will be shown in this chapter.

4.2.1 Mathematical formulation

As stated previously, the membrane is a structure that has stiffness in–plane with no stiffness in bending. Stress and traction components through the thickness are assumed to be constant. In York's approach [191], a continuous membrane is discretised by a single layer of material points that is overlaid on an computational mesh, see Figure 4.2. Assuming a single layer of material points through the thickness enforces the condition of constant traction through a section automatically. A locally–rotated frame of reference is defined by a component perpendicular to the membrane surface with two components tangent to the surface at each material point. By updating the tangential strains, the stress update at the material point is straightforward assuming linear elastic and plane–stress behaviour. The stresses are then projected back to the global coordinate system where the internal force vector is calculated without distinction between membrane and solid material points. Basically the same momentum equation for solid material is applicable for the membrane as well. Some differences are pointed out later in this section.

Internal forces The internal forces, which are obtained from integrating the internal membrane resistance over the spatial domain, should consider the membrane theory in their formulation. Hence, this consideration of the plane–stress theory should start from the calculation of the strain increment at each material point.

The incremental strain tensor, which is evaluated at the beginning on the global coordinates, is projected onto local coordinates attached to the membrane using the transformation formula of Equation 4.9 on incremental level, which yields

$$\Delta\hat{\boldsymbol{\varepsilon}}_p = \boldsymbol{T}\,\Delta\boldsymbol{\varepsilon}_p\,\boldsymbol{T}^T, \tag{4.14}$$

where $\Delta\hat{\boldsymbol{\varepsilon}}_p$ and $\Delta\boldsymbol{\varepsilon}_p$ are the incremental strain tensor of particle p for local and global coordinates, respectively. The incremental stress tensor $\Delta\hat{\boldsymbol{\sigma}}_p$ is then obtained from applying the membrane constitutive model on local coordinate in the form

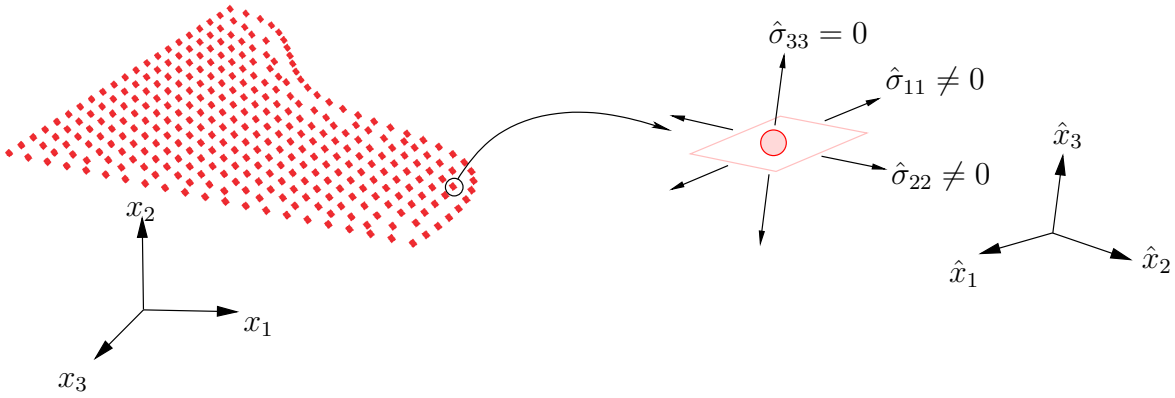

Figure 4.2: York's representation of a membrane showing the plane–stress theory applied on material points

$$\Delta\hat{\boldsymbol{\sigma}}_p = \hat{\boldsymbol{D}} : \Delta\hat{\boldsymbol{\varepsilon}}_p, \tag{4.15}$$

in which $\hat{\boldsymbol{D}}$ being a matrix consistent with the plane–stress assumption as given in Appendix D. Implicit in Equation 4.15 is the assumption that the increments are small enough that rotational effects can be assumed to be negligible. For cases where strain increments are large, the constitutive law must be objective [123]. Finally, the local stress increment is transformed to the global frame of reference

$$\Delta\boldsymbol{\sigma}_p = \boldsymbol{T}^T \, \Delta\hat{\boldsymbol{\sigma}}_p \, \boldsymbol{T}, \tag{4.16}$$

where $\Delta\boldsymbol{\sigma}_p$ is the increment, which is used to update the global stress tensor at the end of the time step. It is important to mention here that the dimension of the incremental rotated stress tensor $\Delta\hat{\boldsymbol{\sigma}}_p$ is extended to match the incremental global stress tensor by imposing zeros. The global stress tensor is updated explicitly at the end of the time step by adding up the contribution of Equation 4.16 in the following form

$$\boldsymbol{\sigma}_p^{n+1} = \boldsymbol{\sigma}_p^n + \Delta\boldsymbol{\sigma}_p^{n+1}, \tag{4.17}$$

in which n is a step counter at time t^n. The internal force vector corresponding to the membrane particles $\boldsymbol{F}^m$ is then calculated in the usual way without distinction between solid and membrane material points; i.e.,

$$\boldsymbol{F}^m = \sum_{p=1}^{n_p} \boldsymbol{B}^T \left(\boldsymbol{x}_p\right) \boldsymbol{\sigma}_p \left(\boldsymbol{x}_p, t\right) \, h \, w_p, \tag{4.18}$$

where n_p is the total number of membrane particles and $\boldsymbol{B}$ is the strain–displacement matrix evaluated at the location $\boldsymbol{x}_p$ of the particle p. h and w_p are the thickness and area of the membrane associated with p, respectively. In other words, in York's approach, the internal force vector is calculated using the $\boldsymbol{B}$ matrix of the three–dimensional element and the integration is performed by summing over the material points, including those

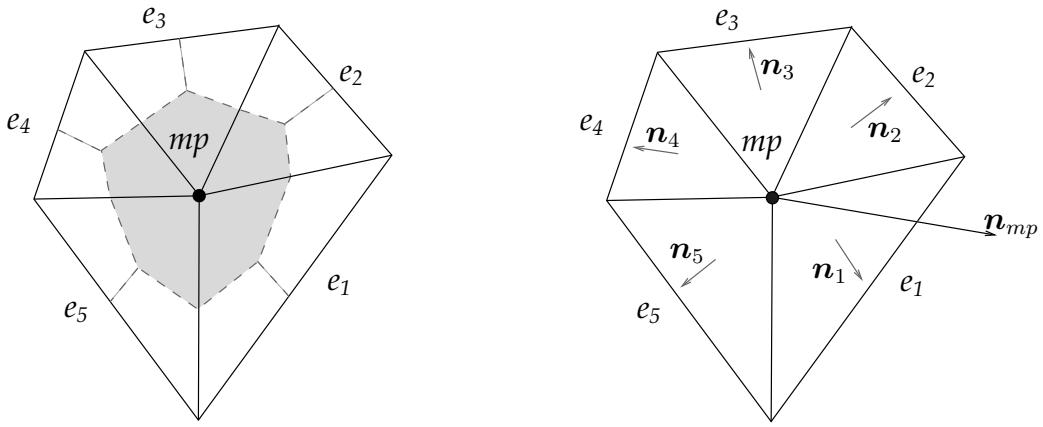

Figure 4.3: Update information at the membrane particle: (left) lumping mass matrix procedure of area and (right) calculation of normal by averaging

of the membrane. The consequence of this procedure on the prediction of the membrane stresses is demonstrated later.

Mass matrix In practice, the membrane mass is small enough to be neglected as compared to the combined structure. However, a sensible mass must assigned to the material points for the explicit dynamic algorithm, as this procedure employs only a mass matrix with no stiffness matrix on the left hand side of the momentum equation. More detail about the minimum mass required for the membrane particle as compared with the other solid particles is presented later.

As long as the considered membrane has only transitional degrees of freedom, the same lumping procedure used before for solid material can be used here. Otherwise, rotational inertias must added for the rotational degree of freedom [18]. Each particle in the single layer membrane must be assigned a mass taking into account the membrane density and the membrane thickness. As proposed by York [191] and Gan et al. [63], the membrane mass is assumed to be equally distributed as

$$m_p = \frac{\varrho_m \, A_m \, h}{n_p}, \tag{4.19}$$

where m_p is the mass of the membrane particle p, which is applied for all number of membrane particles n_p and weighted by the total area of the membrane A_m, mass density ϱ_m and thickness h. The assumption of equal mass to all particles holds only for a regular surface discretisation. Therefore, the variable spacing of the material points in the case of non–regular mesh discretisation has to be considered. To achieve this, the surface is approximated first by a collection of triangular elements. Then, the membrane material points are defined at the vertices of the two–dimensional mesh. In the present procedure, the effect of triangle sizes is included for the particle mass initialisation using lumped mass approach for triangular elements as depicted in Figure 4.3

$$m_p = \varrho_m \, h \sum_{i=1}^{N_{tri}} \frac{A_{tri}^i}{3}, \tag{4.20}$$

where N_{tri} is the number of neighbour triangles to p and A_{tri}^i is the area of the triangle i.

Integration weight In the finite element method theory with large deformation, the formulation is based on the deformed configuration. The area or the integration weight of the membrane changes when forces are applied [33]. Thus the previous procedure of initialising membrane mass can be used for updating the integration weight for the entire calculation process, that is

$$w_p = \sum_{i=1}^{N_{tri}} \frac{A_{tri}^i}{3}, \tag{4.21}$$

in which w_p is the updated integration weight of the membrane particle p. The illustration of the area lumping mass matrix procedure is shown in Figure 4.3.

Calculation of normals A proper application for the membrane theory requires the computation of the normal and tangential vectors. Several approaches were investigated to determine the material point normal such as *simple colour function approach*, *interpolation method*, *mass matrix approach* and *point–set method* [174, 191]. It was found that the *connectivity method* could better handle complex geometries and provided better accuracies when using low order elements. The disadvantage of the additional storage space for the connectivity data is no longer an issue for modern powerful computers.

Adopting the connectivity method for two–dimensional problems simply requires averaging the normals of the neighbour lines to get the normal at the intersection point. This idea was extended for membranes in three–dimensional space by Gan [62]. In other words, the normals of all neighbouring triangles are averaged to obtain the normal at the intersection point as shown in Figure 4.3. The averaging formula takes the form

$$\boldsymbol{n}_p = \frac{\sum \boldsymbol{n}_i}{\| \sum \boldsymbol{n}_i \|}, \tag{4.22}$$

where the summation runs over the number of neighbour triangles N_{tri}, with $\boldsymbol{n}_p$ and $\boldsymbol{n}_i$ being the unit normal at the material point p and the triangle i, respectively. For low order elements, the normals are constant over each element.

After identifying the normal at a material point $\boldsymbol{n}_p$, two tangential vectors $\hat{\boldsymbol{e}}_1$ and $\hat{\boldsymbol{e}}_2$ are calculated, in which the first tangent $\hat{\boldsymbol{e}}_1$ can be constructed by cross product of $\boldsymbol{n}_p$ with any other arbitrary vector. For this purpose, an arbitrary vector $\hat{\boldsymbol{e}}_r$ can be chosen such that it is selected to be aligned with one of the global coordinate axes. To reduce numerical error, the chosen axis corresponds to the normal vector component which has the closest value to zero. For instance if the minimum component of $\boldsymbol{n}_p$ is in the direction of the global axis x_1 then the random vector is aligned with x_1 axis, $\hat{\boldsymbol{e}}_r = \boldsymbol{e}_1$, where $\boldsymbol{e}_1$ is the unit vector in x_1 direction. Therefore, the first tangent followed by the second tangent vector $\hat{\boldsymbol{e}}_2$ are computed from

$$\hat{\boldsymbol{e}}_1 = \boldsymbol{n}_p \times \hat{\boldsymbol{e}}_r \quad \text{and} \quad \hat{\boldsymbol{e}}_2 = \boldsymbol{n}_p \times \hat{\boldsymbol{e}}_1. \tag{4.23}$$

With the tangent vectors $\hat{\boldsymbol{e}}_1$ and $\hat{\boldsymbol{e}}_2$ combined with the unit normal $\boldsymbol{n}_p$, the rotation matrix $\boldsymbol{T}$ is fully constructed for the updated position of the considered particle.

4.2.2 Numerical algorithm

Implementation of the numerical algorithm for the membrane is similar to the algorithm of the solid materials presented in Chapter 3. Keeping in mind, the constitutive model of the membrane should contain the plane–stress theory. Apart from the algorithm itself, defining a new particle set for the membrane is more convenient in terms of the computational efficiency. In this way the membrane and the solid material points are treated separately and coupled via the momentum equation of the entire system. This implementation allows sweeping the information related to the membrane over the elements containing membrane particles only. Furthermore, having separate data structure for the membrane particles gives more freedom for the initialisation process. For the purpose of completeness, the entire calculation algorithm is summarised here, where most of the steps are repeated from the numerical algorithm of the general MPM procedure:

Step one All material parameters and state variables are initialised at the material points. The membrane mass is assigned to each individual particle according to Equation 4.20, with the rotation tensor being constructed at this step using Equations 4.22 and 4.23.

Step two Form the lumped mass matrix of the entire system including solid and membrane particles based on Equation 3.35. In comparison to the solid particles mass, the membrane particles have nearly zero mass. Nevertheless, it should be assigned a value which must be big enough to get the MPM dynamic algorithms working properly.

Step three Map the velocity field from all material points to the computational grid using Equation 3.55. This mapping procedure is equivalent to the momentum conservation calculated at the material points and the one computed at the computational grid.

Step four Calculate the external force vector given by Equations 3.51 and 3.54, which is composed of the gravity force and the traction boundary condition.

Step five Calculate the internal force vector using Equations 3.33 and 4.18 for the solid and the membrane, respectively.

Step six Calculate the nodal acceleration vector by solving the system of equations of the three–dimensional grid.

Step seven Update the velocity of all material points by integrating explicitly the dis-

crete nodal values of the acceleration field using values of shape functions at the material points as in Equation 3.58.

Step eight Evaluate the velocity field at the computational grid by evaluating the momentum at the material points. In other words, repeat step three.

Step nine Use the velocity field obtained from step eight to get the incremental displacement field evaluated at the material points using Equation 3.60.

Step ten Obtain the strain increment and consequently the stress increment for solid and membrane particles. For membrane particles, Equation 4.14 is used to represent the strain increment with respect to the local coordinate system. After applying the membrane constitutive equation to get the stress increment, this is rotated back to the global coordinates where the stress tensor is assembled. The integration weight of the solid particles are updated by the change in volumetric strain using Equation 3.41, while of the membrane particles is performed via Equation 4.21.

Step eleven Set the time step size for the next calculation step and repeat the previous procedure starting from step two. Explicit time integration is carried out on the global system of equations. An important consideration for the integration process is the selection of appropriate time step size. The *Courant–Friedrich–Lewy* (CFL) condition used for solid elements, see; e.g., [169, 189] is also adopted for the membrane element. Stability analysis for the membrane problem shows that this criterion is applicable [191]. The time step Δt is chosen to be equal to or less than the critical time step Δt_e of each element e, $\Delta t = \alpha\, \Delta t_e$, whether membrane or solid element, with

$$\Delta t_e = \frac{l_e}{c_p} \tag{4.24}$$

in which, l_e is a characteristic length within the element e, for example the shortest (height) of a triangle as illustrated in Figure 4.4, c_p is the speed of the elastic compression

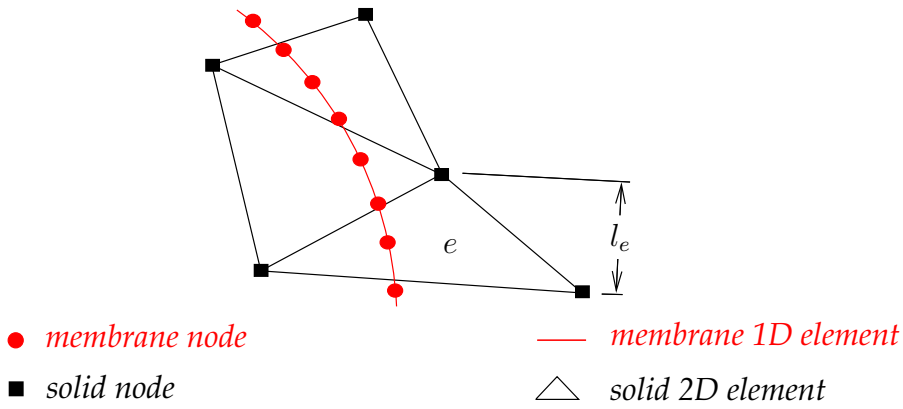

Figure 4.4: Two–dimensional solid reinforced by a linear membrane element

wave, and the factor α should be kept below 1 to maintain stability and accuracy. For all cases considered in this thesis, the factor α is chosen to be $0.8 \leqslant \alpha \leqslant 0.98$ [18]. One should recognize that the time step criterion is related to the most critical condition in the mesh, with the critical time step elsewhere in the domain being greater.

4.2.3 Validation example: spring–mass system

For validation purposes, the single degree of freedom spring–mass system shown in Figure 4.5 was modelled with MPM. The spring has an initial length $l_0 = 0.5\,\mathrm{m}$ and spring constant $k = 40\,\mathrm{kN/m}$ while the oscillating block has a mass of $m = 20\,\mathrm{kg}$. In this application, the normal direction of the spring/membrane is trivial and constant through the computation. The analytical solution of the oscillating mass in the x–direction with time t can be constructed for the instantaneous deformation u as [71]

$$u\,(t) = u_0 \left[1 - \cos\left(\sqrt{k/m}\,t\right)\right], \tag{4.25}$$

in which u_0 is the displacement of the mass at equilibrium, and the period is defined as $2\pi/\sqrt{k/m}$. In MPM, the spring is represented by a membrane with stiffness E_m and thickness h, and is extended through the 4–noded tetrahedral elements as shown in Figure 4.5. In this figure, ten layers of the tetrahedral elements for the spring discretisation are employed with one extra layer for the mass which is represented by a solid material attached to the membrane strip. In the MPM model, the expected zone of particle movement should be covered with elements, some of which are initially empty. The discretisation of the membrane via particles was chosen fine enough to ensure that the analytical solution could be approximated closely. Furthermore, the membrane is assigned a very small mass, approximately 1% of the oscillating body mass. Thus, wave propagation effects can be neglected. A comparison in Figure 4.6 confirms that the algorithm allows the MPM to approximate the analytical solution reasonably well. A tiny difference is noticed between the analytical and the MPM solution.

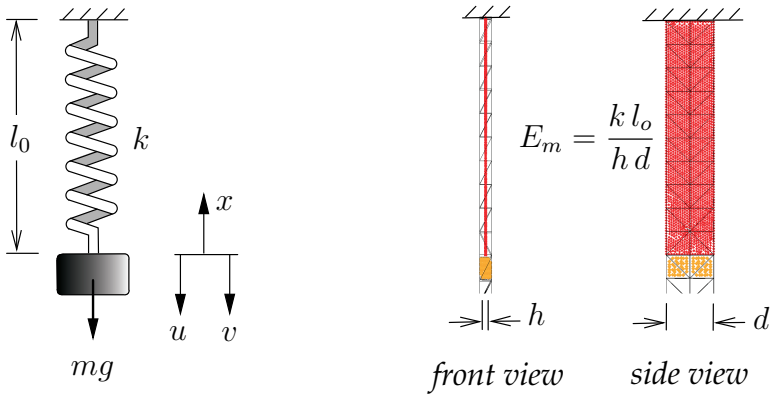

Figure 4.5: Spring–mass system with its MPM representation

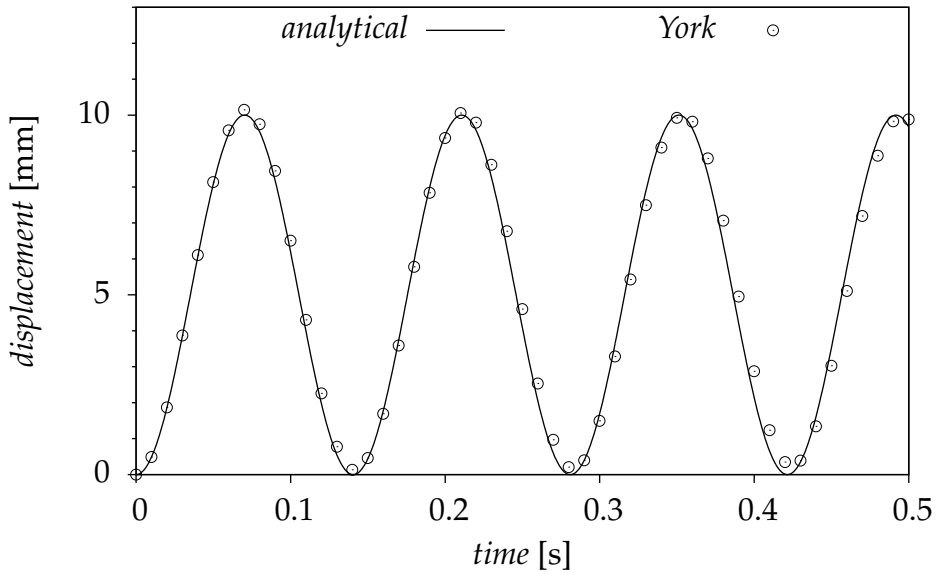

Figure 4.6: Displacement of the oscillating mass using York's approach

4.3 Coupled FEM–MPM membrane

It is known in the MPM literature that non–physical stress oscillations noise are observed when a material point crosses the boundary between two elements, which is referred to as the grid crossing error. This is attributed to the change in the sign of the shape function gradient as a material point crosses the boundary, which in turn has an influence on the internal load vector. Increasing the number of material points per element reduces but does not eliminate the grid crossing error. Procedures have been proposed to correct this problem. Bardenhagen and Kober [12] showed that the *generalised interpolation material point method* (GIMP) performs better by providing a higher level of continuity in the interpolation between material points and the computational grid as it provides gradient functions of higher degree of smoothness. Sadeghirad et al. [151] extended the GIMP by convecting the particle domain. This method, which is given the name *convected particle domain interpolation* (CPDI), has been demonstrated to perform better than GIMP for cases where extreme deformations develop. Both, GIMP and CPDI, replace the grid basis function with a modified one in which the internal force integration is performed in the particle domain.

Following an approach proposed by Lian et al. [108] for modelling the interaction between reinforcement and concrete, a coupled FE–MP method is introduced in this research to model a thin–walled structure in combination with the solid material. In this approach, the membrane can be discretised using a two–dimensional triangular mesh with the membrane nodes being free to move through the three–dimensional tetrahedral mesh. The displacement at each node is obtained from the solution of the momentum

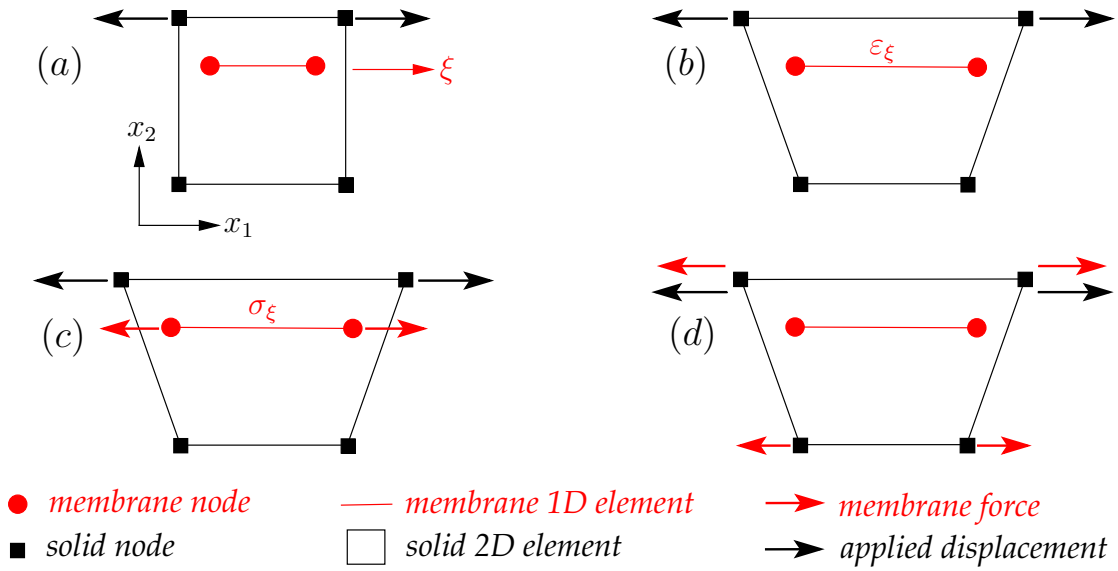

Figure 4.7: Schematics of the coupled FEM–MPM: (a) initial configuration, (b) deformed configuration, (c) stress developed due to strain, and (d) forces mapping

equation on the computational mesh, but the increments of membrane strain and stress are based on the deformation of the triangular mesh. It is a distinct entity that is treated within the conventional finite element framework. The membrane strains and stresses are calculated at the Gauss integration points, not material points. The connection of the membrane influence on the three–dimensional mesh is through the mapping of internal membrane forces to the computational nodes.

Consider, for example, the schematics shown in Figure 4.7 going from (a) to (d), where a membrane element is within an empty two–dimensional rectangular element. In the initial configuration (top left) displacements are applied along the top of the rectangular element. The displacements produce a horizontal strain ε_ξ and a corresponding stress σ_ξ due to the kinematic constraints between the deformation of the rectangular element and the membrane; i.e., the displacements in the membrane are obtained from the nodal displacements and shape functions corresponding to the rectangular mesh. The stresses are then used to determine the internal forces in the membrane. Since the internal forces due to the membrane are determined with respect to the membrane grid and then transferred to the tetrahedral mesh, grid crossing error is avoided as the membrane moves through the tetrahedral mesh. The soil is modelled using the original MPM integration scheme, where properties are collocated at distinct material points [166, 169]. An enhancement technique can be applied to reduce the grid crossing effect [2, 194]. The Gauss quadrature enhancement scheme is adopted in this research to improve the MPM integration [21, 22].

4.3.1 Mathematical formulation

In the proposed representation, the membrane is discretised by a two–dimensional triangular mesh as shown in Figure 4.8. The mesh connectivity is maintained during the computation where the membrane nodes are free to move through the three–dimensional tetrahedral mesh. The displacement of these nodes is obtained from the solution of the momentum equation on the three–dimensional computational mesh, but the increment in membrane strain and stress is based on the deformation of the triangular mesh. The membrane strains and stresses are calculated at the integration point as shown in Figure 4.8. As long as 3–noded triangular elements are adopted in this scheme, the location of the integration point can be anywhere inside the triangle and does not need to correspond to the Gaussian point.

The formulation of a plane element in thee–dimensional space with three translational degrees of freedom per node was used to model the membrane. The formulation of a general shell element presented by Bathe [16] was applied with simplification for the considered membrane. Using the discretisation shown in Figure 4.8, the continuous geometry of the membrane is approximated using the following transformation

$$x_i\left(\xi_1,\xi_2,\xi_3\right) \simeq \sum_{j=1}^{nn} H_j\, x_{ij} + \frac{\xi_3}{2}\sum_{j=1}^{nn} h_j\, H_j\, n_i^j, \tag{4.26}$$

where, x_i is the position vector represented in global coordinate, x_{ij} is the discretised form of x_i at node j with H_j being the corresponding interpolation function that depends on the natural coordinate (ξ_1,ξ_2,ξ_3) (see Appendix E), nn is the number of nodes per element, h is the membrane thickness, and n_i is the component of the outward unit normal $\boldsymbol{n}$. For specific application of the low order element with constant membrane thickness h, Equation 4.26 reduces to

$$x_i\left(\xi_1,\xi_2,\xi_3\right) \simeq \sum_{j=1}^{3} H_j\, x_{ij} + \frac{\xi_3\, h\, n_i}{2}. \tag{4.27}$$

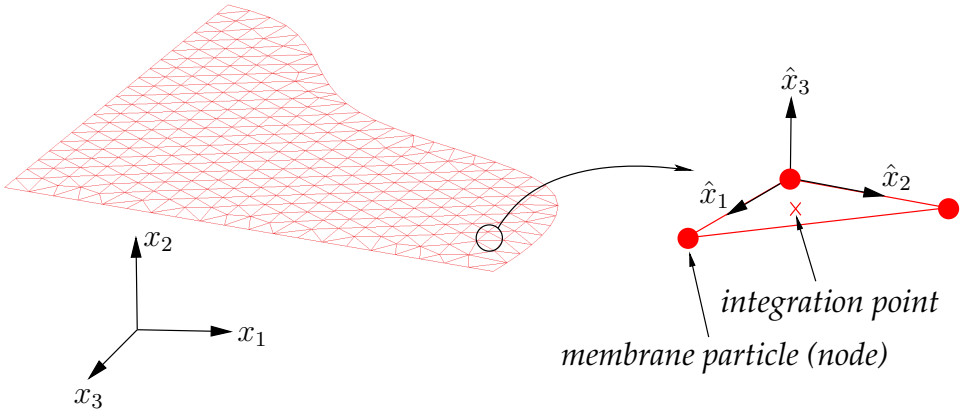

Figure 4.8: Membrane discretisation using the coupled FE–MP approach

Following the isoparametric concept, where the geometry and the displacements are approximated with the same shape functions, displacement is approximated as

$$u_i^m\left(\xi_1,\xi_2,\xi_3\right) \simeq \sum_{j=1}^{3} H_j\, u_{ij}^m + \frac{\xi_3\, h\, n_i}{2}, \tag{4.28}$$

in which, the incremental displacement of the membrane grid nodes $\Delta\boldsymbol{u}^m$ is interpolated from the continuous displacement field of the tetrahedral mesh by $\Delta u_i^m\left(\boldsymbol{x}_i^m, t\right) = N\left(\boldsymbol{x}_i^m\right)\,\Delta\boldsymbol{u}\left(t\right)$, where $N\left(\boldsymbol{x}_i^m\right)$ emphasises that the shape functions are evaluated at the global location of membrane node $\boldsymbol{x}_i^m$. The velocity $\boldsymbol{v}^m$ and acceleration $\boldsymbol{a}^m$ are obtained by taking the first and second time derivatives of Equation 4.28, respectively. In order to calculate gradients and integrate, the standard transformation rules, including the determination of the Jacobian matrix is applied; see for example [16]. For the 3–noded element, the relation between the global coordinates $\boldsymbol{x}$ and the natural coordinates $\boldsymbol{\xi}$, we directly obtain

$$\begin{aligned}
\frac{\partial x_i}{\partial \xi_1} &= \sum_{j=1}^{3} \frac{\partial H_j}{\partial \xi_1} x_{ij},\\
\frac{\partial x_i}{\partial \xi_2} &= \sum_{j=1}^{3} \frac{\partial H_j}{\partial \xi_2} x_{ij},\\
\frac{\partial x_i}{\partial \xi_3} &= \frac{h\, n_i}{2},
\end{aligned} \tag{4.29}$$

which are implemented in the Jacobian matrix $\boldsymbol{J}$ that involves derivatives of both coordinate systems, such that

$$\frac{\partial}{\partial \xi_i} = J_{ij}\frac{\partial}{\partial x_j}, \tag{4.30}$$

for $i, j \in (1, 2, 3)$. Assuming that the gradients are appropriately determined, the *strain–displacement matrix* $\boldsymbol{B}^m$ with regard to the global frame of reference (not the computational mesh) is given by

$$\boldsymbol{B}^m = \boldsymbol{L}\boldsymbol{H}, \tag{4.31}$$

where $\boldsymbol{H}$ represents the interpolation matrix for the membrane element and $\boldsymbol{L}$ is the linear differential operator as defined in Appendix E. The strain increment $\Delta\boldsymbol{\varepsilon}$ is determined using the incremental nodal displacements $\Delta\boldsymbol{u}^m$ of the membrane via

$$\Delta\boldsymbol{\varepsilon} = \boldsymbol{B}^m\,\Delta\boldsymbol{u}^m \tag{4.32}$$

which can then be used to express the strain in terms of local frame of reference $\hat{\boldsymbol{\varepsilon}} = \boldsymbol{T}_{\varepsilon}\,\boldsymbol{\varepsilon}$, see Appendix D, giving the expression

$$\Delta\hat{\boldsymbol{\varepsilon}} = \hat{\boldsymbol{B}}^m\,\Delta\boldsymbol{u}^m \tag{4.33}$$

in which $\hat{\boldsymbol{B}}^m = \boldsymbol{T}_\varepsilon \boldsymbol{B}^m$ [18], where the terms of $\boldsymbol{T}_\varepsilon$ can be extracted from the second order tensor transformation rule $\hat{\boldsymbol{\varepsilon}} = \boldsymbol{T}\,\boldsymbol{\varepsilon}\,\boldsymbol{T}^T$ as shown in Appendix D. The influence of out–of–plane strains are suppressed by setting the corresponding rows in $\boldsymbol{T}_\varepsilon$ to zero. In other words, the energy associated with out–of–plane deformation is assumed to be negligible; thereby enforcing plane stress conditions.

For a 3–noded element, the gradients are constant and only one integration point is required. The incremental membrane stress $\Delta\hat{\boldsymbol{\sigma}}$ at the integration point is now obtained at the membrane integration point via

$$\Delta\hat{\boldsymbol{\sigma}} = \hat{\boldsymbol{D}} : \Delta\hat{\boldsymbol{\varepsilon}}, \tag{4.34}$$

where $\hat{\boldsymbol{D}}$ is consistent with the plane–stress assumption as given in Appendix D. The membrane stress within the element is updated according to

$$\hat{\boldsymbol{\sigma}}^{n+1} = \hat{\boldsymbol{\sigma}}^n + \Delta\hat{\boldsymbol{\sigma}}^{n+1}. \tag{4.35}$$

The internal membrane force $\boldsymbol{F}^{2D}$ is calculated on the membrane mesh using standard finite element integration

$$\boldsymbol{F}^{2D} = \int_S \hat{\boldsymbol{B}}_m^T\, \hat{\boldsymbol{\sigma}}^{n+1}\, h\, dS, \tag{4.36}$$

where the superscript $2D$ implies that the internal force correspond to the membrane mesh, however, the forces are written with respect to the global frame of reference defined by $\boldsymbol{e}$, and S is the membrane surface area. As a final step, the force $\boldsymbol{F}^{2D}$ is transferred from the triangular mesh nodes to the tetrahedral mesh, where the computation is conducted, using the following mapping procedure [108]

$$\boldsymbol{F}_i^{\mathrm{m}} = \sum_{j=1}^{nm} N_i^j\ \boldsymbol{F}_j^{2D} \tag{4.37}$$

where $\boldsymbol{F}_i^{\mathrm{m}}$ is the membrane force vector of tetrahedral element node i, nm is the total number of membrane nodes in the tetrahedral element, N_i^j is the shape function of node i evaluated at the location of the membrane node j, and $\boldsymbol{F}_j^{2D}$ is the force vector of node j. After evaluating the membrane force contributions within a three–dimensional element, the element contribution is added to the global internal force $\boldsymbol{F}^{\mathrm{int}}$ in Equation 3.33. This is repeated for all tetrahedral elements where applicable.

4.3.2 Numerical algorithm

As shown previously, the coupled FE–MP approach introduces integration points for the membrane discretisation. In this discretisation the material points, or the membrane nodes, describe the kinematics only and no information about the stresses is stored there. In this case the data structure type to be remembered by the membrane particles is different from that of the solid particles, which confirms a need to define totally new particle set for the membrane. It is important to say that setting only the kinematic information

at the material points is neither obvious nor trivial procedure. It is found to be more efficient to keep the mass at the material points rather than at the integration points. Within the MPM procedure, however, momentum has to be mapped from particles to nodes and vice versa (step three and eight mentioned later), which requires the mass to be conjugate with the velocity. In other words, the mass should be defined at the same place where the velocity is defined which is at the membrane particles in this case.

Beside the new particle set, a set of integration points must be traced during computations. Furthermore, the rotation tensor must be evaluated at the integration points with no need to move it back to the material point like in York's procedure. The entire algorithm of the coupled FE–MP method can be summarised in the following steps

Step one Initialise material parameters, except mass as justified before, and state variables at the integration points for the membrane and at the material points for the solid material. The rotation tensor is evaluated at the integration points where the constitutive model is applied. As long as 3–noded triangular element is involved, the rotation tensor at the integration point is the same as for the element. The normal on a plane of three known points is combined with Equation 4.23 to form the rotation tensor.

Step two Form the lumped mass matrix of the entire system. The membrane mass can be introduced at the membrane particles or at the integration points. Finally, it has to be mapped to the three–dimensional mesh where the computation is carried out. Equation 3.35 is used for the mapping process.

Step three Map the velocity field from the material points to the computational grid using Equation 3.55. This mapping procedure is equivalent to the momentum conservation calculated at the material points and the one computed at the computational grid.

Step four Calculate the external force vector given by Equations 3.51 and 3.54, which is composed of the gravity force and the traction boundary condition.

Step five Calculate the internal force vector for the solid and the membrane. The membrane internal force has to be calculated at the integration points first (Equation 4.36) before mapping these forces to the three–dimensional mesh (Equation 4.37).

Step six Calculate the nodal acceleration vector by solving the system of equations on the three–dimensional grid.

Step seven Update the velocity of all material points by integrating explicitly the discrete nodal values of the acceleration field using values of shape functions at the material points.

Step eight Evaluate the velocity field at the computational grid by evaluating the momentum at the material points. In essence, repeat step three upward mentioned.

Step nine Use the velocity field obtained from step eight to get the incremental displacement field evaluated at the material points using Equation 3.60.

Step ten Obtain the strain rate and consequently the stress rate for solid and membrane particles. The incremental membrane stresses are evaluated and updated at the integration points in Equation 4.34 and 4.35, respectively. Also, the integration weight of the membrane can be updated, for large deformation problems, by updating the area of the two–dimensional mesh or kept constant during the calculation.

Step eleven Set the time step size for the next calculation step and repeat the previous procedure starting from step two. The smaller critical value of the time step for the solid and the membrane material is chosen. Similar to York's procedure, Equation 4.24 is applied compute the critical time step for the coupled approach.

4.3.3 Validation example: spring–mass system

The elementary problem of an oscillating mass presented in Section 4.2 is repeated here using the proposed approach of coupled FEM–MPM with the same discretisation. The displacement of the oscillating mass is shown in Figure 4.9, which demonstrates excellent agreement with the analytical solution. At first glance, both membrane approaches show good agreement with the analytical solution. However, the sensitivity of each solution scheme for some parameters will be investigated in details next.

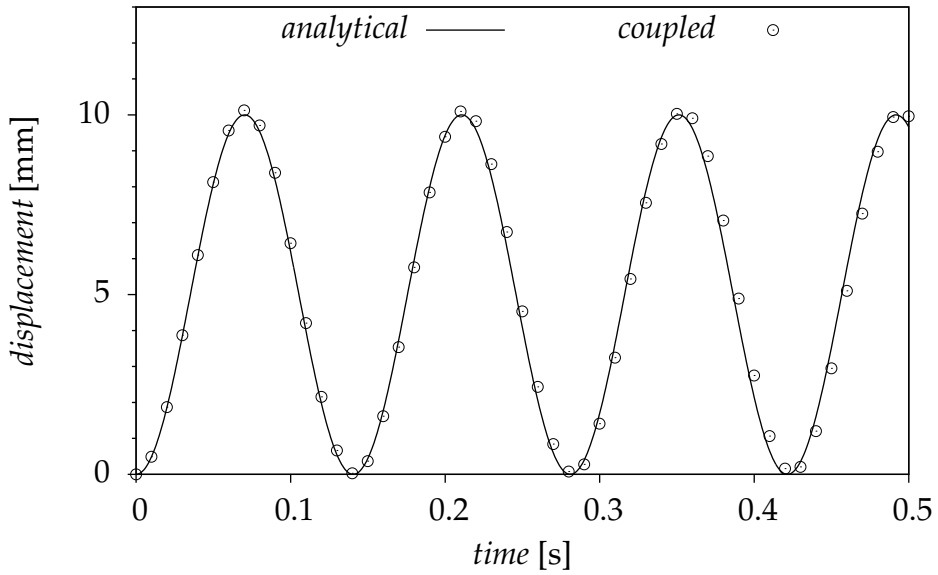

Figure 4.9: Displacement of the oscillating mass using the coupled FE–MP approach

4.4 Comparison of the two membrane approaches

Comparing the mathematical formulations of the two presented membrane approaches shows that the essential difference is the way of calculating the internal force. Use of low order elements within MPM makes the gradients of the shape functions discontinuous at element boundaries. Hence, when material points change elements during the calculation, the sign of the internal force contribution changes for conventional formulations, which causes grid crossing error. An important motivation to develop the coupled FE–MP approach was to reduce the effect of grid crossing error, which causes the numerical oscillation. Two examples are presented that compare the solution from York's approach to that obtained from the proposed procedure in this thesis.

4.4.1 Mesh sensitivity

Nonphysical membrane rupture may happen when using insufficient number of particles due to the separation of membrane particles by one or more cells. It has been mentioned that the membrane discretisation in the spring–mass problem must be chosen fine enough to capture the analytical solution. Here we address the required fineness of the membrane mesh. To help with the discussion, an objective criterion is required to describe membrane mesh refinement relative to the three–dimensional mesh. Gan [62] suggests a trial procedure to reach a balance between the number of membrane particles and the computation cost. In this study, we use a *Mesh Ratio* MR that is defined by

$$MR = \frac{\sqrt[3]{\bar{V}}}{\sqrt[2]{\bar{A}}}, \tag{4.38}$$

as a measure of relative fineness, where $\bar{V}$ and $\bar{A}$ are average values of volume and area of all tetrahedral and the triangular elements, respectively. Knowing MR, a priori, helps identify the minimum number of allowable particles, below which nonphysical behaviour is predicted. Implicit in the use of Equation 4.38 is that the elements are of similar size. The previous spring–mass results are correspond to a mesh ratio of 8.

In order to determine the sensitivity of each algorithm to the membrane discretisation, the mesh ratio was reduced from 8 to 3 to 1 by changing the triangular mesh and letting the tetrahedral mesh remain fixed. The density of the membrane particles relative to the tetrahedral mesh is shown in Figure 4.10. A comparison of displacement histories in Figure 4.11 clearly shows that York's approach requires a higher mesh ratio to obtain a good solution. The coupled approach is seen to be not as sensitive to the membrane particle density. The poorer performance of York's approach is attributed to stresses being calculated using the strains for the tetrahedral element, where the material point resides. On the other hand, the coupled FEM–MPM derivation provides stepwise stress variations along the membrane that are independent of the tetrahedral gradients. This helps mitigate the problem of stress oscillation, as well as non–physical oscillations of internal forces and the velocity field.

4.4.2 Stress prediction

A comparison between the two approaches with regard to stress prediction can be best achieved by considering a tension bar $3l$ long and composed of four membrane particles arranged distance l apart. Two linear elements are used to perform the solution with σ_0 initial stress. A prescribed displacement d is applied at the end of the second element for three load steps. For the linear displacement interpolation inside the element, the value of d is chosen to have a displacement of $l/2$ at the last membrane particle. Aiming for a quasi–static solution, one can find the solution for both membrane approaches using the following procedures:

York's approach The total length of the bar $3l$ is regularly distributed over the four particles to assume equaled integration weight $3l/4$ for all particles as illustrated in Figure 4.12. The initial stress value σ_0 is applied directly at the material point. Before applying the first load step, the internal force contribution from element I is computed from the initial stress times the integration weight of the first three particles

$$f^{\text{left}} = +\sum_{i=1}^{3}\left(\frac{3}{4}\,l\,\sigma_0\right)_i, \tag{4.39}$$

where f^{left} is the contribution of element I to node j, the counter i is the particle number in element I. In a similar manner the force f^{right} is the contribution of the single particle in element II to the node j is calculated from the stress value at this particle multiplied by its integration weight such as

$$f^{\text{right}} = -\frac{3}{4}\,l\,\sigma_0, \tag{4.40}$$

in which, the minus sign means that the force direction is to the left while the plus means to the right. Summing up Equations 4.39 and 4.40 gives f^j, or the internal force at node j, which yields

$$f_0^j = 0.5\,l\,\sigma_0, \tag{4.41}$$

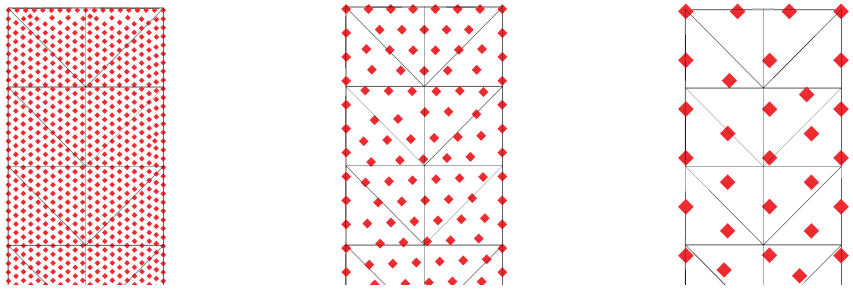

Figure 4.10: Refinement of the membrane discretisation for the same tetrahedral mesh: (left) fine $MR = 8.0$, (middle) medium $MR = 3.0$ and (right) coarse $MR = 1.0$

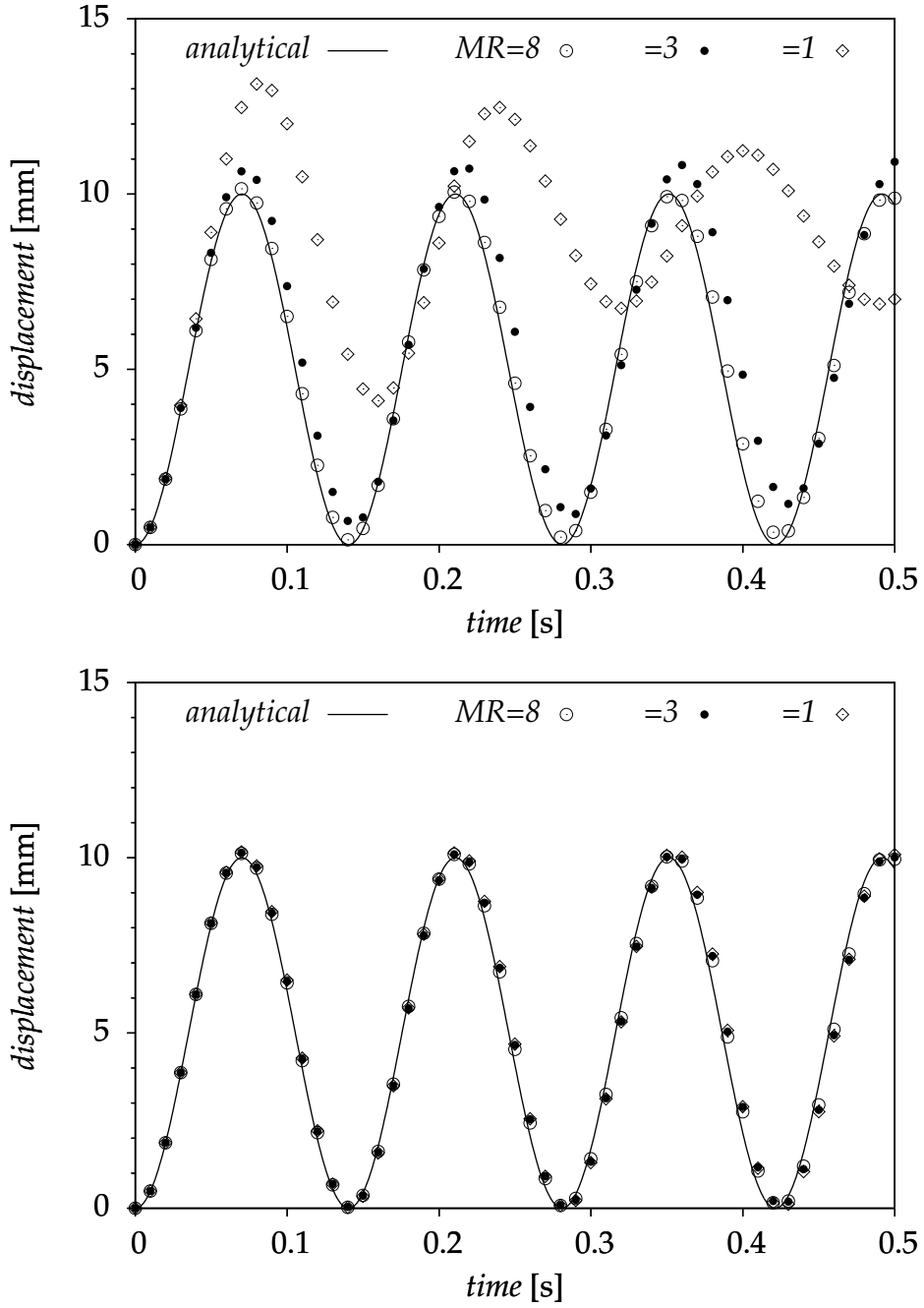

Figure 4.11: Sensitivity to the mesh ratio: (top) York's approach and (bottom) coupled FEM–MPM

where the superscript indicates the load step number. Applying the first load step gives a uniform deformation through all membrane particles, yielding the stress update

$$\sigma_1 = \sigma_0 + 0.17\, E_m, \tag{4.42}$$

in which the strain value 0.17 is obtained from the uniform deformation $(d = 0.83\, l)$ divided by the length of the two elements $5\, l$. By normalising the stress with respect to the membrane stiffness E_m, Equation 4.42 reduces to $\sigma_1 = 1.17\, \sigma_0$. Repeating the procedure of getting the internal force, Equations 4.39, 4.40 and 4.41, gives

$$f_1^j = 0.5\, l\, \sigma_1 = 0.58\, l\, \sigma_0. \tag{4.43}$$

Until now no crossing of particles occurs and the internal force increases gradually at the grid node j. As the displacement d increased, when a particle crosses the boundary in the second load step, the number of particles becomes equaled in each of the two linear elements. As a result the internal force becomes zero at node j.

Coupled FEM–MPM membrane In this approach, the initial stress σ_0 is applied at the integration point whereas the integration weight equals l for all elements as illustrated in Figure 4.13. Consequently, the internal force is evaluated at the membrane particles first rather than directly at the node j of the linear elements. For this specific case of equaled integration weight, the stress integration over the membrane elements contributes with an equal force for the membrane particle i as follows

$$\bar{f}^i = \bar{f}^{\text{right}} + \bar{f}^{\text{left}}, \tag{4.44}$$

where $\bar{f}^i$ is the internal force at membrane particle i. Using a similar procedure, the internal forces for all membrane particles can be computed as

$$\bar{f}^1 = -l\, \sigma_0 \quad : \quad \bar{f}^2 = 0 \quad : \quad \bar{f}^3 = 0 \quad : \quad \bar{f}^4 = l\, \sigma_0, \tag{4.45}$$

where the superscript is the counter index for the membrane particle starting from left to right. The next step in the coupled FE–MP approach is to map the forces to the global

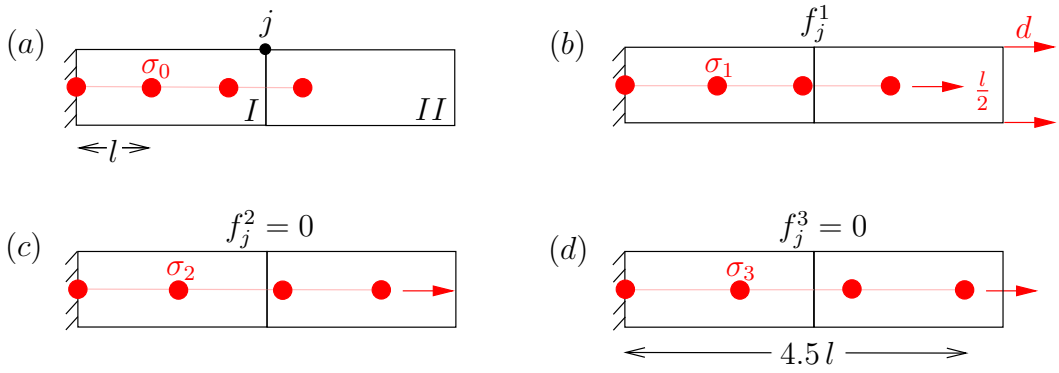

Figure 4.12: Position of the material points in York's approach: (a) initial configuration, (b) first load step, (c) second, and (d) third load step

discretisation via the shape function of the membrane particles according to Equation 4.37, or simply

$$f^j = \sum_{i=1}^{4} N_j\left(x_i\right)\ \bar{f}^i, \tag{4.46}$$

with $N_j\left(x_i\right)$ being the shape function of node j evaluated at the location of the membrane particle i and the summation runs over the number of particles that contribute to the node j. In this summation, the second and third particle have zero forces while the contribution of the first particle is weighted by zero shape function and becomes zero as well. Therefore, the only force contribution to the nodal force f^j comes from the fourth particle which is computed by substituting the force value from Equation 4.45 and its corresponding shape function $N_j\left(3\,l\right) = 0.8$, as illustrated in Figure 4.13, yielding

$$f_0^j = 0.8\,l\,\sigma_0, \tag{4.47}$$

where the superscript indicates the load step number. In a similar way, the stress at the integration point is updated to $\sigma_1 = 1.17\,\sigma_0$. Thereafter, the internal force of the first load step is obtained at the material points and then transferred to the computational grid via

$$f_1^j = N_j\left(x_4\right)\ \bar{f}^4 = 0.6\,l\,\sigma_1, \tag{4.48}$$

in which the internal force at node j is simplified to $0.7\,l\,\sigma_0$. The results of the other two steps are included in Figure 4.14.

Internal force oscillation Comparing the two approaches via displacement control problem shows that York's approach has a larger oscillation in internal force values, see Figure 4.14. The force increases in the first load step until particle crossing occurs then it becomes zero suddenly. The coupled FE–MP approach shows a much smoother

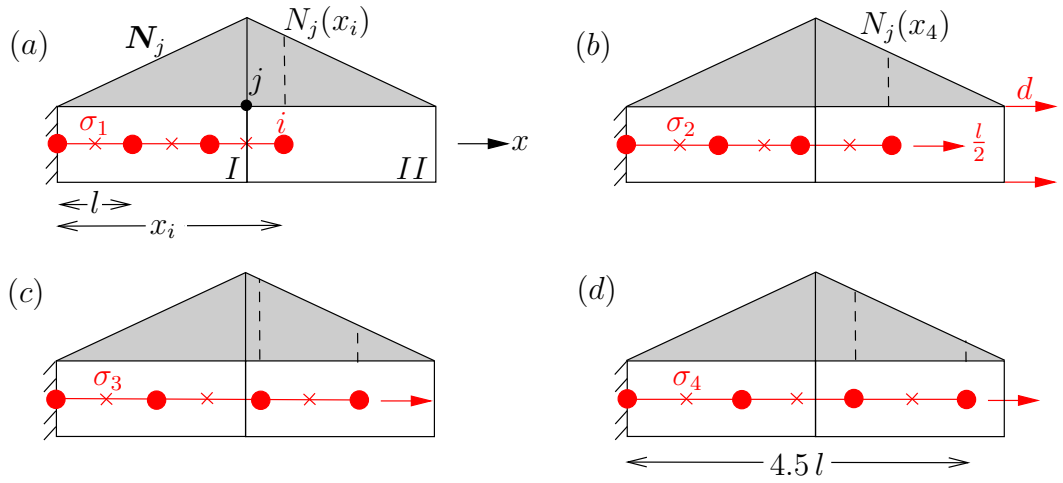

Figure 4.13: Shape functions' diagrams for the coupled FE–MP approach: (a) initial configuration, (b) first load step, (c) second, and (d) third load step

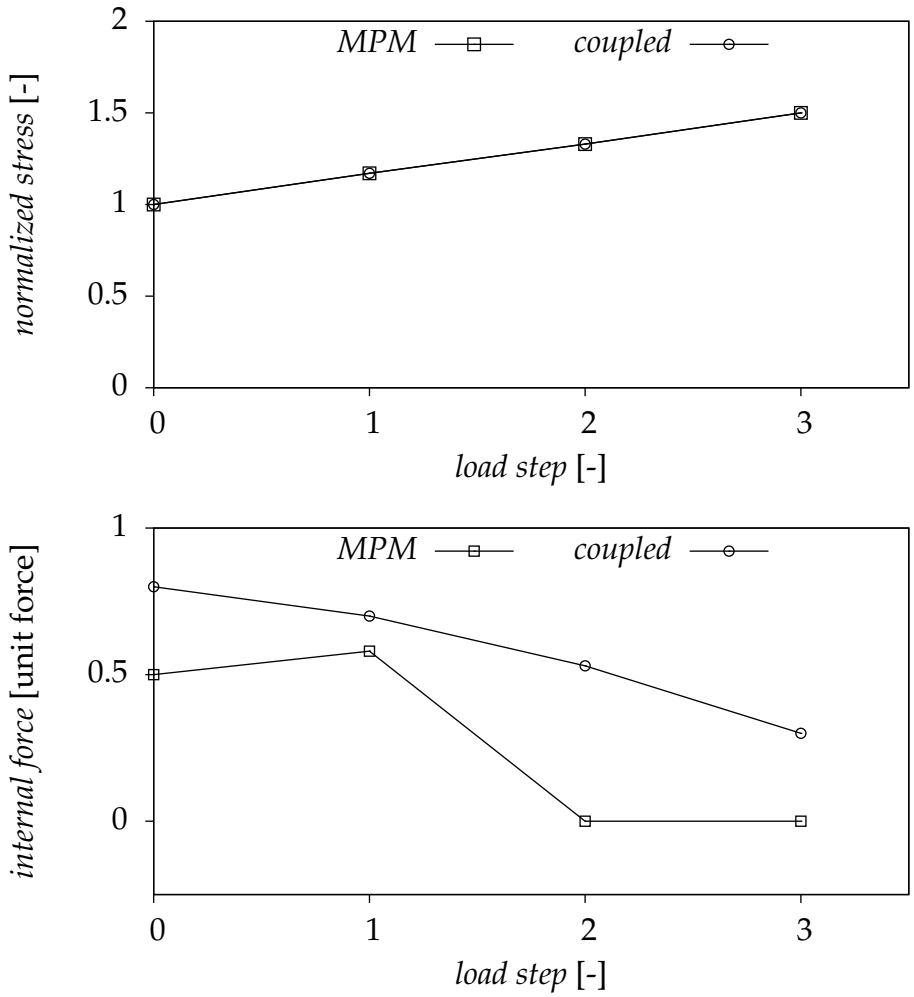

Figure 4.14: Variation of stresses (top) and internal force (bottom) for the two membrane approaches

variation of the internal force values as compared with York's approach. The internal force oscillation is independent of the stress variation, which is shown to be equal in this simple example as shown in Figure 4.14.

Considering the problem of the spring–mass system, Figure 4.15 shows that the proposed algorithm yields an axial stress solution, which better matches the analytical solution when compared to that obtained via York algorithm. The theoretical value of the vertical stress at the maximum deformation should be $4\,\mathrm{kPa}$. The stresses obtained by the coupled approach have a piecewise uniform stress variations about the analytical solution and shows virtually no spatial spurious stress distribution. On the other hand, York's approach predicts spurious variations in stress over the entire membrane strip. The banded stress pattern predicted by the proposed model is associated with the connection between the membrane and the computational (tetrahedral) mesh. As the membrane moves though space, the calculations for displacement are carried out on the computational grid as indicated previously. These displacements are then mapped from

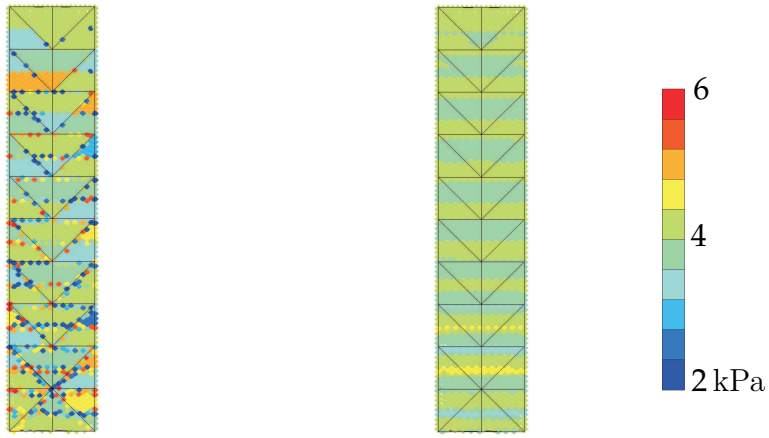

Figure 4.15: Vertical stress distribution in the membrane of spring–mass problem: (left) York's approach and (right) coupled FEM–MPM

the computational grid to the membrane nodes using the interpolation functions of the tetrahedral elements. The membrane stresses are then determined from the membrane displacement via the strain calculations. Had a finer tetrahedral mesh been used, the bands would have been narrower, but not necessarily eliminated.

4.4.3 Minimum required mass

In order to perform a solution within the MPM procedure, mass must be assigned for all particles. On the other hand, in most engineering applications, the mass of the membrane is very small and is often neglected. In the spring–mass problem the membrane has been given very small mass of about 1% of the oscillating mass. Nevertheless, checking the minimum required mass of each membrane approach to get the correct solution is investigated by changing the *mass ratio* SR. Three mass ratios have been considered (10^{-2}, 10^{-4} and 10^{-6}) for the oscillating mass problem by reducing the membrane mass and letting the number of particles constant.

Figure 4.16 clearly shows that York's solution starts to deviate from the analytical solution when reducing the membrane mass, whereas the other approach gives the correct solution for all considered mesh ratios. The deviation of the first approach can be interpreted by the non uniformity of the deformation along the spring as a consequence of poor stress prediction.

As stated before, increasing the number of material points reduces the inherent spurious stress variation in the MPM algorithm but does not eliminate it completely. On the other hand, this particular problem has an extreme mass difference between the oscillating mass and the spring mass. As a result, the solution quality is sensitive to noise in the internal force calculation. Returning back to the discretised momentum equation, both schemes have the same mass matrix and the gravity force vector but different internal force. As a suggested remedy for York's approach, the particles density must be increased more in order to improve the result quality.

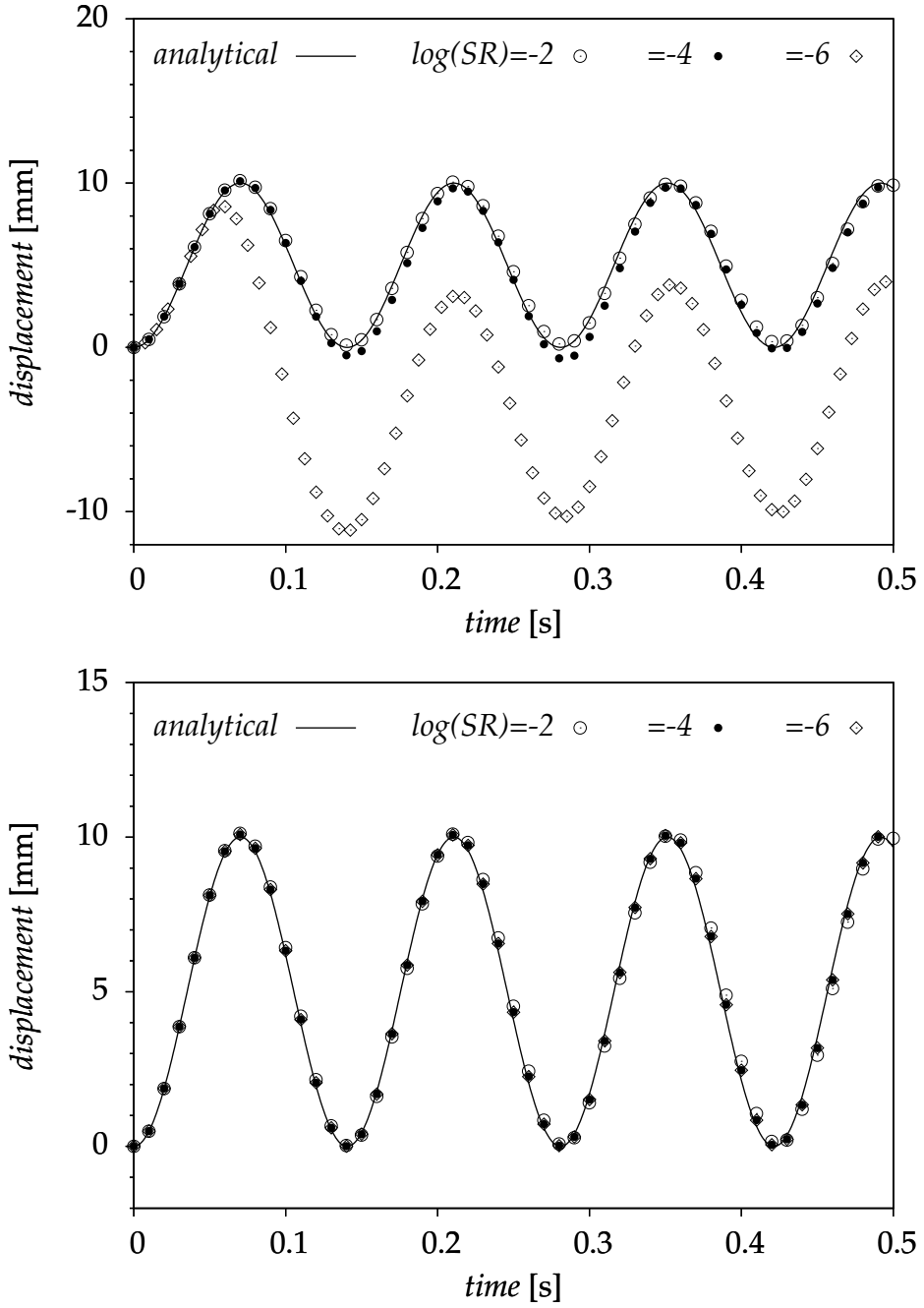

Figure 4.16: Sensitivity to the mass ratio: (top) York's approach and (bottom) coupled FEM–MPM

4.4.4 Sensitivity to transverse oscillation

Referring back to the single–degree–of freedom spring–mass system, the motion was only along the membrane direction as the angle θ between the applied load and the membrane direction is zero. The following example compares the solution obtained from each approach for the case of transverse oscillation. The representation of this problem, which is composed of two springs with equal initial length l_0 and stiffness k, attached to one mass m, is shown in Figure 4.17. A mass oscillates due to gravitational acceleration g in the transverse direction to the two springs as depicted in Figure 4.17. Owing to nonlinearity, the effective spring stiffness acting on the mass is a function of the mass location x. Applying Newton's second law yields

$$m\,g - 2\,k\,(l - l_0)\,\sin\theta = m\,\ddot{x} \tag{4.49}$$

where $\ddot{x}$ is the mass acceleration in x–direction and l is the deformed length. Assuming small angle theory, Equation 4.49 becomes

$$\ddot{x} = g - \frac{2k}{m}\left(1 - \frac{l_0}{\sqrt{l_0^2 + x^2}}\right) x. \tag{4.50}$$

To determine the out–of–plane displacement, the second–order non–linear ordinary differential equation was solved numerically, using the Runge–Kutta method together with the parameters used for the previous example.

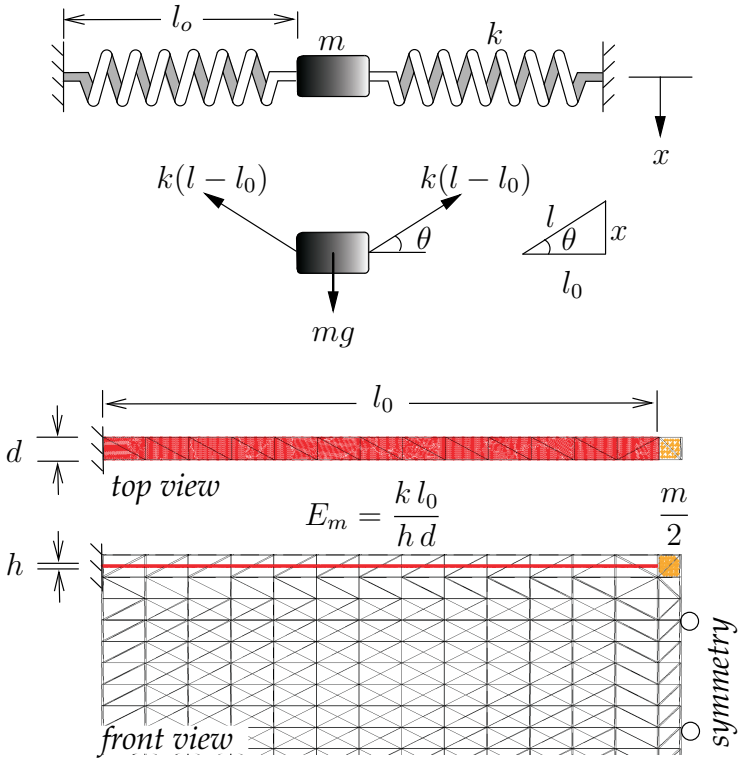

Figure 4.17: Laterally oscillating mass model and its MPM representation

Owing to symmetry, only one half of the problem is simulated with MPM. The spring with stiffness k is replaced by a membrane with modulus E_m and thickness h that give the equivalent stiffness. A solid material with mass m is used to simulate the oscillated mass, which has much bigger value when compared with the membrane mass. Thus wave propagation in the membrane can be ignored. The mesh discretisation using tetrahedral elements is illustrated in Figure 4.17, with the membrane being discretised with high mesh ratio of 26. Unlike for the uniaxial problem, the 1% mass added to the membrane was not enough to get stable results with the York procedure. Therefore, the membrane mass was increased to 5% of that of oscillating body. Providing that the maximum stretch in the spring is $0.175\,\mathrm{m}$, obtained from Equation 4.50 at the lowest location, produces a maximum strain evaluated from $\varepsilon = \ln(l/l_0)$ is 5.8%. Therefore, the tensile force is $58\,\mathrm{kN/m}$ calculated from the membrane stiffness times the developed strain, see Figure 4.17. For the numerical model, the stresses along the membrane were with a range of $58 - 60\,\mathrm{kN/m}$.

Figure 4.18 compares the analytical solution with that based on York's approach (Case 1). It is observed that the MPM solution predicts a stiffer behaviour when compared to the analytical solution. On the other hand, the coupled scheme shows a trend that is much closer to the close form solution. The coupled approach is less sensitive to the discretisation of the tetrahedral mesh. This is observed when analysing the same problem with different mesh discretisation. With reference to Figure 4.18 the solutions from both formulations are also shown for the case when the computational mesh is rotated $90°$ (Case 2). Whereas the FEM–MPM solution displays negligible sensitivity to the mesh rotation, the solution based on York's algorithm is shown to have increasing sensitivity as the time increases for the interval shown.

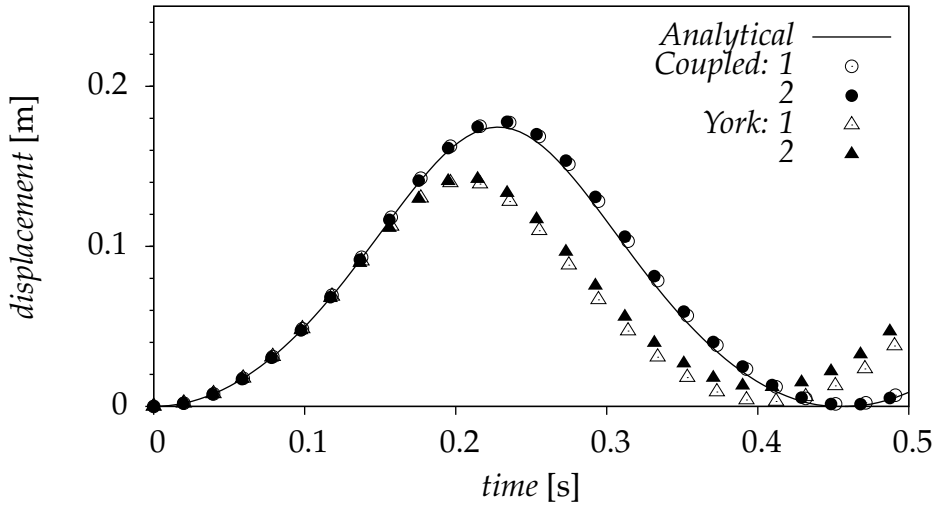

Figure 4.18: Displacement history of the laterally oscillating mass using the two membrane approaches

4.5 Considerations for geosynthetics simulation

Geosynthetics modelling is one of the most important applications of membrane in Geotechnique. They are used to reinforce soil or to be combined with filling material as a construction element; e.g., soil bags. For some applications, the thin material is expected to undergo large deflections and deformations before failure. Therefore, large deformation theory in the membrane formulation must be considered. In addition, the *textile* behaviour of geosynthetic materials implies sustaining the tensile forces but not compression. Hence, the constitutive model of the membrane should include a proper criteria to cut the compression stresses off. This is introduced in this section.

4.5.1 Large deformation membrane

In the case of large deformation analysis, the behaviour is no longer linear. The stiffness matrix, or the internal force in our explicit formulation, is based on a continuous deforming configuration. Since the body may undergo large displacements and large strains combined with nonlinear constitutive relations, an approximate solution can best be obtained by referring all variables to a previously calculated known equilibrium configuration. This permits linearising the equilibrium equation.

In practice, two formulations are used to tackle the large deformation problems: *total Lagrangian* and *updated Lagrangian* formulations [16]. In the total Lagrangian, or simply called *Lagrangian*, all static and kinematic variables are referred to the initial configuration, whereas the variables in the updated Lagrangian scheme are based on the configuration at the previous time step.

During large deformations cases, attention must be paid to correctly model the stress changes when finite material rotations occur. Therefore the constitutive relation must be established eliminating the influence of rigid material rotation by using a corotational coordinate system to describe stresses. The present membrane formulation includes rate objectivity as introduced in Equation 4.12. Furthermore, the integration weight of the finite element membrane mesh must be updated for the deformed configuration.

Numerical example: large deflection of a pre–stressed membrane The problem of large deflection of a pre–stressed membrane subjected to a lateral force presented by van Langen [178] for which analytical solution is available is repeated. Figure 4.19 shows a membrane fixed at both ends being subjected to a lateral force mg. The initial stress is $\hat{\sigma}_0$. Consequently, the force mg displaced downward in the direction x by a displacement u. Assuming the updated membrane stress per cross–sectional area and the length to be $\hat{\sigma}$ and l respectively, a relation between the external force can be constructed per unit depth in the form

$$mg = \frac{4\,\hat{\sigma}\,u}{l}. \tag{4.51}$$

Normalising the stresses and force with respect to the membrane stiffness, the stress rate $\dot{\hat{\sigma}}$ becomes simply $\dot{l}/l$. Integrating the stress rate equation with respect to time and

substituting Equation 4.51 into it yields

$$mg = 4\,\frac{u}{l}\left(\ln\frac{l}{l_0} + \hat{\sigma}_0\right). \tag{4.52}$$

This problem is modelled in MPM using the coupled FE–MP approach by adopting the mesh shown in Figure 4.19. The force mg is applied directly on the last particle as an external load, with gravity being excluded from the computation. The external force is increased gradually in a stepwise manner allowing quasi–static equilibrium to be obtained at each loading step; i.e., equilibrium between the external load and the internal stresses is reached. The comparison of solutions between Equation 4.52 and the MPM results is demonstrated in Figure 4.20. In this figure, the only difference between the MPM curves is updating the integration weight in Equation 4.21. Without considering large deformation formulation, the MPM result shows a considerable deviation from the closed–form solution.

4.5.2 Tensile membrane

Setting the bending moments of the structure to zero is justified when the structure has a very small flexural stiffness for instance such as for materials made from cloth. An absolutely flexible structure is not able to sustain compressive forces, therefore, these structures may resist the applied loads only in tension. Because of their geometry the membranes wrinkle easily when not in tension. This wrinkling has much influence on

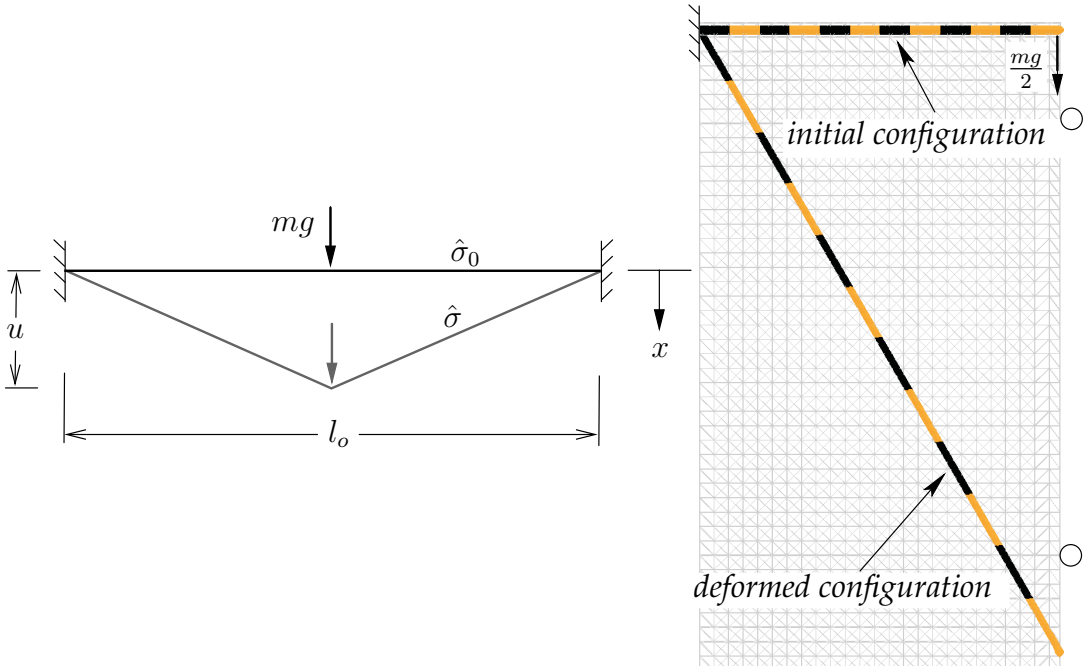

Figure 4.19: Pre–stressed membrane under large deflection: (left) physical model and (right) MPM representaion

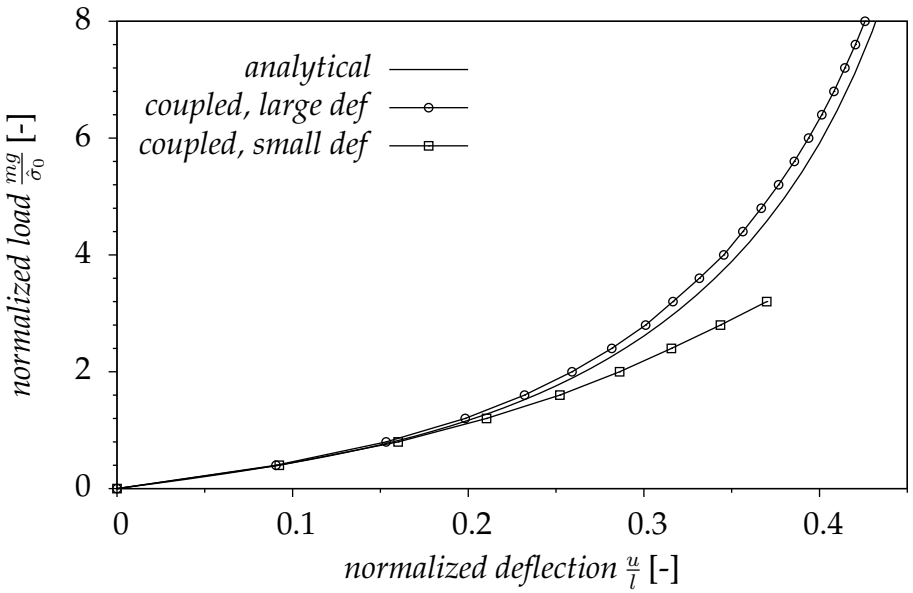

Figure 4.20: Load–deflection curve of a pre–stressed membrane

the stress state and the force transmission.

Fundamentally there are two approaches tackling the wrinkling problem in a membrane. In the first, the membrane is regarded as a thin shell with a very small, but finite flexural stiffness, whereas the second approach neglects the flexural stiffness and assumes the thin membrane to be capable of resisting only the in–plane tensile stresses, and the wrinkled surface is replaced with a smooth surface representing average deformations. This second approach is called the *tension field approach* [129] which is adopted in this thesis.

In the present study the folds and wrinkles in the membrane are not considered but rather a simplified version is implemented by correcting the principal stresses to be positive. By the same token, the principal stresses are adjusted by not allowing compression components. Hence, this formulation is implemented as a *compression cut–off* criterion. A similar technique is adopted for geomechanical applications in the commercial software PLAXIS [33]. Using the definition of the rotated stress tensor $\hat{\boldsymbol{\sigma}}$ in Equation 4.13, the principal stresses are given by the Mohr circle as

$$\hat{\sigma}_{I,\,II} = \frac{\hat{\sigma}_{11} + \hat{\sigma_{22}}}{2} \mp r_m, \tag{4.53}$$

where $\hat{\sigma}_I$ and $\hat{\sigma}_{II}$ are the major and minor principal in–plane membrane stresses in the rotated coordinates, and r_m is the radius of the Mohr circle defined as

$$r_m = \sqrt{\left(\frac{\hat{\sigma}_{11} - \hat{\sigma}_{22}}{2}\right)^2 + (\hat{\sigma}_{12})^2}. \tag{4.54}$$

The compression cut–off criterion requires positive signs for the principal stresses; i.e., both of them are in tension, otherwise a correction must be applied. A function f is in-

troduced such that the minor principal stress $\hat{\sigma}_{11}$ can not become less than zero; i.e.,

$$f = \frac{\hat{\sigma}_{11} + \hat{\sigma}_{22}}{2} - r_m. \tag{4.55}$$

If the value of the function f in Equation 4.55 becomes positive, no stress correction is required. Otherwise, correction should be done as follows [46]

$$\hat{\boldsymbol{\sigma}}_{\text{corrected}} = \hat{\boldsymbol{\sigma}} - \lambda\, f\left(\hat{\boldsymbol{\sigma}}\right) \hat{\boldsymbol{D}}\, \frac{\partial f}{\partial \hat{\boldsymbol{\sigma}}}, \tag{4.56}$$

with $\hat{\boldsymbol{\sigma}}_{\text{corrected}}$ being the corrected stress tensor of $\hat{\boldsymbol{\sigma}}$, $\hat{\boldsymbol{D}}$ is defined in Appendix D for linear elastic material, and λ is given by

$$\lambda^{-1} = \left(\frac{\partial f}{\partial \hat{\boldsymbol{\sigma}}}\right)^T \hat{\boldsymbol{D}} \left(\frac{\partial f}{\partial \hat{\boldsymbol{\sigma}}}\right), \tag{4.57}$$

which is reduced to $\lambda^{-1} = E_m$ in the case of zero Poisson's ratio. Differentiating Equation 4.55 with respect to $\hat{\boldsymbol{\sigma}}$ provides

$$\begin{aligned}
\frac{\partial f}{\partial \hat{\sigma}_{11}} &= \frac{1}{2} - \frac{\hat{\sigma}_{11} - \hat{\sigma}_{22}}{4\, r_m} \\
\frac{\partial f}{\partial \hat{\sigma}_{22}} &= \frac{1}{2} + \frac{\hat{\sigma}_{11} - \hat{\sigma}_{22}}{4\, r_m} \\
\frac{\partial f}{\partial \hat{\sigma}_{12}} &= -\frac{\hat{\sigma}_{12}}{4\, r_m}.
\end{aligned} \tag{4.58}$$

Back substitution of the Equations 4.55 and 4.58 into Equation 4.56 yields the components of the corrected stress vector $\hat{\boldsymbol{\sigma}}_{\text{corrected}}$; i.e.,

$$\begin{aligned}
\hat{\sigma}_{11,\,\text{corrected}} &= \frac{\hat{\sigma}_{11} + r_m}{2} + \frac{\left(\hat{\sigma}_{11}\right)^2 - \left(\hat{\sigma}_{22}\right)^2}{8\, r_m} \\
\hat{\sigma}_{22,\,\text{corrected}} &= \frac{\hat{\sigma}_{22} + r_m}{2} + \frac{\left(\hat{\sigma}_{11}\right)^2 - \left(\hat{\sigma}_{22}\right)^2}{8\, r_m} \\
\hat{\sigma}_{12,\,\text{corrected}} &= \frac{\hat{\sigma}_{12}\left(\hat{\sigma}_{11} + \hat{\sigma}_{22}\right)}{2\, r_m}.
\end{aligned} \tag{4.59}$$

The graphical representation of the stress correction corresponding to Equation 4.59, is depicted on Mohr circle in Figure 4.21. In this figure, the minor principal stress $\hat{\sigma}_{II}$ is assumed to be in compression and needs to be corrected by shifting it to zero. All related stress components are corrected accordingly.

Numerical example: hemispherical dome Several researchers have studied the construction of hemispherical domes being subjected to self weight or to an external traction; e.g. [75, 153]. In these studies, the two principal stresses of a hemispherical dome with uniform thickness are introduced. The first principal stress acts along the *meridian*

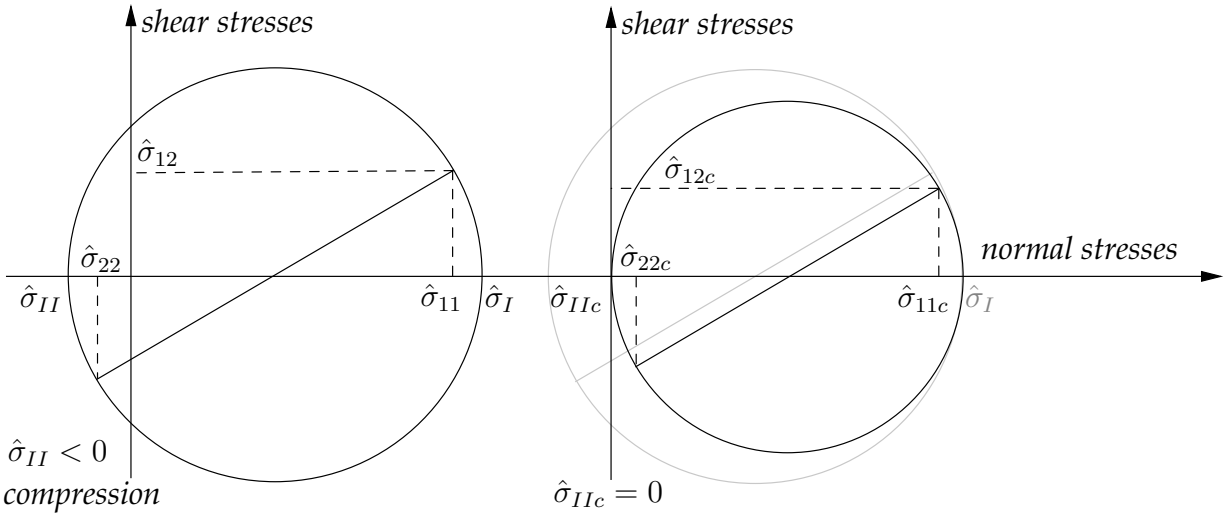

Figure 4.21: Compression cut–off criterion on Mohr circle: (left) before and (right) after correction

direction or the line of longitude arch, and is defined as

$$\hat{\sigma}_I = - \frac{\varrho_m \, g \, r}{1 + \cos \phi}, \tag{4.60}$$

with the other principal stress being introduced along the circumferential or *hoop direction* and is given by

$$\hat{\sigma}_{II} = - \left(\hat{\sigma}_I \, + \, \varrho_m \, g \, r \, \cos \phi \right), \tag{4.61}$$

in which $\varrho_m \, g$ is the unit weight of the membrane, whereas r and ϕ are the radius of the hemisphere and the polar angle measured from top point, respectively.

For small ϕ, near the crown of the dome, both principal stresses are compressive. As ϕ increases, however, the hoop stress $\hat{\sigma}_{II}$ changes sign and becomes tensile which occurs at $\phi \sim 52^\circ$ [75]. For the specific case where ϕ equals to 52°, the dome edge is neither in compression nor tension. This plane of zero hoop stresses is called the *neutral plane* similar to the neutral axis for beams. Two simulations are considered, the first without compression cut–off, and the second with the cut–off criterion being implemented.

The MPM modelling is carried out using one quarter of the hemispherical dome. Both tetrahedral mesh and the membrane discretisation with the mechanical properties are shown in Figure 4.22 where roller boundary conditions are imposed for the three orthogonal planes. Aiming for quasi–static solution, the final deformation and the principal stresses are illustrated in Figure 4.23. From this figure, the location where the principal stress $\hat{\sigma}_{II}$ becomes zero is checked to be at $\phi = 52^\circ$ which matches the analytical value. The analytical principal stresses at points A and B, see Figure 4.23, are obtained from Equations 4.60 and 4.61. Owing to the numerical singularity of the crown point, it is decided to shift point A slightly with an angle $\phi = 13^\circ$ from the very top point. Correspondingly the MPM results are achieved at these two locations and compared with the analytical results in Table 4.1.

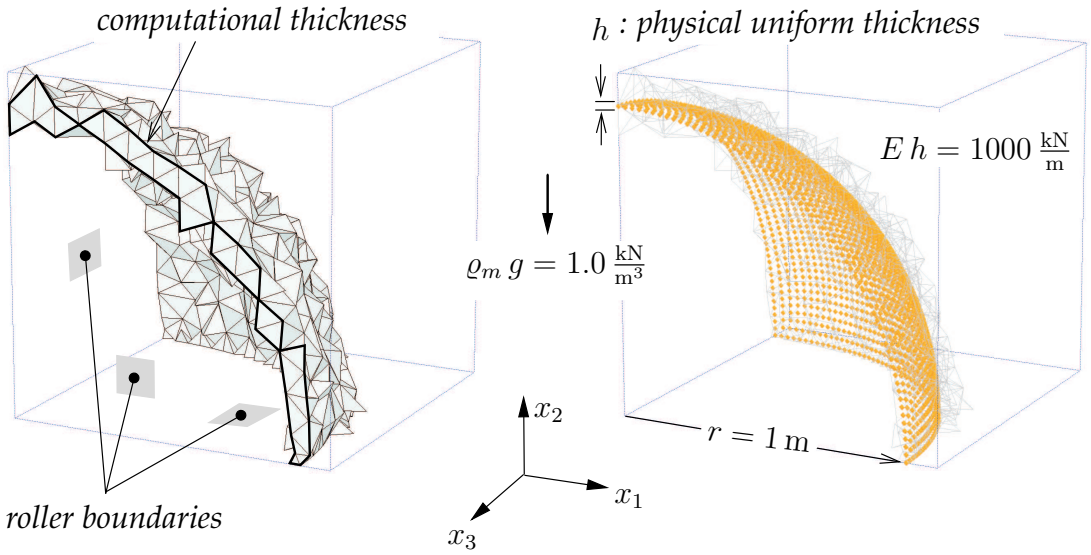

Figure 4.22: MPM discretisation of the hemispherical dome: (left) tetrahedral mesh discretisation and (right) particles discretisation

In both MPM membrane formulations, the forces are distributed over a wider area than the physical thickness h. As shown in Figure 4.22, the computational thickness of the membrane depends on the mesh size where the computation is achieved. For the hemispherical dome example, however, the smearing of the membrane does not have a big influence on the resolution of the results. The analysis of the hemispherical dome is repeated excluding the compression stiffness by applying the compression cut–off criterion presented earlier. Such a structure would collapse if it were made out of textile

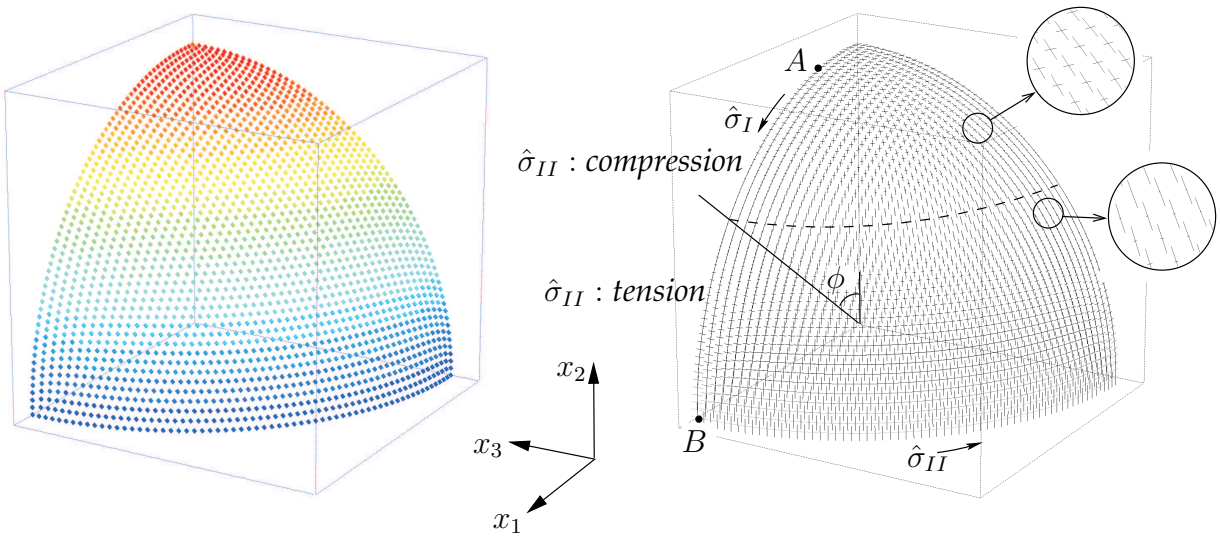

Figure 4.23: Coupled FEM–MPM results: (left) vertical displacement; blue colour is zero displacement with red is $-0.34\,\mathrm{mm}$, and (right) principal stresses

Table 4.1: Analytical and numerical results of the hemispherical dome

point	$\hat{\sigma}_I$		$\hat{\sigma}_{II}$	
	analytical	coupled	analytical	coupled
A	-0.51	-0.48	-0.47	-0.47
B	-1.0	-1.04	$+1.0$	$+1.05$

material. As a result, the final deformation shape of the membrane becomes flat as illustrated in Figure 4.24. It should be noted that the compression cut–off criterion does not count for the shape of wrinkles which is out of the scope of this research.

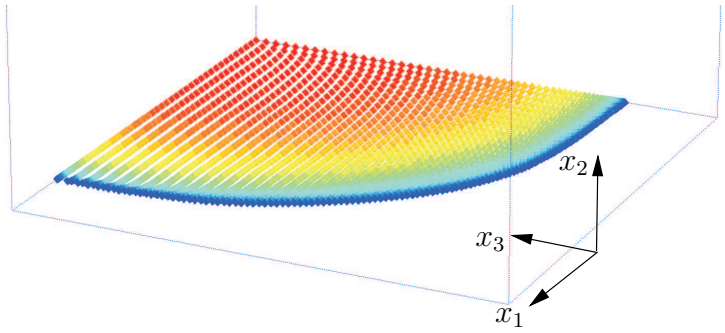

Figure 4.24: Vertical displacement of the hemispherical dome with compression cut–off criterion; blue colour is zero displacement and red is $-1.0\,\mathrm{m}$

4.6 Test study: geotextile–reinforced embankment

Geosynthetics materials are involved in most reinforcement of earth works. Soil slopes, retaining walls, roads and embankments are some applications that require some form of stabilisation including the use of geotextiles. To evaluate the effect of reinforcement numerically, various modelling techniques have been used. These range from the conventional methods derived from limit equilibrium analysis [148] to the continuum modelling based on constitutive relationships, and micro–mechanical modelling for the earth structures reinforced with geosynthetic [82].

The finite element method has the advantage over traditional analysis techniques that the displacements and stresses within the soil are coupled. Depending on the constitutive model, more realistic soil behaviour can be represented. Early parametric studies using large deformation finite element formulations on the effects of reinforcement on stability and deformations done by Rowe and Soderman [147] and Rowe et al. [149].

The test embankments of Almere in the Netherlands, which were constructed in 1979 have been back–calculated in many references; e.g., [178]. Two embankments were built on a soft clay deposit to measure the effect of geotextile reinforcement on stability as shown in Figure 4.25. One of them is reinforced with geotextile whilst the other served as a non–reinforced reference. After constructing the retaining bank on the subsoil, each

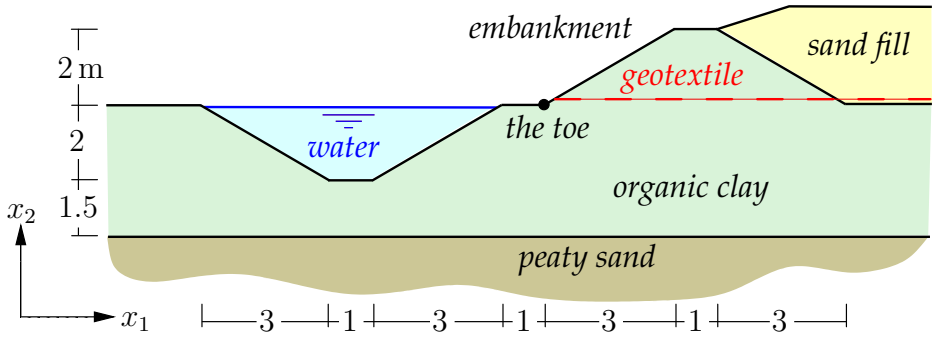

Figure 4.25: Almere test embankment reinforced with geotextile after van Langen [178]

embankment was loaded by hydraulic sand filling. At failure, the reinforced one had a sand height of $3\,\mathrm{m}$ while the non–reinforced failed at a height of $1.75\,\mathrm{m}$ [178].

4.6.1 Assumptions and material modelling

For the numerical model requirements, boundaries need to be established. The strong peaty sand layer underneath serves as a fixed bottom for the numerical model while the side boundaries are assumed rigid in the horizontal directions. The soil is simplified as an elastoplastic material with a Mohr–Coulomb failure criterion. The geotextile is treated as linear elastic with an axial stiffness of $1900\,\mathrm{kN/m}$. It is also assumed to be rough enough that failure would happen inside the soil.

The construction procedure was repeated such that the ditch was excavated in the clay layer while at the same time the retaining bank was made with the excavated clay. As next, the hydraulic fill with fully saturated sand was achieved. In this analysis, the embankment is constructed sufficiently quickly such that consolidation of the subsoil can be neglected. For the loose fill, the shear modulus is proportional to the pressure level, which is an average of a constant value in this study. The mechanical properties of the embankment and the filling sand are listed in Table 4.2 [178].

Table 4.2: Properties of the soils

parameter	symbol	clay	sand
saturated weight	γ_{sat} $[\mathrm{kN/m^3}]$	20	20
stiffness	E $[\mathrm{kN/m^2}]$	1043	4000
Poisson's ratio	ν $[-]$	0.49	0.35
cohesion	c $[\mathrm{kN/m^2}]$	10	1
friction angle	ϕ $[^\circ]$	0	32
dilatancy angle	ψ $[^\circ]$	0	2

4.6.2 Reference solution (Plaxis) vs MPM

Since the embankment test was achieved in–situ, little much detailed information is available about failure. Therefore, the finite element software (Plaxis 2D) including large deformation is considered as a reference solution for this study. A 6–noded triangular element for the plane–strain problem was adopted. Following the classical procedure of phase construction, the embankment is numerically built by having the subsoil layer with $K_0 = 1$ followed by second phase of removing the ditch and constructing the retaining bank. Finally, the loading phase is performed by gradually increasing the unit weight of the $3\,\mathrm{m}$ height of sand. The horizontal displacement of the toe point is recorded as a control point as shown in Figure 4.26 for the non–reinforced embankment. Figure 4.27 shows the mesh discretisation related to Plaxis model with the boundary conditions.

In MPM, the embankment problem is modelled using 4–noded tetrahedral elements with ten particles initially placed in each element. Here, the K_0 procedure is not considered. Instead, the gravity load of the retaining bank is applied in ten load steps. As the MPM procedure follows a dynamic formulation, some local damping has been added to obtain the quasi–static solution by reducing the kinetic energy equally over all degrees of freedom. After constructing the retaining bank, the gravity weight of the sand particles increased in stepwise manner with a step value of $2\,\mathrm{kN/m^3}$. As low order elements are adopted in the MPM, volumetric locking was expected especially for the clay with high value of Poisson's ratio. Therefore, a strain smoothening technique was applied to enhance the performance of the tetrahedral elements [89].

For the non–reinforced embankment, the load–displacement curve of the toe point shows very good prediction for the displacements. Similar to the non–reinforced embankment, the reinforced predicts good agreement between MPM and FEM as demonstrated in Figure 4.26. In this figure, the explicit nature of the MPM scheme is clearly illustrated in the deviation from the implicit FEM solution. Both solutions at the end of loading phase predict similar improvement due to reinforcement with maximum displacement value $0.56\,\mathrm{m}$ as shown in Figure 4.27, corresponding to $1.2\,\mathrm{m}$ for the non–reinforced embankment. However, the vertical stress distribution of both solutions show spurious stress variation at the failed integration points as seen in Figure 4.28. Nevertheless, the failure mechanism of both schemes match quite well after using the strain enhancement technique. For the developed forces in the geotextile, the MPM underpredict these forces slightly as shown in Figure 4.29, which can be attributed to the underpredicted MPM deformations, see Figure 4.26.

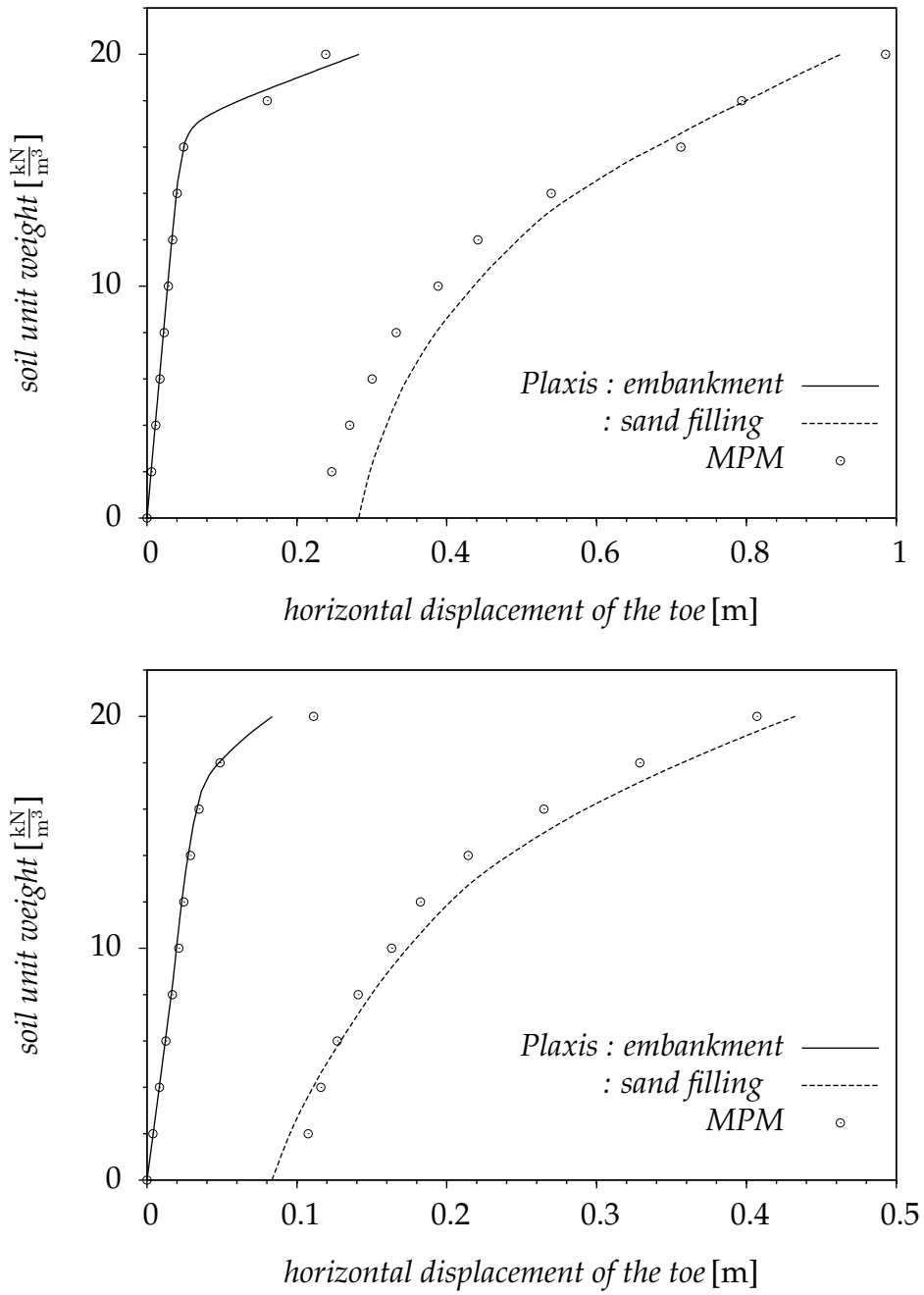

Figure 4.26: Horizontal displacement of the toe without reinforcement (top) and with reinforcement (bottom)

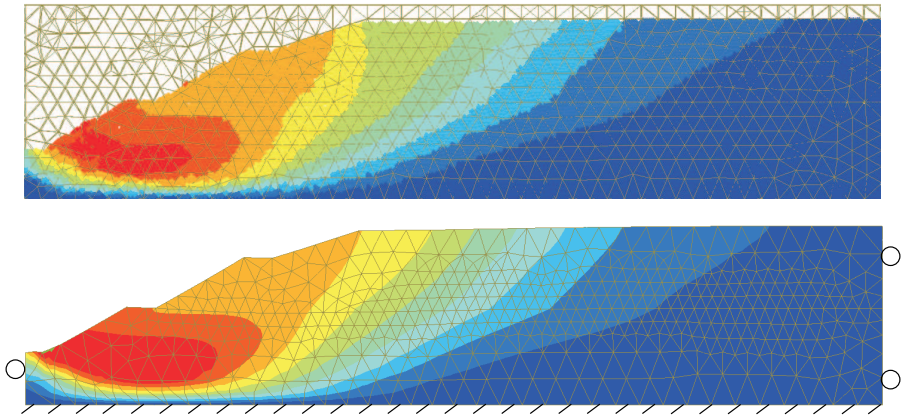

Figure 4.27: Total displacements of the reinforced embankment; blue colour is zero displacement and red is 0.56 m: (bottom) Plaxis 2D and (top) MPM

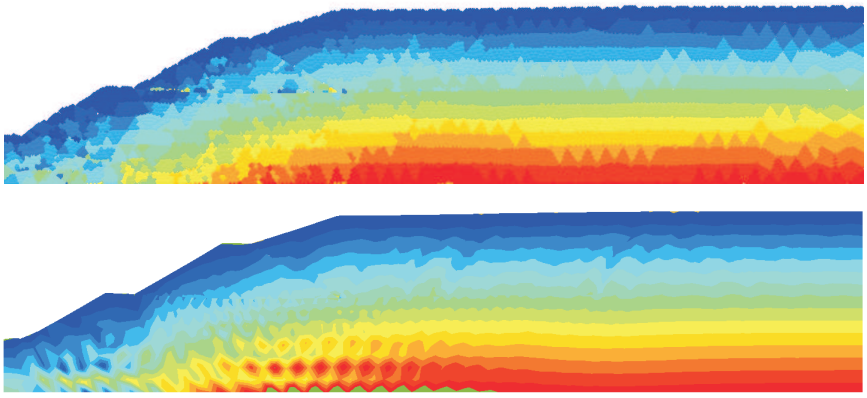

Figure 4.28: Vertical stress for the reinforced embankment; blue colour is zero stress and red is $-130\,\mathrm{kN/m^2}$: (bottom) Plaxis 2D and (top) MPM

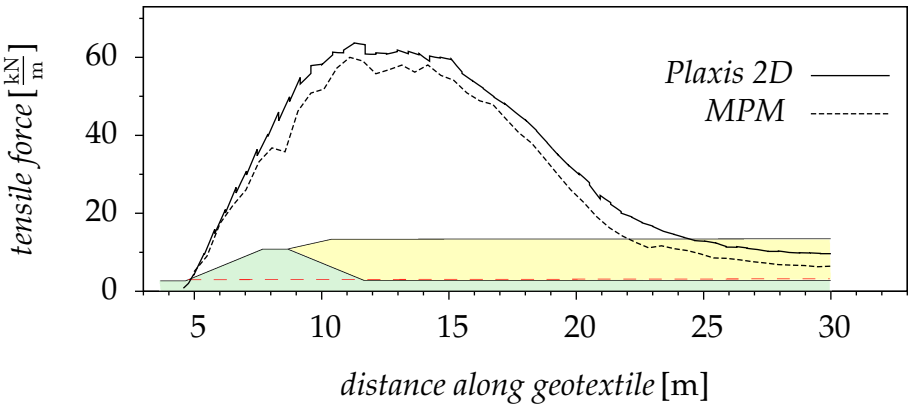

Figure 4.29: Comparison of the tensile forces along the geotextile

Chapter 5

Fluid modelling in MPM

For geomechanical applications involving geotextile and soil, it is most probable that water is present, especially for coastal works and soil improvement. The presence of water makes the numerical modelling of the problem more challenging in terms it is *incompressible* or near incompressible. This implies that density is approximately constant. The governing differential equations of fluid and some fundamental definitions are introduced in Section 5.1. Many numerical schemes dealing with fully incompressible material introduce some algorithm compressibility to avoid singularity in the discretised equations; e.g., the fractional step method (FSM) [134], which is briefly introduced in Section 5.2. This section details MPM modelling for nearly incompressible fluid and provides a one–dimensional validation case.

The property of incompressibility leads to explicit numerical algorithms that predict inaccurate solutions and are numerically unstable unless very small time steps are taken. It is essential to introduce enhancement procedures to get an acceptable pressure field. Although the nodal mixed discretisation (NMD) scheme, which is used for soil [2], helps improving the solution, a modified average nodal pressure (ANP) scheme [29] is required to get fairly smooth pressure field. The details regarding the enhancements, and the corresponding MPM computational algorithm with validation cases are presented in Section 5.3.

Although MPM replaces the continuum material with distinct material points, the contributions of material points is averaged within a computational cell. Therefore, there is no precise detection inside a cell for the location of the free surface when the cell is partially filled with points. An algorithm based on a continuous density field is developed in Section 5.4 and is then applied to the problem of water column collapse, for which experimental and numerical solutions exist. A related topic to the free surface detection, is the fluid–solid interaction modelling in MPM, which is elaborated in Section 5.5.

The geotube, which is normally used for shoreline protection, is a geomechanical application that combines geotextile with nearly incompressible material inside. The analytical solution [103] of a simplified geotube that disregards dynamic effects, deformable ground, and frictional material inside is compared with that of MPM. The predicted final configuration of the geotextile and the pressure distribution inside are illustrated in Section 5.6. Finally, some concluding remarks about the modelling of nearly incompressible fluid within the MPM framework are presented in Section 5.7.

5.1 Navier–Stokes equations of fluid dynamics

In fluid dynamics, the conservation equations that characterise the viscous fluid flow are called the *Navier–Stokes equations* in which mass, momentum, and energy are conserved over an infinitesimal volume of the fluid.

5.1.1 Basic definitions

A fluid, in general, is a material that continuously deforms under shear stress, whereas a solid does not. However, there are some solids that also deform continuously when the shear stress exceeds a certain limit value resulting in plastic deformations. The mechanics of fluid can be investigated in terms of the molecules interactions, however, the macroscopic scaling is more preferable for engineering applications where the properties are averaged and represented in terms of a continuum material model.

Stresses and constitutive equation for fluid When fluid undergoes deformation, it builds up stresses that consist of spherical and deviatoric components. Whereas the deviatoric stress vanishes at rest or in uniform fluid flow, solids can have deviatoric stress at rest. In other words, the fluid stresses are related to the strain rate and pressure by

$$\sigma_{ij} = -p\,\delta_{ij} + s_{ijkl}\,\dot{\varepsilon}_{kl}, \tag{5.1}$$

where σ_{ij} is the stress tensor, p is the pressure, δ_{ij} is the Kronecker delta, s_{ijkl} is a symmetric fourth–order tensor containing the viscous coefficients, and $\dot{\varepsilon}_{ij}$ is the strain rate tensor defined as

$$\dot{\varepsilon}_{ij} = \frac{1}{2}\left(\frac{\partial v_i}{\partial x_j} + \frac{\partial v_j}{\partial x_i}\right), \tag{5.2}$$

in which x_i and v_i are the location and velocity components, respectively. In the case of a linear isotropic fluid, Equation 5.1 reduces to the *Navier–Poisson law* for a Newtonian fluid [123]

$$\sigma_{ij} = -p\,\delta_{ij} + \lambda\,\dot{\varepsilon}_{kk}\,\delta_{ij} + 2\,\mu\,\dot{\varepsilon}_{ij}, \tag{5.3}$$

where λ and μ are independent parameters that characterise the viscosity of the fluid, and $\dot{\varepsilon}_{kk}$ denotes the volumetric strain rate. Introducing the strain rate tensor in terms of the deviatoric and spherical components, $\dot{\varepsilon}_{ij} = \dot{\varepsilon}'_{ij} + \dot{\varepsilon}_{kk}\,\delta_{ij}/3$ with $\dot{\varepsilon}'_{ij}$ being the deviatoric strain rate, Equation 5.3 yields

$$\sigma_{ij} = (-p + \kappa\,\dot{\varepsilon}_{kk})\,\delta_{ij} + 2\,\mu\,\dot{\varepsilon}'_{ij}, \tag{5.4}$$

with $\kappa = \lambda + \frac{2}{3}\,\mu$ is defined as the bulk viscosity. Equation 5.4 tells us that the thermodynamic pressure p equals the spherical component of the stress tensor $-\sigma_{kk}/3$ only when the term $\kappa\,\dot{\varepsilon}_{kk}$ vanishes.

Equation of state In thermodynamics the pressure in a fluid is assumed to be related to the density ϱ and the absolute temperature θ by an equation of state

$$\varrho = \varrho\,(p,\,\theta)\,. \tag{5.5}$$

In the case of barotropic flow, where the density depends only on pressure, the temperature is dropped from Equation 5.5.

5.1.2 Governing equations

We consider a system Ω in the flow domain with a closed control surface Γ, which coincides with a fixed control volume at certain time t_0. As the time advances to t, a difference between the two configurations is developed as illustrated in Figure 5.1 by the shaded areas. For such a flow the extensive thermodynamic property F, which may be mass, momentum, or energy, is written such that

$$F\,(t) = \int_{\Omega} \varrho\, f\,(\boldsymbol{x}, t)\; d\Omega, \tag{5.6}$$

with f being the corresponding intensive property. The material time derivative of F with respect to the moving system can be correlated to the fixed control volume by applying the *Reynolds transport theorem*, which states [123]

$$\frac{d}{dt}\int_{\Omega} F\;\varrho\, d\Omega = \int_{\Omega} \frac{\partial}{\partial t}\,(F\;\varrho)\; d\Omega + \int_{\Gamma} F\;\varrho\,\boldsymbol{v}\cdot\boldsymbol{n}\, d\Gamma, \tag{5.7}$$

where t is time, $\boldsymbol{v}$ is the velocity field, and $\boldsymbol{n}$ is the outward unit normal. Alternative to Equation 5.7, the motion can be described such that the control volume moves with

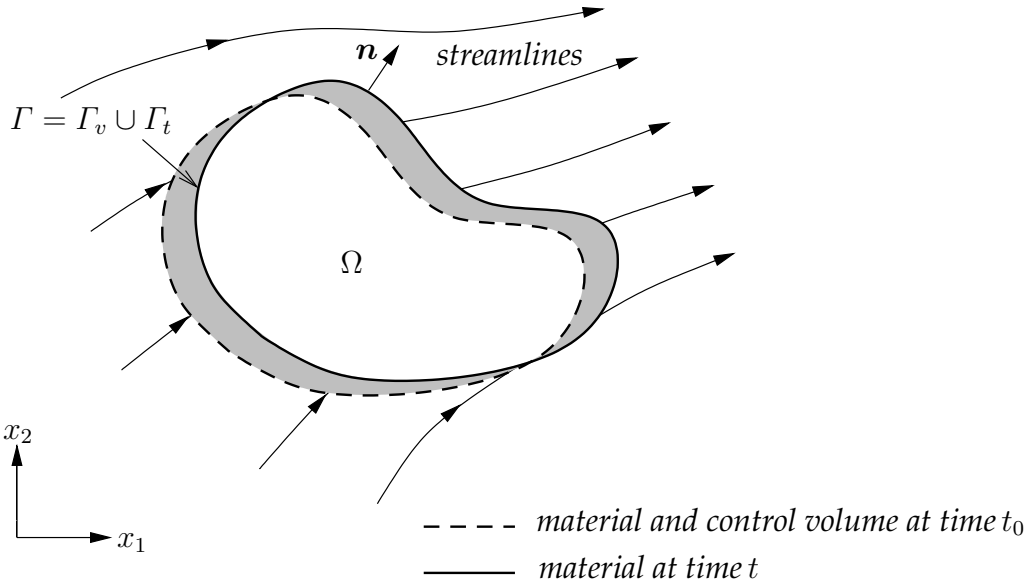

Figure 5.1: Finite control volume approach for fluid modelling

the fluid keeping same fluid particles in the same volume; i.e., the last term of Equation 5.7 is omitted. Therefore, the mass inside stays constant under any deformation that the volume might experience during the flow. As the mass conserved over the finite volume, the rate of change of fluid density ϱ is constant in the absence of source or sink and can be written mathematically as

$$\frac{1}{\varrho}\frac{d\varrho}{dt} + \frac{\partial v_i}{\partial x_i} = 0, \tag{5.8}$$

which represents the continuity equation. Applying Newton's second law, we obtain

$$\varrho\,\frac{dv_i}{dt} = \frac{\partial \sigma_{ij}}{\partial x_j} + \varrho\, g_i, \tag{5.9}$$

where σ_{ij} is the stress tensor defined by Equation 5.4, and ϱg_i is the gravitational force vector. For the sake of completeness, the conservation of energy equation supplements the necessary balance between the total energy per unit mass r and the energy dissipation due to internal stresses. Neglecting the conductive heat flux and the heat generated, we have

$$\varrho\,\frac{dr}{dt} = \tau_{ij}\frac{\partial v_i}{\partial x_j} - p\frac{\partial v_i}{\partial x_i} + \varrho\, g_i\, v_i. \tag{5.10}$$

where the stress tensor $\sigma_{ij} = \tau_{ij} - \delta_{ij}\, p$ is decomposed into isotropic and deviatoric part τ_{ij}. In previous equations, d denotes the material time derivative, which reduces to be the partial time derivative ∂ in the case of the considered Lagrangian formulation. A close look at the *Navier–Stokes equations* (Equations 5.8, 5.9 and 5.10) for a viscous fluid shows no difference from the conservation equations already shown in Chapter 3 for solid continuum.

5.1.3 Initial and boundary conditions

In order to have a unique solution for the system of equations, proper initial condition and boundary conditions must be provided. Since only first derivatives of time are present in Equation 5.9, it is sufficient to prescribe the initial velocity and pressure fields at t_0 as

$$v_i\,(\boldsymbol{x}, t_0) = V_{0i} \quad \text{and} \quad p\,(\boldsymbol{x}, t_0) = p_0, \tag{5.11}$$

where V_{0i} and p_0 are the initial fields of velocity and pressure, respectively, specified for the entire domain. As the boundary conditions provide physical constraints associated to the problem type, they are derived based on the conservative principles. Apart from a phase change boundary, we have the following common kinds of boundary conditions:

Solid wall boundary Depending on the fluid viscosity, a *no–slip* or *slip* condition can be applied along a solid wall [154]. The first can be applied for fluids with large viscosity

values in the form

$$v_i(\boldsymbol{x}, t) = 0. \tag{5.12}$$

For fluids with negligible viscosity, we only enforce no wall penetration by applying roller boundary in the following condition

$$v_i(\boldsymbol{x}, t)\ n_i = 0, \tag{5.13}$$

where n_i is the outward unit normal to the boundary $\Gamma_v(t)$.

In and outflow boundary The inflow and outflow boundary conditions are applied when the flow domain is truncated. Therefore, the prescribed velocity at the boundary Γ_v is written as

$$v_i(\boldsymbol{x}, t) = V_i(t) \qquad \text{on} \quad \Gamma_v(t), \tag{5.14}$$

in which V_i is the prescribed velocity on part of the boundary Γ_v.

Free surface The interface between a liquid and a gas phase is referred to as a *free boundary*, whereas the *moving boundary* refers to an interface between phases of comparable densities such as solid–liquid or boundary between two different liquids [104].

So far, all previous conditions are related to the momentum equation by specifying kinematic conditions on the boundary Γ_v. As next, the free surface condition along the interface Γ_t is derived from two conditions. The *kinematic continuity* which implies that there is no flow through the surface as

$$\frac{\partial F_s}{\partial t} + v_j \frac{\partial F_s}{\partial x_j} = 0, \tag{5.15}$$

with F_s being the function of the free surface that simply ensures no mass transfer across the boundary. The second condition is the *dynamic free surface condition* which states that the stress is continuous across the interface. In general, this condition can be interpreted mathematically for any surface traction as

$$\sigma_{ij}(\boldsymbol{x}, t)\, n_j = \boldsymbol{t}_i(\boldsymbol{x}, t), \tag{5.16}$$

where $\boldsymbol{t}_i(\boldsymbol{x}, t)$ denotes the surface traction vector and n_i is the outward unit normal vector of the free surface. In the absence of surface tension and setting the standard atmospheric pressure gauge to zero, this condition is reduced to

$$\sigma_{ij}(\boldsymbol{x}, t)\, n_j = 0. \tag{5.17}$$

5.2 Fully and nearly incompressible fluid modelling

The solution methods change markedly for compressible and incompressible fluids. Although there might be very little compressibility of the fluid, the mathematical nature of the considered problem changes. In this section, the description of each category is described mathematically with possible numerical techniques to treat each. Finally, the aim is to approximate the fully incompressible fluid to nearly incompressible where the MPM algorithm can be applied. This approximation is normally associated with numerical difficulties, which is mitigated here.

5.2.1 Fully incompressible fluid flow

Although fully incompressible fluid, $\varrho = \text{constant}$, in reality does not exist, the effect of compressibility is negligible in liquids and even in gases with low speed. For a fully incompressible viscous flow, one can rewrite the governing momentum equation 5.9 including the constitutive equation 5.4 in the form

$$\varrho \frac{dv_i}{dt} = 2\,\mu \frac{\partial \dot{\varepsilon}'_{ij}}{\partial x_j} - \frac{\partial p}{\partial x_i} + \varrho\, g_i, \tag{5.18}$$

with $\kappa\, \dot{\varepsilon}_{kk}$ being zero, which is combined with the continuity equation 5.8 that provides the incompressibility constraint; i.e.,

$$\frac{1}{\varrho}\frac{d\varrho}{dt} = 0. \tag{5.19}$$

By adopting a spatial discretisation scheme, Equations 5.18 and 5.19 yield a system of equations for steady–state of the form [99]

$$\begin{bmatrix} \boldsymbol{\mathcal{K}} & \boldsymbol{\mathcal{G}} \\ \boldsymbol{\mathcal{G}}^T & \mathbf{0} \end{bmatrix} \begin{bmatrix} \tilde{\boldsymbol{v}} \\ \tilde{\boldsymbol{p}} \end{bmatrix} = \begin{bmatrix} \tilde{\boldsymbol{g}} \\ \mathbf{0} \end{bmatrix} \tag{5.20}$$

in which $\boldsymbol{\mathcal{K}}$ and $\boldsymbol{\mathcal{G}}$ are square matrices. The vectors $\tilde{\boldsymbol{v}}$, $\tilde{\boldsymbol{p}}$, and $\tilde{\boldsymbol{g}}$, written bold, represent the velocity, pressure, and body forces at grid nodes. To avoid introducing too many symbols in Equation 5.20 and in this section, similar notation is used for the continuous and discrete variables; i.e., the symbol ($\tilde{}$) is dropped and the context signals the nature of the variable.

Care must be taken to avoid singularity in Equation 5.20 and to satisfy the Babuška–Brezzi (BB) condition [202], some numerical techniques have been developed. For example, the velocity and pressure can be interpolated using two different interpolation functions as will be addressed in this chapter. An alternative procedure is to introduce some *stabilisation technique*. Stabilisation circumvents the singularity of Equation 5.20 by replacing the zero matrix on the diagonal with a non–zero matrix that can be correlated to physics or other means [99, 202]. One of the most popular schemes to stabilise the governing equation is based on operator splitting.

Operator splitting involves breaking the momentum equation into two components:

one characterised by velocity $\boldsymbol{v}^*$ that corresponds to deviatoric stresses; and the second by velocity $\boldsymbol{v}^c$ that is a velocity corrector and is associated with the pressure field. In other words the velocity at time t^{n+1} is represented by

$$\boldsymbol{v}^{n+1} = \boldsymbol{v}^* + \boldsymbol{v}^c, \tag{5.21}$$

where the superscript n denotes a step counter. An iterative procedure can be established to get the sought solution $\boldsymbol{v}^{n+1}$ which satisfying the incompressibility constraint. Numerous versions for operator splitting are described in the literature, with the *fractional step method* (FSM) [134, 135] being the most popular. FSM introduces some algorithmic compressibility into the transient relaxation as a means for obtaining a steady–state solution for which the incompressibility constraint, $\boldsymbol{\nabla} \cdot \boldsymbol{v} = 0$, is satisfied exactly. This technique allows velocity and pressure to be interpolated with the same order [202]. The FSM procedure can be formulated in Eulerian description, for a unit density fluid, according to three basic steps [134].

Step one Remove the pressure term completely from the momentum equation to obtain an intermediate velocity field $\boldsymbol{v}^*$ corresponding to the deviatoric components

$$\frac{\boldsymbol{v}^* - \boldsymbol{v}^n}{\Delta t} = (-\boldsymbol{v} \cdot \boldsymbol{\nabla}\boldsymbol{v} + \boldsymbol{\nabla} \cdot \boldsymbol{\tau})^n + H.O.T, \tag{5.22}$$

where the body forces are not considered here and the higher order terms on the right are obtained from the Taylor series and works as a convection stabilising operator.

Step two Recover the actual velocity $\boldsymbol{v}^{n+1}$ from the correction step that counts for the pressure update; i.e.,

$$\frac{\boldsymbol{v}^{n+1} - \boldsymbol{v}^*}{\Delta t} = -\boldsymbol{\nabla} p^{n+\vartheta_2} + H.O.T, \tag{5.23}$$

in which the parameter $(0 \leq \vartheta_2 \leq 1)$ is to switch between fully explicit and semi–implicit scheme. In fact this step is the third step as the updated pressure $p^{n+\vartheta_2}$ is unknown yet. It is obtained from the following step.

Step three Solve the conservation of mass equation by introducing compressibility to the fluid such that

$$\frac{1}{\beta^2} \frac{p^{n+1} - p^n}{\Delta t} = -\boldsymbol{\nabla} \cdot \boldsymbol{v}^{n+\vartheta_1}, \tag{5.24}$$

where β is the compressible wave speed [135], while the updated velocity $\boldsymbol{v}^{n+\vartheta_1}$ is obtained from the combination of the old and the new velocity vector; i.e.,

$$\boldsymbol{v}^{n+\vartheta_1} = (1 - \vartheta_1)\ \boldsymbol{v}^n + \vartheta_1 \left(\boldsymbol{v}^* - \Delta t\, \boldsymbol{\nabla} p^{n+\vartheta_2} + H.O.T \right), \tag{5.25}$$

in which the parameter $(0.5 < \vartheta_1 \leq 1.0)$ controls the contribution of the stabilisation term that is introduced by the pressure gradient $\boldsymbol{\nabla} p$. Repeating the process of the three steps

iteratively, the velocity field converges to the steady–state solution. For unsteady problems, a dual time stepping algorithm can be employed where a pseudo time step is used for convergence within the real time step loop [133, 137]. The key in all numerical schemes dealing with incompressible fluid is to introduce a non–zero term in the diagonal of Equation 5.20. Using a slight compressibility in the fluid and equal interpolation for velocity and pressure introduces a pressure derivative in the continuity equation 5.19 which makes the simple explicit time stepping methods applicable.

5.2.2 MPM for fluid modelling

The particle–in–cell (PIC) method is an early version of MPM, which was dedicated for fluid mechanics problems late fifties [73]. The reader is refereed to Chapter 2 for more details about the MPM applications into problems involving fluid modelling.

Most of the research carried out in MPM, which adopts matrix free algorithms, are based on explicit time integration that is conditionally stable [39, 166, 169, 189]. A thorough investigation examining a single–degree of freedom tension bar for different integration schemes concludes that even the schemes that are supposed to be unconditionally stable have restricted time step size [2]. Hence, developing an iterative scheme; e.g. FSM, for the nearly incompressible fluid in MPM is not efficient if it is combined with the explicit time step for solids. Nevertheless, the success of modelling two–phase process dealing with water and soil has demonstrated that good quality predictions of pressure and flow field of water are possible with explicit schemes that incorporate enhancement [90, 162]. The next sections develops an MPM algorithm for *near* incompressible fluid, which is simply referred to compressible fluid.

5.2.3 Compressible fluid flow

As mentioned earlier, having fully incompressible fluid causes numerical instability. In addition solving fully incompressible fluid using an explicit scheme is not possible as the time step size simply becomes zero. Therefore, assigning small compressibility to the fluid is important. The density change, as a result of elastic deformation, is related to the pressure change via

$$\frac{\partial \varrho}{\partial t} = \frac{1}{{c_p}^2} \frac{\partial p}{\partial t}, \tag{5.26}$$

where $c_p = \sqrt{K_f/\varrho}$ is the acoustic wave speed with K_f being the elastic bulk modulus of the fluid. For nearly incompressible fluid during isothermal process the pressure–density correlation might takes the form [105]

$$\frac{p}{p_{\text{ref}}} = \left(\frac{\varrho}{\varrho_{\text{ref}}}\right)^{\varkappa} - 1, \tag{5.27}$$

where the subscript (ref) indicates reference values and $\varkappa$ is a material parameter. More sophisticated relationships can be established, although these need more parameters to calibrate [156]. Equation 5.27, can be replaced by a linear formula for relatively small range of pressure in such a way

$$p = p_{\mathrm{ref}} - K_f\, \varepsilon_v, \tag{5.28}$$

where ε_v is the volumetric strain and p_{ref} is the reference pressure. Given the Equations 5.26; and 5.28; and Equation 5.9 with proper boundary and initial conditions, the initial value problem is solvable using explicit scheme.

5.2.4 Discretised form of momentum equation

The fluid domain described by the governing equations is discretised here using suitable form for the adopted numerical scheme. The continuous equation is first represented in a *strong form* and is then transformed into the *weak form* using the principle of virtual work. During this procedure the traction boundary condition formulated in Equation 5.16 is introduced; i.e.,

$$\int_{\Omega} \delta v_i\, \varrho\, \frac{dv_i}{dt}\, d\Omega = \int_{\Gamma_t} \delta v_i\, t_i\, d\Gamma + \int_{\Omega} \delta v_i\, \varrho\, g_i\, d\Omega - \int_{\Omega} \delta\dot{\varepsilon}_{ij}\, \sigma_{ij}\, d\Omega, \tag{5.29}$$

where δv_i is a test function. Following Galerkin's procedure, this weak representation of the momentum equation is discretised by choosing an approximation to the solution via finite elements. Finally, the discrete set of equations over all elements is swept over the entire domain by the assemblage procedure. Referring back to Chapter 3 for details, the final form of the discrete momentum equation is

$$\boldsymbol{M}\boldsymbol{a} = \boldsymbol{F}^{\mathrm{ext}} - \boldsymbol{F}^{\mathrm{int}}, \tag{5.30}$$

in which $\boldsymbol{F}^{\mathrm{ext}}$ is the vector of external forces composed of the gravity force and the surface traction, $\boldsymbol{F}^{\mathrm{int}}$ is the internal force vector due to internal stresses, $\boldsymbol{M}$ is the lumped mass matrix, and $\boldsymbol{a}$ denotes the acceleration vector, where

$$\boldsymbol{M} = \sum_{p=1}^{n_p} |\boldsymbol{J}_p|\, \varrho_p\, \boldsymbol{N}\left(\boldsymbol{\xi}_p\right)\, w_p,$$

$$\boldsymbol{F}^{\mathrm{ext}} = \sum_{p=1}^{n_p} |\boldsymbol{J}_p|\, \varrho_p\, \boldsymbol{N}^T\left(\boldsymbol{\xi}_p\right)\, \boldsymbol{g}\, w_p + \sum_{b=1}^{n_b} |\boldsymbol{J}_b|\, \boldsymbol{N}^T\left(\boldsymbol{\xi}_b\right)\, \boldsymbol{t}\left(\boldsymbol{x}_b, t\right)\, w_b,$$

$$\boldsymbol{F}^{\mathrm{int}} = \sum_{p=1}^{n_p} |\boldsymbol{J}_p|\, \boldsymbol{B}_p^T\, \boldsymbol{\sigma}_p\, w_p,$$

where $|\boldsymbol{J}_p|$, $\boldsymbol{N}$, and w_p are the determinant of the Jacobian matrix defined in Appendix A, the interpolation functions, and the integration weight of particle p, respectively. While

n_p is the total number of particles, n_b is the number of boundary particles where the external force is applied, see Chapter 3 for more details.

Equation 5.30 needs to be integrated in time. The explicit Euler forward integration scheme is applied to get the velocity field followed by Euler backward for the velocity integration to update the material points location. The critical time step size Δt_{crt} is obtained from the *Courant–Friedrichs–Lewy* stability condition to be equal to or less than the minimum time step Δt_e of each element e such that

$$\triangle\, t_e = \frac{l_e}{c_p} \quad \text{with} \quad c_p = \sqrt{\frac{K_f}{\varrho}}, \tag{5.31}$$

where l_e is the characteristic length of element e. For all cases considered in this chapter, the critical time step is multiplied by a factor with a value of $0.5 - 0.9$ to avoid instability in the numerical scheme. A problem associated with this scheme, however, is that the time step is limited by the elastic wave speed in the fluid, which gives a very small time step as the bulk modulus increases.

5.2.5 MPM solution procedure

The MPM solution procedure for the nearly incompressible fluid starts with the initialisation of the material points. Where the continuous volume is replaced by discontinuous quantities constant in a subregion represented by the material points; i.e.,

$$\int_{\Omega} \varrho\, \chi\, d\Omega \simeq \sum_{p} \chi_p\, m_p, \tag{5.32}$$

where m_p is the mass of the material point p with χ_p being the mass specific quantity represented at p. After initialising the lumped mass matrix $\boldsymbol{M}$, the external $\boldsymbol{F}^{\text{ext}}$ and internal $\boldsymbol{F}^{\text{int}}$ force vectors in Equation 5.30, the acceleration can be obtained directly as the solution of this equation becomes trivial; i.e.,

$$\boldsymbol{a}^n = \boldsymbol{M}^{n,-1} \left(\boldsymbol{F}^{\text{ext}} - \boldsymbol{F}^{\text{int}}\right)^n, \tag{5.33}$$

which is integrated explicitly in time accordingly to get the updated particle velocity $\boldsymbol{v}_p^{n+1}$ in the form

$$\boldsymbol{v}_p^{n+1} = \boldsymbol{v}_p^n + \sum_i \Delta t\, N_{i,p}\, \boldsymbol{a}_i^n, \tag{5.34}$$

where the summation index i varies from 1 to the number of nodes per element and $N_{i,p}$ is the shape function of node i evaluated at the location of the particle p. The updated nodal velocity $\boldsymbol{v}^{n+1}$ of the entire field yields

$$\boldsymbol{M}^n \boldsymbol{v}^{n+1} = \sum_{p=1}^{n_p} m_p\, \boldsymbol{N}_p^T\, \boldsymbol{v}_p^{n+1}, \tag{5.35}$$

in which m_p is the mass of the material point p and n_p is the total number of particles. Subsequently, the pressure change due to the spatial velocity variation can be achieved from Equation 5.28 with a simplified linear pressure–density relationship such that

$$p^{n+1} = p^n - K_f \, \Delta\varepsilon_v^{n+1}, \tag{5.36}$$

where $\Delta\varepsilon_v^{n+1} = \Delta t \, \dot{\varepsilon}_{ii}$ is the volumetric strain increment. The constitutive model of the fluid is then applied to get the updated stress field $\boldsymbol{\sigma}^{n+1}$.

The incremental displacement and accordingly the position of the fluid particles are updated from the velocity field, which is obtained from

$$\boldsymbol{u}_p^{n+1} = \boldsymbol{u}_p^n + \sum_i \Delta t \, N_{i,p} \, \boldsymbol{v}_i^{n+1}, \tag{5.37}$$

where $\boldsymbol{u}_p^{n+1}$ contains the total displacements of the fluid particle p at the end of the time step. Keeping in mind that the particle position is updated according to the incremental displacement obtained from the last term in Equation 5.37.

5.2.6 Validation example: plane Poiseuille flow

Plane Poiseuille flow is a flow between two parallel stationary infinite plates separated by a fixed distance h. The initially stationary incompressible viscous fluid is driven by a force F which in turn induces a parallel flow in the horizontal direction with no vertical components; i.e., the flow is laminar. Ignoring the gravity effect, the time–dependent solution [112] along the vertical axis x_2 is

$$v\left(x_2, t\right) = \frac{\varrho \, F}{2\mu} x_2 \left(x_2 - h\right) + \sum_{n=0}^{\infty} \frac{4 \, \varrho \, F \, h^2}{\mu \pi^3 \left(2n+1\right)^3} \, \sin\left(\frac{\pi x_2}{h} \left(2n+1\right)\right) \exp\left(-\frac{\left(2n+1\right)^2 \pi^2 \mu}{\varrho \, h^2} \, t\right). \tag{5.38}$$

For the sake of testing the algorithm to capture the real time behaviour, this problem is modelled with the present MPM formulation with no update of the particle locations. The $5\,\mathrm{m}$ length of the plates has been taken long enough relative to the $1\,\mathrm{m}$ apart plates to reduce the corner effect. Slight compressibility has been introduced to the unit density fluid $K_f = 20\,\mathrm{GPa}$ with $\mu = 1\,\mathrm{Pa.s}$, and a pressure gradients $F = -8\,\mathrm{kPa/m}$ is imposed as a driving force. The reason for using large value for the bulk modulus is to approach the fully–incompressible fluid solution in Equation 5.38. Figure 5.2 shows that MPM results matches the series solution quite well. The mesh related to the problem with the boundary conditions is shown in Figure 5.3. In the figure, the pressure contour shows some non–uniformity at the entrance and exist sections which can be attributed to the effect of corners. However, the pressure distribution along the middle horizontal plane shows a near linear relationship.

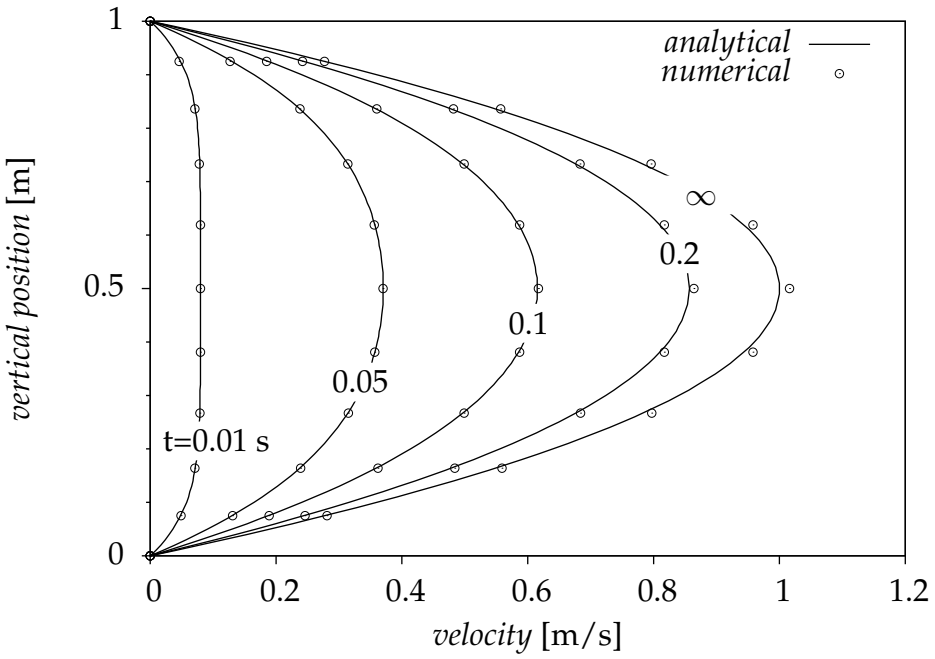

Figure 5.2: Comparison of analytical and MPM solution for the Poiseuille flow

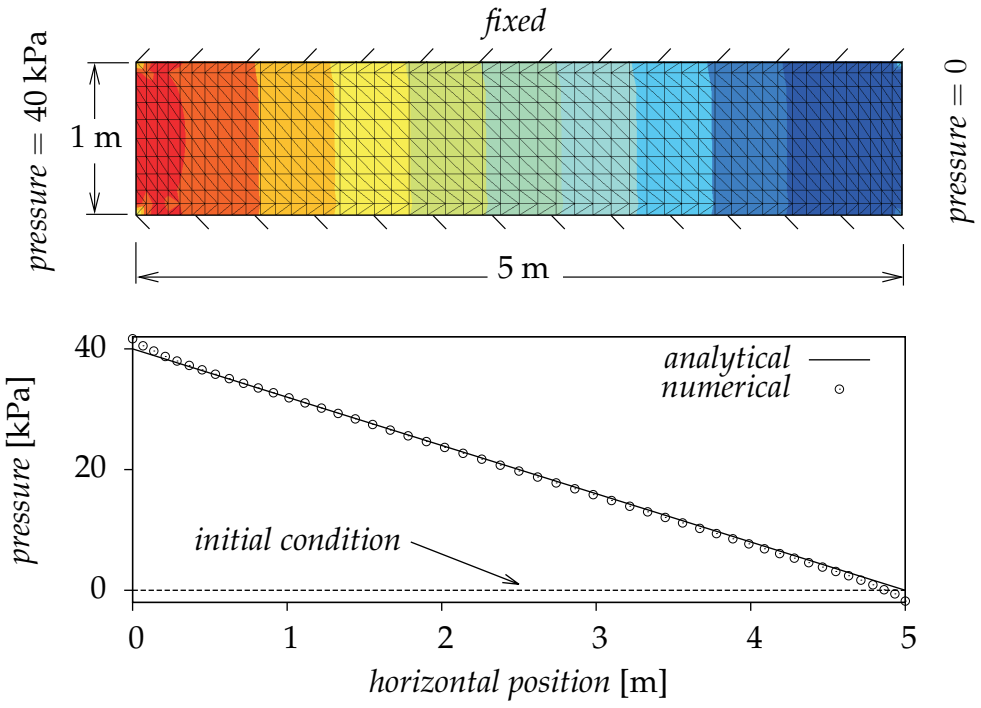

Figure 5.3: Poiseuille flow description and pressure at steady–state: (top) pressure contour from 42 to -2 kPa, and (bottom) linear distribution along midplane

5.3 Volumetric locking: existence and alleviation

It is well known that low order finite elements tend to exhibit a *volumetric locking* when the bulk modulus is high. The classical illustration of this problem is presented in Figure 5.4, which shows a quadrilateral region being discretised by two triangular elements, holding three nodes constrained. Assuming fully incompressible material, the deformation must be volume preserving; i.e., the linear shape functions of the element only allow a velocity of the node in the direction parallel to its base. Therefore, the node can not move at all to satisfy conditions of both elements. As a first remedy, the volumetric locking can be avoided by using the cross–diagonal discretisation pattern shown in Figure 5.4. Unfortunately, if the centre node is not exactly at the centre, such a configuration also suffers from locking and pressure oscillations [18].

In more complicated problems with more elements, the kinematic locking due to the high bulk modulus spreads through the entire domain leading to the velocities that are underpredicted, with oscillations in pressure called *checkerboarding* as demonstrated in Figure 5.5 for shear flow driven velocity field within a cavity.

In the preceding section, the Poiseuille flow problem showed good agreement with the analytical solution. The flow in this problem, however, is one–dimensional and does not suffer from the volumetric locking. An extreme exercise for testing the volumetric locking is the *lid driven cavity* problem in which a continuous velocity is applied along the upper edge resulting eddy flow inside the cell. Picking a high value for the bulk modulus and trying to get the correct solution using the MPM procedure early described is not possible. The velocity field is completely locked and the pressure is dominated by the checkerboarding mode as shown in Figure 5.5. An expected conclusion is that an enhancement technique is essential when using low order elements.

The problem of volumetric locking in low order elements has been tackled by different methods. As the locking problem is associated with the spherical component of the stress tensor, a mixed element formulation provides a suitable scheme of defining more than one field variable [202, 203]. Therefore, the pressure or the volumetric strain can be defined as an independent degree of freedom on the discretisation grid beside ve-

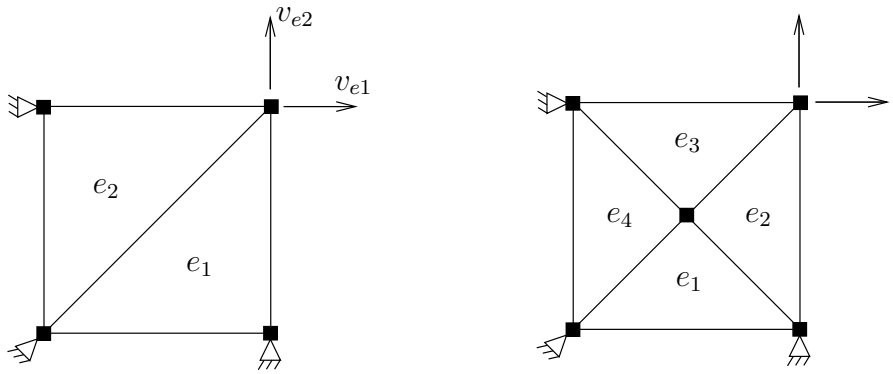

Figure 5.4: Volumetric locking in low order elements: existing in two triangular elements (left) and avoiding by the cross–diagonal mesh pattern (right)

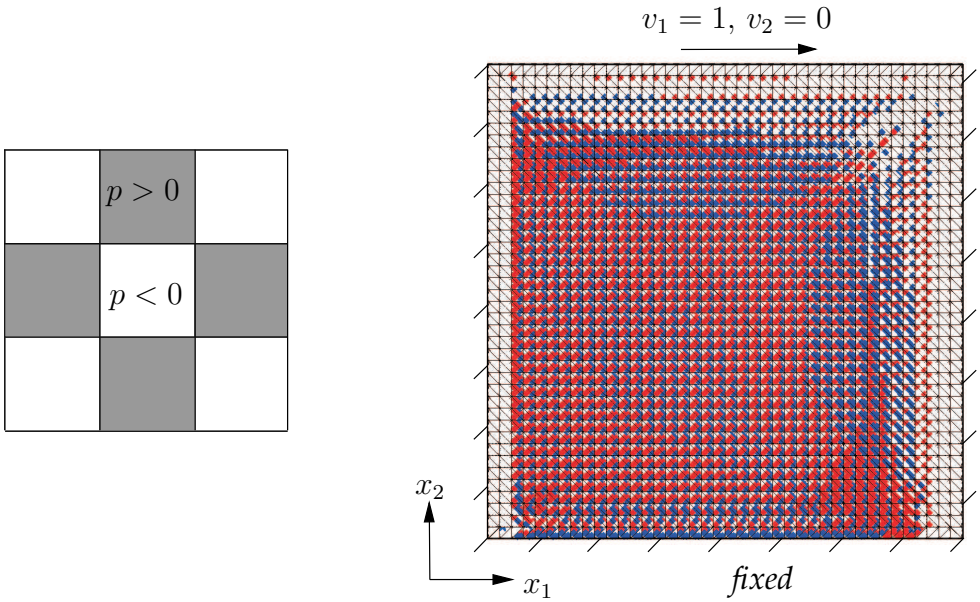

Figure 5.5: Illustration of checkerboarding mode (left) and application to the lid driven cavity with a pressure range from -10 to $+10$ MPa (right)

locities. The fractional step method (FSM) or any other scheme based on splitting the governing differential equation can be introduced [134, 205]. As an alternative, the *nodal mixed discrestisation* (NMD) treats both: nearly incompressible elastic material and the locking problem associated with plastic deformation [53].

5.3.1 Nodal mixed discrestisation (NMD)

The NMD being considered in Section 3.4 for solid materials is applied here for fluids. As a result, the smoothen volumetric part of the strain tensor alleviates the locking problem. To begin with the mixed formulation involving the velocity $\boldsymbol{v}$ and volumetric strain ε_v as independent field variables, the weak form in Equation 5.29 can be rewritten in the form

$$\int_{\Omega} \delta\boldsymbol{v}\, \varrho\, \frac{d\boldsymbol{v}}{dt}\, d\Omega = \int_{\Gamma_t} \delta\boldsymbol{v}\, \boldsymbol{t}\, d\Gamma + \int_{\Omega} \delta\boldsymbol{v}\, \varrho\, \boldsymbol{g}\, d\Omega - \int_{\Omega} \delta\dot{\boldsymbol{\varepsilon}}\, \boldsymbol{\tau}\, d\Omega + \int_{\Omega} \delta\dot{\boldsymbol{\varepsilon}}\, \boldsymbol{\delta} p\, d\Omega, \tag{5.39}$$

where $\boldsymbol{\delta}$ is the Kronecker delta. In addition, the weak form of Equation 5.28 in terms of the virtual volumetric strain $\delta\varepsilon_v$ is written in the rate form as

$$\int_{\Omega} \delta\dot{\varepsilon}_v \left(\dot{p} + K_f\, \dot{\varepsilon}_v\right)\, d\Omega = 0, \tag{5.40}$$

which is simplified for Newtonian fluid with constant bulk modulus K_f. The pressure rate $\dot{p}$ is obtained from the nodal volumetric strain rate, which yields

$$\int_{\Omega} \delta\dot{\varepsilon}_v \left(\dot{\epsilon}_v - \dot{\varepsilon}_v\right) \, d\Omega = 0, \tag{5.41}$$

in which $\dot{\epsilon}_v$ is interpolated value from the nodal discretisation of the volumetric strain rate $\dot{\boldsymbol{\epsilon}}_v$ and the interpolation function $\boldsymbol{N}$

$$\dot{\epsilon}_v \simeq \boldsymbol{N}\, \dot{\boldsymbol{\epsilon}}_v, \tag{5.42}$$

whereas $\dot{\varepsilon}_v$ in Equation 5.41 is computed from nodal velocity as in the finite element procedure. Back substitution of Equation 5.42 into Equation 5.41 for arbitrary $\delta\dot{\varepsilon}_v$ gives

$$\int_{\Omega} \boldsymbol{N}^T \left(\boldsymbol{N}\, \dot{\boldsymbol{\epsilon}}_v - \dot{\varepsilon}_v\right) \, d\Omega = 0. \tag{5.43}$$

Equation 5.43 provides a least squares fit for nodal volumetric strain rate. Therefore, the smoothening in this approach is considered as an explicit version of the mixed discretisation where the strains are defined as degrees of freedom beside velocity. Following up on this idea, the strain rate tensor is modified in the following form

$$\bar{\dot{\boldsymbol{\varepsilon}}} = \dot{\boldsymbol{\varepsilon}} - \frac{1}{3}\, \dot{\varepsilon}_v \boldsymbol{\delta} + \frac{1}{3}\, \bar{\dot{\varepsilon}}_v \boldsymbol{\delta}, \tag{5.44}$$

where $\bar{\dot{\varepsilon}}_v$ is obtained for an element with n_{en} nodes as

$$\bar{\dot{\varepsilon}}_v = \frac{1}{n_{en}} \sum_{i=1}^{n_{en}} \bar{\dot{\varepsilon}}_{v,i} \qquad \text{with} \qquad \bar{\dot{\varepsilon}}_{v,i} = \frac{\sum\limits_e \dot{\varepsilon}_{v,e}\, \Omega_e}{\sum\limits_e \Omega_e}, \tag{5.45}$$

where $\bar{\dot{\varepsilon}}_{v,i}$ is the volumetric strain rate evaluated at the node i with e being an element attached to this node. The NMD approach has been applied to strip footing problem using MPM where the analytical solution is available [2]. The bearing capacity of the soil showed an improvement after using the volumetric strain enhancement. Furthermore, the approach has been extended for two phase flow analysis successfully where a sea dike under wave attack was analysed [90].

The NMD approach for nearly incompressible fluid is tested by the lid driven cavity problem. The pressure field corresponding to an attempt of solving this problem without applying any enhancement procedure is shown in Figure 5.5, where the white colour in this figure indicates values out of the mentioned scale. The problem is modelled in MPM with regular tetrahedral mesh using one element in depth without updating particle locations. The validation is kept with low value of Reynolds number ($Re = \varrho\, V\, l_c/\mu = 1.0$), where l_c is the characteristic length of the problem and V is defined according to Equation 5.14 as the prescribed velocity at the boundary. Finally, the bulk modulus of the problem is defined to be close to that of water $K_f = 2\,\mathrm{GPa}$. The results in Figure 5.6 showed a limited improvement in the velocity field. As a conclusion, the enhancement of the velocity field by the NMD approach alone is not suitable for nearly incompressible fluid. Therefore, another approach has to be investigated.

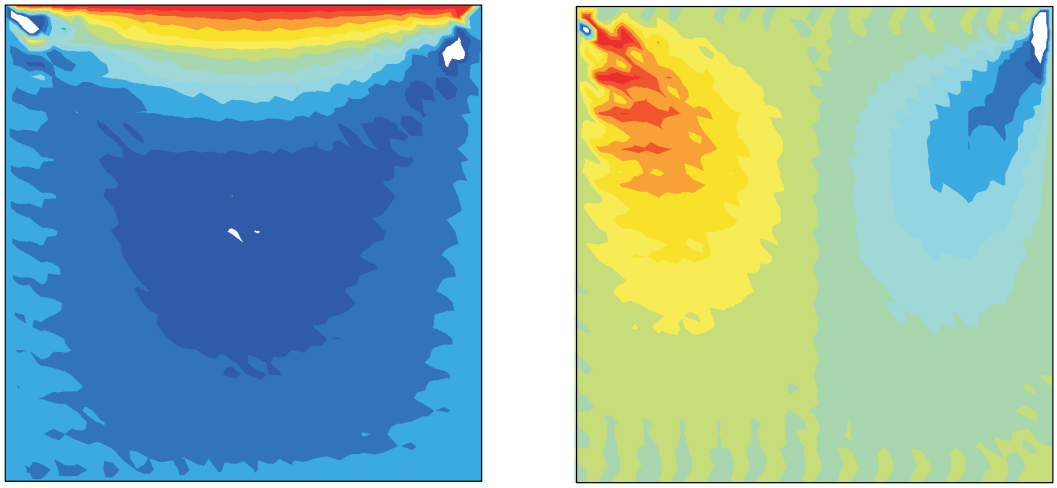

Figure 5.6: Horizontal (left) and vertical (right) velocity components of the driven cavity using NMD approach

5.3.2 Average nodal pressure (ANP)

The *average nodal pressure* (ANP) scheme has been proposed to alleviate the volumetric locking in linear elements [29, 84]. In this approach, the pressure is evaluated at the nodes by defining nodal volumes based on surrounding triangles or tetrahedrals. The formulation of the ANP scheme starts with estimating the average volumetric ratio J_i at the node i as follows

$$J_i = \frac{\Omega_i}{\Omega_{i,0}} \qquad \text{with} \qquad \Omega_i = \frac{1}{n_{en}} \sum_e \Omega_e, \tag{5.46}$$

where the subscript 0 refers to the initial configuration and the summation runs over the number of elements attached to the node i. The lumping procedure of the element volume is demonstrated in Figure 5.7 for two dimensional triangular elements. As fol-

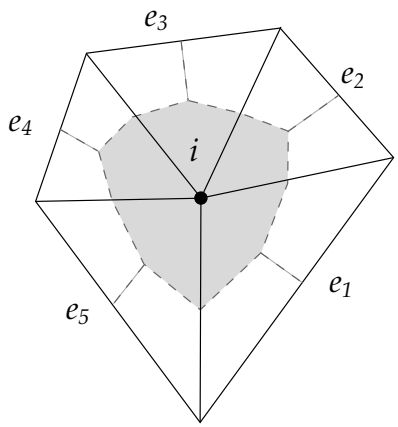

Figure 5.7: Lumping procedure of two dimensional volume

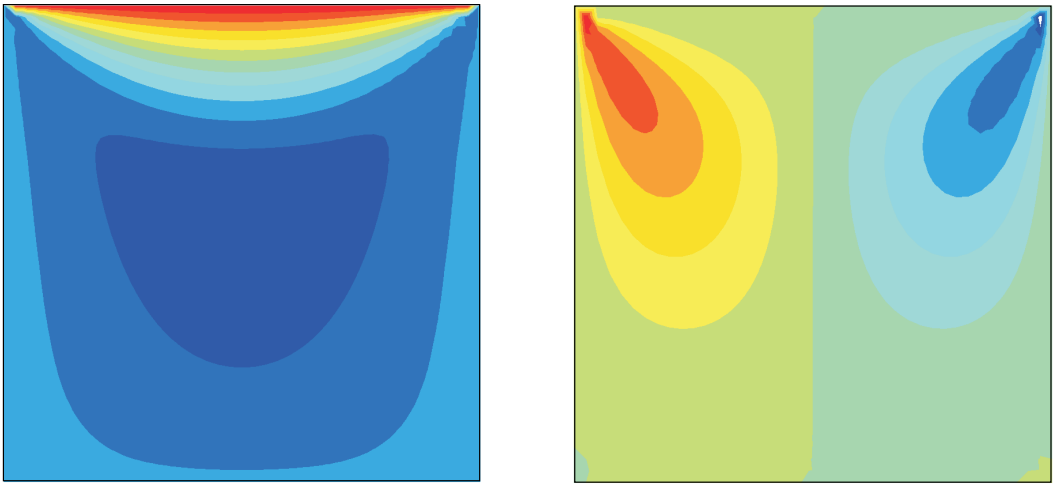

Figure 5.8: Horizontal (left) and vertical (right) velocity components of the driven cavity using modified ANP approach

lows, the average nodal pressure p_i is computed and mapped back as a final step to the element; i.e.,

$$\bar{p}_e = \frac{1}{n_{en}} \sum_{i=1}^{n_{en}} p_i \qquad \text{with} \qquad p_i = K_f \left(J_i - 1 \right), \tag{5.47}$$

with $\bar{p}_e$ being the average element pressure. In this procedure, the spherical part of the stress tensor is evaluated at the nodes while the deviatoric part is kept on the element level with no change. For the present formulation, the entire stress tensor is evaluated at the element followed by explicit averaging of the spherical component at the nodes as

$$\sigma_{ij} = \tau_{ij} - \delta_{ij}\, \bar{p}, \tag{5.48}$$

in which, the enhanced pressure $\bar{p}$ is computed from

$$\bar{p} = \frac{1}{n_{en}} \sum_{i=1}^{n_{en}} \bar{p}_i \qquad \text{with} \qquad \bar{p}_i = \frac{\sum\limits_e p_e\, \Omega_e}{\sum\limits_e \Omega_e}, \tag{5.49}$$

where the summation with e index runs over the number of elements attached to the node i. The driven cavity results related to the ANP enhancement procedure is illustrated in Figure 5.8. For quantitative comparison with other numerical methods [112], the horizontal and vertical velocity components are shown in Figure 5.9. In these figures, the MPM solution is seen to be quite close to the finite difference (FD) solution. The smoothed particle hydrodynamics (SPH) solution slightly underpredicts the proper solution, which requires further tuning of the parameters of this method [65, 112].

So far, the driven cavity problem is discretised with regular tetrahedral mesh. According to Equation 5.49, the smoothen pressure $\bar{p}$ at material points is achieved by volumetric weighting of the average pressure at nodes $\bar{p}_i$. The analysis is repeated with

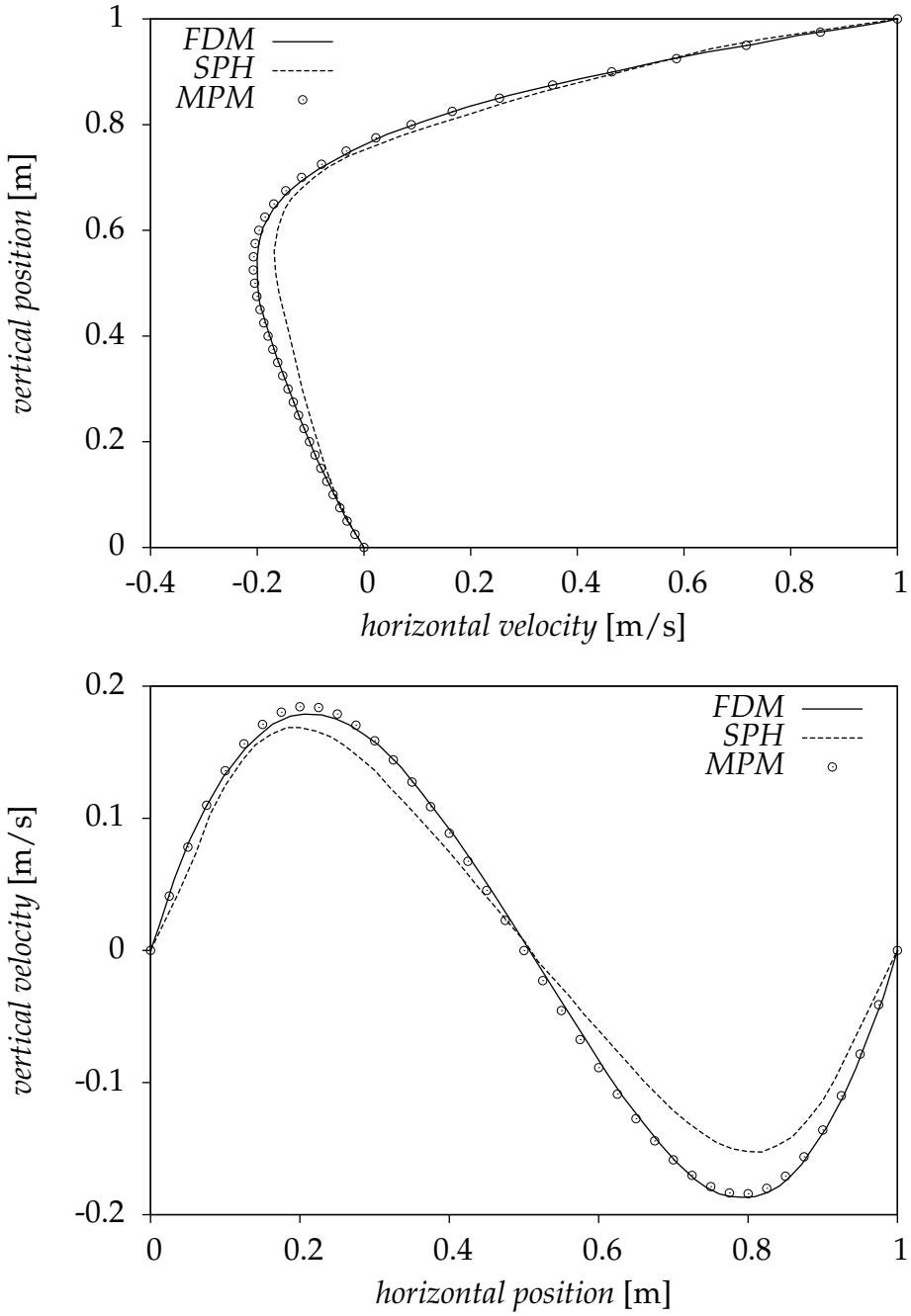

Figure 5.9: Horizontal and vertical velocity components along the vertical and horizontal centrelines, respectively

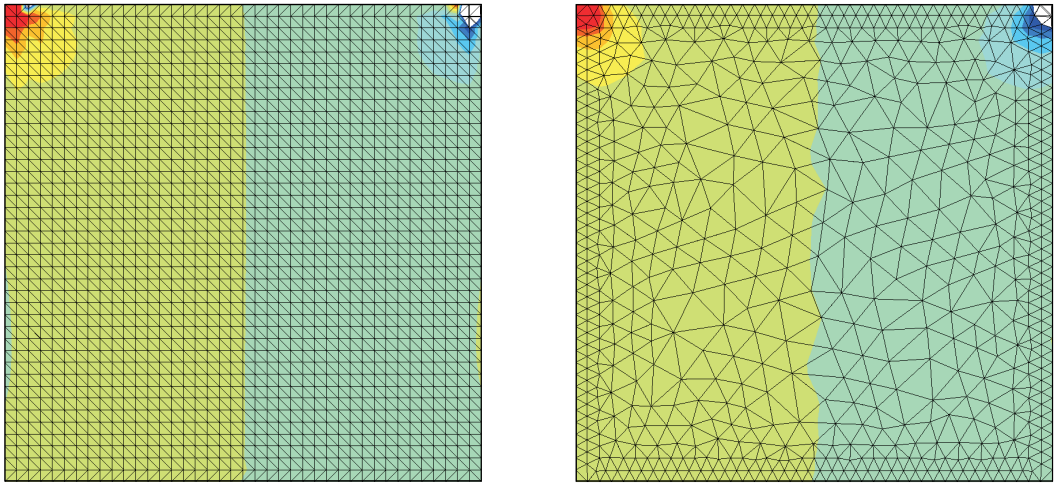

Figure 5.10: Effect of the mesh regularity of the pressure field: regular (left) and irregular (right) tetrahedral meshes, the pressure range from -50 to $+50\,\mathrm{kPa}$

irregular tetrahedral mesh. A comparison of the pressure field for the regular and irregular meshes is presented in Figure 5.10. Excluding the edges effects where linear variation of velocity is applied along the corner element, the modified ANP approach does not appear to show much dependence on the regularity of the tetrahedral mesh.

The presented lid driven cavity problem shows that the ANP approach produces smoother results than the NMD approach been adopted for soil. The reason can be easily attributed to the total pressure enhancement within the ANP procedure. Whereas, the NMD scheme smooths only the volumetric strain increment that contributes to the total pressure where incremental error is accumulated. In the case of soil, where plasticity might be involved, the total pressure scheme can not by applied. It is however applicable if only elasticity is involved for the pressure field, which is the case for fluid.

In this section, it is proven that the average nodal pressure ANP approach is essential to have smooth pressure prediction for the lid driven cavity problem with no update for the particles location. In the case of MPM when particles might change elements in later cases, however, the ANP approach alone was not enough to stabilise the pressure field and enhance the pathological locking. Therefore, adopting both ANP and NMD approaches at the same time reduces the pressure instability as well as mitigates the volumetric locking problem.

5.4 Free surface problem

The *free surface problem* is an important topic in coastal applications and many engineering problems. The expression for free surface is due to the contact of two fluids having different densities where free surface is developed at the interface. It is important to detect this surface properly. In most applications where single fluid flow is involved, a fluid experiences a free surface as exposed to the atmospheric pressure, where the air pressure corresponds to gauge pressure. The important feature of this type of problem is that the shape of the surface is unknown, a priori, as it depends on the developed flow.

In numerical modelling, two distinct approaches or the combination of both are used to tackle the free surface flow problem. The *interface tracking*, is also called the front tracking method, in which the free surface is considered as a movable Lagrangian boundary where the kinematic and the kinetic boundary conditions are applied [58]. The motion of the free surface is advanced explicitly, being defined as a sharp interface. Even though the interface is sharply tracked in such methods they encounter mesh related problems when a mesh becomes heavily distorted. For instance, the *Particle Finite Element method* (PFEM) uses continuous remeshing with new topology in each time step to obtain a new Lagrangian mesh, where the boundary conditions are applied [86, 139].

For Eulerian approaches where the material flows through fixed mesh, some techniques are applied to distinguish the free surface within the element space. *Interface capturing* method or the volume tracking performs the solution on a fixed grid where the position and the movement of the free surface is captured by the solution algorithm in one of three different ways: tracking the seeded particles; introducing a level set function; and finally by tracking the fluid volumes using an indicator function [20]. Among these three categories, the *volume–of–fluid* (VoF) method is the most widely used. In this method, the physical volume fraction is used as an indicator to track the discontinuous volume change across the interface as shown in Figure 5.11. The indicator function equals to unity at any point occupied by the fluid and zero elsewhere, or interface is detected if the value between zero and one. Moreover, the formulation of the VoF strategy is formulated in an *Arbitrary Lagrangian–Eulerian* (ALE) framework where the structure is modelled in a Lagrangian finite element way, while the fluid domain is treated with the finite volume method [91].

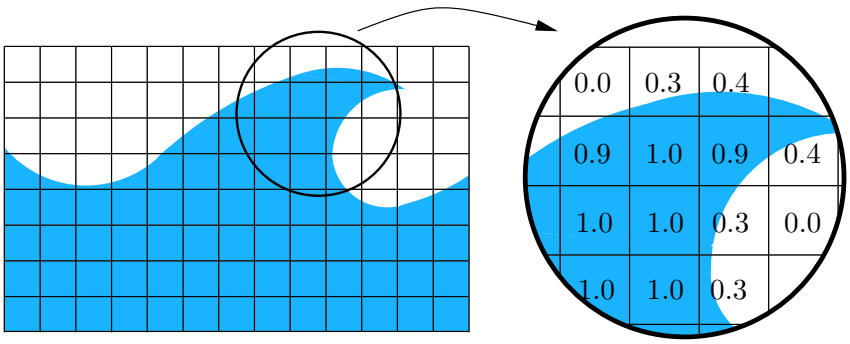

Figure 5.11: Illustration of the volume–of–fluid method

In MPM, *mass density field* can be evaluated at nodes each time increment [185]. In this approach, the density field is represented at the grid nodes using the following formula

$$\varrho_i = \frac{\sum_e \sum_p N_i\left(\boldsymbol{x}_p\right)\, m_p}{\frac{1}{n_{en}} \sum_e \Omega_e}, \tag{5.50}$$

where the summations with the indices e and p run over the elements attached to the node i and particles in element e, respectively, and N_i denotes the shape function of node i being evaluated at the location $\boldsymbol{x}_p$ of the particle p which has the distinct mass m_p. Important to highlight here that the denominator of Equation 5.50 involves only the non–empty elements, so that the density if approximated properly. In this expression, the nodal density field is expressed by the lumped mass corresponding to the node divided by the lumped nodal volume as computed in Equation 5.46. Consequently, the density at any location $\boldsymbol{x}$ inside elements can be interpolated using

$$\bar{\varrho}\left(\boldsymbol{x}\right) = \sum_i N_i\, \varrho_i, \tag{5.51}$$

in which $\bar{\varrho}$ is the smoothen density field. Using this procedure, the smoothen density $\bar{\varrho}$ is evaluated for all material points, which is used in the current MPM formulation to capture the free surface; i.e.,

$$\left(\bar{\varrho}_p\right)^{t+\Delta t} \leq f_{\text{it}}\, \varrho_p^{t+\Delta t}, \tag{5.52}$$

where f_{it} is a factor controls the continuity of the free surface being detected in MPM. Satisfying the inequality of Equation 5.52 means that particle p is lying on the free surface, otherwise, the particle is detected as interior particle. The factor f_{it} is mesh dependent and needs to be tuned accordingly. Figure 5.12 shows the effect of this factor on the detected interface. Based on experience a value of 0.6 is considered to be reasonable.

Kinematic and kinetic boundary conditions, Equations 5.15 and 5.16, of the free surface condition must be satisfied. In MPM procedure, however, the kinematic movement of the particles is obtained by solving the momentum equation. Therefore, the kinematic equation of the free surface flow is solved inherently and the two conditions of the free surface reduced to the dynamic condition only. In the absence of surface tension and considering the usual case of gas being in contact with liquid, the inertia effect of the gas is negligible and the only influence of the gas is the pressure that acts on the interface [5]. Therefore, the dynamic condition is reduced to the hydrostatic pressure, which set to zero gauge for the detected particles.

Validation example: collapse of water column The problem of water column collapsing has been addressed in many references. The column is supported at the bottom by a horizontal surface and along the sides by a removable supports. Depending on the column shape being circular or rectangular, the supporting walls are removed suddenly to let the water flow, with the horizontal velocities and the residual column height being measured with time. In addition to physical modelling [42, 125], the water column problem inspires many authors as a fundamental validation for numerical modelling of

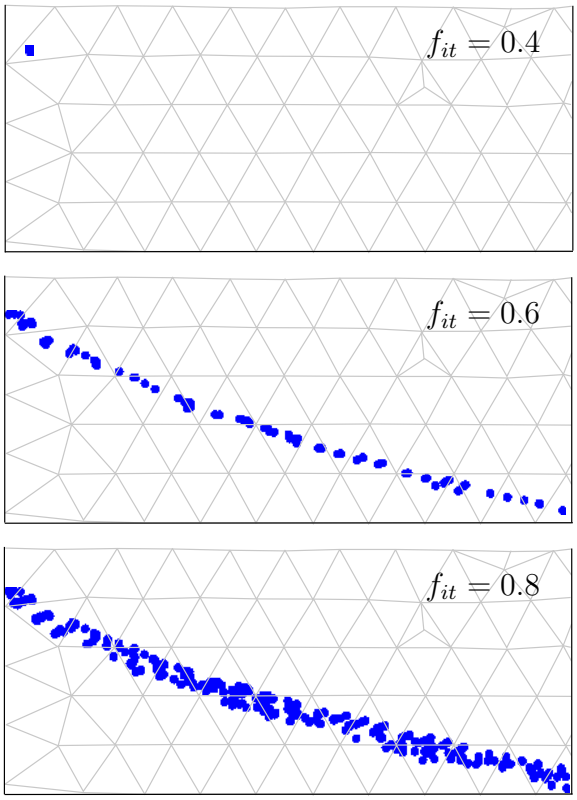

Figure 5.12: Effect of the free surface settings of the interface detection

incompressible fluid [127, 155]. Furthermore, special attention must be paid to model the free surface formulation [85, 100].

In this thesis, the problem of the water column collapsing is modelled in MPM using tetrahedral mesh discretisation with an initial hydrostatic pressure been assigned to the particles as illustrated in Figure 5.13, in which the dimensions of the column are given by the width w_0 and the height h_0 at the beginning of the simulation. Since the time step size is controlled by the minimum characteristic element height which becomes small in the case of irregular mesh, a regular discretisation has been adopted. The viscosity of the water was assumed constant $\mu = 8.9 \times 10^{-4}\,\mathrm{Pa.s}$ with a bulk modulus of $K_f = 2.13\,\mathrm{GPa}$.

As discussed earlier in this chapter, the MPM solution procedure requires an enhancement to mitigate the problem of volumetric locking associated with using low order element for nearly incompressible fluid. Hence, two algorithms were investigated. The average nodal pressure (ANP) algorithm was found to show smoother results when compared to the nodal mixed discretisation (NMD) in the case of driven cavity problem with no update of particles position. However, in the case of water column collapse where the particles are allowed to update position, both enhancements are required simultaneously. Figure 5.14 compares the MPM results with FEM analysis [42]. For this problem, some snapshots for the pressure distribution are shown in Figure 5.15.

Referring to Figure 5.14, the particles being detected on the free surface are coloured lighter as compared with the interior particles. The free surface in this figure does not show continuity at time $0.1\,\mathrm{s}$ for which the factor f_{it} is set to 0.6. Nevertheless, other

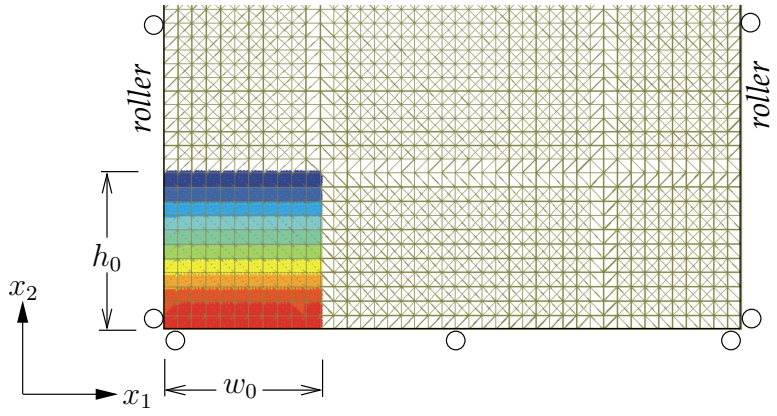

Figure 5.13: MPM discretisation of the water column problem with an initial hydrostatic pressure (0 to 1.1 kPa)

snapshots show distinct and continuous surface. At time $0.7\,\mathrm{s}$, the MPM model predicts more splashing than the FEM solution, which in turn tag many particles on the interface surface. Both MPM and FEM models agree on the trend of the column collapse, where the wave surge hits the right wall and climbs up to form a thin water column up to the time $0.4\,\mathrm{s}$ where it collapses back to form a retreated wave against the primary water wave. It is obvious that the second collapse has different pattern due to the squeezing of its bottom by the primary wave. As a result, the retreated wave interacted with the primary flow to trap some air in between which is captured by both models as shown for $t = 0.7\,\mathrm{s}$.

Figure 5.15 shows reasonably smooth pressure distribution with different time steps. At time $0.2\,\mathrm{s}$ the distribution reflects mainly the hydrostatic linear distribution when the residual height of the column becomes $7.3\,\mathrm{cm}$ with maximum pressure of $0.8\,\mathrm{kPa}$ in the column. On the other hand, the distribution at time $0.4\,\mathrm{s}$ is dominated by the hydrodynamic pressure with the flow changing its direction at the right corner. Apart from this, the forming water column is free of stress and having nearly zero pressure when its particles are moving upward. At the same time, the original water column to the left is becoming more flatten with maximum height of $3.4\,\mathrm{cm}$. The column then starts to plug already at time $0.5\,\mathrm{s}$ and the pressure concentration spreading out over wider area. At time $0.6\,\mathrm{s}$ the particles near the right wall start landing together as a cloud whereas the retreated wave starts moving to the left.

For further validation of the MPM simulation of water column collapse, comparison is conducted with experimental results where the MPM mesh discretisation is extended farther in the horizontal direction. Furthermore, the aspect ratio A_r of the height to the width of the column has been varied holding the column width w_0 constant. In this case, variables are normalized according to the following formulas [125]

$$X_1 = \frac{x_1}{w_0}, \qquad X_2 = \frac{x_2}{h_0}, \qquad \text{and} \qquad T = \sqrt{\frac{g\,A_r}{w_0}}\,t, \tag{5.53}$$

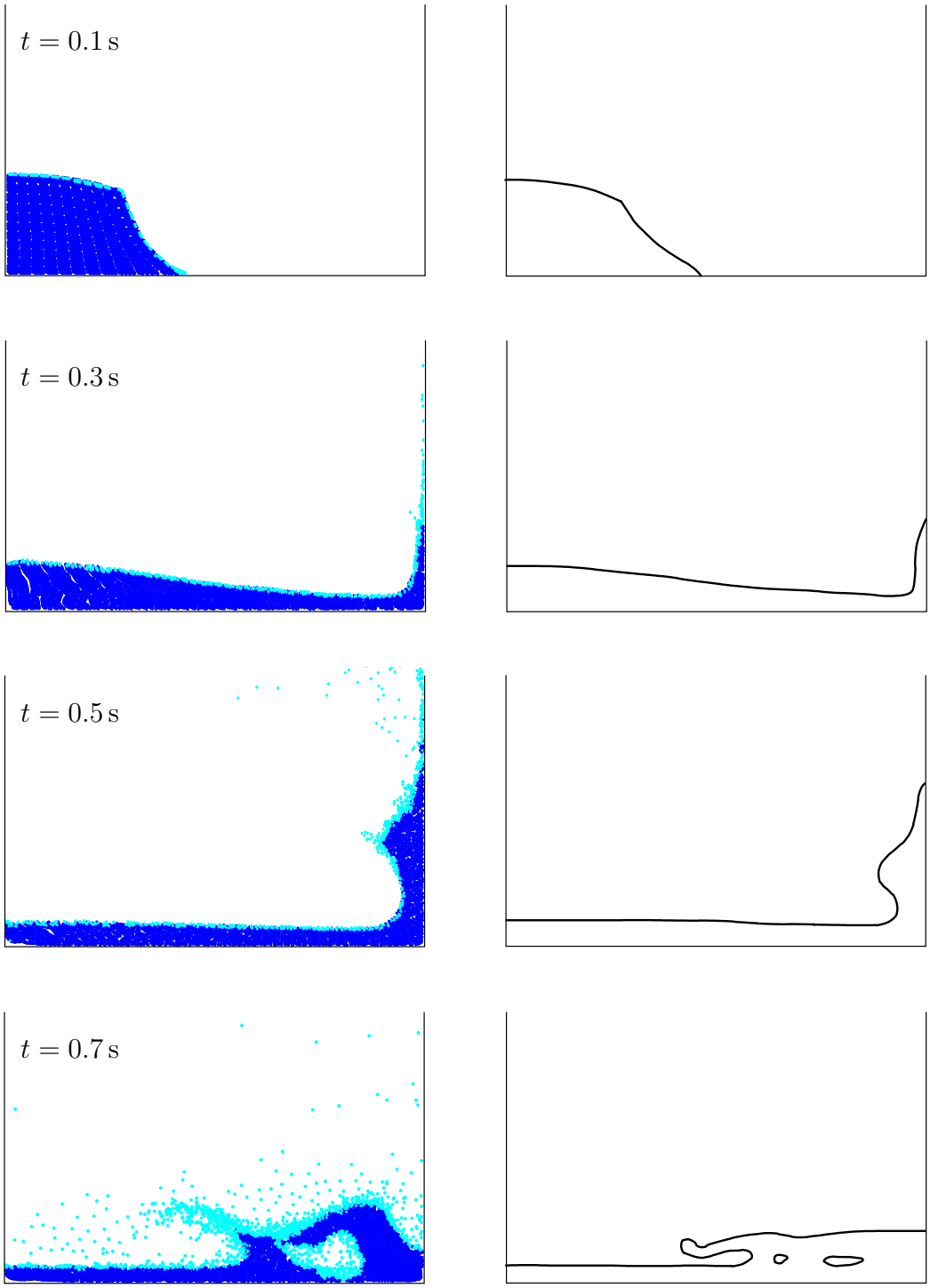

Figure 5.14: Collapse of the water column with free surface condition: MPM (left) and FEM [42] (right)

where X_1 and X_2 are the normalized horizontal and vertical coordinates of the water particle respectively, with T being the normalized time. The gravitational acceleration g is considered as $10\,\mathrm{m/s^2}$ whereas the aspect ratios $A_r = 1, 2$ are chosen for constant column base $w_0 = 11.4\,\mathrm{cm}$. As illustrated in Figure 5.16 good agreement is obtained between predictions and experimental results. The MPM solution however shows little faster movement of the horizontal surge front as compared with experimental. This small deviation is attributed to applying roller boundary condition instead of the *non–slip* condition along the base. A rough condition can be applied for the numerical model but the mesh near the boundary would have to be very fine to capture the boundary layer. Otherwise, the effect of the rough boundary would slow down the stream in unphysical manner. On the other hand, the residual height of the water column shows less deviation between the MPM and the experiment for both aspect ratios as demonstrated in Figure 5.16. Indeed, the MPM has excellent prediction for the column height in both aspect ratios $A_r = 1$, and $A_r = 2$.

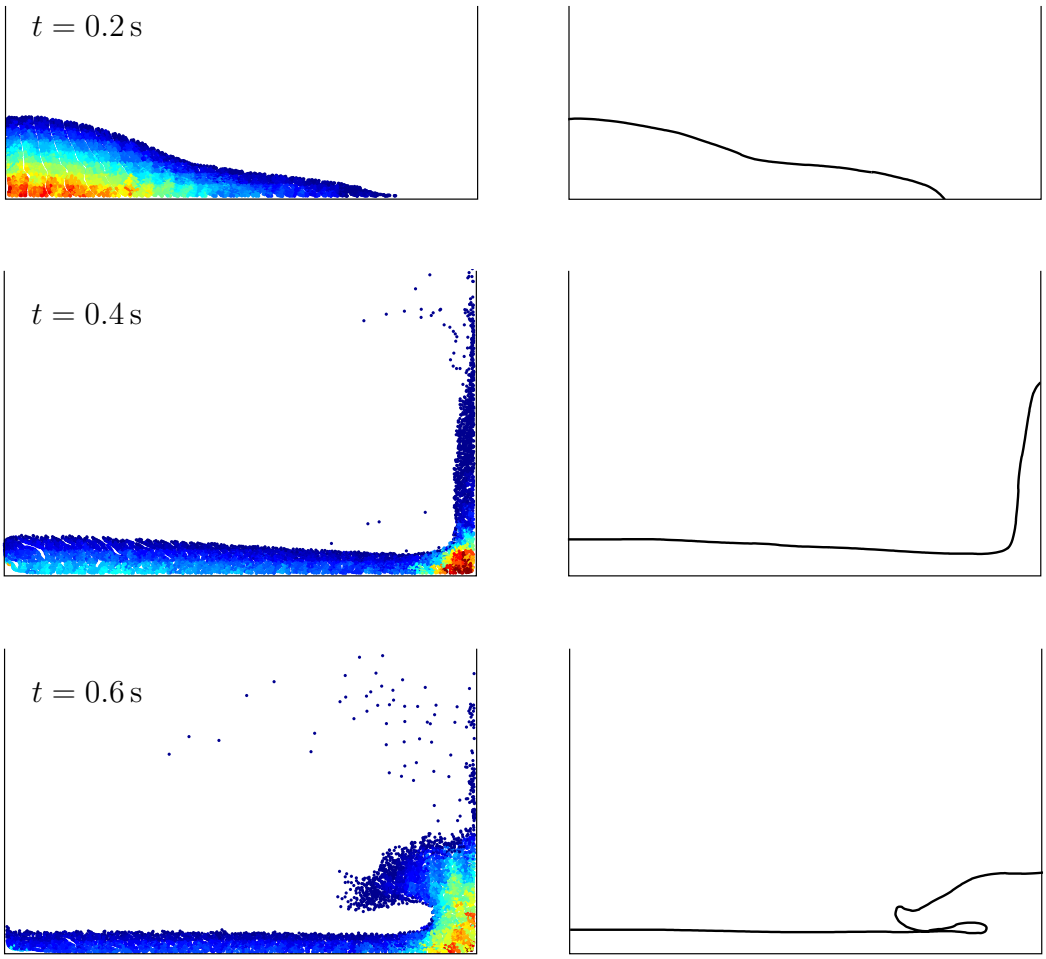

Figure 5.15: Pressure distribution of the MPM water column with the range 0 to $0.9\,\mathrm{kPa}$ (left) and FEM free surface [42] (right)

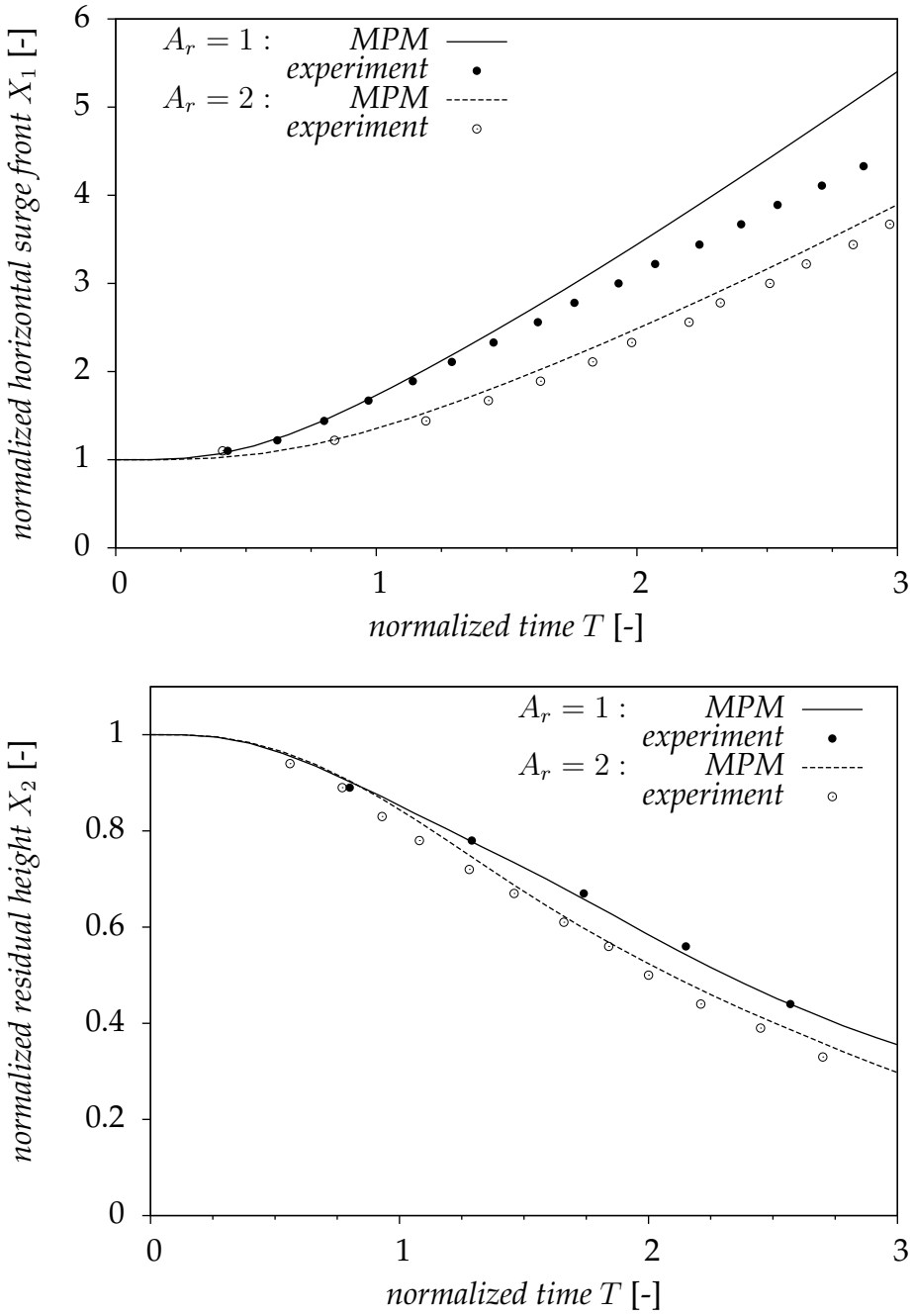

Figure 5.16: Comparison of the horizontal surge front and the residual water column of the collapsed water column using MPM with experimental data [125]

5.5 Fluid–Structure interaction

In many scientific and engineering fields, interaction between fluid and structures exists. Owing to the nature of coupling, the *fluid–structure interaction* (FSI) problem has strong geometrical nonlinearity, making it challenging to obtain an analytical solution, and even a solution via classical numerical methods. For the FSI problem, two strategies can be used: the *monolithic* and the *partition* strategy [52, 79, 91]. In the monolithic approach, both fluid and structure are solved simultaneously to form single system of equations for the entire problem such that their mutual influence can be taken into account directly. Therefore the interfacial condition is implicitly included in the solution procedure, which makes this scheme more favorable for the stability of the calculation [52]. On the other hand, partitioned schemes treat the fluid and the structure as two separate computational fields, with the interface condition being used to explicitly communicate information between the two medium, which makes this approach useful to integrate two available algorithms due to less time for coding [79]. Different classification for the FSI approaches based upon the treatment of the mesh. *Conforming mesh* methods track the interface condition as a physical boundary that requires updating the mesh, whereas the *non–conforming mesh* methods treat the interface via constraints imposed on the model equations, keeping the same original mesh [79, 179].

5.5.1 Mathematical description

The FSI problem can be described mathematically by considering the three–dimensional domain Ω, which is composed of the structural Ω_s, and the fluid Ω_f subdomains interacting with each other through the interface Γ_s; e.g., $\Gamma_s = \Omega_s \cap \Omega_f$. For such a system, the conservation of mass of the solid body described in the Lagrangian formulation can be written as

$$\frac{d\varrho^s}{dt} + \varrho^s \frac{\partial v_i^s}{\partial x_i} = 0, \tag{5.54}$$

in which the superscript s refers to the solid body, with conservation of linear momentum reading

$$\varrho^s \frac{dv_i^s}{dt} = \frac{\partial \sigma_{ij}^s}{\partial x_j} + \varrho\, g_i^s. \tag{5.55}$$

On the other hand, the mass conservation law for fluid is mostly given in an Eulerian description as

$$\frac{\partial \varrho^f}{\partial t} + \varrho^f \frac{\partial v_i^f}{\partial x_i} + v_i^f \frac{\partial \varrho^f}{\partial x_i} = 0, \tag{5.56}$$

with the conservation of linear momentum equation given by

$$\varrho^f \left[\frac{\partial v_i^f}{\partial t} + v_j^f \frac{\partial v_i^f}{\partial x_j} \right] = \frac{\partial \tau_{ij}^f}{\partial x_j} - \frac{\partial p}{\partial x_i} + \varrho\, g_i^f, \tag{5.57}$$

where the superscript f denotes the fluid continuum. The solid and fluid in Equations 5.55 and 5.57 follow constitutive equations consistent with their properties. Kinematic and dynamic boundary conditions are then imposed along the interface Γ_s, as already described in Section 5.1, to ensure continuity in displacement/velocity and stresses in the form

$$v_i^s\left(\boldsymbol{x}, t\right) = v_i^f\left(\boldsymbol{x}, t\right) \qquad \text{and} \quad \sigma_{ij}^s\left(\boldsymbol{x}, t\right) n_j = -\sigma_{ij}^f\left(\boldsymbol{x}, t\right) n_j, \tag{5.58}$$

where $\boldsymbol{n}$ is the outward unit normal at the solid boundary. It is important to mention that the conservation of energy equation is dropped out of this formulation for isothermal process.

5.5.2 Arbitrary Lagrangian–Eulerian methods (ALE)

The ALE methods are the most frequently used methods to treat the FSI problem. For these strategies, both the Lagrangian solid and the Eulerian fluid are discretised such that they share the interface. However, the Eulerian mesh is not being restricted to conforming mesh but rather it can move arbitrarily, thus an extra convection term must be taken into account [179]. The fluid–solid interface is made to follow the movement of the Lagrangian solid and consequently Equations 5.56 and 5.57 become [79]

$$\frac{\partial \varrho^f}{\partial t} + \varrho^f \frac{\partial v_i^f}{\partial x_i} + \left(v_i^f - v_i^m \right) \frac{\partial \varrho^f}{\partial x_i} = 0, \tag{5.59}$$

$$\varrho^f \left[\frac{\partial v_i^f}{\partial t} + \left(v_j^f - v_j^m \right) \frac{\partial v_i}{\partial x_j} \right] = \frac{\partial \tau_{ij}^f}{\partial x_j} - \frac{\partial p}{\partial x_i} + \varrho\, g_i^f, \tag{5.60}$$

where v_j^m is the velocity of the fluid mesh. The Navier–Stokes equations are solved in the ALE methods by splitting the differential operator, allowing the Lagrangian phase calculation to be performed first with the mesh moving with the fluid particle. Changes in velocity, pressure and internal energy due to external and internal forces are computed in this phase, which represents a linearized Stokes problem. A non–linear advection phase follows, including transportation of mass, momentum and energy across element boundaries are obtained. The second phase can be regarded as remapping the displaced mesh at the Lagrangian phase back to its initial position. More details about this approach can be found in [7].

5.5.3 Immersed boundary methods

In contrast to the ALE methods where the fluid–structure interface is accurately captured, the immersed boundary methods employ non–conforming mesh for the interface where forces are applied to the fluid to represent the interaction, thereby avoiding the mesh update. According to the literature [179, 191], the history of this method goes back to the late seventies when it was used first to study the blood flow through the heart.

In the immersed methods, the Dirichlet condition is enforced by adopting Lagrange multipliers, which appears as a source term in the governing equation [79]. The additional terms, which represents the immersed boundary effect, is obtained explicitly from the structural body. Applying this theorem to Equation 5.57 results in

$$\varrho^f \left[\frac{\partial v_i^f}{\partial t} + v_j^f \frac{\partial v_i}{\partial x_j} \right] = \frac{\partial \tau_{ij}^f}{\partial x_j} - \frac{\partial p}{\partial x_i} + \varrho\, g_i^f + \Lambda_i\, \delta\left(\Gamma_s\right), \tag{5.61}$$

in which the delta function δ is a unit function only where $v_i \in \Gamma_s$ and zero elsewhere. The Lagrange multiplier Λ_i is obtained explicitly from [79]

$$\varrho^s \frac{dv_i^s}{dt} = \frac{\partial \sigma_{ij}^s}{\partial x_j} + \varrho\, g_i^s - \Lambda_i. \tag{5.62}$$

The last term in Equation 5.62 represents the fluid–structure interaction force that acts in Equation 5.61.

5.5.4 Smoothed particle hydrodynamics (SPH)

As introduced in Chapter 2, the continuum is represented in SPH by cloud of Lagrangian material points where the equation of motion is solved. Interaction between material points is controlled by the size of the smoothening length. As a first approach in SPH to deal with the FSI problem, the influence of particles close to the interface can be extended to include the other particle type on the other side. Therefore, the interpolation is performed over all particles with no distinction between fluid and solid, which can be regarded as no–slip contact condition.

In order to relax the glue condition, a contact algorithm can be introduced where the particles of each material are solved separately [6]. As SPH is unable to enforce kinematic boundary condition precisely, similar troubles are expected with the FSI problem. The interpenetration between fluid and solid is prevented then by correcting the velocity fields of the two media.

5.5.5 Material Point Method (MPM)

MPM solves automatically the problem of no–slip contact between bodies, and of course the problem of self–contact of a body. Within one computational cycle, the momentum

equations are carried out in a Lagrangian manner, contributing forces to the same computational grid points. Dynamic equations are formulated in Lagrangian way. Convection is treated by mapping velocity field from material points to the mesh nodes. This combination of Lagrangian and Eulerian processes inherently handles a no–slip contact between different materials. An application of the FSI problem using MPM was introduced first to model the fluid–membrane interaction of an airbag system [191]. Since the position of the material points is updated using a single–valued continuous velocity field, the interpenetration of material is avoided, which allows simulations of no–slip contact between different bodies without the need for special interface tracking and contact algorithms [169].

The coupling of the fluid and structure in MPM is done via the combination of the internal forces of each substance on the grid nodes where the divergence of the stress is evaluated. Therefore, the *implicit* tracking of the interface via the internal forces is different from that of the confined finite element methods that capture the interface explicitly by dividing the computational domain into two separate domains. Hu et al. [80] define an *explicit* procedure to treat the fluid and structure separately. They interpolate the force and displacement directly to the background grid.

The fact that MPM uses one computational mesh in the background for both medium gives the same strain rate increment over the interface element. Therefore, one should expect that the accuracy of MPM for the FSI problem is of the order of element size where the information is smeared. In different words, if a nearly incompressible fluid is used in combination with relatively low volumetric stiffness solid, the pressure in the fluid is expected to be high at the interface at the expense of low stresses in the solid boundary. Refining the mesh is expected to enhance the solution but does not solve the problem. It can be found in literature the coupling of structures modelling in MPM with fluid modelled by another numerical scheme utilising the advantageous of both [66, 170].

5.6 Test study: Geotextile tube

The geotextile tube, or *geotube*, is defined by Pilarczyk [144] as a tube formed in–situ consisting of permeable but soil–tight geotextile. Sand or dredged materials are commonly pumped as a water–soil filler using a suction dredge delivery line. Geotubes are used for a range of hydraulic and coastal applications, where the gravity barrier type structures are required. The sizes range from $1\,\mathrm{m}$ to $10\,\mathrm{m}$ in diameter and up to $200\,\mathrm{m}$ length [101]. As depicted in Figure 5.17, geotextile tubes have been used for many marine applications; e.g., revetment structures to prevent erosion of the foundation, protection dikes against floods and storms, containment structures containing a reclamation area over soft soil, groynes to prevent the movement of the sediments, etc. [64, 92, 144].

Geotubes are usually made of geosynthetic sheets sewn together to form the required shape. One of the most essential design considerations of these tubes is the seaming strength as well as the maximum tensile strength of the synthetic. Excluding time–dependent variables such as creep, abrasion, chemical and biological degradation, the

Figure 5.17: Applications of Geotubes [64]: (top) sand dune core, (middle) groynes, and (bottom) offshore breakwater

geotube must be designed such that it can withstand the installation damage. An important aspect to study is the stability of geotubes against dynamic loads like wave forces or current actions by developing a numerical model that can capture realistic physical conditions. Other aspects like the effect of deformable ground and design of anchoring system for the tube stabilisation are not considered.

5.6.1 Analytical solution

The problem of pressurised fluid encapsulated inside a geosynthetic tube is formulated analytically by Leshchinsky et al. [103]. The analysis is simplified for plane–strain problem with no shear stress inside the filling material or within the geotextile. An equilibrium state is assumed for the hydrostatic pressure of the fluid with the tensile force along the geotextile. As a result, the radius of the geotextile curvature is expressed eventually in terms of the pumping pressure and the circumference of the tube for a certain fluid density. The procedure shows agreement with published experimental data for various dimensions. Accordingly, a computer program GeoCoPS was developed by Leshchin-

sky et al. [103] that gives the final geometry of the geotube for certain circumference and tensile force along the geotextile.

In this thesis, the GeoCoPS solution is the reference solution to which the MPM prediction is compared. The aim of this comparison is to validate the interaction of geotextile with the nearly incompressible fluid in MPM. In this comparison, the dynamic MPM algorithm is tested for capturing the steady–state solution to investigate the effect of the enhancements being implemented. For the sake of comparison, three tubes were filled with different amounts of fluid $\gamma_{\text{fluid}} = 12\,\text{kN/m}^3$ with the same circumference length $9.2\,\text{m}$ being selected. The filling of fluid inside tube is indicated in terms of cross–sectional area $6.45, 5.56$ and $3.36\,\text{m}^2$, which give a corresponding final configuration $H/W = 0.78, 0.50$ and 0.22 where H and W are the final height and width of the tube respectively. In this analysis, the geotextile is assumed to be inextensible.

5.6.2 MPM model

The different filling ratios of the geotube are modelled in MPM by having different initial configuration of the tube as illustrated in Figure 5.18, in which the initial oval shape of the tube is selected in a way that approximately matches the different filling ratios tested by GeoCoPS for the same $9.2\,\text{m}$ geotextile length. Four–noded tetrahedral elements are used to model the plane–strain problem with one element in depth. The fluid is modelled with bulk modulus $K_f = 2.13\,\text{GPa}$ and relatively high viscosity $\mu = 1.0\,\text{Pa.s}$, which works as an artificial damping to converge faster to the quasi–static solution. The geotextile was assigned a very high stiffness and negligible weight to match the analytical model. Zero stress state was initially assigned to all particles with gravity being the only external force.

After letting the initial, assumed profile of the geotextile tube rest on the smooth ground, it keeps bouncing up and down for few cycles after being released until the viscosity dissipates energy completely. Two criteria had to be satisfied for checking the

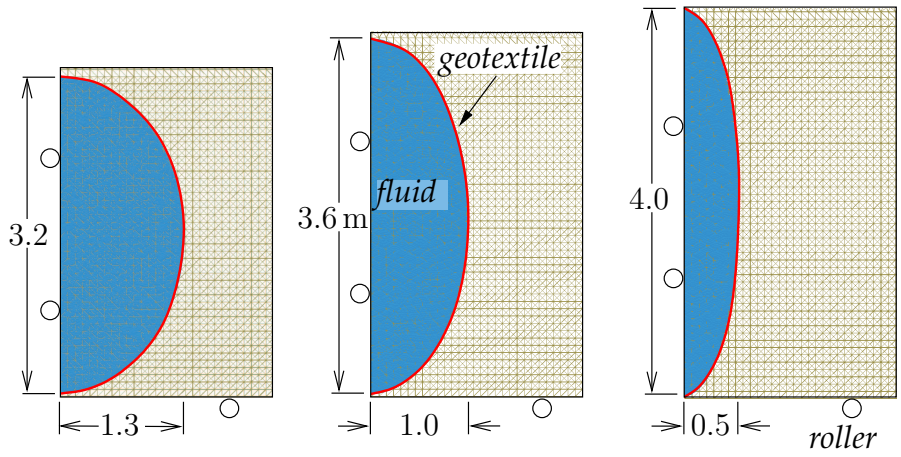

Figure 5.18: Initial configuration of the MPM model for different geotubes filling

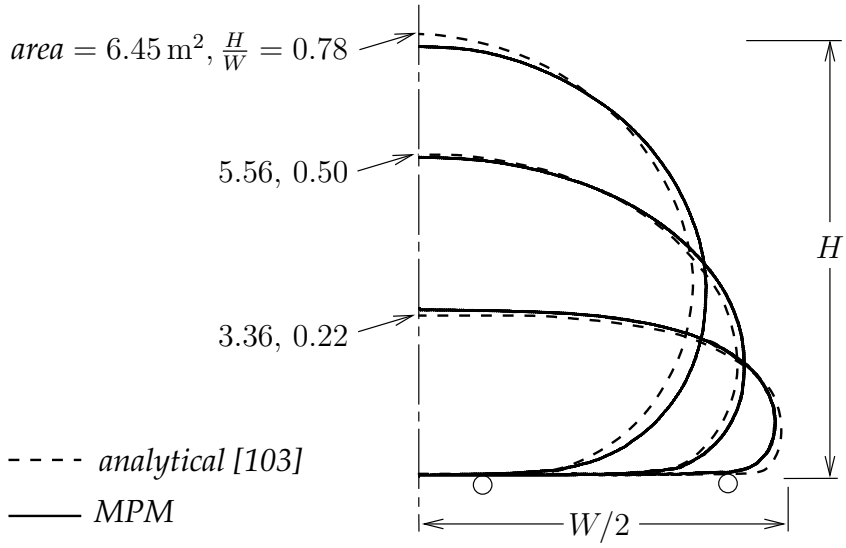

Figure 5.19: Final configuration of the geotextile tube

quasi–static solution: the overall kinetic energy, and the out–of–balance between external and internal forces must meet certain tolerance; e.g. a tolerance of 0.05 is selected for both criteria in the geotube application. At the quasi–static state, the MPM geotextile for the final shape of the tube is compared with the analytical solution as shown in Figure 5.19. Considering the approximation of the initial configuration, the MPM profiles are close except for some small deviation in the case of high and low filling.

Looking at the pressure distribution of the moderate filling in Figure 5.20, the MPM shows a good reproduction of the linear pressure variation. This is attributed to the ANP technique. The fact that the locking enhancement does spatial averaging, the layering of the pressure distribution has some wrinkles. As a summary for the geotube problem, the MPM fluid model in combination with the geotextile gives good prediction for the quasi–static solution.

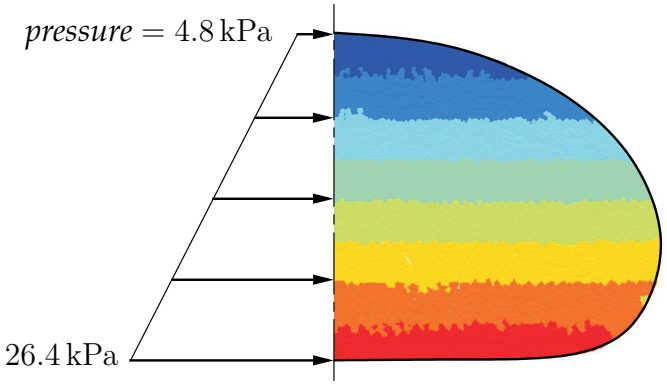

Figure 5.20: Pressure distribution in the tube with $5.56\,\mathrm{m}^2$ filling: (left) analytical solution after Leshchinsky et al. [103] and (right) MPM with the range 4.4 to 26.7 kPa

5.7 Concluding remarks

Solving the fully or nearly incompressible media using an explicit numerical algorithm is a challenging topic. Apart from the small time step constraint, the algorithm requires an enhancement procedure to improve the checkerboarding mode associated with using low order elements. The nodal mixed discretisation (NMD), which is based on smoothening the spherical part of the strain rate tensor [53], has been shown to work well for high bulk modulus soil material [2] and for two phase flow modelling [90, 162]. However, the NMD approach gives a limited improvement when it is applied to the lid driven cavity problem containing a nearly incompressible fluid. As an alternative for fluid, or elastic material in general, the average nodal pressure (ANP) approach can be used. Dislike the NMD approach, the ANP shows excellent solution for the fluid flow inside a cavity driven by shear forces. Applying both: the NMD and the ANP enhancement schemes stabilises the MPM algorithm, making it suitable for modelling viscous flow of nearly incompressible fluid in combination with solid materials. It should be realised that the positive effect of the double enhancements techniques requires further validation for different fluid flow problems.

The MPM fluid modelling approach is combined with an algorithm for detecting the free surface based on the continuous density field of the material points. The continuation of the free surface is controlled by a factor, which can be tuned according to the mesh size. The collapse of water column problem is reproduced by MPM, which gives fairly good match with experiments. It is however noticed that the MPM model has more water splashing, which complies with others experience [155]. Therefore, care should be taken for the solution sensitivity when the problem nature is changing from the laminar current assumption.

The enhanced MPM algorithm has been tested for a practical application of the geotube, for which the analytical solution for simplified model is available. The aim of the comparison is to evaluate the MPM fluid modelling as it converges to the steady–state solution and the interaction with the geotextile elements. In this analysis, the stopping criteria have been selected as the residual of the kinetic energy and the out–of–balance norms reach certain tolerance. As the solution proceeds toward steady–state, the size of the error reduces until certain limit where proceeding with the calculations does not help the convergence any more. This is attributed to the enhancement algorithms. Iterative and non–iterative solvers using NMD scheme and others for nearly incompressible elastic solid show that a residual exists, which does not improved with iteration [96].

Chapter 6

Dropping geocontainers

For many coastal structures, geocontainers are becoming more often used in combination with conventional construction materials. The proper installation of the large sand–filled containers is challenging. Most studies performed in this young field of engineering are either hydraulic scaled models or simple theoretical formulas with little field measurements. The lack of numerical techniques for the area, however, was the motive to establish an MPM model capable of simulating the dropping of geocontainers.

Modelling the dropping process numerically requires three basic components: soil, water, and geotextile, all being formulated in the MPM framework of earlier chapters. Moreover, air bouncy and other technical difficulties are involved in the real problem, which are not yet available in the current MPM formulation. Nevertheless, the dropping problem is tackled in this chapter with more focus on important design aspects, which are addressed in Section 6.1, along with the corresponding limitations and assumptions.

One of the assumptions in the existing implementation is that the geocontainer is released from the barge neglecting water. This assumption follows the experimental experience that the tensile forces along the geotextile are more dominant than the flow resistance during the releasing phase [144]. Furthermore following practice, wrinkles are added to the container to reduce the developed tensile forces. Even though implementing such folds is not currently possible, it has shown that adding extra length to the geotextile is good alternative and provides earlier releasing for the container as expected. Another factor which might increase the chance of the container damage is the influence of geotextile–barge friction. It has been found that friction not only affects the tensile forces, but also the shape of the released container. Details related to the releasing phase with the control parameters are reported in Section 6.2.

As a container is completely released from the barge, the highest geotextile force is expected when it hits the bottom, which is simulated in Section 6.3 by dumping the container on a soil bed. The installed container is followed by second one where interaction between the two is taking place. The increases in the geotextile forces due to the sudden landing of the second container is evaluated and compared to the final residual value.

Dropping a geocontainer in water reduces the dumping velocity because of the drag forces. In order to predict the container terminal velocity properly, the numerical model should be able to reproduce the fluid velocity field and the interaction with the sinking body. Therefore, Section 6.4 is dedicated to validate the velocity field of the nearly incompressible fluid model as compared with lab test measurements [32]. Extending the lab model simulation to field measurements [180], where the geocontainer has more focus of interests is achieved in Section 6.5.

6.1 Introduction

An important application for membranes is the modelling of a *geotextile sand container* (GSC) for shore protection structure. Owing to its economical and ecological advantages over conventional materials, the use of GSC is becoming increasingly popular for reinforcement of existing threatened coastal barriers and structures [140]. Studying the stability, interaction and failure of sand containers has been an attractive topic for numerous researchers [45, 78, 146]. Another application of geotextiles is for the construction of *geocontainer units*, which consist of prefabricated geotextile placed in a split barge and filled with sand or slurry up to several hundred cubic meters. Thereafter the container is closed by sewing and subsequently dumped from the scow bed in the desired position as shown in Figure 6.1. Geocontainer units are used for underwater structures such as breakwaters, and disposal of contaminated sludges. See, for example, Pilarczyk [144] for more applications.

Owing to the complexity of the problem, the understanding of what happens to a container during the releasing process and interaction with other geocontainers is still poor. Theoretical models based on equilibrium have helped to identify the sensitivity of the forces that develop as a function of physical variables [27, 48, 143]. Furthermore, large scale physical models have provided data that can be used to estimate the deformation and developed pressure inside the geocontainer; although it has been difficult to reproduce measured values owing to the variation of the control parameters from one test to another [26, 152, 180]. For better understanding of placing geocontainers accurately, lab tests were conducted on a scaled simplified geocontainer. These tests have provided good estimation for the dropping velocity and stability of multi containers [25, 49].

With regard to numerical modelling, there have been attempts to develop models based on distinct element method to simulate the releasing and dropping process [141, 142]. Nevertheless, there is a need for further investigation. This chapter applies a continuum model to study each step of the process separately and to establish the variations of stresses associated with the large deformations that take place in the large soil bags.

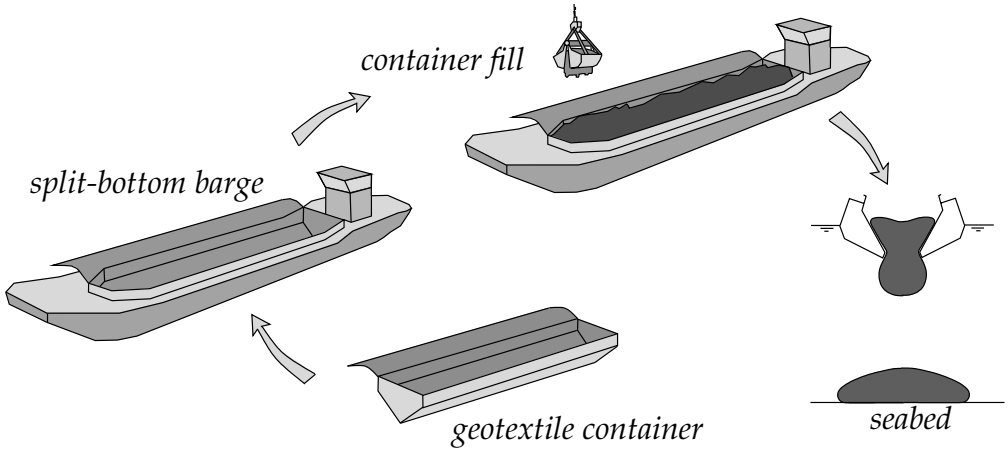

Figure 6.1: Procedure of filling and placing geocontainer [101]

6.1.1 Geotextile materials

A geotextile is a flexible, porous fabric made from synthetic fibers of polymeric material; e.g. polyester, or polypropylene. Depending on the manufacturing process and material used, a geotextile is classified as *woven* where the polymer is oriented in perpendicular directions, or as *nonwoven*, in which discrete fibers are randomly oriented. For sand size filling materials only layer strength is required, while an additional inner liner is important to hold the fine particles in the case of dredged materials [38].

The geocontainer shape is usually formed on site using geotextile sheets, in which the seam strength is the limiting design factor. For example, the fabric strength of woven geotextiles is about 175 to $193\,\mathrm{kN/m}$, whereas the seam strength is approximately 50 to $60\,\%$ of these values depending on the seam quality [38]. To prevent failure, the geocontainer is normally filled with 60 to $70\,\%$ of the theoretical fill volume [59, 144].

6.1.2 Design considerations

One of the major concerns associated with dropping geocontainers is the strength of the fabric and the seam. The geotextile should resist the forces during filling, releasing and impacting on the seabed. In practice, four phases can be categorised within the dumping process as illustrated in Figure 6.2 [144]. The *filling phase* is not considered in this classification, where the container is laid out in the barge and filled with the filling material, due to the relatively low forces of this phase. The first phase starts with opening the barge and *releasing* the container outside, which is normally associated with the big shape change of the container. As a result, tensile forces develop in the lower part of the geocontainer, whereas friction forces develop with the barge wall acting opposite to the container movement. At this stage, the developed forces are not yet maximum as compared with later stages, however, these forces might increase due to the clinching of the container sheet passing the bin or additional jamming forces. Several parameters control the tension in a textile during this phase; e.g., ratio of internal barge width to the opening width, speed of opening, surface condition of the barge, etc. [101].

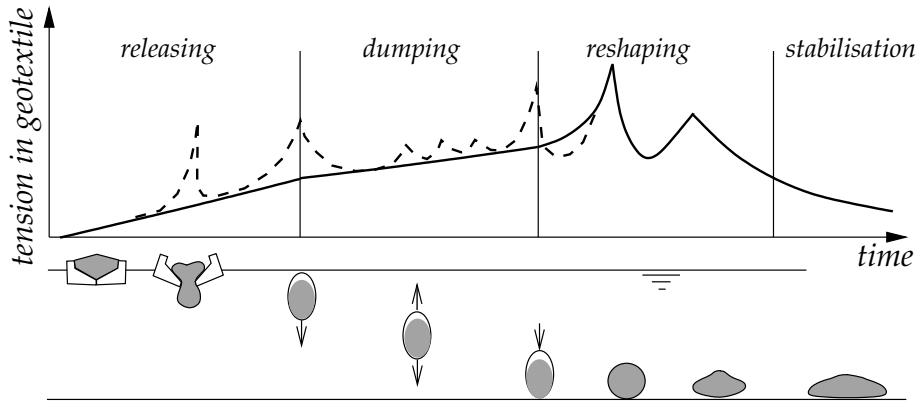

Figure 6.2: Geotextile forces during the dumping process after Pilarczyk [144]

In order to facilitate the geocontainer passing through the bin and to obtain a more flatten final shape, a surplus of geotextile is usually added. The extra length and the voids in the filling material tend to form air pockets in the container. These pockets, which act as balloons during sinking, reduce the falling velocity and increase the forces along the geotextile. Therefore, some air vents are added to the upper part of the geocontainer that facilitate the air to escape outside. After releasing the geocontainer completely from the bin, the *dumping phase* through the water begins. The geocontainer starts gaining velocity and can reach the terminal value if the water is deep enough. During this stage, the geocontainer does not necessarily undergo a big change in shape. The geotextile tension must be in balance with the soil weight, water drag, and buoyancy force from trapped air, even through analytical studies show that the last is rather small [144].

As the container approaches the bottom, it decelerates quickly due to a water cushion that develops before eventually hitting the seabed. Hence, the kinetic energy obtained during the journey is dissipated through the subsoil and the *reshaping* of the container. Owing to the impact, the soil inside the container moves sideways inducing a decrease in the geocontainer height. Therefore, the geotextile undergoes high tension as illustrated in Figure 6.2. The short time process prevents water or air to escape out of the container, which increases the pressure inside [180]. As a result of rapid shape changes the geotextile forces are expected to be maximum during releasing and the dropping process where the characteristics of the filling material play a role beside the permeability of the textile itself and the condition of the seabed.

The final stage in the construction procedure is the *stabilisation* stage where the geocontainer ends up with semi–oval or more rectangular shape depending on the amount of the filling material. During the construction process, the geocontainer might be subjected to the installation load of the next container, see Figure 6.1, or another load type after installation; e.g., waves, ship collision etc. The risk of bursting geocontainers in deep water, inaccurate placement due to waves and current, or even slope failure of a heap of geocontainers are important issues for the feasibility of using geocontainers [50]. Bursting geocontainers can be correlated to high forces in the geotextile when compared with its ultimate strength. Maximum forces could be during the releasing from the bin or the impacting on the ground, which is largely controlled by the amount of filling material and barge design.

The dumping velocity is a key factor in the impacting phase. Using a simple model based on drag force of a rigid body [1], produces a good estimate for the terminal velocity of a model test [25] or even for field measurements [27]. However, the failure in the geocontainer might be more localised due to the extreme reshaping at impact. Furthermore, interaction between geocontainers is an important aspect for the design of an individual container or structure of multicontainers. All that has been mentioned here regarding the design parameters, emphasises the need for a model capable of modelling the entire process of the large deformation problem associated with material movement in the presence of thin–walled structure and water. Owing to the difficulty of the considered problem of releasing and dropping geocontainer in water, the current numerical treatment has some limitations and assumptions that are addressed in the next section.

6.1.3 Assumptions and limitations of the numerical model

As mentioned earlier there are some limitations in the current MPM implementation due to the simplification of the complex physical problem.

Impermeable geotextile The geotextile itself can be permeable or impermeable by adding an inner liner. Infiltration of water has an impact on the deformation of the filling material and the dropping velocity. In the case of dry soil, the water can penetrate through the container if the air escapes. Owing to the quick process of dumping, little water infiltrates inside. Therefore, the assumption of dry soil when it reaches the bottom is valid [144]. Furthermore, in some cases and due to the clogging of fine particles, the permeable geotextile can be resembled as an impermeable [143]. A similar behaviour of impermeability is expected when contaminated dredged material is dumped and impermeable geotextile is used.

Rough geotextile–soil contact The common value of the geotextile–soil friction coefficient is about 0.2, which correspond to a friction angle of 11° [144], which is much less than the internal friction angle for sand. At this stage of model development, it is assumed that a rough contact exists. A rough contact relationship implies that failure takes place first inside the soil rather than at the geotextile–soil interface. In other words, a thin layer of soil is assumed to stick to the geotextile. From a modelling point of view, the thickness of this layer is within the order of the computational element thickness. Element refinement should thus reduce the effect of the rough contact assumption.

No surplus in the geotextile The surplus, or the extra length, of geotextile is essential to reduce the developed tensile forces and to obtain a more flatten final shape. The surplus added usually at the top of the geocontainer is not effective during the releasing phase. Some wrinkles are added also in the lower part of the container [180], between the soil and the barge. These have an impact on the required opening of the barge. In the MPM model, the geotextile is assumed to fully wrap the soil with no surplus. Nevertheless, this assumption is relaxed by extending the geotextile outside the barge as will be described later without violating the rough geotextile–soil assumption.

No bouncy effect of the trapped air Excluding the bouncy effect of the trapped air means no additional uplift force during sinking, i.e. the MPM geocontainer would sink faster. Fortunately, this force has minor influence as mentioned earlier.

Consistent soil filling Mechanical and hydraulic filling procedures are used for sand or dredged filling materials. Experience shows [27, 180] that the uneven releasing of a containers is probable. Bezuijen et al. [26] recorded a tilting angle of up to 45° in the longitudinal direction due to irregular releasing. In practice, it is advised to fill the container with more filling material at both ends than in the middle to have more even releasing. For the numerical model, the filling is assumed to be consistent in the longitudinal and the transverse directions. Furthermore, the length of the geocontainer is assumed to be large enough to ensure no deformation in the longitudinal direction is taking place; e.g.

the length to the width ratio about $5 : 1$ [180]. Therefore, the plane–strain theory for two–dimensional problem is applicable.

Isotropic and elastic geotextile The manufacturers of geotextile normally provide the tensile strength with the corresponding strains up to the break point. For example, the polypropylene woven geotextile GEOLON 120 implemented in the test of van Oord [180] has the properties listed in Table 6.1 [173]. Quick check of these values confirms nearly linear stress–strain relationship, which is considered here in the MPM model. Furthermore, the properties of the geotextile is assumed homogeneous in all directions and independent of orientation; i.e. isotropic, which is consistent with the plane–strain assumption being adopted here. As most calculated geotextile forces in this chapter are within the maximum limit of Table 6.1, only elastic behaviour is considered.

Elastic–perfectly plastic soil The fill can be different depending on the type of application; e.g. sand, clayey–sand, slurry, etc. which can be completely or partially dry for the granular material. Combining each of these soil types with the variable loading condition, especially after the container being released from the split barge, makes the problem challenging for any constitutive model. By assuming loose state for soil initially in the barge, the importance of stresses dependency on the density variation and the stress level is unclear when it is subjected to the external hydrodynamic load. Advanced constitutive models that take into account density variation; e.g. hypoplastic model, are applicable for dynamic problems; for example the pile driving problem [2, 74]. Furthermore, including a more sophisticated constitutive model such as hypoplasticity, are known to suffer from numerical stability problems. Therefore the elastic–perfectly plastic Mohr–Coulomb model is applied herein for all applications in order to avoid numerical difficulties with advanced constitutive models.

Decomposing the geocontainer problem Considering the explicit implementation of the nearly incompressible fluid, where the time step becomes extremely small, for a problem like dropping geocontainers requires high–end computational resources with multi processing units. It is well known that MPM has high computational power needs as compared with the classical numerical methods. All solved problems in this research are performed on personal computer with quad core processors. Therefore, the entire process of installing geocontainers is decomposed into smaller problems where the significant aspects are treated with more focus on the design consideration mentioned be-

Table 6.1: Mechanical properties of polypropylene woven geotextile, GEOLON 120 [173]

elongation [%]	tensile strength [kN/m]
2	30
5	84
9	120

fore. In other words, the releasing phase of the geocontainer from the split barge is performed dry without considering the water effect. Similarly the simulation of building geocontainers construction is carried out via studying the interaction of two containers only. On the other hand, the dropping phase of a single container is obtained by placing it directly in the water. More details about the feasibility of each assumption follow.

6.2 Releasing of geocontainers from barge

The first important loading of the geotextile is when the barge opens and the geotextile is stretched across the opening. Four stages are distinguished for the opening of the barge and releasing the geocontainer [48]. The first stage begins by stretching and uplifting the lower part of the geocontainer. As the container descends without much deformation in the second stage, more deformation is taking place in the third stage while it is passing through the opening. Finally, the whole container passes through the opening although the open is kept constant. Numerous methods are presented in literature focusing on these stages, but mainly on the last one to predict the geotextile forces at the releasing moment. Most of these methods however are based on dividing the container into rigid blocks where the interaction forces are obtained from the mobilised friction at failure combined with equilibrium state.

Depending on the particular parameter being measured in the dropping process, experimental model tests are performed differently. For instance dropping geocontainer in air, see Figure 6.3, can be used when the tensile forces and the soil deformation are more important than the flow resistance [144]. Furthermore, the barge profile has an influence on the smooth unloading of the container. A sudden opening of the bin reduces the forces that develop. The focus in the MPM model will be on the tensile forces along the geotextile with the corresponding soil stresses inside for certain barge configurations. In addition, the effect of internal soil friction angle and external angle of the barge friction on the evolution of the tensile forces will be investigated.

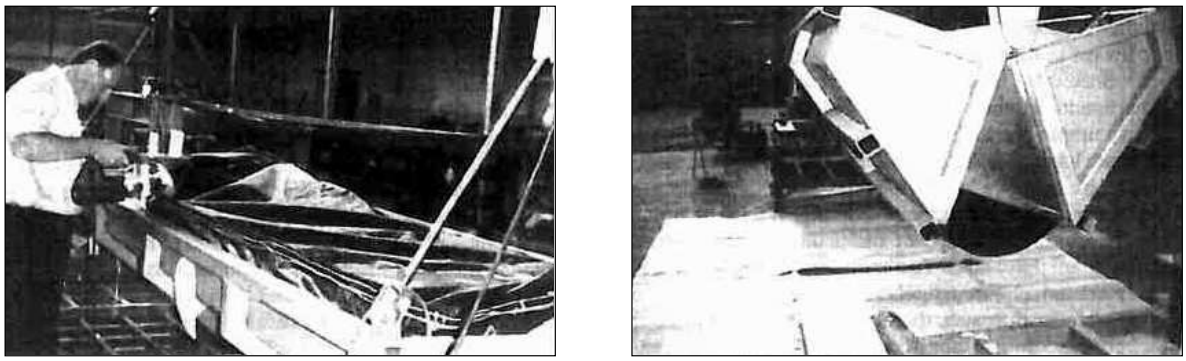

Figure 6.3: Dropping geocontainers in air by NICOLON [144]

6.2.1 Problem description

The dimensions of the barge, as described by de Groot et al. [48], with the MPM discretisations is illustrated in Figure 6.4. Owing to symmetry, only a half of the problem is modelled. The lower tip of the container is modelled as the soil is completely wrapped with *no slack* in the geotextile. A scenario is also examined where extra *slack* placed in practice nearby the barge tip is taken into account in the MPM model by extending the geotextile $0.5\,\mathrm{m}$ outside the barge as shown in the details of Figure 6.4.

The plane–strain problem is represented in a three–dimensional code using 4–noded tetrahedral elements. Failure conditions in the soil are modelled by the Mohr–Coulomb approximation with an elastic modulus of $820\,\mathrm{kPa}$, Poisson's ratio of 0.333, cohesion of $1\,\mathrm{kPa}$, friction angle of 30° and unit weight of $16\,\mathrm{kN/m^3}$. The low value of the elastic modulus is estimated for the case of loose sand poured into the barge such that it is proportional to the square root of the mean stress. For this purpose, the reference value is approximated as $6\,\mathrm{MPa}$, whereas the reference mean stress is proposed to be $100\,\mathrm{kPa}$. The representative mean stress point is taken in the middle of the barge. Linear elastic geotextile is considered with (Young's modulus $\times$ thickness) = $400\,\mathrm{kN/m}$, with Poisson's ratio being zero. Frictional contact is assumed between the barge and the geotextile with a friction coefficient (μ) of 0.3. For the present calculations, the effect of water is not considered and the soil inside the geocontainer is assumed dry.

Initially, the gravitational stresses are approximated using $(K_0 = 0.5)$ and are assigned directly to the soil particles. A prescribed angular velocity $0.5\,\mathrm{degree/s}$ for the opening rate around the centre of rotation has been assigned to the barge material points.

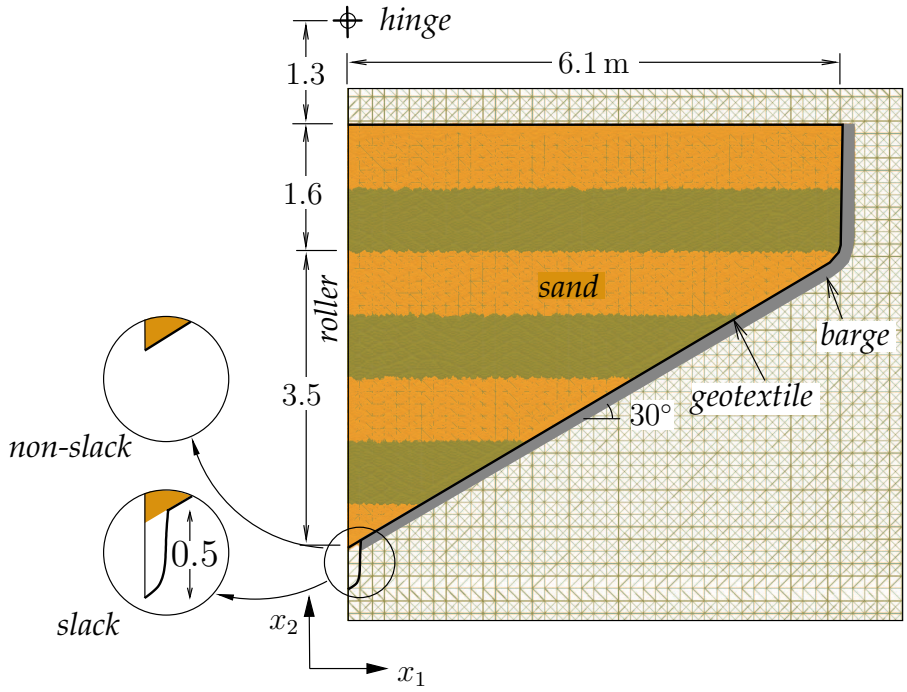

Figure 6.4: Initial MPM configuration of releasing geocontainer from a split barge

6.2.2 MPM results

Considering that the opening phase is achieved slowly, the process is nearly quasi–static, therefore, the force equilibrium shown in Figure 6.5 is applicable. In this figure, the force (F_S) representing the load that squeezes the soil results from the horizontal stress in soil integrated along the plane symmetry. Moreover, the normal reaction force to the barge (F_n) produces the frictional force $(\mu\, F_n)$. All these forces plus gravity and the geotextile tensile force (F_{GT}) should keep the geocontainer in place when the barge stops opening.

The development of the soil and geotextile forces with the opening angle (θ) is shown in Figure 6.6. The small drop at the beginning of the soil force is most likely related to the assumption of the initial equilibrium with K_0 procedure, which quickly varies linearly. On the other hand, the geotextile force starts from a zero value, tending to also follow a straight line trend. The sharp drop in the soil force and the corresponding increase in the geotextile tension are indications that the soil becomes more free to dilate outside the barge. After this point, the two forces (F_S) and (F_{GT}) eventually approach each other, which tells that the barge does not apply any significant force on the geocontainer [71].

As the barge opening increases, tensile forces in the geotextile (F_{GT}) increase as they keep the soil together. Eventually, these forces pull the soil away from the barge, which in turn decreases the frictional forces between the geotextile and the barge. As a result, the geocontainer loses contact gradually with increasing angle of opening. Holding quasi–static equilibrium, the difference between the soil and geotextile force increases with loading, which is due to the loss of contact during the releasing. Since the frictional force $(\mu\, F_n)$ and the force normal to the barge (F_n) decrease, the term $(F_S - F_{GT})$ must increase to insure an equilibrium state. The linear variation between the two forces can be proven for the quasi–static equilibrium case [143].

Comparing the forces for the geotextile *with* and *without* slack shows a small difference, which indicates that the one without slack experiences higher forces. The impor-

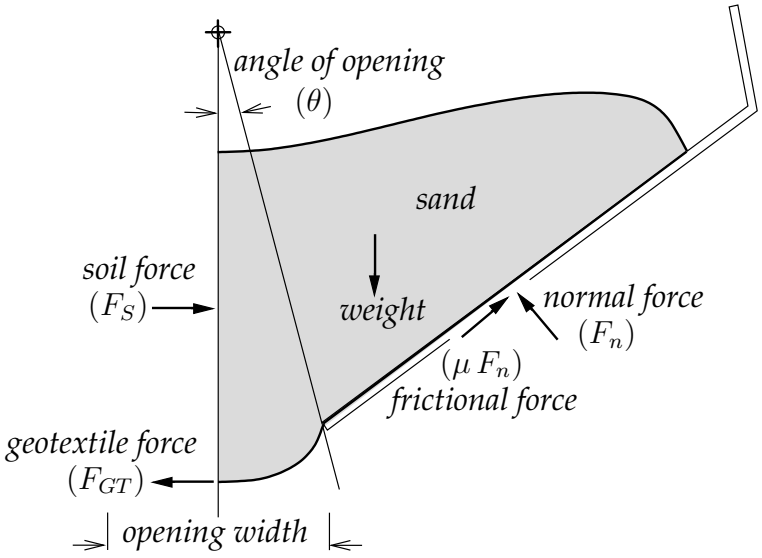

Figure 6.5: Equilibrium forces on the geocontainer

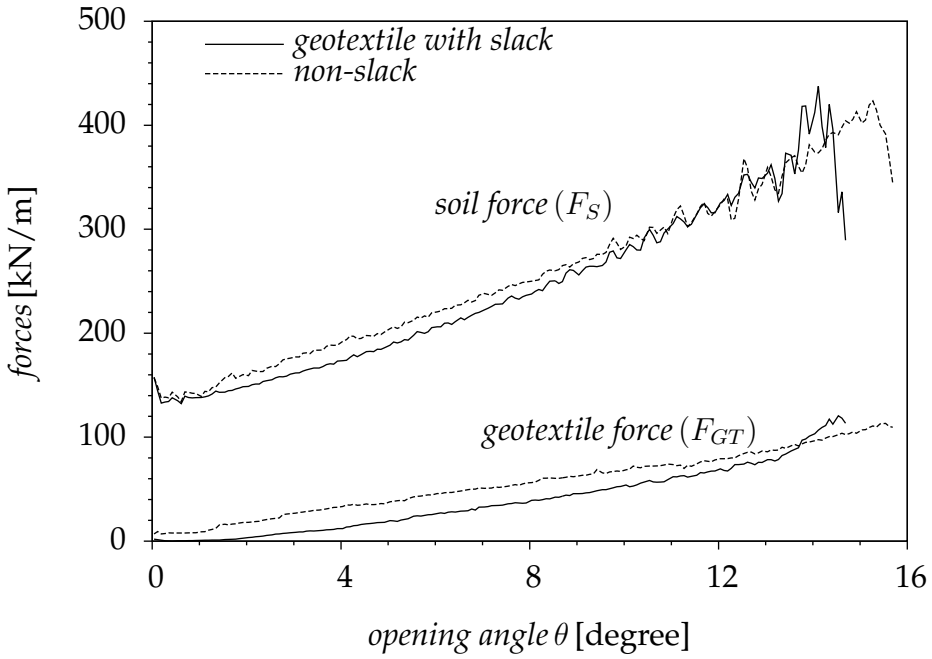

Figure 6.6: Development of forces in the geocontainer

tant gain of adding the extra slack is clearly demonstrated by having a releasing with 2° less than the non–slack case as shown in Figure 6.6.

Roughly speaking, from the opening angle $\theta = 13^\circ$ upward, the variation becomes nonlinear and is most probably dominated by dynamics. The soil layering and the vertical stress are demonstrated in Figure 6.7 for opening angle 13°. During the opening process and due to the location of the hinge, part of the soil is lifted up by the barge. At the same time, the centre part of the geocontainer moves downward as it loses the bot-

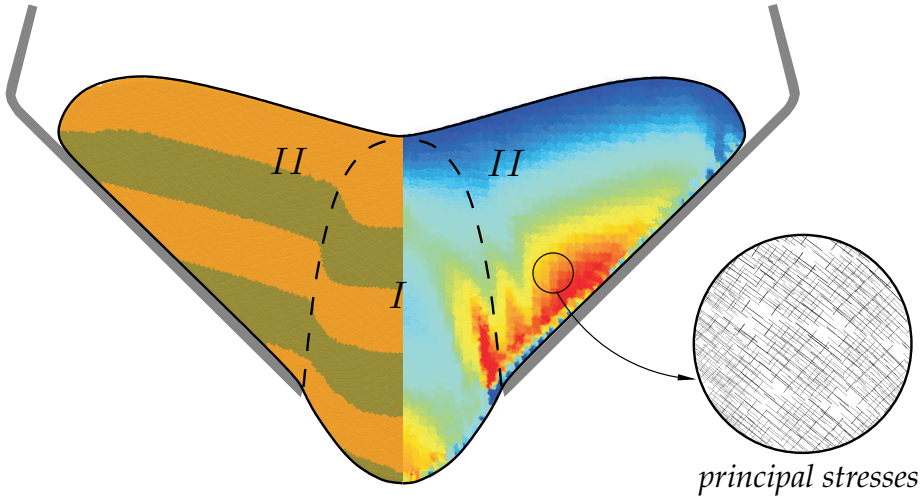

Figure 6.7: Deformation (left) and vertical stress from 0 to -60 kPa (right) for the geocontainer with slack at $\theta = 13^\circ$

tom support. When adding the geotextile slack, the deformation in the soil layering becomes more pronounced and recognisable. The stress field inside the soil is redistributed during loading, showing the effect of arching as illustrated in the details of Figure 6.7. Because of arching there is a load transfer from the middle block *I* to the side blocks *II*, thereby increasing the vertical stresses at the geotextile–barge interface. In Figure 6.7, the narrow area near the geotextile–barge interface has low stresses. The stress oscillation near the prescribed boundary is expected in MPM due to the mapping procedure from the boundary particles to the computational nodes, see Chapter 3.

As shown in this example, the extra geotextile length at the bottom of the geocontainer facilitates earlier releasing of about 2° as compared with no slack. The effect of changing the extra length on the opening angle and the developed forces is not discussed in the course of this thesis, however, the containers considered in the following cases have slack underneath.

6.2.3 Effect of geotextile–barge wall friction

To provide smooth releasing of the container from the steel barge, the friction coefficient should be reduced. Geotextile–steel coefficient might have a value $0.4 - 0.6$, which can be reduced to 0.2 by lining the barge with a geotextile layer [144]. Different type of liner can reduce this value further more; e.g. high density polyethylene (HDPE) [59].

Although practical values of the friction coefficient are bounded within certain limits, testing the extreme cases of fully rough or smooth surface yields the limiting values for the geotextile forces. By repeating the same problem of releasing the geocontainer and changing the coefficient of friction $0.0,\ 0.3$ and 1.0 gives different developed forces along the geotextile as shown in Figure 6.8, which correspond to an opening angle (θ) of 8°. In all curves, the maximum corresponding value of the tensile force is located at the edge of the barge. Even though this segment of the barge bottom is slightly curved in the numerical model, forces concentrate where the free hanging part is held. In this figure the (black dot) represents the location of the barge edge, at which the left part is free hanging geotextile while the right is still in contact with the barge.

As expected in the rough wall case, the geotextile is pinned in the barge due to the high friction while the hanging part is subjected to high tensile forces due to the continuous opening of the barge. On the other hand, the smooth case has better distribution of the tensile forces along the geotextile length, as the entire container is sliding down. In order to hold the soil weight, therefore, the geotextile experiences more tension in the smooth case as compared to $\mu = 0.3$ where the geotextile does not releasing that much.

For each of the three cases, the required barge opening to complete the releasing is different and the tensile force varies accordingly. The maximum opening angles are $11,\ 15,$ and 24°, which correspond to friction coefficients of $0.0,\ 0.3,$ and 1.0, respectively. The location of the maximum geotextile forces within the opening is always at the barge edge and nearly limited with the values shown Figure 6.8. At the last moment of releasing, different geocontainer configuration is expected for each case, even though all cases have about the same length outside the barge. The two cases with low friction coeffi-

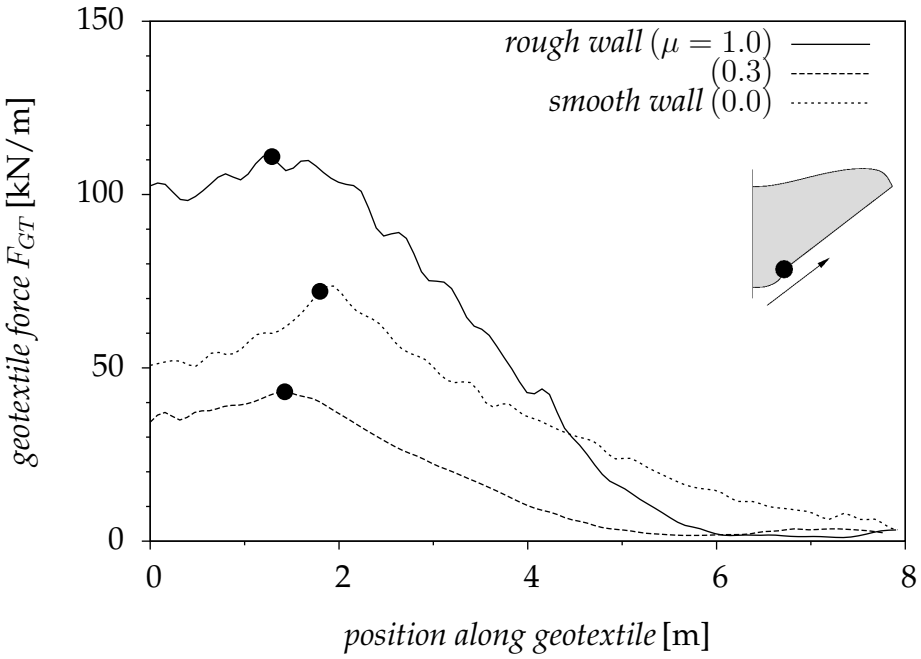

Figure 6.8: Tensile forces along the geotextile for different barge wall friction at $\theta = 8°$

cients have more slender container shapes when the container is fully released. On the other hand, the container with rough wall has more regular width compared to released length. The process is not quasi–static anymore and inertia effect is expected to have influence before the end of releasing, which has an impact on the developed forces.

6.2.4 Influence of variation of filling materials

The fill materials can vary from frictional material to a more liquid behaviour material; e.g. sand or slurry, respectively. As expected when the filling material has higher shear strength, more opening angle is required to release the bag. However, the tensile forces reduce due to arching effect, see Figure 6.7. It is important to recognise that the variation of the fill does not have influence on the tensile forces at the releasing phase only, but also on the impacting when the container hits the subsoil where the kinetic energy should be dissipated.

In this research, the effect of the internal friction angle (ϕ) is investigated by considering three different values 25, 30, and $35°$. The displacement and the geotextile forces shown in Figure 6.9 are traced at the lowest point of the container. The little downward jump in the displacement of the three soils is expected due to falling of the traced point into the slack underneath. However, the jump value did not catch the length of the added slack $0.5\,\mathrm{m}$ completely, which can be justified by two reasons. Firstly, the added slack is pulled away with the barge opening, therefore, the relaxed geotextile will be lifted up accordingly. Secondly, the relation between the geotextile and the soil inside is assumed rough in the MPM model even though an initial gap is assumed. Hence, a

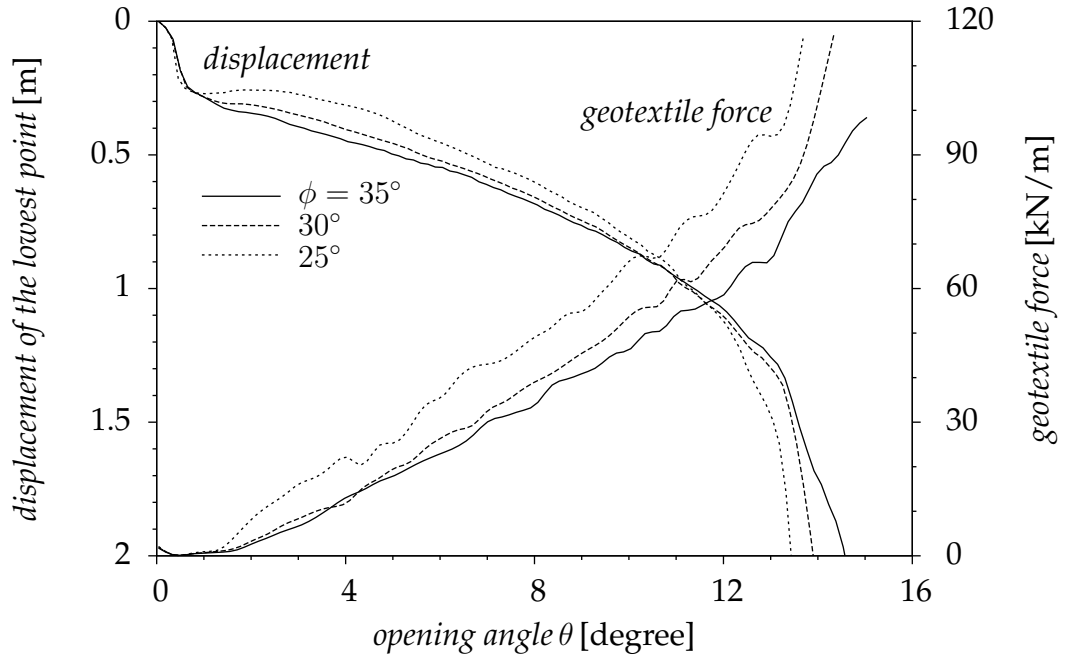

Figure 6.9: Displacement and geotextile force of the lowest point in the container for different soil type

falling soil particle will slow down as soon as it shares the same element of the geotextile. Nevertheless, the displacement curves can be linearised up to an opening angle of $\theta = 11°$ which indicates a dominant quasi–static process. The steep non–linear trend afterward is most likely due to the influence of dynamics.

Although the geotextile forces in Figure 6.9 show different values for different soil friction angle, the difference can be attributed to the earlier releasing of the soil with lower soil friction angle. This can be proven by taking a horizontal section at certain geotextile force value. Along this section, the difference in the opening angle is similar to the difference at the end of the releasing.

The last part of investigating the releasing of the geocontainer from the split barge considers the effect of water buoyancy by replacing the dry soil density (γ_{dry}) with a *reduced* density ($\gamma_{dry} - \gamma_{water}$). This assumption implies that the container is completely under the water and the process is done slowly; therefore, the effect of drag is negligible. As illustrated in Figure 6.10, the linear reduction in the soil and the geotextile forces is associated with a higher opening angle. Provided that the soil density is reduced with the ratio $16 : 6$, the soil force reduces with similar ratio while the tensile force is scaled with smaller value. The reason for this difference is better understood by checking the equilibrium in Figure 6.5, in which the frictional force is yielded in the case of higher density. Therefore, sliding of the container is taking place with $5°$ earlier than the reduced density case. Reduced and dry densities provide the limits for tensile forces in the presence of water or not. In practice, the design of the split barge decides which value is more practical.

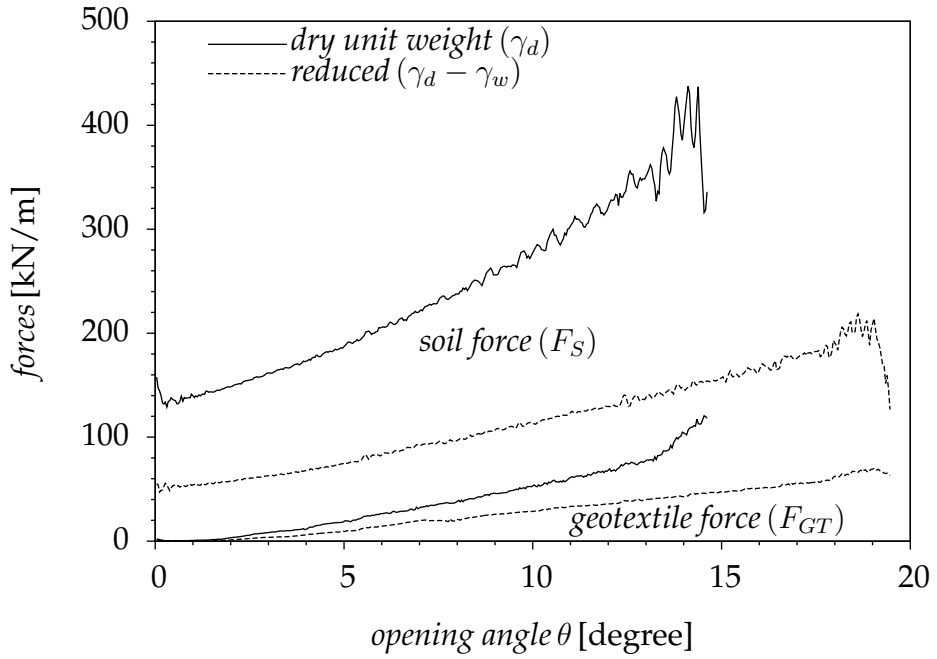

Figure 6.10: Effect of the soil unit weight on the developed forces

6.3 Dumping of geocontainers

One of the most important aspects of installing filled geotextile containers is the dumping phase where the exerted tensile forces reach maximum values. For sand–filled containers, non–elastic deformation is expected to take place when compared with fluid behaviour materials. Adel [1] developed a simple analytical model based on converting the kinetic energy to friction in order to estimate the final configuration of the container.

The deformable subsoil helps dissipate the impact energy via the internal shear resistance of the contained material. Since a soft ground soil decelerates the container gradually deeper penetration is expected as compared with a stiff ground. More deformation for the ground soil reduces the load on the geotextile. Another complexity during the dumping phase is coming from the inconsistency of the subsoil layer, which can be added as an extra strain in the geotextile in order to overcome a soil bump in the ground [144].

Container units can be stacked on top of each other to have a structure of multi–containers. An experimental attempt was made to investigate the stability of dropping a container on stack of already dumped containers [23]. Apart from the installation effects of single or multiple containers, the stability of geocontainer structure needs better understanding of the local failure mechanism of containers under hydrodynamic load [140, 146].

6.3.1 Dumping of single container

The objective of the following example is to model the salient features associated with installing geocontainers. The problem illustrated in Figure 6.4 is similar to that discussed by de Groot et al. [48]. The sand–filled container, having a percentage of fill of approximately $58\,\%$, is dropped in place. The *percentage of fill* refers to the actual fill volume divided by the maximum possible fill volume that allows a container to comfortably pass through the barge bottom [48]. In our case, the container is falling through air and not water, which implies that the effective unit weight and the velocity of the container before impact are higher than would be encountered in practice. Thus the stress predictions are expected to be higher than those developed when a container falls through water. Nevertheless, the example demonstrates the ability of the MPM to capture the physics associated with allowing a container to drop into place, as well as interact with a second container.

A two–dimensional problem is analysed using a three–dimensional model. The initial location of the container is $8\,\mathrm{m}$ above the ground that consists of $1.5\,\mathrm{m}$ layer of soil. Much of the domain consists of empty elements. An element is not considered in the computation until it contains at least one particle. The placement process is simulated by allowing the lowest point of the barge to swing open about the hinge at a separation rate of $6.4\,\mathrm{m/s}$.

The geotextile is modelled as a linear–elastic material having an axial stiffness of $400\,\mathrm{kN/m}$ and negligible mass. An elastic–perfectly plastic Mohr–Coulomb model is adopted for the soil. Assuming the soil inside the container is very loose, its elastic modulus is estimated to have a value $820\,\mathrm{kPa}$ whereas that of the ground is assumed to be $6000\,\mathrm{kPa}$. The unit weight of the soil inside the container and that of the ground is taken as 18 and $20\,\mathrm{kN/m^3}$, respectively, with both soils having a friction angle 30°, zero dilatancy, 0.333 Poisson's ratio and a cohesion of $1\,\mathrm{kPa}$. A dynamic friction coefficient of 0.3 is adopted when modelling the resistance that develops between the geotextile of the container and the bottom of the barge. A similar value of friction coefficient is used for geotextile–geotextile and geotextile–ground soil contact.

The first snapshot in Figure 6.11 shows the barge at maximum opening and the geocontainer is sliding out of the barge while its top part is squeezed toward the centreline. In the same figure, the deformed geocontainer shape after hitting the ground is illustrated, which clearly shows by tracking the layering that the soil in the upper half is redistributing with the lower half compressing. In an actual application, where a container falls through water, this effect is expected to be less pronounced due to the effect of the water. After dropping the first geocontainer, see Figure 6.12, the geocontainer seated on the ground such that it pushes the ground down and out under the container and up along the edges.

When the equilibrium state is approached where the kinetic energy is almost fully dissipated, the container resting on the ground should have a rectangular or a semi–oval shape depending on the amount of soil in the container. Pilarczyk [144] presents the upper and the lower limits for the maximum height of the geocontainer, which depends on the amount of fill. Substituting the characteristics of the problem gives lower and upper limits of 3.7 and $7.7\,\mathrm{m}$, respectively. Referring to Figure 6.12, the final geocontainer thick-

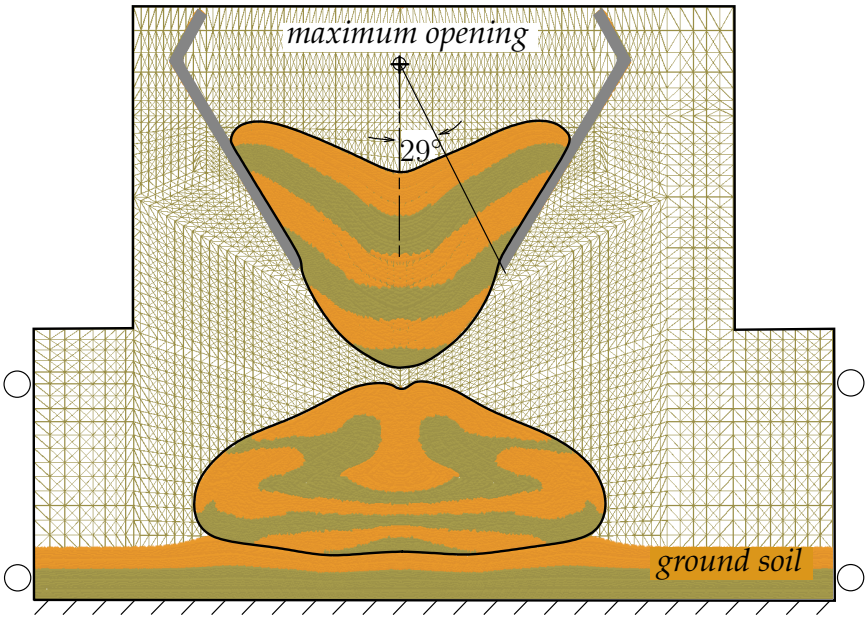

Figure 6.11: Snapshots for the first geocontainer during installation process

ness is $3.9\,\mathrm{m}$, which corresponds to the rectangular shape. Figure 6.13 shows the vertical stresses within the first geocontainer after being placed on the ground. The gravitational stresses are seen to be symmetric through the centreline and almost linearly distributed with depth except for some oscillation near the contact with the ground. These oscillations can be reduced by having finer mesh along the interface.

6.3.2 Interaction of geocontainers

To construct an underwater structure, many containers are required. For example, the submerged containment dike on the river Elbe in Twielenfleth/Germany consists of more than 600 geocontainers, with each containing $300\,\mathrm{m}^3$ of soil [64]. As a first step of modelling such a structure, a second geocontainer is introduced in this study with $2\,\mathrm{m}$ offset to the right as illustrated in Figure 6.12. At the end of the second bag installation, it is seen to have rotated on the first container and eventually rest partially on the ground as depicted in Figure 6.13. A large part of the second container is laying on the first one increasing its vertical stresses considerably. The fact that the ground layer is deformable has an impact on the uniformity of the stress distribution along the bottom of the first container. Again the small stress oscillation along the interface between the two geocontainers is related to the contact algorithm.

A last point to investigate in this study is the force variation developed along the geotextile upper surface $A-B$ in Figure 6.13. The distribution of the tensile force per length of geocontainer (tensile stress in the geotextile times thickness) along the upper part of the first container is shown in Figure 6.14 after first stage of installation. The forces are in the range of $80-90\,\mathrm{kN/m}$ and almost equally distributed along the section. It goes up

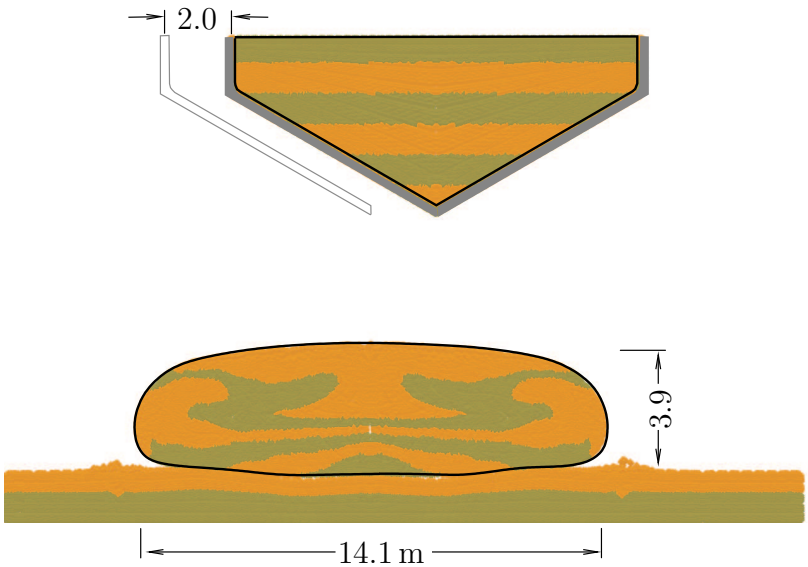

Figure 6.12: Offset of the second geocontainer in barge after dropping the first one

to $105\,\mathrm{kN/m}$ near to the centreline after the second installation stage. The figure shows that the forces at the far ends of the container are released especially where the second container is resting to the right as the soil inside is squeezed down. The maximum curve refers to the force variation in the membrane of the first geocontainer as it is being loaded by the second container at the time it reaches the most critical condition, which is about $7\,\mathrm{s}$ before the final state. We see that there is an approximate 30 percent increase of the peak force relative to the peak force that develops after the second container has come to rest. In other words, the critical stress condition for design does not correspond to the

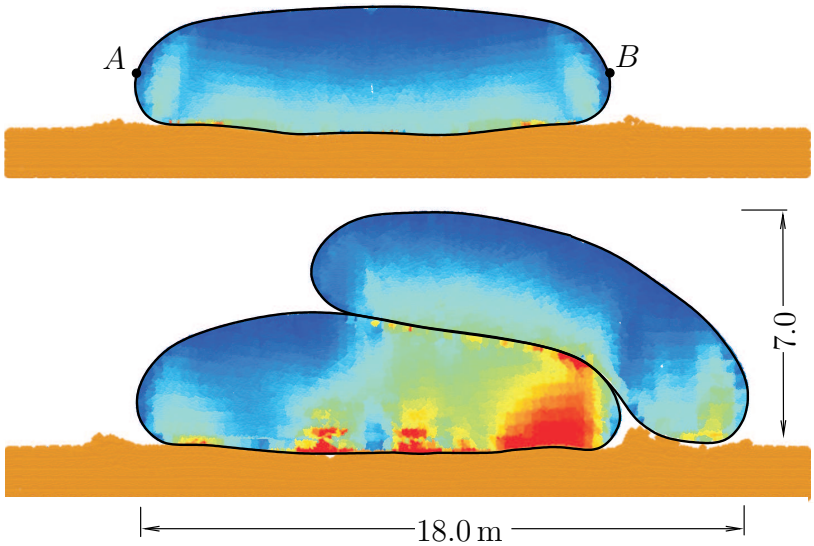

Figure 6.13: Vertical stress; blue colour is zero stress and red is $-170\,\mathrm{kN/m^2}$: (top) after first geocontainer is released and (bottom) after the second is released

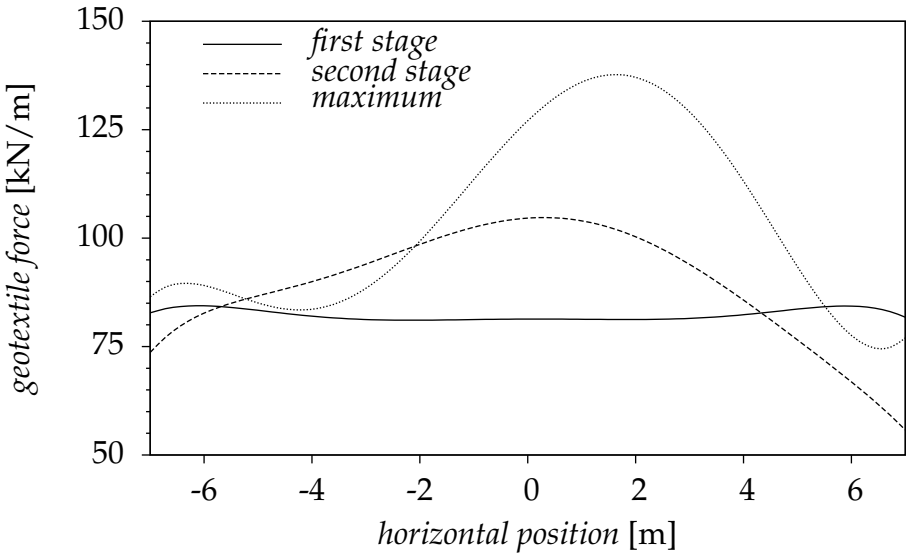

Figure 6.14: Geotextile forces along section *A-B*

final equilibrium state, but rather to time during impact before equilibrium is attained.

The simulation of dropping a geocontainer in place demonstrates that the MPM model is capable of predicting the shape and thickness of the container that consistent with the criteria proposed by Pilarczyk [144]. The model also predicts vertical stresses that are consistent with what one would expect. It is also shown that the formulation can handle the interaction of two containers.

6.4 Validation with a model test

Owing to the complexity of dropping the sand–filled container in water, lab tests were performed as reported in literature to provide more insight about the basic concepts of the process. An example of these tests is the one carried out at the Brutus facility of GeoDelft/Deltares [23, 32]. The series of tests simulated the mechanism of dropping scaled containers, in which the effect of soil and geotextile properties on the dropping velocity and the positioning were studied. Furthermore, the interaction of multi containers was investigated in these experiments, as well as the stability of a container stack.

Scaling a model down in lab implies using different scaling factors for the measured quantities. For instance, performing a test n times smaller than the prototype in gravitational acceleration produces a geotextile force, which must be scaled with n^2. Therefore selecting such a soft geotextile material for the model test becomes tricky, unless different scaling rule is employed. Moreover, the selection of the fill must obey the scaling, otherwise, different permeability of soil might interfere the dropping process.

The available measurements are based on experiments performed in gravitational acceleration, which makes the control of the physical quantities challenging. Moreover, no precise information about the mechanical properties of the soil or the geotextile are

provided. Hence, the focus of the MPM model is to validate the water model without paying attention to the container.

6.4.1 Deltares model test

The modelling was performed at a facility of $2\,\mathrm{m}$ length and $1\,\mathrm{m}$ width, provided with two parallel glass windows for visual monitoring. The level of water in the testing box was $0.8\,\mathrm{m}$ height as depicted in Figure 6.15. A textile sheet was used for the bag, which was filled with sand material. The size of the container is scaled down by a factor of 20 as compared with the prototype. The length of the container did not follow the scaling factor strictly. The final specifications of the sand bag is listed in Table 6.2.

Figure 6.15: Deltares model test for geocontainer [24]

Initially, the container was placed horizontally above the water level using a beam instead of a split barge [25]. The falling and impacting of the containers were monitored using digital camera as well as a sensor placed inside the bag. Few tests among the measurement set a reasonable dropping velocity profile. Nevertheless, the selected case matches the analytical model [1] and a numerical model [23] quite well.

Table 6.2: Parameters of dropping container model into water [23, 25]

parameter	unit	value
sand density	$\mathrm{kg/m^3}$	1900
mass	kg	25
geotextile area	$\mathrm{m^2}$	0.25
container length	m	0.65

6.4.2 MPM simulation

The lab test is simulated in MPM including water and the interaction between the three components: soil, water and geotextile. As mentioned earlier, the focus in the MPM simulation is on the water modelling. Thus, the mechanical properties of the soil and the geotextile are assumed to match those presented in Table 6.2 without spending much effort to optimize them. The viscosity of the water is assumed to be constant $\mu = 8.9 \times 10^{-4}\,\mathrm{Pa.s}$ with a bulk modulus of $K_f = 2.13\,\mathrm{GPa}$.

The configuration of the bag textile is tailored such that it matches the shape of the prototype. Knowing that the prototype is polygon shape, see Figure 6.4, the container is placed on top of the water level with the corresponding dimensions shown in Figure 6.16. Since the time step size of the explicit scheme depends on the minimum characteristic element length and to avoid small length caused by poor discretisation of the tetrahedral mesh, a regular mesh is adopted. Both, the container and water are discretised using tetrahedral mesh where 10 particles are placed initially in each element. Since regular mesh used for the entire domain, some elements of the container are partially filled with particles at the beginning of the computation, see Appendix B. According to the coupled FE–MP approach, the textile bag is discretised using triangular mesh that ensure a mesh ratio $MR = 10$. Hydrostatic pressure distribution is assigned for the water particles, whereas $K_0 = 0.5$ is assumed for the sand bag.

The process of the soil container sinking into the water is shown in Figure 6.17. The sudden drop of the container produces a water wave at the edge of the container traveling toward the tank boundaries. Simultaneously, the container deforms into more an elliptical shape while it sinks deeper in the water. At time $0.5\,\mathrm{s}$, the two water parts come together to cover the container completely. It can be noticed that the flow symmetry until the container starts tilting to the right whereas a water circulation is forming in the wake at time $0.6\,\mathrm{s}$. A noticeable reshaping in the lower water layer can be seen at time $0.8\,\mathrm{s}$, which indicates deceleration of the bag due to water cushion underneath. The intensity

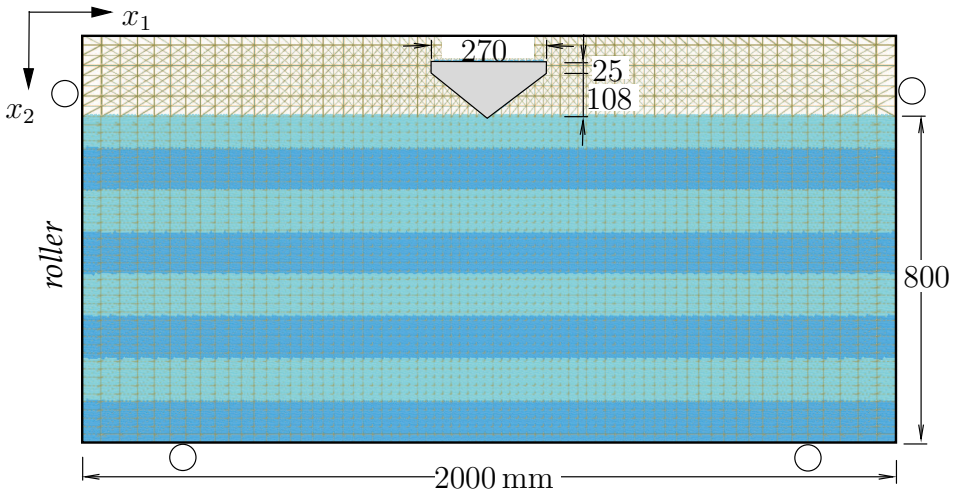

Figure 6.16: Initial MPM configuration to model Deltares test

and size of the circulation behind increase as the bag moves downward. At time $1.1\,\mathrm{s}$ the container lands first to the right and then bounces up off the floor at time $1.2\,\mathrm{s}$. At this time, the accelerated water around the bag turns its direction outside and lifts the lower layer of the water. The computation stops here as the turbulent flow becomes dominant.

In the case of moving fluid flow across fixed solid object, or moving solid through stationary fluid like our case, a circular movement of the fluid is expected in the wake of the solid. In order to evaluate the size of the circulation, the vorticity of any point in the domain can be written as

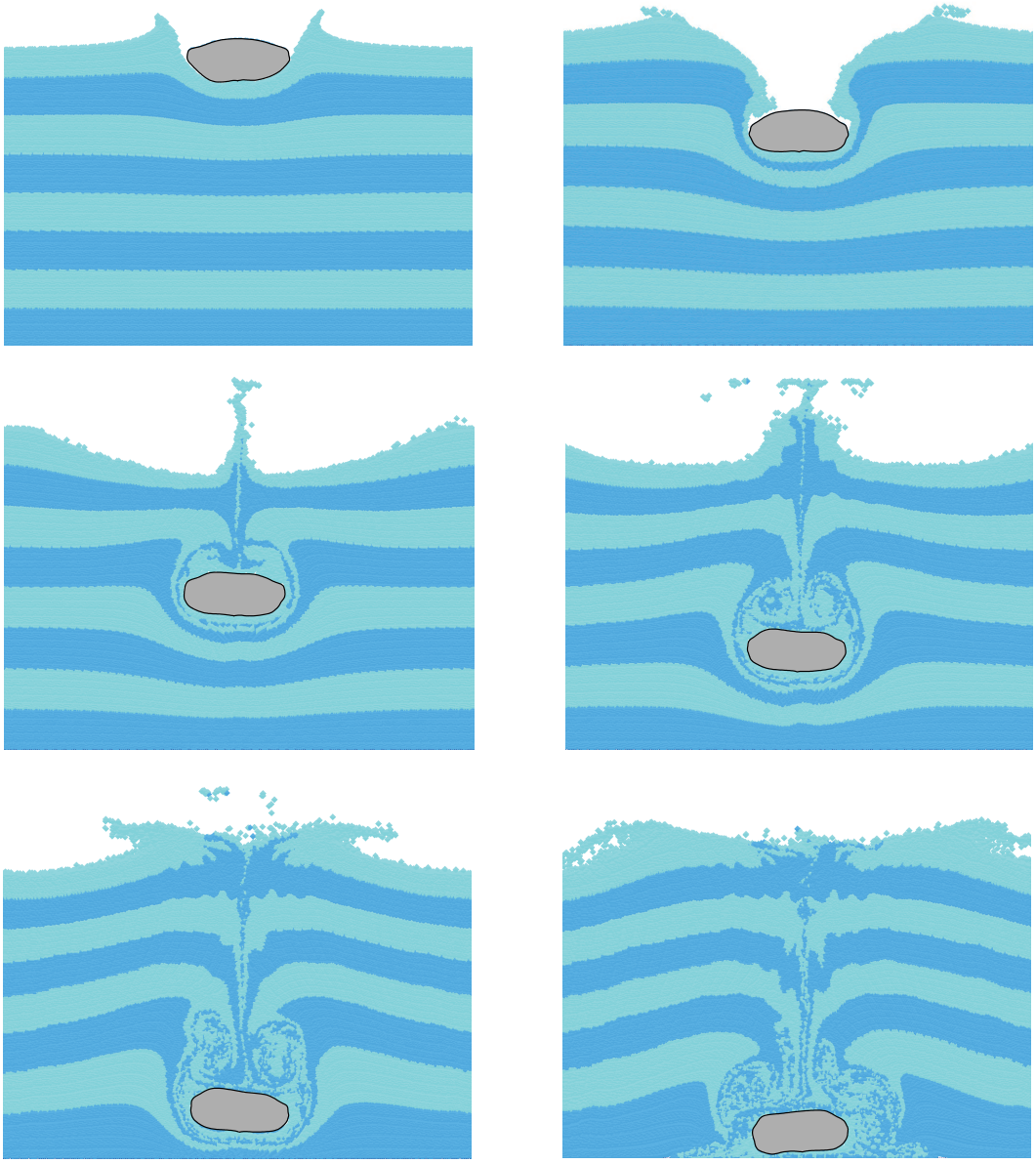

Figure 6.17: Snapshots for the container sinking into the water with $0.2\,\mathrm{s}$ time interval

$$\boldsymbol{\omega} = \boldsymbol{\nabla} \times \boldsymbol{v}, \tag{6.1}$$

where $\boldsymbol{\omega}$ is the vorticity of the velocity field $\boldsymbol{v}$. For the considered plane–strain assumption with one tetrahedral element in depth, the vorticity vector $\boldsymbol{\omega}$ reduces to

$$\omega_3 = \frac{\partial v_2}{\partial x_1} - \frac{\partial v_1}{\partial x_2}, \tag{6.2}$$

which represents the vorticity scalar in the x_3 direction. Applying Equation 6.2 to the linear velocity interpolation of the low–order tetrahedral element adopted in MPM, gives constant value across the element. Therefore, the accuracy of the current MPM algorithm is first–order and care should be taken if high rotation is taking place in the flow. The vorticity distribution of the entire flow problem is shown in Figure 6.18. The region around the bag has nearly symmetry vorticity distribution, whereas outside this region the flow is almost irrotational. A close look at the velocity vectors around the container shows an acceleration of the nearly incompressible fluid due to the penetration of the solid body, while the domain far away from this region is hardly moving. The area next to container boundary shows irregular velocity distribution which is caused by the fluid–structure interaction in MPM. However, the size of the irregular velocity field is bounded with the size of one computational element.

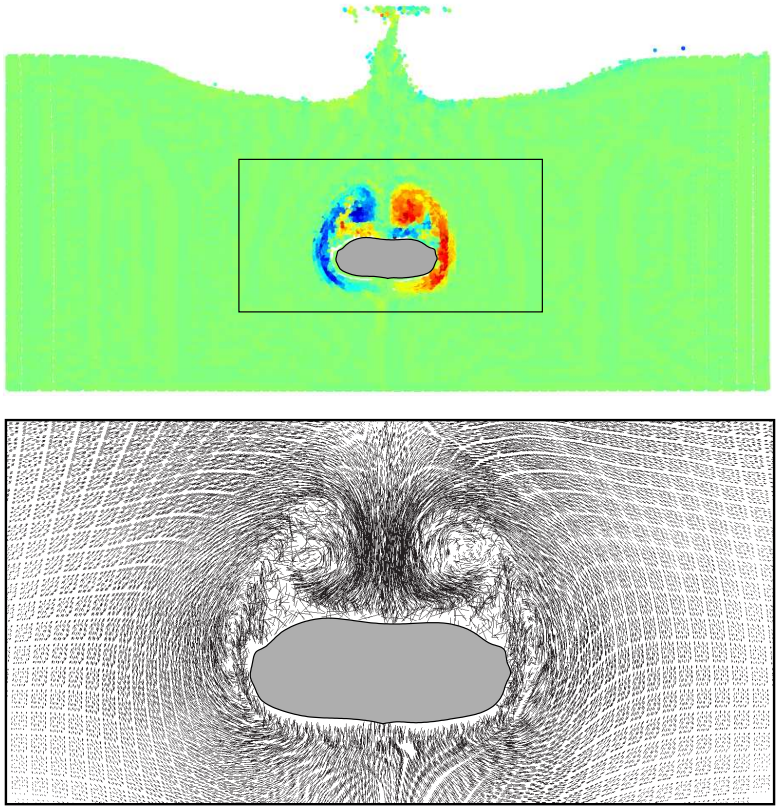

Figure 6.18: Vorticity (top) varies from -90 to $+90\,\mathrm{s}^{-1}$, and close–up to the velocity profile (bottom) around the container at $0.7\,\mathrm{s}$

The initial hydrostatic pressure distribution in the water does not change much for the first $0.3\,\mathrm{s}$ of the dropping process except for slight compression under the container as illustrated in Figure 6.19. In this snapshot, the imposed free surface condition can be seen clearly along the two steep water columns. As the flow around the bag becomes more turbulent at time $0.6\,\mathrm{s}$, the layered pattern of the pressure does not exist anymore. Nevertheless, the first and the last third of the computational grid still reflects the hydrostatic state. Furthermore, the water column above the container is building up pressure from the free surface state. Proceeding further downward, the pressure difference across the container is increasing to reduce the dropping velocity at time $0.8\,\mathrm{s}$ while the initial pressure distribution of the first and last third are almost intact. Important to mention here is that the rigid boundaries must be far away from the disturbed region, otherwise, an efficient silent boundary must be placed. As a conclusion from the current model test, placing the rigid boundary at a distance about the same as the dropping height gives reasonable pressure distribution with little boundary reflection.

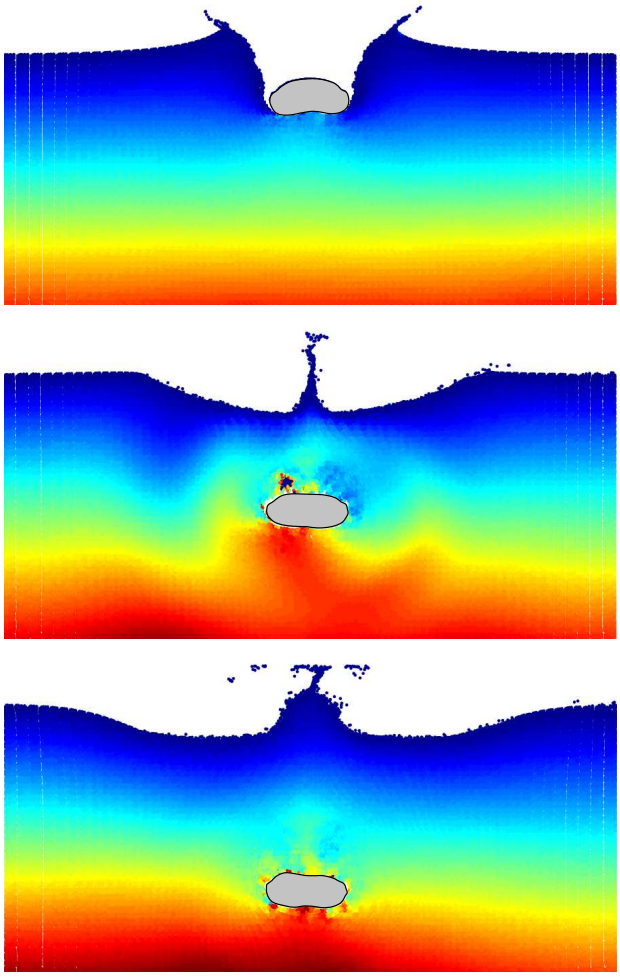

Figure 6.19: Pressure distribution in the water tank; blue colour is zero pressure and red is $9\,\mathrm{kPa}$ at different time: (top) $0.3\,\mathrm{s}$, (middle) $0.6\,\mathrm{s}$, and (bottom) $0.8\,\mathrm{s}$

6.4.3 Effect of initial configuration

In the previous MPM simulation, the initial configuration of the soil container is assumed as a polygon shape similar to the original prototype geocontainer. There are few details regarding the initial shape of the container of the lab experiments carried out at Deltares. To see the effect of the initial shape on the dropping velocity, an elliptical hypothesized shape is assumed. The cross sectional area of the bag and the geotextile length is kept the same as for the polygon shape. The shape is illustrated in Figure 6.20.

Performing the MPM simulation for the new elliptical shape gives about the same flow field as the polygon shape, except the initial penetration of the container is found to be slightly slower than that of the polygon shape. The velocity of a point at the centre of the bag for both configurations is compared with the experimental measurement in Figure 6.21. In this figure, the MPM container accelerate with constant rate for the first $0.1\,\mathrm{s}$, whereas the polygon shape has steeper inclination. The sharp head of the polygon allows it to penetrate faster, however, the results for both MPM containers are close to each other after $0.4\,\mathrm{s}$.

In spite of oscillation shown in the experimental curve, the entrance effect can be detected as an acceleration up to $0.4\,\mathrm{s}$. After $0.6\,\mathrm{s}$ of begin the dropping, the lab model bag accelerates up to a value of $0.8\,\mathrm{m/s}$ at $0.8\,\mathrm{s}$. Adel [1] formulates an analytical equation based on drag force against single point expects $1.0\,\mathrm{m/s}$ at the same time. This formula

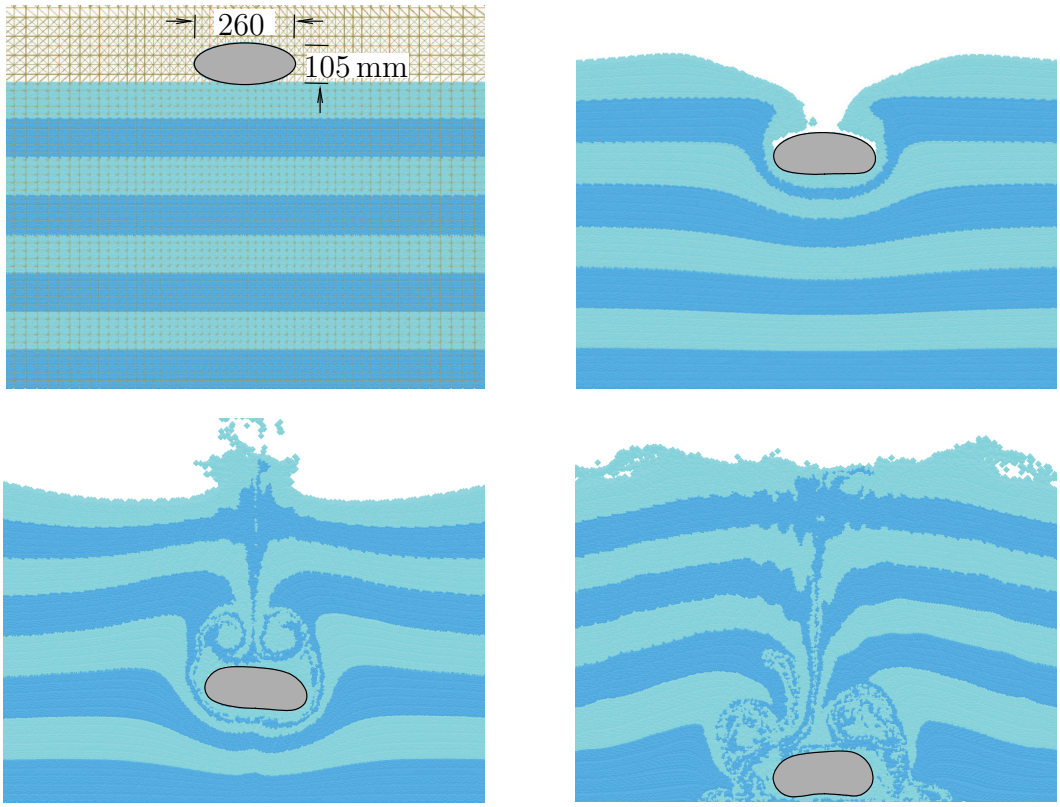

Figure 6.20: Initial configuration of the elliptical shape container and snapshots with $0.4\,\mathrm{s}$ time interval

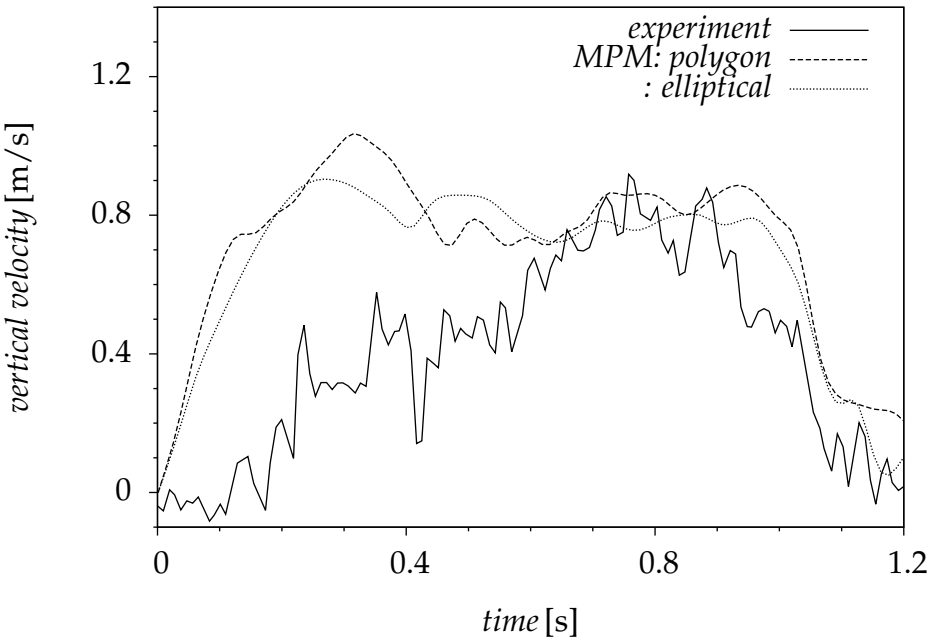

Figure 6.21: Comparison of the measured vertical velocity [25] with the MPM results

anticipates a constant terminal velocity slightly larger than $1.0\,\mathrm{m/s}$. Regardless the entrance length, which is shown to depend much on the initial shape, both MPM shapes predict the experimental velocity quite well.

6.5 Dumping of geocontainers in water

Dumping geocontainers in water has many applications varying from constructing dams to disposing materials. Constructing the core of a dam is an attractive use of geocontainers as a replacement of rock and rubble. For such an application, the water depth is usually within the range of $20\,\mathrm{m}$ [26, 59, 180], whereas disposing contaminated dredged materials is usually performed in deep water. Due to the water depth, which might reach $6000\,\mathrm{m}$ in the last application, a vortex shedding is expected to cause big change in the container shape [177]. Different numerical models can be adopted according to the problem type, however, the deep dumping problem requires precise solving of the Navier–Stokes equation with a suitable turbulent model that is out of this research scope.

Performing large–scale measurement for dumping geocontainer is a demanding task requiring control of many parameters depending on the objective of the experiments. Installing geocontainer without tearing the geotextile is the most critical issue during the placement. When the container leaves the barge safely, it gains velocity during its travel through the water column. During this stage, no high tensile force is expected in the geotextile according to Figure 6.2, while the highest values are most probable during

the impact of the container on the subsoil. In this section, the dumping phase will be investigated by simulating the field measurement obtained by van Oord [180]. The aim of the numerical model is to estimate the maximum tensile forces with the deformation of the sand–filled material.

6.5.1 Field measurements of sand–filled container

The prototype test performed in 1994 by van Oord [180] is considered as a field measurements reference in this section. The test was carried out in the sand pit at Kekerdom in the Netherlands. Four geocontainers were dumped in different water depths. The aim of the test was to develop an appropriate method for dumping geocontainers without failure and to investigate their behaviour during dumping. As a conclusion of the test, two containers were failed during installation. The first failed very early due to quick release of the highly filled container, while the other failed later when it hit the ground due to the incorrect sand filling in the longitudinal direction. The unequal filling in the lateral direction causes rotation of the container, which in turn predicted higher vertical displacement than the real one. On the other hand, the measurements of the dumping velocity and the pressure inside the geocontainer are considered successful.

One of the two surviving geocontainers was filled with sand up to $130\,\mathrm{m}^3$, compared to the theoretical volume of $368\,\mathrm{m}^3$. It had a length of $24.5\,\mathrm{m}$. Although the water depth was $13\,\mathrm{m}$, the fall height was approximated as $9.8\,\mathrm{m}$ assuming that the split barge was impeded inside the water. Polypropylene woven geotextile GEOLON 120 was used having a specific mass of $630\,\mathrm{g/m}^2$, and Young's modulus $1000\,\mathrm{kN/m}^2$, with $120\,\mathrm{kN/m}$ tensile strength. Two longitudinal seams, having a strength of $70\,\%$ of the nominal value, were located on top of the container. Two places along the container length were selected to measure velocity and pressure. The front and rear sensors were placed about $3\,\mathrm{m}$ from the edges. The final inspection of the geocontainer after being placed were investigated by specific divers.

6.5.2 The MPM numerical model

Owing to limitations in the current implementation of the MPM model, the releasing phase is omitted from the simulation. The emphasis is on the dumping phase. To initialise the numerical model, the container is assumed as an elliptical shape outside the barge. The dimensions of the ellipse oriented vertically are selected such that the length of the geotextile and the amount of the soil inside are the same as in the field test. The soil container is impeded initially inside water to resemble the height of the actual height in the experiment. The soil characteristics of the container and the subsoil layer are modelled using Mohr–Coulomb failure criteria as listed in Table 6.3. The water is given the same properties as for the lab test in Section 6.4.

The three dimensional problem is approximated as a plane–strain problem. A regular tetrahedral discretisation is adopted with finer mesh at the centre where the high

Table 6.3: Soils characteristics for dumping geocontainer in water

property	unit	container	subsoil
unit weight	$\mathrm{kN/m^3}$	16	20
elasticity modulus	MPa	2.8	10
cohesion	kPa	0	0
Poisson's ratio	–	0.333	0.333
friction angle	degree	30	30
dilatancy angle	degree	0	0
drainage type	–	drained	undrained

deformation is expected. The configuration of the problem and the boundary conditions are shown in Figure 6.22. Similar to the lab test validation, initial hydrostatic pressure distribution is assumed for the water and K_0 condition for the soil considering the effect of the water column for the subsoil layer. The control point for checking vertical velocity and pressure is selected at the centre of the container.

6.5.3 Comparison of the two models

Owing to the uneven release of the prototype model in the experiment, an out–of–phase in the velocity of about $2\,\mathrm{s}$ was recorded between the front and rear point as shown in Figure 6.23. Since the front part of the container was released first from the barge, it is pulled up due to the sticking of the rear end. In both curves, the first peak represents the releasing from the split barge stage while the second is when the container reaches the maximum velocity. The final inspection shows that the container rotated to the right

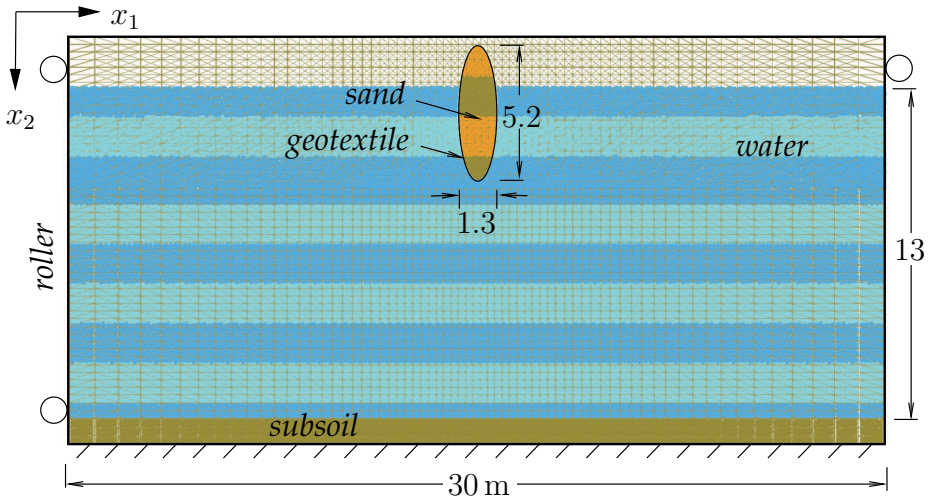

Figure 6.22: Initialisation of the MPM model for the sand–filled container

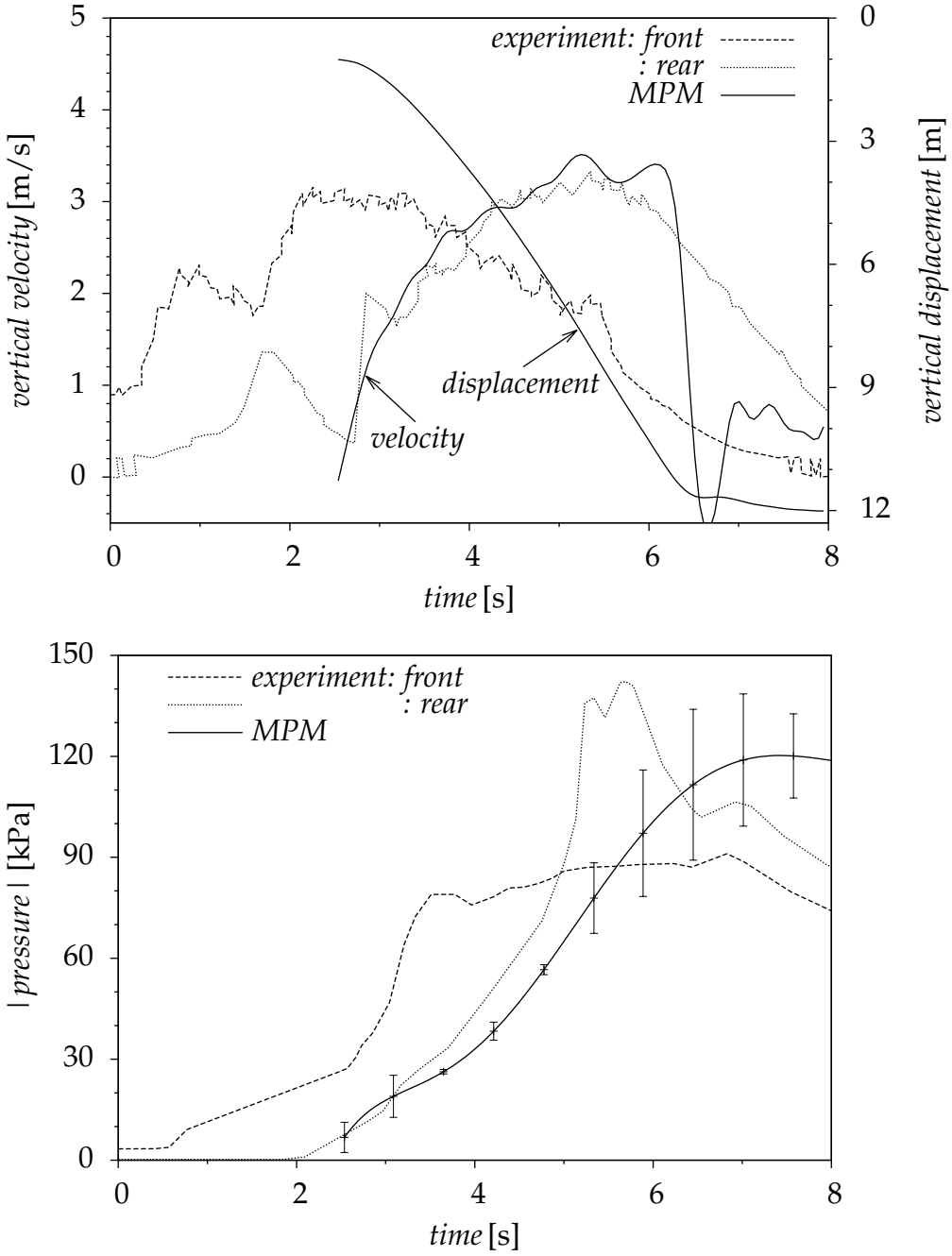

Figure 6.23: Comparison of the measured quantities [180] with the MPM results: (top) vertical velocity and (bottom) pressure

ending up upside down. The vertical displacement of the container was determined by numerical integration of the given velocity, which gives an overestimation of the actual depth. The discrepancy between the calculated displacement and the real water depth was attributed to the geocontainer rotation where the measurement wires are pulled around the container leading to a larger measured depth [144]. Adel [1] compared his analytical model with these measurements and predicted a value of $4.5\,\mathrm{m/s}$ for the terminal velocity without air. However, the last value reduces to the measured value $3.3\,\mathrm{m/s}$ when $17\,\%$ of air is assumed [144].

For the sake of comparison with the MPM container, the rear point is selected as a reference. Hence, the starting point of the MPM velocity is shifted to match the rear point of the prototype model. The trend of the numerical velocity matches the experimental in a quite reasonable manner for the accelerating part, while the MPM expects larger deceleration. In spite of eliminating air bouncy in the MPM modelling, the terminal velocity is nicely estimated. The MPM velocity reaches the terminal velocity in about $3\,\mathrm{s}$. Shortly afterward it starts to feel the ground. The MPM displacement curve, see Figure 6.23, reflects the initial graduate accelerating and the steep decelerating at the end of the dumping phase. The smooth landing of the real container is likely due to the penetration of water through the permeable geotextile, which causes the container to drift to the side combined with flipping it upside down. Even though no information is available regarding the final horizontal location, Bezuijen et al. [27] provided the trend for similar tests with a value of $2\,\mathrm{m}$ aside.

The water pressure was measured inside the sand–filled container of the field experiment. As the MPM container is performed dry, the mean stress is calculated instead of the water pressure with a bar indicating the variation between the horizontal and vertical stress components as illustrated in Figure 6.23 with 0.96 as a coefficient of determination R^2 for the MPM curve. The lower peak of the front end was being related to the material escaping to the rear end, which was still falling [180]. The MPM trend shows a little bump during the first $0.5\,\mathrm{s}$ that is most likely because of the initial conditions, however, it catches quickly a straight behaviour that corresponds to the hydrostatic pressure. The difference between the vertical and horizontal stresses increases when the container approaches the bottom as the vertical component increases rapidly. The final residual value of the MPM mean stress reflects mainly the height of the water column $12\,\mathrm{m}$ while the experiment predicts about $8\,\mathrm{m}$ water column.

During dumping, the geocontainer shape change drastically as demonstrated in Figure 6.24. Soil layering, which are initially horizontal as shown in Figure 6.22, helps the interpretation of the physical phenomena. At time $2\,\mathrm{s}$, the boundaries of the container are pulled up due to the drag being applied by the water flow while the bulb is moving downward. During the falling, not much tensile force is exerted on the geotextile and it is nearly homogeneous around the bag. A maximum value of $10\,\mathrm{kN/m}$ is recorded at the middle of the geotextile that indicates the symmetry of the external hydrodynamic forces. At time $4\,\mathrm{s}$, the geocontainer already touches the subsoil layer and starts to tilt to the right. The core part of the soil is pushed downward inducing $70\,\mathrm{kN/m}$ maximum tensile force in the lower left part of the container as shown in Figure 6.24. Checking the tensile force distribution, the upper half of the bag does not experience high forces.

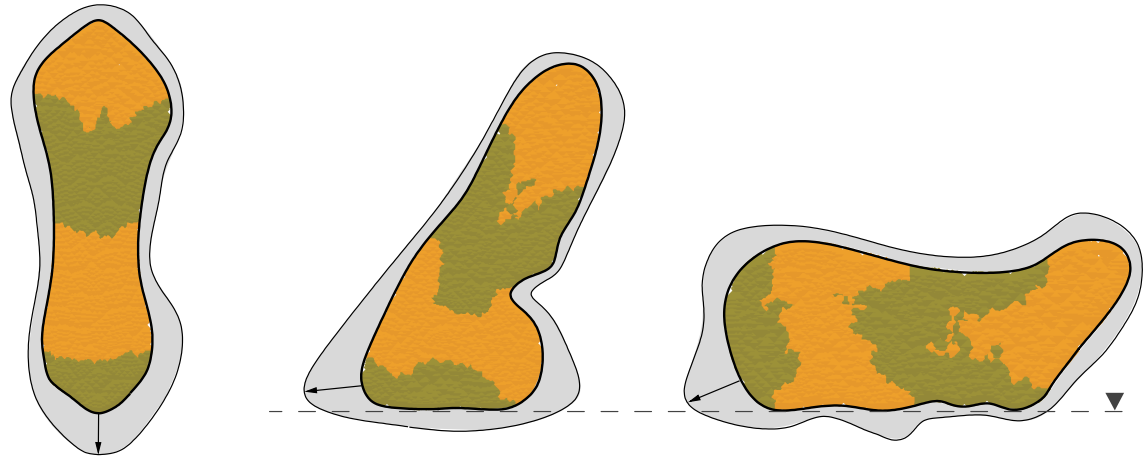

Figure 6.24: Reshape of the sand–filled container with the geotextile tensile force at $2\,\mathrm{s}$ (left), $4\,\mathrm{s}$ (middle), and $6\,\mathrm{s}$ (right)

Owing to the clock–wise tilting, the geocontainer slides on the ground to the left direction producing tensile force along the membrane in contact with the seabed. Proceeding further with the simulation shows that the sand–filled container laid down to the side while it becomes more rectangular shape. At the same time of $6\,\mathrm{s}$, the tensile forces become more homogeneous around the soil bag except for some irregularity along the subsoil layer.

It is important to indicate here that the assumption of rough geotextile–soil contact is expected to have a role on the final geocontainer configuration. For instance, a simulation using distinct element method showed that the soil is separated from the geotextile when the container reaches the ground [141]. On the other hand, the current implementation forces the membrane to follow the soil with no gap. Therefore, the membrane might pull the soil in opposite direction to its movement, see the soil layering in the upper half at time $4\,\mathrm{s}$. Nonetheless, the aim of this study is to estimate the maximum tensile force during the dumping phase, which is shown to take place at the lower half where the material is compressed.

In the present analysis and for the requirement of the fluid modelling, the major part of the considered problem is the fluid material. Hence, the geocontainer itself is discretised relatively coarse. Combining this with the fact that MPM always smears the interface over one computational cell, a thick layer of non–uniform stresses is expected around the geocontainer. Refining the mesh as a quick remedy for this problem would become computationally expensive, especially if we remember that the fluid bulk modulus is the bottleneck of the time step size. Thinking about silent boundary for the water should reduce the problem size, however, care should be taken when fluid particles cross such a boundary.

Chapter 7

Conclusions and recommendations

In the present work, novel geomechanical applications of hydraulic and coastal engineering are highlighted; e.g. problems related to shore protection and breakwaters. For such applications, it is common to build construction units combining soil and geosynthetics materials in site. Large material deformation is expected to take place in the presence of water and hence studying installation effects of these massive units is challenging topic for engineers. Therefore, the physical modelling is the most common admired design procedures in this area. As indicated in Chapter 2, the noticeable lack in numerical simulations was the motive to present a numerical tool able to fill this research gap.

Searching numerical scheme capable of modelling large deformation, few options are available. Among large deformation methods, the material point method is the best suited for history–dependent materials with a flexible framework to include other materials interaction in a single potential structure. Adopting a procedure fits in a finite element configuration, MPM gets a lot of synergy from the well developed finite element method to simulate complex multiphysics applications.

7.1 Conclusions on the numerical modelling

An overview about outcomes and findings from this research including development, validations, and geomechanical applications are highlighted in this section. In general, these conclusions are summarising the whole work as a one consistent unit. Therefore, the reader is referred to more detailed concluding remarks mentioned within the context of the concerned chapters.

7.1.1 Material point method

Starting from the underlying differential equations, original MPM algorithm [169] has been outlined and applied. Although MPM represents the continuum by material points, solution is performed on the the computational mesh. Thus, imposing boundary conditions in MPM is not aligned with the material representation. In order to refine the application of traction boundary conditions is MPM, surface discretisation is proposed. Therefore, the three–dimensional domain is discretised using four–noded tetrahedral elements in a regular manner, while its surface is discretised using three–noded triangular element. The proposed set of particles for traction boundary is placed at the vertices of

the surface mesh. Hence, the traction condition is assigned directly at the surface with no approximation to the superficial layer of material points like in [2].

In order to track surface orientation in MPM, algorithms for calculating the local system has been introduced in literature [191, 198]. These algorithms were developed for regular rectangular mesh, they have difficulties when applied to irregular tetrahedral discretisation. Thus, the surface discretisation concept described earlier is extended here to find local orientation of the surface. By tracking the triangular elements, the deformed surface can be shaped and therefore contact algorithm can be applied accurately. An example of this procedure is presented in the releasing geocontainer problem in Chapter 6 where interpenetration between objects is prevented as an indication of the calculation of accurate normals in spite of the severe deformation; see Figures 6.7 and 6.11.

Since the non–zero kinematic boundary condition is not yet developed in general form in MPM literature, a set of material points is introduced in this study to carry information of the prescribed kinematic boundary. During each computational step, velocity is mapped from the prescribed particles to the computational grid using weighted mapping so that the procedure is consistent with the MPM algorithm. The prescribed boundary particles are applied to simulate the rigid barge for releasing geocontainers where frictional contact is assumed between the barge and the geotextile.

Volumetric locking due to the use of low–order elements is mitigated using nodal mixed discretisation, which is based on smoothening the spherical part of the strain rate tensor. Furthermore, the dynamic relaxation process is employed by applying artificial damping that damps out the wave–propagation problem in efficient way to get the quasi–static solution. Finally, the frictional contact algorithm [14] is implemented and modified to accommodate prescribed boundary condition where the combined solution of all entities is replaced with the trivial solution of the prescribed boundary particles.

7.1.2 Thin–walled structures

Thin–walled elements are incorporated in MPM as defined by York [191] where the membrane effect is dominant. The algorithm shows some drawbacks when it is examined for single–degree of freedom spring–mass system such as sensitivity to the surface discretisation and spurious stress distribution. Therefore, a novel method called coupled FEM–MPM is suggested by treating the thin elements similarly to the finite element method where spatial integration is achieved over the element span instead of the material points. Apart from membrane, traditional MPM is used for any other solid or fluid materials. Coupling between the FE membrane and MPM substances is obtained via internal forces where all materials contribute to the same computational mesh. The proposed method is proved to be less mesh sensitive and produce smooth stress distribution as compared to York's method. Furthermore, the latter approach tends to underpredict lateral deformation, while the coupled scheme is able to match the close form solution.

The main target of the present work is to model geosynthetics materials combined with soil for geomechanical applications. Geosynthetics materials are often made of polymeric products having light weight as compared with soil. Owing to the explicit na-

ture of the dynamic MPM algorithm, mass must be assigned to the particles so that they get acceleration. Therefore, studying stability each of the two membrane approaches for minimum amount of mass is essential. For the spring–mass system, the coupled FE–MP approach shows superior with the ability of reproducing the exact solution for very small value of the membrane mass over York's method.

The geometry non–linearity associated with large deformation is incorporated in the current membrane formulations, which has been proven for a prestressed membrane being stretched laterally with $80\,\%$ extension relative to its original length. In order to cope with the textile feature of the geosynthetic materials, in which only tensile stresses are allowed, a criterion called compression cut–off is integrated and validated for the membrane elements.

7.1.3 Incompressible fluid

In a brief mathematical formulation of a fully incompressible fluid flow, the structure of equations expects numerical instability unless some compressibility is imposed. Assigning algorithmic compressibility to an incompressible fluid helps the numerical scheme to converge towards the correct solution in iterative nature. The artificial fluid compressibility should vanish when convergence is satisfied. In nature, most fluids have some physical compressibility therefore explicit scheme is becoming applicable.

Keeping a unified time integration scheme, explicit integration is applied for fluid as well. Due to the high bulk modulus, volumetric locking destroys the solution quality and is soon becoming fully dominated by spurious modes. As a first remedy, nodal mixed discretisation is applied for a cavity filled with nearly incompressible fluid where the flow is driven by shear forces. Dissimilar to solid materials, the enhancement approach gives inadequate improvement in the velocity and pressure fields of the fluid. On the other hand, the average nodal pressure scheme [29] based on smoothening the total spherical component of the stress tensor gives much smoother velocity field with small variation in the pressure distribution.

Seeing the lid driven cavity problem as the most severe case of testing enhancement procedures, the material points are kept fixed with no update of locations. However, it has been experienced from the collapse of water column where extreme deformation is taking place that both smoothening procedures are required at the same time. The initial rectangular water column collapses due to removing the side support wall. Due to the separation and reattachment the fluid might experience, imposing zero traction condition at the free surface is important to satisfy the free surface condition, which is not a trivial issue in MPM. For this purpose, a continuous density field approach is developed so that the material points are acknowledged to be in free stress state or not. The continuation of the free surface needs to be tuned with a mesh dependent parameter, which is found to be bounded with certain values. The experiments of water column collapse is reproduced by MPM fairly well. Finally, the interaction of geotextile–water is validated with the application of geotextile tube where simplified analytical solution is available.

7.1.4 Geomechanical applications

Along this research, some applications are considered to validate the numerical scheme where reference solutions are available. Remembering the three basic elements of soil, water and geotextile, the validation cases are more oriented toward geomechanical simulations involving one or more of these elements. For example, the ability of the original MPM as a continuum–based method to simulate the dynamics of granular materials using simple elasto–plastic constitutive relation is investigated with the collapse of sand column. The present MPM model expects higher run–out of the collapsed column, which complies with other literature conclusions [95, 124]. However, the performance of the MPM is not only close to experiments, but excellently matches the generalised interpolation material point method (GIMP). GIMP is considered as a modified version of the classical MPM as introduced in Chapter 2.

The stability analysis of an embankment reinforced with geotextile is presented as a validation for the proposed membrane approach in combination with soil. To overcome numerical instability associated with the undrained condition of Poisson's ratio being 0.49, the strain enhancement technique is introduced to the soil. The construction procedure of the embankment is reproduced in MPM by increasing the sand material density, which corresponds to the induced external load. Referring to the finite element software (Plaxis 2D) with high–order element type, the tetrahedral elements in MPM are able to give comparative stress distribution. Similarly, the MPM membrane forces are quite similar to the reference results. Although the inherent no–slip contact condition in MPM is assumed here between the soil and the geotextile, frictional contact can be modelled as well. For further research about this application, the consolidation effect can be included if real time dynamic behaviour is of concern to investigate.

Large geotextile tube filled with dredged material is an important application being widely used for shoreline protection. The so called geotube is modelled in MPM combining geotextile and liquid behaviour material. Beside validating geotextile–fluid interaction in this application, the ability of the MPM fluid algorithm and the smoothening techniques to capture the steady–state solution is studied. Different filling ratios are resembled in MPM by assuming different initial configurations of the tube. Exploiting the advantage of the proposed membrane formulation, the geotextile assigned almost negligible mass as compared to the filling material. The final configuration as well as the fluid pressure are compared to a computer software (GeoCoPS), which is based on equilibrium state analysis. The obtained results confirmed the need for enhancement algorithms to get stable and fairly correct prediction.

7.1.5 Dropping geocontainers

In coastal engineering, geocontainers are becoming more frequently used instead of conventional materials. The numerical modelling of the dropping process is simulated in this research involving soil, water and geotextile. Due to complexity of the problem, the dropping process is broke down into four phases. Excluding filling phase, the container releasing out of the barge is followed by dumping into the water and finally interacts

with the sea bed. The key issue in designing geocontainers is to ensure no rupture through all phases, or the tensile forces through the geotextile to be within the design strength limits.

Following experimental with dropping geocontainer in air [144] when the water uplift has minor effects, the MPM releasing phase is carried out with no water while the tensile forces and the container configuration are traced. Providing wrinkles or folds along the geotextile in practice is simplified with adding slack in the MPM model. The numerical alternative seems to provide releasing with smaller barge opening, which is similar to the experimental observations. Furthermore about releasing phase, the influence of geotextile–barge friction coefficient has been investigated. It is shown that friction does not affect the tensile forces only but rather the shape of the released container.

In order to study the interaction effect of more geocontainers, an installed container on a soil bed is followed by second one where interaction between the two is taking place. A shift with $2\,\mathrm{m}$ is assumed for the initial location of the second bag, which is most common in field to have eccentric releasing. Owing to the sudden landing of the second container, the geotextile forces increased in the first with about $30\,\%$ of the final residual value. Slowly after hitting each other, the second slides down resting on the ground while the stress distribution through the large bags reflects the process physically.

A step ahead dumping geocontainer in full model test where physical quantities are difficult to measure, a scaled lab test is simulated with the numerical model. The lab test conducted at GeoDelft/Deltares is reconsidered in MPM with more focus on the water velocity and pressure fields. Due to uncertainty of the initial configuration of the small soil bag in lab, two different shapes in MPM are assumed with the same volume size. Sooner after sinking into the water thank, both shapes match the measured vertical velocity quite well. In spite of the severe deformation in the wake of the soil bag, vorticity and pressure distributions look plausible.

After validating the velocity field with the lab test model so that the prediction of the terminal velocity is reproducible, the last research point in this thesis is to model full scale container being dumped into water. Here, more focus has been paid to the evolution of geotextile forces and the container configuration. Keeping in mind that the current numerical model simplifies the application to a uniform two–dimensional problem, whereas nonuniformity in the experimental model leads to release one end earlier than the other. Nevertheless, the terminal velocity of the container is well predicted. Maximum calculated geotextile force is about $70\,\mathrm{kN/m}$ during the entire process, which is within the design limits of maximum tensile strength of the geotextile material. Although no measured value to compare with theses forces is available, field observation says that the geocontainer lands on the sea bed safely.

7.1.6 Other research issues

There are some additional research issues, which have been carried out in this research. Due to time limitation, development of these issues do not achieved the state of the art yet. Nevertheless, the preliminary outcome looks promising and they need further in-

vestigation. For example, OpenMP parallelisation has been applied to the MPM code, which is suitable for shared memory machines. Parallelisation has been applied on loop level only, which has been found to be heavily dependent on the sequence of data access inside the loop. Owing to the existence of two loop types in MPM, grid nodes and particles, care should be taken to avoid *data race* in the nodal loop with no need to do so for the other. The data racing is expected to occur when multiple threads update the same shared variable at the same time. For this purpose, the *critical* section or the *reduction* clause can be used. As a part of the improvement in the current MPM version, only active nodes that belong to element containing particles are considered in the calculation loop. Furthermore, the book–keeping procedure of the membrane and other substances are constructed separately, which has found to speed up the access of data quite a lot.

An example about the efficiency of the current OpenMP parallelisation is given here for the case of dumping geocontainers in water presented in Section 6.5. In this example, the domain is discretised to 21306 tetrahedral elements using 199534 particle including water, soil and geotextile material. The computer is equipped with Quad–Core Intel processor $3.2\,\mathrm{GHz}$ and $4.0\,\mathrm{GB}$ memory. Real computational time with no parallelisation was about 55 hour. The *speedup factor* was 2.6, defined as the ratio of the parallel computational time to the sequential.

Using the hypoplastic constitutive model with MPM is another research issue, which has been implemented in this research. An attempt to adopt explicit time integration with the sub–stepping procedure [2] for the material model has been successfully applied for small deformation problems with monotonic loading. However, earlier experience with this model in MPM obliged implicit integration to get the silo discharge problem working properly [188]. For more details about the current implementation including the small strain stiffness, the reader is referred to [2].

7.2 Recommendations for further research

In this thesis, the Gauss integration method [2, 21] is used as a smoothening technique based on least square to reduce the effect of grid–crossing error. However, the energy conservation in this method is questionable and no detailed investigation about this issue is carried out so far. Other methods [12, 151, 194] are recommended to implement, which are well tested for energy conservation. For granular materials where no excessive tensile exists, methods like CPDI [151] adds complexity to the implementation beside loosing one of the MPM important feature of being mesh independent.

The current coupled membrane formulation can be extended to consider flexural stiffness so that it can be applied to model beam elements. For applications such as reinforced embankment, in which the geotextile is embedded between two soil layers, the current contact algorithm [14] has some limitation if attempt to apply on both sides of the thin structure. This can be explained better by assuming the scenario of having the three entities (geotextile and two soil layers) in one computational element. Whether each of the two interfaces is sliding or sticking, four options for the final state are possible, whereas the current algorithm checks for two solutions only. In a related work, one

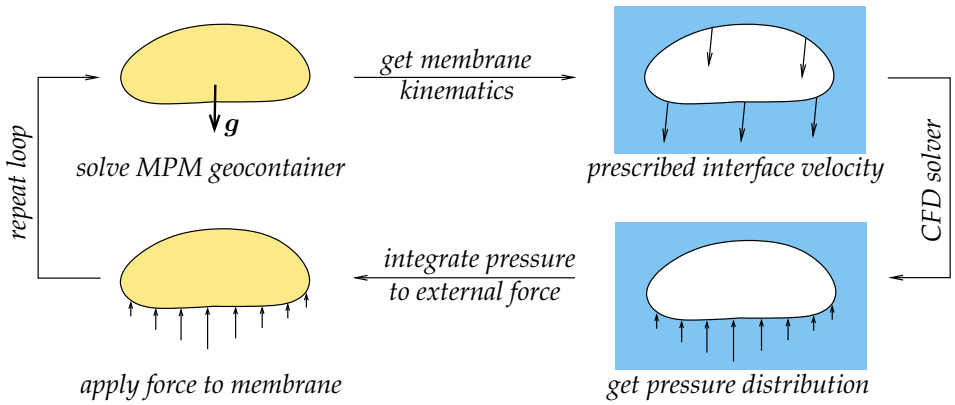

Figure 7.1: Concepts of a coupling procedure between MPM and CFD solver

might think about expanding the cohesive contact formulation [2] for large deformation.

In spite of the achieved improvement with explicit formulation for high bulk modulus fluids, iterative implicit scheme like the fractional step method can be used as it has long tradition with modelling fluid flow problems. The idea of coupling numerical methods in one computational framework has shown its efficiency in this study for the coupled FEM–MPM approach, as many other literature; e.g., [66, 108, 196]. For example, dropping geocontainers can be modelled by coupling MPM with other CFD solver if the flow field is the key focal point or in the case of deep dumping where geocontainer drift from initial location is important. Therefore, we present here the concepts of coupling the MPM algorithm with other CFD solvers in Figure 7.1.

More about improving the geocontainer problem, interaction of water–soil should be included in the case of permeable geotextile. For this specific application where density variation in the soil is expected to play a role, more advanced constitutive models that counts for density and pressure variations are important to include. Finally, The parachute effect of the air can be examined on the dropping process by introducing air materials points and solve the associated governing equations.

No doubt the geocontainer problem is in the range of turbulent flow with high values of Reynolds number. Although the effect of turbulence is bounded in the wake of the flow and expected to have little effect of the geocontainer deformation, however, it plays a significant role in the final location of the container. Hence, a turbulence model must be included in deep dumping applications or for accurate geocontainer positioning problems.

In order to improve the computation efficiency, message passing interface (MPI) parallelisation should be included in combination with OpenMP so that distributed memory machines are supported. Thus, the computational domain is decomposed into numerous subdomains where information are exchanged between patches.

Bibliography

[1] H. D. Adel. Forces due to impact and deformation of geotubes (in Dutch). Technical report, Delft Geotechnics, report CO–345040, 1996.

[2] I. J. Al-Kafaji. *Formulation of a dynamic material point method (MPM) for geomechanical problems*. PhD thesis, Institute of Geotechnical Engineering, University of Stuttgart, 2013.

[3] S. Andersen. *Material–point analysis of large–strain problems: modelling of landslides*. PhD thesis, Department of Civil Engineering, Aalborg University, Aalborg, Denmark, 2009.

[4] M. Anghileri, L. M. Castelletti, and M. Tirelli. Fluid–structure interaction of water filled tanks during the impact with the ground. *International Journal of Impact Engineering*, 31(3):235–254, 2005.

[5] I. Ansys. Ansys Mechanical APDL and Mechanical Applications Theory Reference, Ansys. *Inc, release*, 13, 2010.

[6] C. Antoci, M. Gallati, and S. Sibilla. Numerical simulation of fluid–structure interaction by SPH. *Computers & Structures*, 85(11):879–890, 2007.

[7] N. Aquelet, M. Souli, and L. Olovsson. Euler–Lagrange coupling with damping effects: Application to slamming problems. *Computer Methods in Applied Mechanics and Engineering*, 195(1):110–132, 2006.

[8] N. Balmforth and R. Kerswell. Granular collapse in two dimensions. *Journal of Fluid Mechanics*, 538:399–428, 2005.

[9] B. Banerjee. Shell formulation for the material point method. 2003. URL `www.eng.utah.edu/ banerjee/Papers/shellPaper.pdf`.

[10] B. Banerjee. MPM validation: A myriad of Taylor impact tests. Technical Report C-SAFE–CD–IR–04–004, Department of Mechanical Engineering, University of Utah, 2012.

[11] S. Bardenhagen. Energy conservation error in the material point method for solid mechanics. *Journal of Computational Physics*, 180(1):383–403, 2002.

[12] S. Bardenhagen and E. Kober. The generalized interpolation material point method. *CMES: Computer Modeling in Engineering & Sciences*, 5(6):477–495, 2004.

[13] S. Bardenhagen, J. Brackbill, and D. Sulsky. Shear deformation in granular material. In *11th International Detonation Symposium*, 1998.

[14] S. Bardenhagen, J. Brackbill, and D. Sulsky. The material–point method for granular materials. *Computer Methods in Applied Mechanics and Engineering*, 187(3–4): 529–541, 2000.

[15] S. Bardenhagen, J. Guilkey, K. Roessig, J. Brackbill, W. Witzel, and J. Foster. An improved contact algorithm for the material point method and application to stress propagation in granular material. *CMES: Computer Modeling in Engineering & Sciences*, 2(4):509–522, 2001.

[16] K. J. Bathe. *Finite Element Procedures*, volume 2. Prentice Hall, 1996.

[17] T. Belytschko, Y. Krongauz, D. Organ, M. Fleming, and P. Krysl. Meshless methods: An overview and recent developments. *Computer Methods in Applied Mechanics and Engineering*, 139(1):3–47, 1996.

[18] T. Belytschko, W. K. Liu, B. Moran, and K. Elkhodary. *Nonlinear Finite Elements for Continua and Structures*. John Wiley & Sons, 2013.

[19] D. J. Benson. Computational methods in Lagrangian and Eulerian hydrocodes. *Computer Methods in Applied Mechanics and Engineering*, 99(2):235–394, 1992.

[20] E. Berberovic. *Investigation of free-surface flow associated with drop impact: numerical simulations and theoretical modeling*. PhD thesis, TU Darmstadt/FG Strömungslehre und Aerodynamik, 2010.

[21] L. Beuth. *Formulation and application of a quasi–static material point method*. PhD thesis, Institute of Geotechnical Engineering, University of Stuttgart, 2012.

[22] L. Beuth, Z. Więckowski, and P. Vermeer. Solution of quasi–static large–strain problems by the material point method. *International Journal for Numerical and Analytical Methods in Geomechanics*, 35(13):1451–1465, 2011.

[23] A. Bezuijen. Geocontainers: analyse resultaten Brutusbakproeven. Report 03.02.01–04, Delft Cluster, 2001.

[24] A. Bezuijen. Geosystems, introduction and design methods. *A presentation given at Delft University of Technology, NL*, 2010.

[25] A. Bezuijen, O. Oung, M. Breteler, E. Berendesen, and K. Pilarczyk. Model tests on geocontainers, placing accuracy and geotechnical aspects. *Proceedings of 7th International Conference on Geosynthetics*, pages 1001–1006, 2002.

[26] A. Bezuijen, R. Schrijver, M. Breteler, E. Berendesen, and K. Pilarczyk. Field tests on geocontainers. In *Proceedings of 7th International Conference on Geosynthetics*, Nice, 2002.

[27] A. Bezuijen, M. de Groot, M. Breteler, and E. Berendsen. Placing accuracy and stability of geocontainers. In *Third European Geosynthetics Conference, Munich, Germany*, 2004.

[28] M. Bischoff, K. Bletzinger, W. Wall, and E. Ramm. Models and finite elements for thin-walled structures. *Encyclopedia of Computational Mechanics*, 2004.

[29] J. Bonet and A. Burton. A simple average nodal pressure tetrahedral element for incompressible and nearly incompressible dynamic explicit applications. *Communications in Numerical Methods in Engineering*, 14(5):437–449, 1998.

[30] J. Brackbill and H. Ruppel. FLIP: A method for adaptively zoned, particle–in–cell calculations of fluid flows in two dimensions. *Journal of Computational Physics*, 65 (2):314–343, 1986.

[31] J. U. Brackbill, D. B. Kothe, and H. M. Ruppel. FLIP: A low-dissipation, particle–in–cell method for fluid flow. *Computer Physics Communications*, 48(1):25–38, 1988.

[32] M. K. Breteler and M. B. de Groot. Storten van geocontainers in stroming en golven (in dutch). Technical Report H3820, GeoDelft, 03.02.01–05, 2001.

[33] R. Brinkgreve, W. Broere, and D. Waterman. *PLAXIS: 2D, Version 8*, 2004.

[34] K. H. Brown, S. P. Burns, and M. A. Christon. Coupled Eulerian–Lagrangian methods for earth penetrating weapon applications. *SAND2002–1014, Sandia National Laboratories, Albuquerque, NM*, 2002.

[35] H. H. Bui, R. Fukagawa, K. Sako, and S. Ohno. Lagrangian meshfree particles method (SPH) for large deformation and failure flows of geomaterial using elastic–plastic soil constitutive model. *International Journal for Numerical and Analytical Methods in Geomechanics*, 32(12):1537–1570, 2008.

[36] D. Burgess, D. Sulsky, and J. Brackbill. Mass matrix formulation of the FLIP particle–in–cell method. *Journal of Computational Physics*, 103(1):1–15, 1992.

[37] Z. Chen and R. Brannon. An evaluation of the material point method. *Report : SAND*, 482:87185–0893, 2002.

[38] J. Clausner, M. Palermo, D. Banks, and J. Palmerton. Potential application of geosynthetic fabric containers for open water placement of contaminated dredged material. *Environmental Effects of Dredging Technical Notes*, 1996.

[39] C. Coetzee. *The modelling of granular flow using the particle-in-cell method*. PhD thesis, Department of Mechanical Engineering, University of Stellenbosch, Stellenbosch, South Africa, 2004.

[40] C. Coetzee, P. Vermeer, and A. Basson. The modelling of anchors using the material point method. *International Journal for Numerical and Analytical Methods in Geomechanics*, 29(9):879–895, 2005.

[41] R. Courant, K. Friedrichs, and H. Lewy. On the partial difference equations of mathematical physics. *IBM Journal of Research and Development*, 11(2):215–234, 1967.

[42] M. A. Cruchaga, D. J. Celentano, and T. E. Tezduyar. Collapse of a liquid column: numerical simulation and experimental validation. *Computational Mechanics*, 39(4): 453–476, 2007.

[43] P. Cundall. Adaptive density–scaling for time–explicit calculations. In *Procs. 4th. International Conference on Numerical Methods in Geomechanics. Edmonton, Canada*, volume 1, pages 23–26, 1982.

[44] P. Cundall. Distinct element models of rock and soil structure. *Analytical and Computational Methods in Engineering Rock Mechanics.*, 4:129–163, 1987.

[45] D. Dassanayake and H. Oumeraci. Hydraulic stability of coastal structures made of geotextile sand containers (GSCS): effect of engineering properties of GSCS. *Coastal Engineering Proceedings*, 1(33):structures–55, 2012.

[46] R. de Borst and P. Vermeer. Possibilities and limitations of finite elements for limit analysis. *Géotechnique*, 34(2):199–210, 1984.

[47] R. de Borst, M. A. Crisfield, J. J. Remmers, and C. V. Verhoosel. Non–linear finite element analysis. *Non–Linear Finite Element Analysis of Solids and Structures, Second Edition*, pages 31–62, 1997.

[48] M. de Groot, A. Bezuijen, and K. Pilarczyk. Forces in geocontainer geotextile during dumping from barge. In *Proceedings of 2nd EuroGeo2*, pages 623–628, 2000.

[49] M. de Groot, M. Breteler, and A. Bezuijen. Resultaten geocontainer–onderzoek (Results geocontainer research). Technical report, Delft Cluster Report, DC1–321–11, 2003.

[50] M. de Groot, M. Breteler, and E. Berendsen. Feasibility of geocontainers at the sea shore. In *Proceedings of 29th ICCE conference*, pages 3904–3913. World Scientific, 2004.

[51] J. V. de Lemos. Explicit codes in geomechanics–FLAC, UDEC and PFC. In *Innovative Numerical Modelling in Geomechanics*, pages 299–315, 2012.

[52] J. Degroote, K. J. Bathe, and J. Vierendeels. Performance of a new partitioned procedure versus a monolithic procedure in fluid–structure interaction. *Computers & Structures*, 87(11):793–801, 2009.

[53] C. Detournay and E. Dzik. Nodal mixed discretization for tetrahedral elements. In *4th international FLAC symposium on numerical modeling in geomechanics. Itasca Consulting Group, Inc., Minneapolis. Paper*, number 07–02, 2006.

[54] J. Donea, A. Huerta, J. Ponthot, and A. Rodríguez-Ferran. Arbitrary Lagrangian–Eulerian methods. *Encyclopedia of Computational Mechanics*, 2004.

[55] E. E. Doyle, H. E. Huppert, G. Lube, H. M. Mader, and R. S. J. Sparks. Static and flowing regions in granular collapses down channels: Insights from a sedimenting shallow water model. *Physics of Fluids*, 19(10):106601, 2007.

[56] Q. Du and D. Wang. Tetrahedral mesh generation and optimization based on centroidal Voronoi tessellations. *International Journal for Numerical Methods in Engineering*, 56(9):1355–1373, 2003.

[57] I. A. Fernandes. Exploring quadratic shape functions in material point method. Masters thesis, Department of Mechanical Engineering, University of Utah, 2004.

[58] J. H. Ferziger and M. Perić. *Computational Methods for Fluid Dynamics*. Springer-Verlag GmbH, 3rd edition, 2002.

[59] J. Fowler and E. Trainer. Overview of geocontainer projects in the United States. *Geotec Associates*, 1995.

[60] L. A. Freitag and C. Ollivier-Gooch. Tetrahedral mesh improvement using swapping and smoothing. *International Journal for Numerical Methods in Engineering*, 40 (21):3979–4002, 1997.

[61] I. Fried and D. S. Malkus. Finite element mass matrix lumping by numerical integration with no convergence rate loss. *International Journal of Solids and Structures*, 11(4):461–466, 1975.

[62] Y. Gan. *Model–based simulations of the piercing process in piezo–ICSI*. PhD thesis, University of Missouri–Columbia, 2008.

[63] Y. Gan, Z. Chen, and S. Montgomery-Smith. Improved material point method for simulating the zona failure response in piezo-assisted intracytoplasmic sperm injection. *Computer Modeling in Engineering & Sciences (CMES)*, 73(1):45–75, 2011.

[64] T. Geosynthetics North America. *Geosystems for Shoreline Protection*. 2007. URL `www.tencate.com/flippingbook/publicaties/geotube-shoreline`.

[65] U. Ghia, K. N. Ghia, and C. Shin. High–Re solutions for incompressible flow using the Navier–Stokes equations and a multigrid method. *Journal of Computational Physics*, 48(3):387–411, 1982.

[66] A. Gilmanov and S. Acharya. A hybrid immersed boundary and material point method for simulating 3D fluid–structure interaction problems. *International Journal for Numerical methods in Fluids*, 56(12):2151–2177, 2008.

[67] J. Guilkey and J. Weiss. Implicit time integration for the material point method: Quantitative and algorithmic comparisons with the finite element method. *International Journal for Numerical Methods in Engineering*, 57(9):1323–1338, 2003.

[68] J. Guilkey, J. Hoying, and J. Weiss. Computational modeling of multicellular constructs with the material point method. *Journal of Biomechanics*, 39(11):2074–2086, 2006.

[69] Y. Guo and J. Nairn. Three–dimensional dynamic fracture analysis using the material point method. *Computer Modeling in Engineering and Sciences*, 1(1):11–25, 2006.

[70] Y. Guo and J. A. Nairn. Calculation of J–integral and stress intensity factors using the material point method. *Computer Modeling in Engineering and Sciences*, 6(3): 295–308, 2004.

[71] F. Hamad, B. Westrich, and P. Vermeer. MPM formulation with accurate integration for a 3D membrane and an application of releasing geocontainer from barge. *5th European Geosynthetics Congress (EuroGeo5). Valencia (Spain) 2012*, 1:78–87.

[72] F. Hamad, P. Vermeer, and C. Moormann. Development of a coupled FEM-MPM approach to model a 3D membrane with an application of releasing geocontainer from barge. *Installation Effects in Geotechnical Engineering*, pages 176–183, 2013.

[73] F. H. Harlow. Hydrodynamic problems involving large fluid distortions. *Journal of the ACM (JACM)*, 4(2):137–142, 1957.

[74] S. Henke and J. Grabe. Simulation of pile driving by 3–dimensional Finite-Element analysis. In *Proceedings of the 17th European Young Geotechnical Engineers Conference, Zagreb*, pages 215–233, 2006.

[75] J. Heyman. The stone skeleton. *International Journal of Solids and Structures*, 2(2): 249–256, 1966.

[76] R. Hill. Some basic principles in the mechanics of solids without a natural time. *Journal of the Mechanics and Physics of Solids*, 7(3):209–225, 1959.

[77] E. Hinton, T. Rock, and O. Zienkiewicz. A note on mass lumping and related processes in the finite element method. *Earthquake Engineering & Structural Dynamics*, 4(3):245–249, 1976.

[78] W. Hornsey, J. Carley, I. Coghlan, and R. Cox. Geotextile sand container shoreline protection systems: Design and application. *Geotextiles and Geomembranes*, 29(4): 425–439, 2011.

[79] G. Hou, J. Wang, and A. Layton. Numerical methods for fluid-structure interaction – A review. *Commun. Comput. Phys.*, 12(2):337–377, 2012.

[80] P. Hu, L. Xue, K. Qu, K. Ni, and M. Brenner. Unified solver for modeling and simulation of nonlinear aeroelasticity and fluid-structure interactions. In *AIAA Atmospheric Flight Mechanics Conference*, volume 6148, 2009.

[81] W. Hu and Z. Chen. A multi–mesh MPM for simulating the meshing process of spur gears. *Computers & Structures*, 81(20):1991–2002, 2003.

[82] J. Huang, A. Bhandari, and X. Yang. Numerical modeling of geosynthetic-reinforced earth structures and geosynthetic-soil interactions. *Geotechnical Engineering Journal of the SEAGS & AGSSEA*, 42(1):43, 2011.

[83] P. Huang, X. Zhang, S. Ma, and X. Huang. Contact algorithms for the material point method in impact and penetration simulation. *International Journal for Numerical Methods in Engineering*, 85(4):498–517, 2011.

[84] T. Hughes. *The Finite Element Method: Linear Static and Dynamic Finite Element Analysis*. Prentice–Hall, Inc., Englewood Cliffs, New Jersey, 1987.

[85] S. R. Idelsohn, M. A. Storti, and E. Oñate. Lagrangian formulations to solve free surface incompressible inviscid fluid flows. *Computer Methods in Applied Mechanics and Engineering*, 191(6):583–593, 2001.

[86] S. R. Idelsohn, E. Oñate, and F. D. Pin. The particle finite element method: a powerful tool to solve incompressible flows with free–surfaces and breaking waves. *International Journal for Numerical Methods in Engineering*, 61(7):964–989, 2004.

[87] I. Ionescu, J. E. Guilkey, M. Berzins, R. M. Kirby, and J. A. Weiss. Simulation of soft tissue failure using the material point method. *Journal of Biomechanical Engineering*, 128(6):917–924, 2006.

[88] Itasca. *FLAC 3D: Fast Lagrangian Analysis of Continua In 3 Dimensions*. Itasca Consulting Group, Online Manual, 2002.

[89] I. Jassim, F. Hamad, and P. Vermeer. Dynamic material point method with applications in geomechanics. In *2nd International Symposium on Computational Geomechanics (COMGEO II)*, Cavtat–Dubrovnik, Croatia, 27-29 April 2011.

[90] I. Jassim, D. Stolle, and P. Vermeer. Two–phase dynamic analysis by material point method. *International Journal for Numerical and Analytical Methods in Geomechanics*, 37(15):2502–2522, 2013.

[91] C. Kassiotis, A. Ibrahimbegovic, and H. Matthies. Partitioned solution to fluid–structure interaction problem in application to free–surface flows. *European Journal of Mechanics – B/Fluids*, 29(6):510–521, 2010.

[92] A. Koffler, M. Choura, A. Bendriss, and E. Zengerink. Geosynthetics in protection against erosion for river and coastal banks and marine and hydraulic construction. *Journal of Coastal Conservation*, 12(1):11–17, 2008.

[93] H. Koivurova and A. Pramila. Nonlinear vibration of axially moving membrane by finite element method. *Computational Mechanics*, 20(6):573–581, 1997.

[94] P. Krysl and T. Belytschko. Analysis of thin shells by the element-free Galerkin method. *International Journal of Solids and Structures*, 33(20):3057–3080, 1996.

[95] K. Kumar, K. Soga, and J. Y. Delenne. Multi–scale modelling of granular avalanches. In *AIP Conference Proceedings*, volume 1542, page 1250, 2013.

[96] M. Kyle. Problems with incompressibility in finite element analysis. Masters thesis, Department of Civil Engineering, The University of McMaster, 2012.

[97] P. Y. Lagrée, L. Staron, and S. Popinet. The granular column collapse as a continuum: validity of a two–dimensional Navier–Stokes model with a μ (I)–rheology. *Journal of Fluid Mechanics*, 686:378–408, 2011.

[98] E. Lajeunesse, A. Mangeney-Castelnau, and J. Vilotte. Spreading of a granular mass on a horizontal plane. *Physics of Fluids*, 16(7):2371–2381, 2004.

[99] H. P. Langtangen, K. A. Mardal, and R. Winther. Numerical methods for incompressible viscous flow. *Advances in Water Resources*, 25(8):1125–1146, 2002.

[100] A. Larese, R. Rossi, E. Oñate, and S. R. Idelsohn. Validation of the particle finite element method (PFEM) for simulation of free surface flows. *Engineering Computations*, 25(4):385–425, 2008.

[101] C. Lawson. Geotextile containment for hydraulic and environmental engineering. *Geosynthetics International*, 15(6):384–427, 2008.

[102] V. Lemiale, J. Nairn, and A. Hurmane. Material point method simulation of equal channel angular pressing involving large plastic strain and contact through sharp corners. *Computer Modeling in Engineering and Sciences*, 70(1):41–66, 2010.

[103] D. Leshchinsky, O. Leshchinsky, H. I. Ling, and P. Gilbert. Geosynthetic tubes for confining pressurized slurry: some design aspects. *Journal of Geotechnical Engineering*, 122(8):682–690, 1996.

[104] B. Q. Li. *Discontinuous Finite Elements in Fluid Dynamics and Heat Transfer*. Springer, 2006.

[105] S. Li and W. K. Liu. *Meshfree Particle Methods*. Springer, 2007.

[106] S. Li, W. Hao, and W. K. Liu. Numerical simulations of large deformation of thin shell structures using meshfree methods. *Computational Mechanics*, 25(2–3):102–116, 2000.

[107] Y. Lian, X. Zhang, and Y. Liu. Coupling of finite element method with material point method by local multi–mesh contact method. *Computer Methods in Applied Mechanics and Engineering*, 200(47):3482–3494, 2011.

[108] Y. Lian, X. Zhang, X. Zhou, and Z. Ma. A FEMP method and its application in modeling dynamic response of reinforced concrete subjected to impact loading. *Computer Methods in Applied Mechanics and Engineering*, 200(17):1659–1670, 2011.

[109] Y. Lian, X. Zhang, and Y. Liu. An adaptive finite element material point method and its application in extreme deformation problems. *Computer Methods in Applied Mechanics and Engineering*, 241:275–285, 2012.

[110] L. Lim, A. Andreykiv, and R. Brinkgreve. Pile penetration simulation with material point method. *Installation Effects in Geotechnical Engineering*, pages 24–30, 2013.

[111] G. R. Liu. *Meshfree Methods: Moving Beyond the Finite Element Method*. CRC press, 2010.

[112] G. R. Liu and M. Liu. *Smoothed Particle Hydrodynamics: A Meshfree Particle Method*. World scientific publishing company incorporated, 2003.

[113] G. Lube, H. E. Huppert, R. S. J. Sparks, and M. A. Hallworth. Axisymmetric collapses of granular columns. *Journal of Fluid Mechanics*, 508(1):175–199, 2004.

[114] G. Lube, H. E. Huppert, R. S. J. Sparks, and A. Freundt. Collapses of two-dimensional granular columns. *Physical Review E*, 72(4):041301, 2005.

[115] G. Lube, H. E. Huppert, R. S. J. Sparks, and A. Freundt. Static and flowing regions in granular collapses down channels. *Physics of Fluids*, 19(4):043301, 2007.

[116] L. B. Lucy. A numerical approach to the testing of the fission hypothesis. *The Astronomical Journal*, 82(12):1013–1024, 1977.

[117] J. Lysmer and R. Kuhlemeyer. Finite dynamic model for infinite media. *Journal of the Engineering Mechanics Division*, 95(EM4):859–877, 1969.

[118] J. Ma. *Multiscale simulation using the generalized interpolation material point method, discrete dislocations and molecular dynamics*. PhD thesis, Oklahoma State University, 2006.

[119] S. Ma, X. Zhang, and X. Qiu. Comparison study of MPM and SPH in modeling hypervelocity impact problems. *International Journal of Impact Engineering*, 36(2): 272–282, 2009.

[120] X. Ma, D. Z. Zhang, P. T. Giguere, and C. Liu. Axisymmetric computation of Taylor cylinder impacts of ductile and brittle materials using original and dual domain material point methods. *International Journal of Impact Engineering*, 54:96–104, 2012.

[121] Z. Ma, X. Zhang, and P. Huang. An object–oriented MPM framework for simulation of large deformation and contact of numerous grains. *Computer Modeling in Engineering and Sciences (CMES)*, 55(1):61–88, 2010.

[122] P. Mackenzie-Helnwein, P. Arduino, W. Shin, J. Moore, and G. Miller. Modeling strategies for multiphase drag interactions using the material point method. *International Journal for Numerical Methods in Engineering*, 83(3):295–322, 2010.

[123] L. Malvern. *Introduction to the Mechanics of a Continuous Medium*. Prentice-Hall, Englewood Cliffs, New Jersey, 1969.

[124] A. Mangeney, L. Staron, D. Volfson, and L. Tsimring. Comparison between discrete and continuum modeling of granular spreading. *WSEAS Transactions on Mathematics*, 6(2):373, 2007.

[125] J. C. Martin and W. J. Moyce. Part IV. An experimental study of the collapse of liquid columns on a rigid horizontal plane. *Philosophical Transactions Of The Royal Society Of London. Series A, Mathematical And Physical Sciences*, 244(882):312–324, 1952.

[126] C. Mast. *Modeling landslide-induced flow interactions with structures using the Material Point Method*. PhD thesis, Civil and Environmental Engineering, University of Washington, Washington, US, 2013.

[127] C. M. Mast, P. Mackenzie-Helnwein, P. Arduino, G. R. Miller, and W. Shin. Mitigating kinematic locking in the material point method. *Journal of Computational Physics*, 231(16):5351–5373, 2012.

[128] J. J. Monaghan. An introduction to SPH. *Computer physics Communications*, 48(1): 89–96, 1988.

[129] C. H. Mseikeh. *Wrinkling of membranes, plates, and shells*. PhD thesis, McGill University, Monteréal, Québec, Canada, 1997.

[130] J. A. Nairn. Material point method calculations with explicit cracks. *Computer Modeling in Engineering and Sciences*, 4(6):649–663, 2003.

[131] M. Nazem, J. Carter, and D. Airey. Arbitrary Lagrangian–Eulerian method for dynamic analysis of geotechnical problems. *Computers and Geotechnics*, 36(4):549–557, 2009.

[132] S. Nemat-Nasser and M. Hori. *Micromechanics: Overall Properties of Heterogeneous Materials*, volume 2. Elsevier Amsterdam, 1999.

[133] P. Nithiarasu. A matrix free fractional step method for static and dynamic incompressible solid mechanics. *International Journal for Computational Methods in Engineering Science and Mechanics*, 7(5):369–380, 2006.

[134] P. Nithiarasu. A unified fractional step method for compressible and incompressible flows, heat transfer and incompressible solid mechanics. *International Journal of Numerical Methods for Heat & Fluid Flow*, 18(2):111–130, 2008.

[135] P. Nithiarasu and O. C. Zienkiewicz. Analysis of an explicit and matrix free fractional step method for incompressible flows. *Computer Methods in Applied Mechanics and Engineering*, 195(41):5537–5551, 2006.

[136] P. Nithiarasu, R. Codina, and O. C. Zienkiewicz. The Characteristic–Based Split (CBS) scheme–a unified approach to fluid dynamics. *International Journal for Numerical Methods in Engineering*, 66(10):1514–1546, 2006.

[137] P. Nithiarasu, R. Bevan, and K. Murali. An artificial compressibility based fractional step method for solving time dependent incompressible flow equations. temporal accuracy and similarity with a monolithic method. *Computational Mechanics*, 51(3):255–260, 2013.

[138] W. Noh. CEL: A time–dependent, two–space–dimensional, coupled Eulerian-Lagrange code. Technical report, Lawrence Radiation Lab., Univ. of California, Livermore, 1963.

[139] E. Oñate, S. R. Idelsohn, M. A. Celigueta, and R. Rossi. Advances in the particle finite element method for the analysis of fluid–multibody interaction and bed erosion in free surface flows. *Computer Methods in Applied Mechanics and Engineering*, 197(19):1777–1800, 2008.

[140] H. Oumeraci, M. Hinz, M. Bleck, and A. Kortenhaus. Sand–filled geotextile containers for shore protection. *Coastal Structures*, 2003.

[141] J. Palmerton. Overview of code ScowDropSim–a distinct element method formulation. *Confidential document at Deltares, The Netherlands*, 1996.

[142] J. Palmerton. Distinct element modelling of geosynthetic fabric containers. In *Proceedings of the 7th International Conference on Geosynthetics*, volume 3, pages 1021–1024, Nice, 2002.

[143] K. Pilarczyk. Design aspects of geotubes and geocontainers. Technical report, HYDROpil, 1996.

[144] K. Pilarczyk. *Geosynthetics and Geosystems in Hydraulic and Coastal Engineering*. Taylor & Francis, 2000.

[145] G. Qiu, S. Henke, and J. Grabe. Application of a coupled Eulerian–Lagrangian approach on geomechanical problems involving large deformations. *Computers and Geotechnics*, 38(1):30–39, 2011.

[146] J. Recio and H. Oumeraci. Effect of deformations on the hydraulic stability of coastal structures made of geotextile sand containers. *Geotextiles and Geomembranes*, 25(4):278–292, 2007.

[147] R. K. Rowe and K. L. Soderman. Comparison of predicted and observed behaviour of two test embankments. *Geotextiles and Geomembranes*, 1(2):143–160, 1984.

[148] R. K. Rowe and K. L. Soderman. An approximate method for estimating the stability of geotextile-reinforced embankments. *Canadian Geotechnical Journal*, 22(3): 392–398, 1985.

[149] R. K. Rowe, M. D. MacLean, and K. L. Soderman. Analysis of a geotextile-reinforced embankment constructed on peat. *Canadian Geotechnical Journal*, 21(3): 563–576, 1984.

[150] K. P. Ruggirello and S. C. Schumacher. A dynamic adaptation technique for the material point method. In *III International Conference on Particle–Based Methods – Fundamentals and Applications*, Stuttgart, Germany, 2013.

[151] A. Sadeghirad, R. Brannon, and J. Burghardt. A convected particle domain interpolation technique to extend applicability of the material point method for problems involving massive deformations. *International Journal for Numerical Methods in Engineering*, 86(12):1435–1456, 2011.

[152] R. Schrijver, A. Bezuijen, A. Peters, and E. Berendsen. Large-scale field measurements on geocontainers during the dumping process. In *Field Measurements in Geomechanics: Proceedings of the 6th International Symposium, Oslo, Norway, 23–26 September 2003*, page 341. Taylor & Francis, 2010.

[153] W. Schueller. *The Design of Building Structures*, volume 48. Prentice Hall, 1996.

[154] B. Seibold. *M–Matrices in Meshless Finite Difference Methods*. PhD thesis, Department of Mathematics, University of Kaiserslautern, 2006.

[155] W. K. Shin. *Numerical simulation of landslides and debris flows using an enhanced material point method*. PhD thesis, University of Washington, 2009.

[156] D. Simulia. Abaqus 6.11 theory manual. *Providence, RI, USA: DS SIMULIA Corp*, 2011.

[157] S. Smith and D. Stolle. Numerical simulation of film casting using an updated Lagrangian finite element algorithm. *Polymer Engineering & Science*, 43(5):1105–1122, 2003.

[158] W. Sołowski and S. Sloan. Modelling of sand column collapse with material point method. In *3rd International Symposium on Computational Geomechanics (COMGEO III)*, Krakow, Poland, 21–23 August 2013.

[159] L. Staron and E. Hinch. Study of the collapse of granular columns using two–dimensional discrete–grain simulation. *Journal of Fluid Mechanics*, 545(1):1–27, 2005.

[160] L. Staron and E. Hinch. The spreading of a granular mass: role of grain properties and initial conditions. *Granular Matter*, 9(3-4):205–217, 2007.

[161] M. Steffen, R. Kirby, and M. Berzins. Analysis and reduction of quadrature errors in the material point method (MPM). *International Journal for Numerical Methods in Engineering*, 76(6):922–948, 2008.

[162] D. Stolle, I. Jassim, and P. Vermeer. Simulation of incompressible problems in geomechanics. In *Computer Methods in Mechanics*, pages 347–361. Springer, 2010.

[163] D. F. Stolle. An interpretation of initial stress and strain methods, and numerical stability. *International Journal for Numerical and Analytical Methods in Geomechanics*, 15(6):399–416, 1991.

[164] D. Sulsky and A. Kaul. Implicit dynamics in the material-point method. *Computer Methods in Applied Mechanics and Engineering*, 193(12):1137–1170, 2004.

[165] D. Sulsky and H. Schreyer. The particle–in–cell method as a natural impact algorithm. *Advanced Computational Methods for Material Modeling, ASME, AMD*, 180: 219–230, 1993.

[166] D. Sulsky and H. Schreyer. A particle method with large rotations applied to the penetration of history–dependent materials. *Advances in Numerical Simulation Techniques for Penetration and Perforation of Solids, ASME, AMD*, 171:95–102, 1993.

[167] D. Sulsky and H. Shreyer. Axisymmetric form of the material point method with application to upsetting and Taylor impact problems. *Computer Methods in Applied Mechanics and Engineering*, 139(1):409–429, 1996.

[168] D. Sulsky, Z. Chen, and H. L. Schreyer. A particle method for history–dependent materials. *Computer Methods in Applied Mechanics and Engineering*, 118(1):179–196, 1994.

[169] D. Sulsky, S. Zhou, and H. Schreyer. Application of a particle–in–cell method to solid mechanics. *Computer Physics Communications*, 87(1):236–252, 1995.

[170] L. Sun, S. R. Mathur, and J. Y. Murthy. An unstructured finite–volume method for incompressible flows with complex immersed boundaries. *Numerical Heat Transfer, Part B: Fundamentals*, 58(4):217–241, 2010.

[171] J. Swegle, D. Hicks, and S. Attaway. Smoothed particle hydrodynamics stability analysis. *Journal of Computational Physics*, 116(1):123–134, 1995.

[172] H. Tan and J. A. Nairn. Hierarchical, adaptive, material point method for dynamic energy release rate calculations. *Computer Methods in Applied Mechanics and Engineering*, 191(19):2123–2137, 2002.

[173] TenCate. *Polyfelt Geosynthetics – Geotextiles [product catalogue]*. TenCate Geosynthetics Austria, 2007.

[174] D. Torres and J. Brackbill. The point–set method: front–tracking without connectivity. *Journal of Computational Physics*, 165(2):620–644, 2000.

[175] V. D. Tran, M. A. Meguid, and L. E. Chouinard. The application of coupled finite–discrete element method in analyzing soil–structure interaction problems. In *III International Conference on Particle–Based Methods - Fundamentals and Applications*, Stuttgart, Germany, 2013.

[176] P. Underwood. Dynamic relaxation (in structural transient analysis). *Computational Methods for Transient Analysis(A 84–29160 12–64). Amsterdam, North–Holland, 1983*, pages 245–265, 1983.

[177] P. J. Valent and D. K. Young. Dredged material isolation on the abyssal seafloor: A feasibility study. Technical report, DTIC document, 1997.

[178] H. van Langen. *Numerical analysis of soil–structure interaction*. PhD thesis, Delft University of Technology, Delft, The Netherlands, 1991.

[179] R. van Loon, P. Anderson, F. van de Vosse, and S. Sherwin. Comparison of various fluid–structure interaction methods for deformable bodies. *Computers & Structures*, 85(11):833–843, 2007.

[180] A. van Oord. Report test programme geocontainers. Technical report, Internal report of van Oord ACZ B.V. and Nicolon B.V. ,The Netherlands, 1995.

[181] P. Wallstedt and J. Guilkey. Improved velocity projection for the material point method. *Computer Modeling in Engineering and Sciences*, 19(3):223–232, 2007.

[182] P. Wallstedt and J. Guilkey. An evaluation of explicit time integration schemes for use with the generalized interpolation material point method. *Journal of Computational Physics*, 227(22):9628–9642, 2008.

[183] W. Wang, L. Sluys, and R. De Borst. Viscoplasticity for instabilities due to strain softening and strain–rate softening. *International Journal for Numerical Methods in Engineering*, 40(20):3839–3864, 1997.

[184] Z. Więckowski. Modelling of silo discharge and filling problems by the material point method. *Task quarterly*, 7(4):701–721, 2003.

[185] Z. Więckowski. The material point method in large strain engineering problems. *Computer Methods in Applied Mechanics and Engineering*, 193(39–41):4417–4438, 2004.

[186] Z. Więckowski. Improvement of the material point method by smoothing the mass density field. In *Computer Methods in Mechanics*, Poland, 2005.

[187] Z. Więckowski. Application of dynamic relaxation in material point method. In *CMM 2011 – Computer Methods in Mechanics*, number 230, Warsaw, Poland, 2011.

[188] Z. Więckowski. Modelling of granular flow in silos: Application of various constitutive models of granular material. In *Proceedings of TUL–ENTPE Workshop*, Szklarska Poreba, Poland, March 3–6, 2004.

[189] Z. Więckowski, S. Youn, and J. Yeon. A particle–in–cell solution to the silo discharging problem. *International Journal for Numerical Methods in Engineering*, 45(9): 1203–1225, 1999.

[190] P. Xiao-Fei, X. Ai-Guo, Z. Guang-Cai, Z. Ping, Z. Jian-Shi, M. Shang, and Z. Xiong. Three–dimensional multi–mesh material point method for solving collision problems. *Communications in Theoretical Physics*, 49(5):1129, 2008.

[191] A. York. *The development of modifications to the material point method for the simulation of thin membranes, compressible fluids, and their interactions*. PhD thesis, The University of New Mexico, 1997.

[192] A. York, D. Sulsky, and H. Schreyer. The material point method for simulation of thin membranes. *International Journal for Numerical Methods in Engineering*, 44(10): 1429–1456, 1999.

[193] A. R. York, D. Sulsky, and H. L. Schreyer. Fluid–membrane interaction based on the material point method. *International Journal for Numerical Methods in Engineering*, 48(6):901–924, 2000.

[194] D. Z. Zhang, X. Ma, and P. T. Giguere. Material point method enhanced by modified gradient of shape function. *Journal of Computational Physics*, 230(16):6379–6398, 2011.

[195] H. Zhang, K. Wang, and Z. Chen. Material point method for dynamic analysis of saturated porous media under external contact/impact of solid bodies. *Computer Methods in Applied Mechanics and Engineering*, 198(17):1456–1472, 2009.

[196] X. Zhang, K. Sze, and S. Ma. An explicit material point finite element method for hyper-velocity impact. *International Journal for Numerical Methods in Engineering*, 66(4):689–706, 2006.

[197] X. Zhang, K. Krabbenhoft, D. Pedroso, A. Lyamin, D. Sheng, M. V. Da Silva, and D. Wang. Particle finite element analysis of large deformation and granular flow problems. *Computers and Geotechnics*, 54:133–142, 2013.

[198] Y. Zheng, F. Gao, H. Zhang, and M. Lu. Improved convected particle domain interpolation method for coupled dynamic analysis of fully saturated porous media involving large deformation. *Computer Methods in Applied Mechanics and Engineering*, 257:150–163, 2013.

[199] S. Zhou, J. Stormont, and Z. Chen. Simulation of geomembrane response to settlement in landfills by using the material point method. *International Journal for Numerical and Analytical Methods in Geomechanics*, 23(15):1977–1994, 1999.

[200] O. Zienkiewicz and I. Cormeau. Visco-plasticity–plasticity and creep in elastic solids–a unified numerical solution approach. *International Journal for Numerical Methods in Engineering*, 8(4):821–845, 1974.

[201] O. Zienkiewicz, R. Taylor, and J. Zhu. The finite element method: its basis and fundamentals. 2005.

[202] O. C. Zienkiewicz and R. L. Taylor. *The Finite Element Method: Solid Mechanics*, volume 2. Butterworth–Heinemann, 2000.

[203] O. C. Zienkiewicz and R. L. Taylor. *The Finite Element Method: Fluid Dynamics*, volume 3. Butterworth–Heinemann, 2000.

[204] O. C. Zienkiewicz and R. L. Taylor. *The Finite Element Method for Solid and Structural Mechanics*. Butterworth–Heinemann, 2005.

[205] O. C. Zienkiewicz, P. Nithiarasu, R. Codina, M. Vázquez, and P. Ortiz. The characteristic–based–split procedure: an efficient and accurate algorithm for fluid problems. *International Journal for Numerical Methods in Fluids*, 31(1):359–392, 1999.

Appendix A

4-noded tetrahedral element

For 4-noded tetrahedral element, the interpolation functions $\boldsymbol{N}$ are defined as

$$\boldsymbol{N}(\boldsymbol{\xi}) = \begin{bmatrix} \boldsymbol{N}_1(\boldsymbol{\xi}) & \boldsymbol{N}_2(\boldsymbol{\xi}) & \boldsymbol{N}_3(\boldsymbol{\xi}) & \boldsymbol{N}_4(\boldsymbol{\xi}) \end{bmatrix} \tag{A.1}$$

with

$$\boldsymbol{N}_i(\boldsymbol{\xi}) = \begin{bmatrix} N_i(\boldsymbol{\xi}) & 0 & 0 \\ 0 & N_i(\boldsymbol{\xi}) & 0 \\ 0 & 0 & N_i(\boldsymbol{\xi}) \end{bmatrix}. \tag{A.2}$$

in which N_i are defined by

$$\begin{aligned} N_1(\boldsymbol{\xi}) &= 1 - \xi_1 - \xi_2 - \xi_3, \\ N_2(\boldsymbol{\xi}) &= \xi_1, \\ N_3(\boldsymbol{\xi}) &= \xi_2, \\ N_4(\boldsymbol{\xi}) &= \xi_3, \end{aligned} \tag{A.3}$$

where the representation of the tetrahedral element in global coordinates x_1, x_2, x_3 and the local coordinates ξ_1, ξ_2, ξ_3 in illustrated in Figure A.1.
For isoparametric interpolation, both displacement and geometry are approximated in the element domain using the same interpolation function defined in Equation A.1; i.e.,

$$\boldsymbol{x}(\boldsymbol{\xi}, t) \approx \sum_{i=1}^{4} N_i(\boldsymbol{\xi})\, \tilde{\boldsymbol{x}}_i(t), \tag{A.4}$$

and,

$$\boldsymbol{u}(\boldsymbol{\xi}, t) \approx \sum_{i=1}^{4} N_i(\boldsymbol{\xi})\, \tilde{\boldsymbol{u}}_i(t), \tag{A.5}$$

where $\boldsymbol{x}$ and $\boldsymbol{u}$ denote the location and deformation inside the element, while the symbol $\tilde{(\cdot)}$ indicate the nodal values of these variables.
To find the spatial derivative of any kinematic value across the element, the derivative of the shape function should be found via

$$\frac{\partial N_i(\boldsymbol{\xi})}{\partial \xi_j} = \frac{\partial N_i(\boldsymbol{\xi})}{\partial x_1}\frac{\partial x_1}{\partial \xi_j} + \frac{\partial N_i(\boldsymbol{\xi})}{\partial x_2}\frac{\partial x_2}{\partial \xi_j} + \frac{\partial N_i(\boldsymbol{\xi})}{\partial x_3}\frac{\partial x_3}{\partial \xi_j}, \tag{A.6}$$

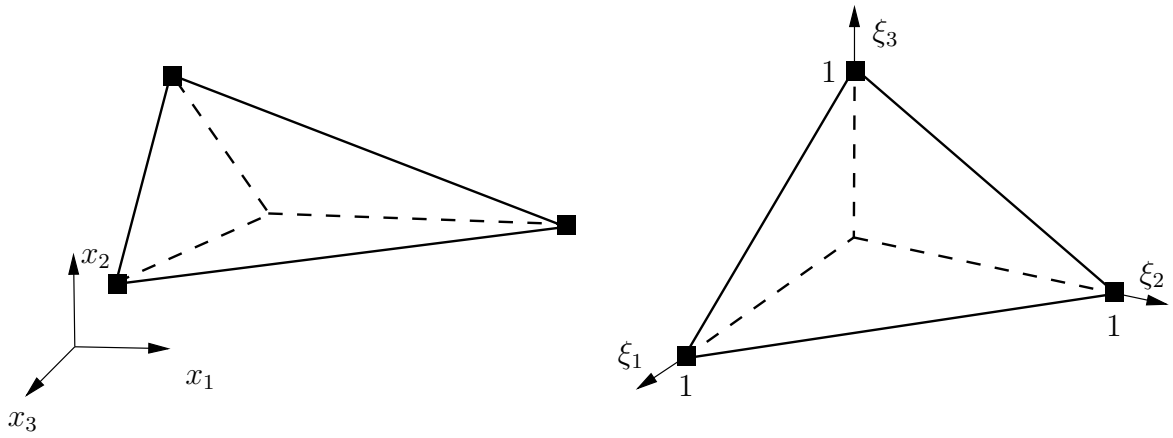

Figure A.1: Global and parent domains of a four-noded tetrahedral element

which can be written as

$$\frac{\partial N_i(\boldsymbol{\xi})}{\partial \xi_j} = J_{jk} \frac{\partial N_i(\boldsymbol{\xi})}{\partial x_k}, \tag{A.7}$$

where $\boldsymbol{J}$ is the Jacobian matrix defined by

$$\boldsymbol{J} = \begin{bmatrix} \dfrac{\partial x_1}{\partial \xi_1} & \dfrac{\partial x_2}{\partial \xi_1} & \dfrac{\partial x_3}{\partial \xi_1} \\ \dfrac{\partial x_1}{\partial \xi_2} & \dfrac{\partial x_2}{\partial \xi_2} & \dfrac{\partial x_3}{\partial \xi_2} \\ \dfrac{\partial x_1}{\partial \xi_3} & \dfrac{\partial x_2}{\partial \xi_3} & \dfrac{\partial x_3}{\partial \xi_3} \end{bmatrix}. \tag{A.8}$$

Therefore, direct mapping is used when variables are mapped from global to local coordinates system, whereas the inverse mapping if variables are represented in global coordinates, such that

$$\frac{\partial N_i}{\partial \boldsymbol{x}} = \boldsymbol{J}^{-1} \frac{\partial N_i}{\partial \boldsymbol{\xi}}, \tag{A.9}$$

where $\boldsymbol{J}^{-1}$ is the inverse of the Jacobian matrix.

Appendix B

Initial position of particles

B.1 Solid and fluid materials

For the MPM initialisation, the number of particles inside each tetrahedral element is assigned. In other words, the Lagrangian body is discretised using non-structured tetrahedral mesh, while the empty elements have no material. Therefore, the element either is fully-filled with material points or empty with no option of having partially-filled element. However, defining partially-filled elements at the beginning of the calculation has been required and used at some places along this thesis as will be shown later.

B.1.1 Fully-filled elements

For the fully-filled elements, three options $(1, 4, 10)$ are available for the initial number of particles per element. The initial position of the particles inside the tetrahedral element is located in the parent space [2, 21] as shown in Figure B.1 and Table B.1, whereas the variable appearing in the table are defined as

$$a = \frac{5-\sqrt{5}}{20} \quad , \quad b = \frac{5+3\sqrt{5}}{20} \quad , \quad c = \frac{3a+b}{4} \quad \text{and} \quad d = \frac{a+b}{2}. \tag{B.1}$$

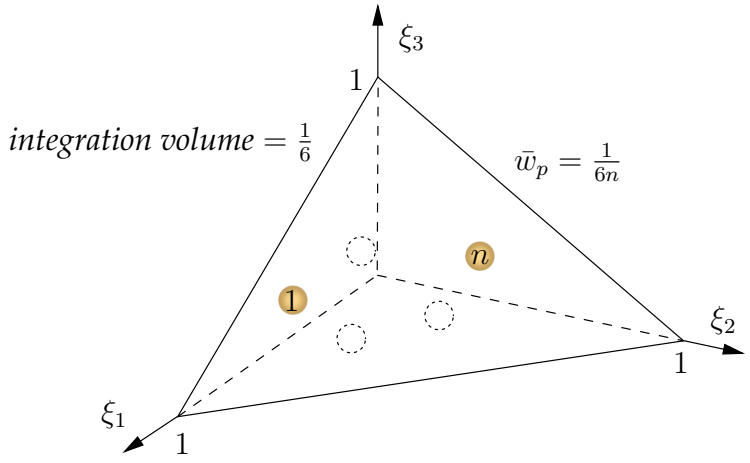

Figure B.1: Initial particles distribution in parent space

Table B.1: Initial position of particles in parent tetrahedral element

particle	ten particles				four particles				one particle			
	ξ_1	ξ_2	ξ_3	$\bar{w}_p$	ξ_1	ξ_2	ξ_3	$\bar{w}_p$	ξ_1	ξ_2	ξ_3	$\bar{w}_p$
1	a	a	a	0.017	a	a	a	0.042	c	c	c	0.167
2	a	a	b	0.017	a	a	b	0.042				
3	b	a	a	0.017	b	a	a	0.042				
4	a	b	a	0.017	a	b	a	0.042				
5	a	a	d	0.017								
6	d	a	a	0.017								
7	a	d	a	0.017								
8	d	a	d	0.017								
9	a	d	d	0.017								
10	d	d	a	0.017								

The integration domain of the tetrahedral element in the parent coordinated is divided linearly among the particles inside. Therefore, the integration domain $\bar{w}_p$ of the material point p is as given in Table B.1. In order to obtain the integration weight of the material points in global coordinate, the following transformation should be applied

$$w_p = \bar{w}_p \, |\boldsymbol{J}\,(\boldsymbol{\xi})\,|, \tag{B.2}$$

with $|\boldsymbol{J}|$ being the determinant of the Jacobian matrix. Let us take an example of discretising the domain shown in Figure B.2 with regular tetrahedral elements. As a first step, the domain is discretised similar to the FE discretisation considering that empty

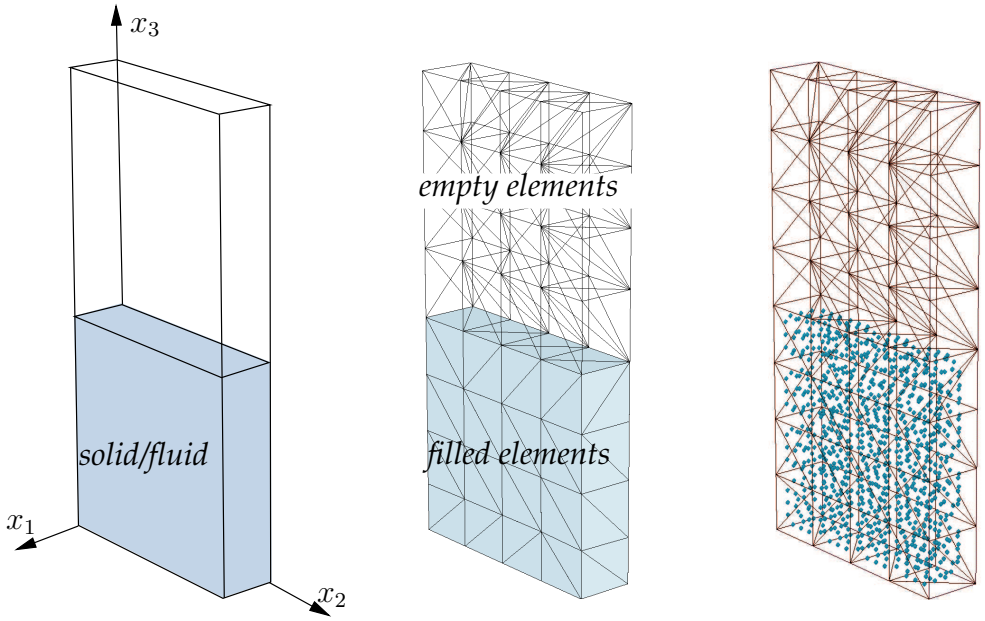

Figure B.2: MPM discretisation: (left) continuum (middle) FE discretisation, and (right) initialisation of particles

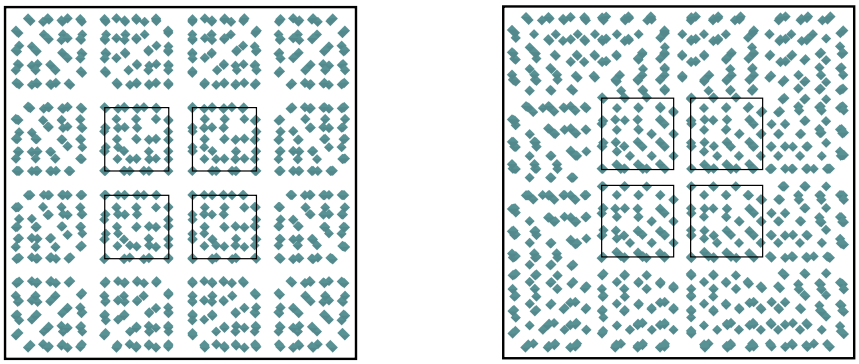

Figure B.3: Effect of initial particles position: (left) using Equation B.1 and (right) modified values

elements must be added at the modelling stage where the material is expected to move. Next after getting the particle position in the parent space, the following transformation is applied to get the particle position in global coordinate

$$\boldsymbol{x}_p = \sum_{i=1}^{n_n} N_i\left(\boldsymbol{\xi}_p\right) \boldsymbol{x}_i, \tag{B.3}$$

where $\boldsymbol{x}_p$ is the global position of the particle p, n_n is the total number of nodes, and $N_i\left(\boldsymbol{\xi}_p\right)$ is the shape function of node i being evaluated at the local position $\boldsymbol{\xi}_p$.
For some cases where regular mesh discretisation is applied, using the values in Equation B.1 concentrates the particles distribution at the center of the tetrahedral element. Adopting different value might gives more regular distribution for the initial particle locations; e.g., adopting the values of $a = 0.1$ and $b = 0.65$ in Table B.1 produces the distribution demonstrated in Figures B.3, which looks more regular. In general, the particles distribution density should be somehow correlated to the mesh size in order to avoid empty elements and consequently inactive nodes inside the continuum body. Furthermore, the particles distribution shown in Figure B.3 might exaggerate the grid-crossing error if the deformation aligned the layering scheme of the particles. In other words, increasing the number of particles crossing the element at the same time increases the instability coming from the grid-crossing error.

B.1.2 Partially-filled elements

As mentioned earlier, the present MPM initialisation procedure exploits the irregular tetrahedral mesh to identify objects in the preprocessing stage. While in this case the element is either fully-filled or empty of particles, there is a chance to have poor element quality with low dihedral angles. As a result, the computational time is becoming extremely small as it is controlled by the minimum height of the element, especially in the case of nearly-incompressible fluid. To improve the mesh quality and consequently the minimum characteristic length, regular mesh discretisation can be used or a regular-

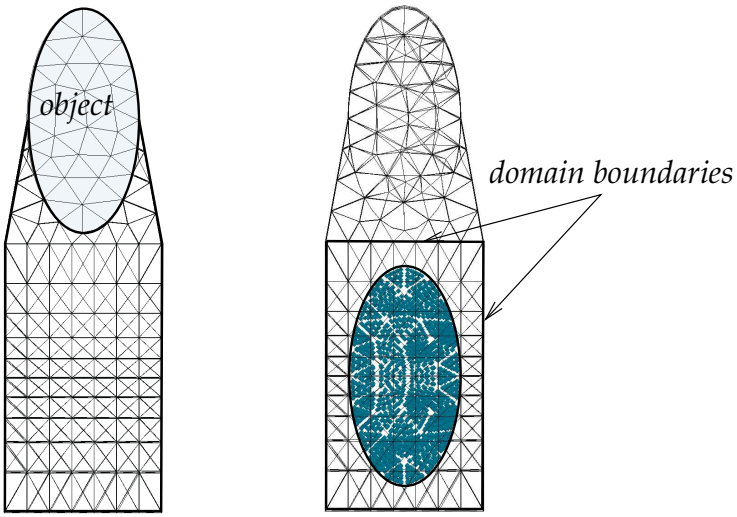

Figure B.4: Initial MPM discretisation with partially-filled elements: (left) object initialisation and (right) shift particles

isation technique can be applied; see e.g. [56, 60]. As regularisation techniques might be expensive in terms of computational time, we adopt a regular mesh where there is a need to speed up the computation.

Since having regular mesh discretisation might not necessarily comply with our preprocessor, which has only the option of fully-filled elements, defining partially-filled elements is required. For instance, an elliptical object need to be initialised in a rectangular domain being discretised with regular tetrahedral mesh. Therefore, the object is created and discretised with particles outside the computational domain. Next, the particles are moved inside the regular area like a rigid body as shown in Figure B.4. The domain boundaries are applied on the computational mesh excluding the mesh outside.

B.2 Surface discretisation

In the case of the membrane, two type of discretisation should be considered: the surface discretisation to define the membrane particles and tetrahedral mesh where the computation is achieved. In this thesis, the triangular element with three nodes is used for the membrane discretisation. The membrane particles are places at the (nodes) locations of the surface mesh. The connectivity of the membrane particles are preserved during the computation.

The surface discretisation is not used for the membrane discretisation only, but also around the solid objects to track the surface properly. Tracking the deformed surface with a mesh is useful to detect the unit normal at each point, which is needed when the contact algorithm is applied. Defining surface normal is also important to apply the surface traction in solids or the free-surface condition in fluids. However, the tangential components are assumed to be zero in this research for the case of water. Therefore,

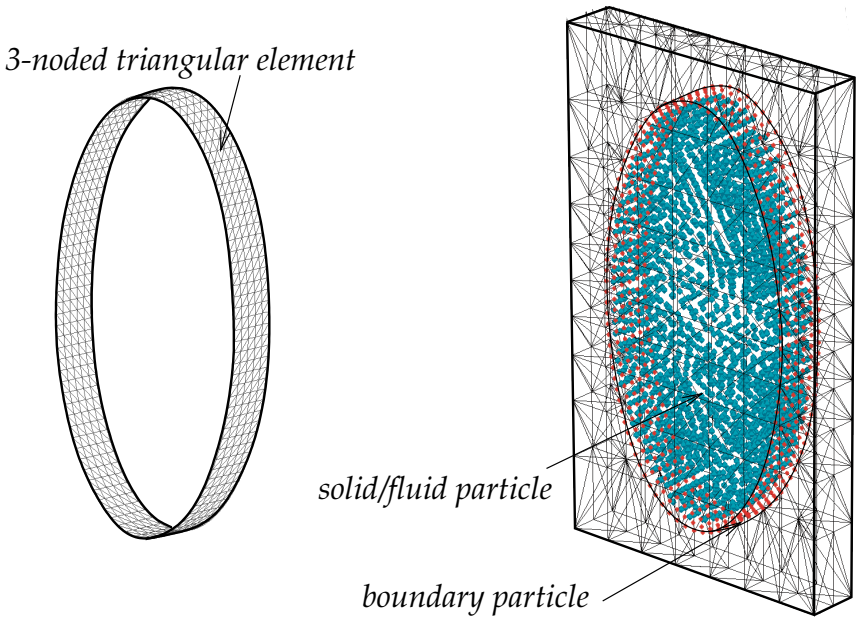

Figure B.5: MPM surface discretisation: (left) surface triangular mesh and (right) overlap of surface and volume discretisations

there is no need for explicit detection of the unit normal. When a surface is discretised, information of the normal vector and the corresponding surface area are stored on the boundary particles. Furthermore, these particles can be assigned very little mass to enter the momentum equation or they have to follow the deformation of the solid particles.

Usually, the surface mesh is selected relatively finer than tetrahedral mesh with a mesh ratio MR higher than 1 to ensure continuous surface with no gaps when information mapped back to the computational mesh. The elliptical object presented previously is considered here in Figure B.5 with surface discretisation. Each boundary particle is assigned a corresponding surface area by lumping the continuous surface as

$$\Gamma_b = \sum_{i=1}^{N_{tri}} \frac{A_{tri}^i}{3}, \tag{B.4}$$

where Γ_b is the corresponding surface area of particle b, N_{tri} is the number of neighbor triangles to b and A_{tri}^i is the area of the triangle i. For this specific case of a plane problem is assumed, the front and the back faces are excluded. The mesh ratio in this figure has a value of 4 with both: the triangular and the tetrahedral meshes are being regular. Within the computation process, it is important to update the corresponding surface area over each individual particle. As proven in this research, updating the surface area of the boundary particle has an influence at least in the case of membrane modelling.

Appendix C

Particles searching algorithm

Irregular mesh discretisation has been applied in many applications [22, 89, 184]. Using different mesh refinement in the same model is important to get higher accuracy in zones where high gradient is taking place. Although there are some attempts to implement local refinement with regular grid by tracing the deformation intensity and then dividing the computational domain into multiple nested levels of refinement [172], however, refining the material points needs extra time for communication [118]. Therefore, a searching algorithm is required to relocate particles in elements instead of the trivial searching in the case of regular mesh [126, 155].

A systematic searching method can be constructed in a way similar to that in Figure C.1. Although the discretisation must cover the entire area where particles are expected to move, only active degrees of freedom are considered in the computation cycle. Therefore, the size of the mesh should not affect the computation efficiency that much. After updating the coordinate of the material point and checking that the point belong to the current mesh, the first location to search inside for the particle is the existing element where the particle belongs to. As long as explicit time integration scheme is adopted, it is most probable that the particle does not cross many elements during one time step.

In order to track the particle path, let us consider a particle P moving outside a triangle ABC as demonstrated in Figure C.2. To check from which of the three triangle sides the particle has left, we need to define a reference point inside the triangle; for example the center of the triangle O. Considering the sub-triangle OCB, the only possibility for P to be outside is to fall inside one of the three gray zones. Defining vectors connecting points together using the format $\overrightarrow{BA}$, which means the vector indicating toward B starting from A. The condition to check whether P is inside the triangle or not is obtained by applying the following inequality for all the three sides

$$\left(\overrightarrow{BC} \cdot \overrightarrow{PC}\right) \times \left(\overrightarrow{BC} \cdot \overrightarrow{OC}\right) \geqslant 0, \tag{C.1}$$

which is nothing more than a condition for the two points P and O to be on the same side of the line BC or not. If Equation C.1 is true at least for one side, the tracking will proceed in this direction, otherwise, the particle is still inside the element. Getting the side number allows us to move toward the neighbor element, which is attached to this side. Similar procedure is repeated in a recursive way till the final destination of the particle is located. In the case of tetrahedral element, four faces are checked with four sub-tetrahedrons. As next, the book-keeping is updated for the final number of particles inside each element and the connectivity between the particle and the associated cell.

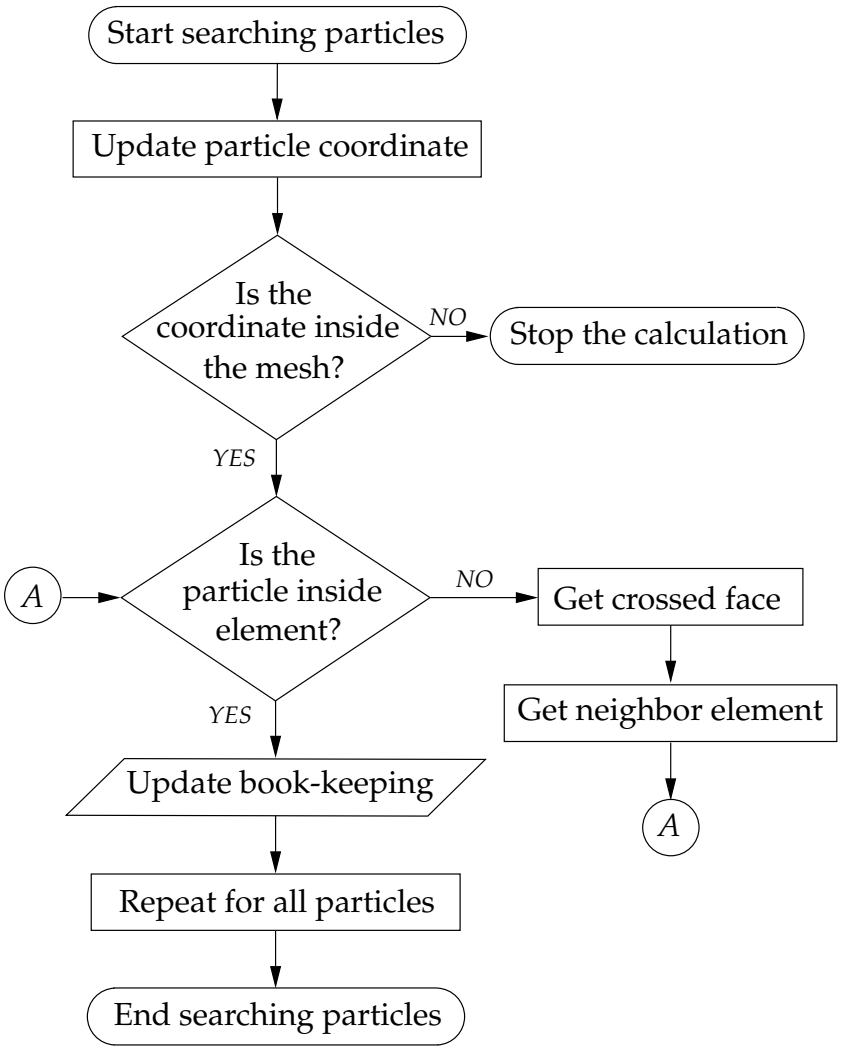

Figure C.1: Searching algorithm for particles in an irregular mesh discretisation

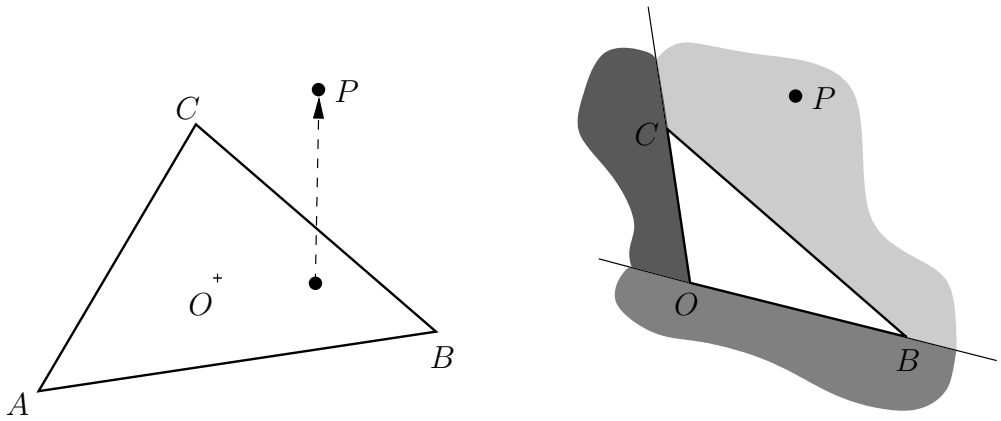

Figure C.2: Illustration of tracking a point moving outside a triangle

Appendix D

Vector notation

Transformation for the displacement vector from the global $\boldsymbol{u} = [u_1 \quad u_2 \quad u_3]^T$ to local $\hat{\boldsymbol{u}}$ frames of reference is given by

$$\hat{\boldsymbol{u}} = \boldsymbol{T}\boldsymbol{u} \tag{D.1}$$

where the rotation matrix $\boldsymbol{T}$ reads

$$\boldsymbol{T} = \begin{bmatrix} \cos(\hat{e}_1, e_1) & \cos(\hat{e}_1, e_2) & \cos(\hat{e}_1, e_3) \\ \cos(\hat{e}_2, e_1) & \cos(\hat{e}_2, e_2) & \cos(\hat{e}_2, e_3) \\ \cos(\hat{e}_3, e_1) & \cos(\hat{e}_3, e_2) & \cos(\hat{e}_3, e_3) \end{bmatrix} \tag{D.2}$$

with $\boldsymbol{e} = [e_1 \quad e_2 \quad e_3]^T$ and $\hat{\boldsymbol{e}} = [\hat{e}_1 \quad \hat{e}_2 \quad \hat{e}_3]^T$ are the bases vectors in terms of global and corotated frame of references, respectively.
The strain tensor can be written in vector form such that $\boldsymbol{\varepsilon} = [\varepsilon_{11} \quad \varepsilon_{22} \quad \varepsilon_{33} \quad 2\varepsilon_{12} \quad 2\varepsilon_{23} \quad 2\varepsilon_{13}]^T$, which can be transformed according to $\hat{\boldsymbol{\varepsilon}} = \boldsymbol{T}_\varepsilon \boldsymbol{\varepsilon}$, where $\boldsymbol{T}_\varepsilon$ is defined as [204]

$$\boldsymbol{T}_\varepsilon = \begin{bmatrix} t_{11}t_{11} & t_{12}t_{12} & t_{13}t_{13} & t_{11}t_{12} & t_{12}t_{13} & t_{13}t_{11} \\ t_{21}t_{21} & t_{22}t_{22} & t_{23}t_{23} & t_{21}t_{22} & t_{22}t_{23} & t_{23}t_{21} \\ t_{31}t_{31} & t_{32}t_{32} & t_{33}t_{33} & t_{31}t_{32} & t_{32}t_{33} & t_{33}t_{31} \\ 2t_{11}t_{21} & 2t_{12}t_{22} & 2t_{13}t_{23} & (t_{11}t_{22} + t_{12}t_{21}) & (t_{12}t_{23} + t_{13}t_{22}) & (t_{13}t_{21} + t_{11}t_{23}) \\ 2t_{21}t_{31} & 2t_{22}t_{32} & 2t_{23}t_{33} & (t_{21}t_{32} + t_{22}t_{31}) & (t_{22}t_{33} + t_{23}t_{32}) & (t_{23}t_{31} + t_{21}t_{33}) \\ 2t_{31}t_{11} & 2t_{32}t_{12} & 2t_{33}t_{13} & (t_{31}t_{12} + t_{32}t_{11}) & (t_{32}t_{13} + t_{33}t_{12}) & (t_{33}t_{11} + t_{31}t_{13}) \end{bmatrix} \tag{D.3}$$

while the stress vector $\boldsymbol{\sigma} = [\sigma_{11} \quad \sigma_{22} \quad \sigma_{33} \quad \sigma_{12} \quad \sigma_{23} \quad \sigma_{13}]^T$ is transformed $\hat{\boldsymbol{\sigma}} = \boldsymbol{T}_\sigma \boldsymbol{\sigma}$ using slightly different transformation matrix; i.e.,

$$\boldsymbol{T}_\sigma = \begin{bmatrix} t_{11}t_{11} & t_{12}t_{12} & t_{13}t_{13} & 2t_{11}t_{12} & 2t_{12}t_{13} & 2t_{13}t_{11} \\ t_{21}t_{21} & t_{22}t_{22} & t_{23}t_{23} & 2t_{21}t_{22} & 2t_{22}t_{23} & 2t_{23}t_{21} \\ t_{31}t_{31} & t_{32}t_{32} & t_{33}t_{33} & 2t_{31}t_{32} & 2t_{32}t_{33} & 2t_{33}t_{31} \\ t_{11}t_{21} & t_{12}t_{22} & t_{13}t_{23} & (t_{11}t_{22} + t_{12}t_{21}) & (t_{12}t_{23} + t_{13}t_{22}) & (t_{13}t_{21} + t_{11}t_{23}) \\ t_{21}t_{31} & t_{22}t_{32} & t_{23}t_{33} & (t_{21}t_{32} + t_{22}t_{31}) & (t_{22}t_{33} + t_{23}t_{32}) & (t_{23}t_{31} + t_{21}t_{33}) \\ t_{31}t_{11} & t_{32}t_{12} & t_{33}t_{13} & (t_{31}t_{12} + t_{32}t_{11}) & (t_{32}t_{13} + t_{33}t_{12}) & (t_{33}t_{11} + t_{31}t_{13}) \end{bmatrix} \tag{D.4}$$

in both transformation matrices, t_{ij} is obtained from Equation D.2.
For isotropic elastic materials, the constitutive equation $\boldsymbol{\sigma} = \boldsymbol{D}\,\boldsymbol{\varepsilon}$ can be written in vector notation as follows:

$$\begin{bmatrix}\sigma_{11}\\ \sigma_{22}\\ \sigma_{33}\\ \sigma_{12}\\ \sigma_{23}\\ \sigma_{13}\end{bmatrix} = \bar{E}\begin{bmatrix}1-\nu & \nu & \nu & 0 & 0 & 0\\ \nu & 1-\nu & \nu & 0 & 0 & 0\\ \nu & \nu & 1-\nu & 0 & 0 & 0\\ 0 & 0 & 0 & (1-2\nu)/2 & 0 & 0\\ 0 & 0 & 0 & 0 & (1-2\nu)/2 & 0\\ 0 & 0 & 0 & 0 & 0 & (1-2\nu)/2\end{bmatrix}\begin{bmatrix}\varepsilon_{11}\\ \varepsilon_{22}\\ \varepsilon_{33}\\ 2\varepsilon_{12}\\ 2\varepsilon_{23}\\ 2\varepsilon_{13}\end{bmatrix} \tag{D.5}$$

with $\bar{E} = E/(1+\nu)(1-2\nu)$, where E and ν are Young's modulus of elasticity and Poisson's ratio, respectively.
For the membrane element, matrix $\hat{\boldsymbol{D}}$ can be written for the plane-stress condition in the form

$$\hat{\boldsymbol{D}} = \frac{E_m}{1-\nu^2}\begin{bmatrix}1 & \nu & 0\\ \nu & 1 & 0\\ 0 & 0 & \frac{1-\nu}{2}\end{bmatrix} \tag{D.6}$$

with E_m being the elastic stiffness of the membrane and ν is Poisson's ratio. Implicit use of $\hat{\boldsymbol{D}}$ is the assumption that the non-tangential strain components can be neglected.

Appendix E

3-noded element in 3D space

The interpolation matrix $\boldsymbol{H}$ of a 3-noded triangular element in three-dimensional space is a (3×12) matrix given by

$$\boldsymbol{H}(\boldsymbol{x}) = \left[\boldsymbol{H}_1(\boldsymbol{x}) \quad \boldsymbol{H}_2(\boldsymbol{x}) \quad \boldsymbol{H}_3(\boldsymbol{x}) \right], \tag{E.1}$$

with

$$\boldsymbol{H}_i(\boldsymbol{x}) = \begin{bmatrix} H_i(\boldsymbol{x}) & 0 & 0 \\ 0 & H_i(\boldsymbol{x}) & 0 \\ 0 & 0 & H_i(\boldsymbol{x}) \end{bmatrix}, \tag{E.2}$$

which are given for the specific three-noded element of Figure E.1 by

$$\begin{aligned} H_1(\boldsymbol{\xi}) &= 1 - \xi_1 - \xi_2, \\ H_2(\boldsymbol{\xi}) &= \xi_1, \\ H_3(\boldsymbol{\xi}) &= \xi_2, \end{aligned} \tag{E.3}$$

where $\boldsymbol{\xi}$ are the natural or the parent coordinates.
For the isoparametric approximation, we need the spatial first derivative of displacements and therefore the derivative of the shape functions, which are computed using

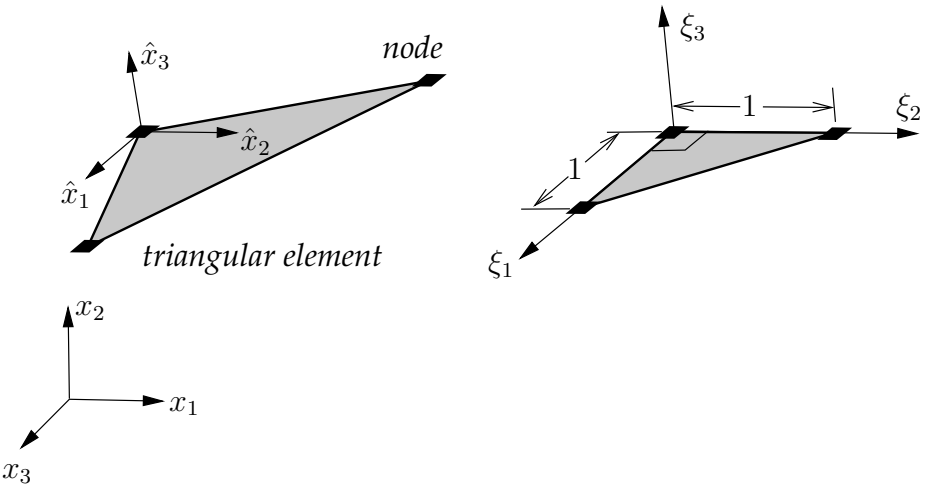

Figure E.1: Global (left) and parent (right) domains of a three-noded triangular element in three-dimensional space

the chain rule

$$\frac{\partial H_i(\boldsymbol{\xi})}{\partial \xi_j} = \frac{\partial H_i(\boldsymbol{\xi})}{\partial x_1}\frac{\partial x_1}{\partial \xi_j} + \frac{\partial H_i(\boldsymbol{\xi})}{\partial x_2}\frac{\partial x_2}{\partial \xi_j} + \frac{\partial H_i(\boldsymbol{\xi})}{\partial x_3}\frac{\partial x_3}{\partial \xi_j}, \tag{E.4}$$

with $i, j \in (1, 2, 3)$. Equation E.4, can be represented in compact form as

$$\frac{\partial H_i(\boldsymbol{\xi})}{\partial \xi_j} = J_{ik}\frac{\partial H_j(\boldsymbol{\xi})}{\partial x_k}, \tag{E.5}$$

where $\boldsymbol{J}$ is the Jacobian matrix defined by

$$\boldsymbol{J} = \begin{bmatrix} \dfrac{\partial x_1}{\partial \xi_1} & \dfrac{\partial x_2}{\partial \xi_1} & \dfrac{\partial x_3}{\partial \xi_1} \\ \dfrac{\partial x_1}{\partial \xi_2} & \dfrac{\partial x_2}{\partial \xi_2} & \dfrac{\partial x_3}{\partial \xi_2} \\ \dfrac{\partial x_1}{\partial \xi_3} & \dfrac{\partial x_2}{\partial \xi_3} & \dfrac{\partial x_3}{\partial \xi_3} \end{bmatrix}, \tag{E.6}$$

which describe the transformation between $\boldsymbol{x}$ and $\boldsymbol{\xi}$. As the aim is to find the derivatives with respect to the global coordinates, the following transformation is applied

$$\frac{\partial H_i}{\partial \boldsymbol{x}} = \boldsymbol{J}^{-1}\frac{\partial H_i}{\partial \boldsymbol{\xi}}, \tag{E.7}$$

with $\boldsymbol{J}^{-1}$ being the inverse of the Jacobian matrix.

Curriculum Vitæ

1 December 1977	Born in Baghdad, Iraq
1995 – 1999	B.Sc. student in Mechanical Engineering, University of Baghdad
1999 – 2002	M.Sc. student in Mechanical Engineering, University of Baghdad
2003 – 2009	Teaching and research associate, University of Baghdad
2009 – 2010	Teaching and research associate, Stuttgart University
2010 – 2012	Secondment at Deltares in the framework of GEO-INSTALL project being funded by the EU
2012 – 2014	Teaching and research associate, Stuttgart University
Since June 2014	Postdoctoral researcher, Stuttgart University

Mitteilungen des Instituts für Geotechnik der Universität Stuttgart

Mitteilungen des Baugrundinstitutes Stuttgart
(Institut für Grundbau und Bodenmechanik)
der Universität Stuttgart
Hrsg.: Prof. Dr.-Ing. Dr. h.c. U. Smoltczyk

Nr. 01	Thamm, B. R.	(1974)	Anfangssetzungen und Anfangsporenwasser-überdrücke eines normalverdichteten wasser-gesättigten Tones
Nr. 02	Gußmann, P.	(1975)	Einheitliche Berechnung von Grundbruch und Böschungsbruch
Nr. 03	Feeser, V.	(1975)	Die Bedeutung des Kalziumkarbonats für die bodenphysikalischen Eigenschaften vom Löß
Nr. 04	Du Thin, K.	(1976)	Standsicherheit von Böschungen: Programm-Dokumentation
Nr. 05	Smoltczyk, U./ Pertschi, O./ Hilmer, K.	(1976)	Messungen an Schleusen in der UDSSR. Schleusennorm der UDSSR (SN 30365)
Nr. 06	Hilmer, K.	(1976)	Erddruck auf Schleusenkammerwände
Nr. 07	Laumans, Q.	(1977)	Verhalten einer ebenen, in Sand eingespannten Wand bei nichtlinearen Stoffeigenschaften des Bodens
Nr. 08	Lächler, W.	(1977)	Beitrag zum Problem der Teilflächenpressung bei Beton am Beispiel der Pfahlkopfanschlüsse

Nr. 09	Spotka, H.	(1977)	Einfluß der Bodenverdichtung mittels Oberflächenrüttelgeräten auf den Erddruck einer Stützwand bei Sand
Nr. 10	Schad, H.	(1979)	Nichtlineare Stoffgleichungen für Böden und ihre Verwendung bei der numerischen Analyse von Grundbauaufgaben
Nr. 11	Ulrich, G.	(1980)	Verschiebungs- und kraftgesteuerte Plattendruckversuche auf konsolidierenden Böden
	Gußmann, P.		Zum Modellgesetz der Konsolidation
Nr. 12	Salden, D.	(1980)	Der Einfluß der Sohlenform auf die Traglast von Fundamenten
Nr. 13	Seeger, H.	(1980)	Beitrag zur Ermittlung des horizontalen Bettungsmoduls von Böden durch Seitendruck-versuche im Bohrloch
Nr. 14	Schmidt, H.H.	(1981)	Beitrag zur Ermittlung des Erddrucks auf Stützwände bei nachgiebigem Baugrund
Nr. 15	Smoltczyk, U./ Schweikert, O.	(1981)	Vorstudie über bauliche Alternativen für Durch-gangsstraßen in Siedlungen
Nr. 16	Malcharek, K./ Smoltczyk, U.	(1981)	Vergleich nationaler Richtlinien für die Berech-nung von Fundamenten
Nr. 17	Gruhle, H.D.	(1981)	Das Verhalten des Baugrundes unter Einwirkung vertikal gezogener Ankerplatten als räumliches Problem des Erdwiderstandes
Nr. 18	Kobler, W.	(1982)	Untersuchungen über Böschungs- und Grund-bruch bei begrenzten Lastflächen

Nr. 19	Lutz, W.	(1983)	Tragfähigkeit des geschlitzten Baugrunds neben Linienlasten
Nr. 20	Smoltczyk, U.	(1983)	Studienunterlagen “Bodenmechanik und Grund-bau“; überarbeitete Ausgabe 1993
Nr. 21	Schweikert, O.	(1984)	Der Einfluß des Böschungswinkels auf die Be-rechnung des aktiven Erddrucks
Nr. 22	Vogt, N.	(1984)	Erdwiderstandsermittlung bei monotonen und wiederholten Wandbewegungen in Sand
Nr. 23	Buchmaier, R.	(1985)	Zur Berechnung von Konsolidationsproblemen bei nichtlinearem Stoffverhalten
Nr. 24	Schad, H. Smoltczyk, U./ Schad, H./Zoller, P.	(1985)	Möglichkeiten der Böschungssicherung bei kleinen Baugruben Sonderkonstruktionen der Böschungssicherung
Nr. 25	Gußmann, P.	(1986)	Die Methode der Kinematischen Elemente
Nr. 26	Steinmann, B.	(1985)	Zum Verhalten bindiger Böden bei monotoner einaxialer Beanspruchung
Nr. 27	Lee, S.D.	(1987)	Untersuchungen zur Standsicherheit von Schlit-zen im Sand neben Einzelfundamenten

Mitteilungen des
Instituts für Geotechnik der Universität Stuttgart
Hrsg.: Prof. Dr.-Ing. Dr. h.c. U. Smoltczyk

Nr. 28	Kolb, H.	(1988)	Ermittlung der Sohlreibung von Gründungskör-pern unter horizontalem kinematischen Zwang
Nr. 29	Ochmann, H.	(1988)	Ebene Grenzzustände von Erdböschungen im stochastischen Sicherheitskonzept
Nr. 30	Breinlinger, F.	(1989)	Bodenmechanische Stoffgleichungen bei großen Deformationen sowie Be- und Entlastungsvor-gängen
Nr. 31	Smoltczyk, U./ Breinlinger, F./ Schad, H./ Wittlinger, M.	(1989)	Beitrag zur Bemessung von Tunneln in offener Bauweise
Nr. 32	Gußmann, P./ Schanz, T./ Smoltczyk, U./ Willand, E.	(1990)	Beiträge zur Anwendung der KEM (Erddruck, Grundbuch, Standsicherheit von Böschungen)
Nr. 33	Gruhle, H.D.	(1990)	Der räumliche Erdwiderstand vor überwiegend horizontal belasteten Ankerplatten
Nr. 34	Henne, J.	(1995)	Zur Bewehrung von verformten Bodenschichten durch Einsatz zugfester Geokunststoffe
Nr. 35	Wittlinger, M.	(1994)	Ebene Verformungsuntersuchungen zur We-ckung des Erdwiderstandes bindiger Böden
Nr. 36	Schad, H.	(1992)	Zeit- und geschwindigkeitsabhängiges Material-verhalten in der Geotechnik – Experimentelle Erfassung und numerische Analyse

Nr. 37	Belz, I.	(1992)	Zur Ermittlung dynamischer Bodenkennwerte in situ aus der Systemantwort des Erregers
Nr. 38	Ma, J.	(1994)	Untersuchungen zur Standsicherheit der durch Stützscheiben stabilisierten Böschungen
Nr. 39	Smoltczyk, U.	(1994)	Sonderheft: 25 Jahre Lehre und Forschung in der Geotechnik
Nr. 40	Rilling, B.	(1994)	Untersuchungen zur Grenztragfähigkeit bindiger Schüttstoffe am Beispiel von Lößlehm

Mitteilungen des
Instituts für Geotechnik der Universität Stuttgart
Hrsg.: Prof. Dr.-Ing. P.A. Vermeer

Nr. 41	Vermeer, P.A.	(1996)	Deponiebau und Geotechnik
Nr. 42	Vermeer, P.A.	(1997)	Baugruben in Locker- und Festgestein
Nr. 43	Brinkmann, C.	(1998)	Untersuchungen zum Verhalten von Dichtungs-übergängen im Staudammbau
Nr. 44	Fiechter-Scharr, I.	(1998)	Beeinflussung von Erdbaustoffen durch Beimi-schen eines organophilen Bentonits
Nr. 45	Schanz, T.	(1998)	Zur Modellierung des mechanischen Verhaltens von Reibungsmaterialien
Nr. 46	Akinrogunde, A.E.	(1999)	Propagation of Cement Grout in Rock Discon-tinuities Under Injection Conditions

Nr. 47	Vogt-Breyer, C.	(1999)	Experimentelle und numerische Untersuchungen zum Tragverhalten und zur Bemessung hori-zontaler Schraubanker
Nr. 48	Vermeer, P.A.	(1999)	Neue Entwicklungen in der Geotechnik
Nr. 49	Marcher, T.	(2002)	Resultate eines Versuchsprogramms an Beau-caire Mergel
Nr. 50	Marcher, T.	(2003)	Nichtlokale Modellierung der Entfestigung dichter Sande und steifer Tone
Nr. 51	Ruse, N.M.	(2004)	Räumliche Betrachtung der Standsicherheit der Ortsbrust beim Tunnelvortrieb
Nr. 52	Beutinger, P.H.	(2005)	Ein geotechnischer Beitrag zur Standsicherheit mobiler Baumaschinen
Nr. 53	Wehnert, M.	(2006)	Ein Beitrag zur drainierten und undrainierten Analyse in der Geotechnik
Nr. 54	Möller, S. C.	(2006)	Tunnel induced settlements and forces in linings
Nr. 55	Benz, T.	(2007)	Small-Strain Stiffness of Soils and its Numerical Consequences
Nr. 56	Abed, A.	(2008)	Numerical Modeling of Expansive Soil Behavior
Nr. 57	Hintner, J.	(2008)	Analyse der Fundamentverschiebungen infolge vertikaler und geneigter Belastung

Nr. 58	Russelli, C.	(2008)	Probabilistic Methods applied to the Bearing Capacity Problem
Nr. 59	Peña Olarte, A.A.	(2008)	Influence of Particle Shape on the Global Mechanical Response of Granular Packings: Micromechanical Investigation of the Critical State in Soil Mechanics
Nr. 60	Neher, H.P.	(2008)	Zeitabhängiges Materialverhalten und Aniso-tropie von weichen Böden – Theorie und Anwendung
Nr. 61	Vermeer, P.A.	(2008)	Von der Forschung zur Praxis: Symposium anlässlich des 80. Geburtstags von Prof. U. Smoltczyk
Nr. 62	Syawal, S.	(2009)	Numerical Analysis and Design Criteria of Embankments on Floating Piles
Nr. 63	Lächler, A.	(2009)	Bedeutung herstellungsbedingter Einflüsse auf das Trag- und Verformungsverhalten von Schlitzwänden
Nr. 64	Möllmann, A.	(2009)	Probabilistische Untersuchung von Hochwasser-schutzdeichen mit analytischen Verfahren und der Finite-Elemente-Methode

Mitteilungen des
Instituts für Geotechnik der Universität Stuttgart
Hrsg.: Prof. Dr.-Ing. habil. Ch. Moormann

Nr. 65	Moormann, Ch.	(2011)	7. Stuttgarter Geotechnik-Symposium

Nr. 66	Beuth, L.	(2012)	Formulation and Application of a Quasi-Static Material Point Method
Nr. 67	Moormann, Ch., Huber, M., Proske, D.	(2012)	Proceedings of the 10th International Probabilistic Workshop
Nr. 68	Schneider, M.	(2013)	Zur energetischen Nutzung von Tunnelbauwerken – Messungen und numerische Berechnungen am Beispiel Fasanenhoftunnel
Nr. 69	Huber, M.	(2013)	Soil variability and its consequences in geotechnical engineering
Nr. 70	Hamad, F.	(2014)	Formulation of a Dynamic Material Point Method and Applications to Soil–Water–Geotextile Systems